MEMÒRIA DE LA TESI PRESENTADA PER A
L' OBTENCIÓ DEL TÍTOL DE DOCTOR EN FÍSICA

Thermal Diagnostics in the

LISA Technology Package Experiment

Miquel Nofrarias i Serra

Octubre 2007

Director: Dr. José Alberto Lobo Gutiérrez

Tutor: Dr. Enric Verdaguer Oms

Programa de Doctorat de Física Avançada. Bienni 2003-2005

Departament de Física Fonamental

Universitat de Barcelona

Contents

Agraïments

Molt em temo que això dels agraïments és una causa perduda per endavant i que no hi haurà lloc per a tots els qui han intervingut en aquesta carrera de fons. Potser hi tindrien lloc si em cenyís als companys de treball i als de l'Institut però això quedaria lluny del que representa per mi el treball que segueix. Com deia el savi grec: Tot és Un.

Quedi clar doncs que no es pretén fer aquí una desfilada exhaustiva de personalitats però clar, tampoc no seria massa just obviar els que han patit aquest procés de més a prop. Així doncs, ja avanço les meves disculpes al qui s'acosti per aquí i no es trobi entre aquests amb qui he compartit amb més intensitat aquest trosset de vida.

Vull agrair l'Alberto Lobo que em donés l'oportunitat de tirar endavant un doctorat i que des de llavors m'hagi sorprès sovint amb una il·lusió contagiosa pel que quedava per fer i pel que calia aprendre. Arribats a aquestes alçades, un sap com mesurar i valorar la il·lusió, l'esforç o les preguntes incòmodes i es troba força desarmat davant conceptes com la vocació i la Ciència (amb majúscules!). Per això agraeixo el que per mi ha representat un motiu de motivació constant al que, per fer justícia, també cal afegir-hi la seva visió crítica, que m'ha permès caminar endavant amb passos més segurs.

Aquesta feina ha estat portada a terme en un ambient de continu canvi i reubicació: aquesta setmana em toca l'última mudança (*sic.*). Compartir aquestes tribulacions amb els companys de l'IEEC ha sigut una sort i a ells dec el sentir-me un més de la família. Moltes gràcies a tots els actuals *cybers* (Violeta, Moi, Anna's, Carlo, Silvia, Nil, Anaïs), *excybers* (Marc, Alina) i *outcybers* (Jose, Pep, Ignasi). Ànims als qui us enfronteu al "tesi.tex" i molta sort a tots ! Merci també a la gent d'administració Pilar, Anna, Eva i també Delfi per gestionar el que jo no sabia que era gestionable. *Last but not least*, moltes gràcies Josep per les incomptables solucions que m'has proporcionat i per la teva incansable dedicació que facilita la vida als mai prou desesperats usuaris.

He tingut la sort de treballar amb un equip de gent del que he après moltíssim i, el que és més important, que aprecio i dintre del qual em sento molt còmode. Gràcies doncs Xevi, Nacho, Carlos, Priscilla i molt especialment al meu *partenaire* tèrmic i filosòfic Pep i al mestre Juan. I, com no, al sofert manager-geek i company de zulo, Ivan. També gràcies als qui van passar en algun

Acronym list

AOM Acousto-Optical Modulator

A/D Analog-to-Digital Converter

AEI Albert Einstein Institute

ARMA Auto Regressive Moving Average

BMLS Binary Maximum Length Sequence

CGS Carlo Gavazzi Space

CFRP Carbon Fiber Reinforced Plastic

CTE Coefficient of Thermal Expansion

CVCM Collected Volatile Condensed Materials

DDS Data and Diagnostics Subsystem

DLR Direct Linear Regression

DMU Data Management Unit

DRS Disturbance Reduction System

EH Electrode Housing

EMRI Extreme Mass Ratio Inspiral

ESA European Space Agency

FEE Front-End Electronics

FEEP Field Emision Electric Propulsion

FEM Finite Elements Method

FPGA Field Programmable Gate Array

GCR Galactic Cosmic Rays

GR General Relativity

GRS Gravitational Reference Sensor

IA Instrumental Amplifier

IEEC Institut d'Estudis Espacials de Catalunya

INL Integrated NonLinearity

LCA LTP Core Assembly

LIGO Laser Interferometer Gravitational Wave Observatory

LISA Laser Interferometer Space Antenna

LPF LISA PathFinder

LTP LISA Technology Package

MBW Measuring BandWidth

MUX Multiplexer

NASA National Aeronautics and Space Administration

NTC Negative Temperature Coefficient

OMS Optical Metrology Subsystem

PDE Partial Differential Equations

PGA Programmable Gain Amplifier

PTC Positive Temperature Coefficient

PRN Pseudo-Random Noise

PRT Platinium Resistance Thermometer

PSA Pressure Sensitive Adhesive

PSD Power Spectral Density

SEP Solar Energetic Particles

RTD Resistance Temperature Detector

CONTENTS

SGWB Stochastic Gravitational Wave Background

SMBH Super Massive Black Hole

SNR Signal-to-Noise Ratio

SQUID Superconducting Quantum Interference Device

TC Temperature Coefficient

TDI Time Delay Interferometry

TM Test Mass

TML Total Mass Loss

UPC Universitat Politècnica de Catalunya

WVR Water Vapor Regained

I. Introduction

" Porque te sé decir que, aunque me costó algún
 trabajo componerla [esta historia], ninguno tuve por
mayor que hacer esta prefación que vas leyendo. "

Prologue to *El Ingenioso Hidalgo*
Don Quijote de la Mancha
Miguel de Cervantes

Chapter 1

Introduction

In the following pages we shall focus our attention in a very specific problem, namely how to deal with thermal related noise in a space borne low frequency gravitational wave detector. Before entering into detail, it is expedient to give an introduction on the gravitational wave subject, which will help to put the work in a proper context.

Although the main part of this thesis is devoted to thermal issues, the background scientific motivation behind the technical discussion is sound: the detection of gravitational waves is the last of Einstein's Theory of General Relativity classical predictions to be experimentally measured directly. Although gravitational wave effects were first measured in 1974 by R.A. Hulse and J.H. Taylor in the decrease of the period of the binary system PSR 1913+16 [43] (this work merited them the 1993 Nobel Prize), a direct detection of this phenomena has never been achieved despite the efforts being devoted. A direct detection of this phenomena would imply the starting point of gravitational wave astronomy and, as such, a step forward to a wider look into our universe.

This step forward requires a technological development which is of scientific interest in its own. From laser stabilisation to the drag-free technology improvements or high stability temperature measurements at $\sim 1\,\mathrm{mHz}$ frequency band, there are a wide variety of matters of ongoing scientific research to achieve the final and difficult goal of building an efficient gravitational wave detection.

As previously stated, this work will focus on some of them, related with thermal diagnostics. The current chapter is however intended as a brief introduction to some aspects of the gravitational wave detection paradigm.

1.1 Gravitational waves

Gravitational waves were introduced by Albert Einstein in his theory of General Relativity as a consequence of the finite velocity of propagation of gravitational interaction [30]. Einstein was able to show that, analogously to electromagnetic waves in Maxwell's theory, the equations of the gravitational field accepted radiative solutions. It was immediately evident, for Einstein himself,

the weakness of these waves and the consequent impossibility of detection at that time.

Gravitational radiation kept as a matter of theoretical discussion until the arrival of the pioneering work of Joseph Weber, who set up the first gravitational wave detector experiment at the University of Maryland: a 1.2 ton aluminium bar at room temperature, whose vibrations were monitored with the aid of piezoelectric transducers. A second bar at the Argonne National Laboratory (Chicago) allowed coincidence experiments between both detectors separated by 1000 km. The announcement of positive results in 1969 [103] raised great excitement which encouraged the construction of other cylindrical gravitational wave detectors by other groups. The negative result of the rest of experiments, together with the limits set by astronomical data was the starting point of technological improvements and the appearance of the second generation experiments together with the interferometric detection alternative.

Before entering in the description of the current experiments, following the seminal work of Weber, we will briefly discuss the General Relativity (GR) framework needed to correctly describe the gravitational wave phenomena.

1.1.1 Gravitational Waves in General Relativity

The context to introduce gravitational waves is Einstein's General Relativity (GR). This theory relates the motion of masses in space with the matter distribution in its surroundings. The relationship between both arises from the dependence of spacetime geometry in a given region with the matter content in that region. In the following, a brief introduction to the matter will be expound. A more thorough description can be found in classical GR textbooks [63, 90, 104].

General Relativity framework

General Relativity (GR) is expressed in the language of differential geometry. In this context, we can write in general the interval between two events[1] x^α and $x^\alpha + dx^\alpha$ in an arbitrary geometric system as

$$ds^2 = g_{\mu\nu} \, dx^\mu dx^\nu \tag{1.1}$$

where $g_{\mu\nu}$ is the metric tensor defining the relation space-time geometry in our particular coordinate system. This geometric entity is the one that will be affected by the matter distribution and thus, by virtue of equation (1.1), will turn into a particular motion law for a massive body travelling through this region. The interdependence between geometry and matter content is a particular property of the gravitational interaction introduced by General Relativity that is clearly stated in Einstein's equations

$$G_{\mu\nu} = 8\pi \, G T_{\mu\nu} \tag{1.2}$$

---

[1]Since we will be dealing with a four dimensional space, we need refer to *events* in the spacetime instead of points in the *space*.

where the *lhs* is known as the *Einstein tensor* and is a purely geometric entity, defined in terms of the Ricci scalar R and the Ricci tensor $R_{\mu\nu}$, both contraction of the Riemann tensor $R_{\alpha\beta\mu\nu}$

$$G_{\mu\nu} = R_{\mu\nu} - \frac{1}{2}gR_{\mu\nu}, \quad R_{\mu\nu} \equiv R^{\beta}_{\mu\beta\nu}, \quad R_{\mu\nu} \equiv g^{\alpha\beta}g^{\mu\nu}R_{\alpha\beta\mu\nu} \tag{1.3}$$

The *rhs* in (1.2) is the stress-energy tensor and gathers the information of matter content, for instance $T_{\mu\nu} = 0$ in vacuum. For our purpose, a crucial property of the set of nonlinear partial differential equations in (1.2) is that they accept wave solutions. The most common way of obtaining a wave-like solution of the Einstein's equation is to work in the weak field approximation, that is to assume a flat background but using the GR equations in the same way to deal with the small variations. In this framework the metric can be expressed as

$$g_{\mu\nu} = \eta_{\mu\nu} + h_{\mu\nu}, \qquad |h_{\mu\nu}| \ll 1 \tag{1.4}$$

where $\eta_{\mu\nu}$ is the flat metric ($\eta_{\mu\nu} = \{-1, 1, 1, 1\}$) and $h_{\mu\nu} \equiv h_{\mu\nu}(\mathbf{x}, t)$ describes small perturbations of the metric.

If this assumptions are used to describe the metric perturbation in vacuum, it can be shown that the propagation is described by wave equations

$$\Box \bar{h}_{\mu\nu} = \left(-\frac{\partial}{\partial t^2} + \nabla^2\right)\bar{h}_{\mu\nu} = 0 \tag{1.5a}$$

where

$$\begin{aligned} \bar{h}_{\mu\nu} &= h_{\mu\nu} - \frac{1}{2}h\eta_{\mu\nu} \\ h &\equiv h^{\alpha}_{\alpha} \end{aligned} \tag{1.5b}$$

The simplest solution is the monochromatic, plane wave solution,

$$\bar{h}_{\mu\nu} = \mathrm{Re}\left[A_{\mu\nu}\exp(ik_{\alpha}x^{\alpha})\right] \tag{1.6a}$$

where the following condition hold

$$\begin{aligned} k_{\alpha}\,k^{\alpha} &= 0 \quad \text{(null vector)} \tag{1.6b} \\ A_{\mu\alpha}\,k^{\alpha} &= 0 \quad \text{(orthogonality)} \tag{1.6c} \end{aligned}$$

being $A_{\mu\nu}$ the amplitude and k_{α} the wave vector. However, the plane wave solution of equation (1.6) has too many degrees of freedom (10 coming from $A_{\mu\nu}$ minus the four orthogonality constraints in (1.6c)) to represent the gravitational field, which can be shown to have only two of them by suitable choice of coordinates. The most common convention to use these degrees of freedom is the *Transverse Traceless gauge*, that is to impose
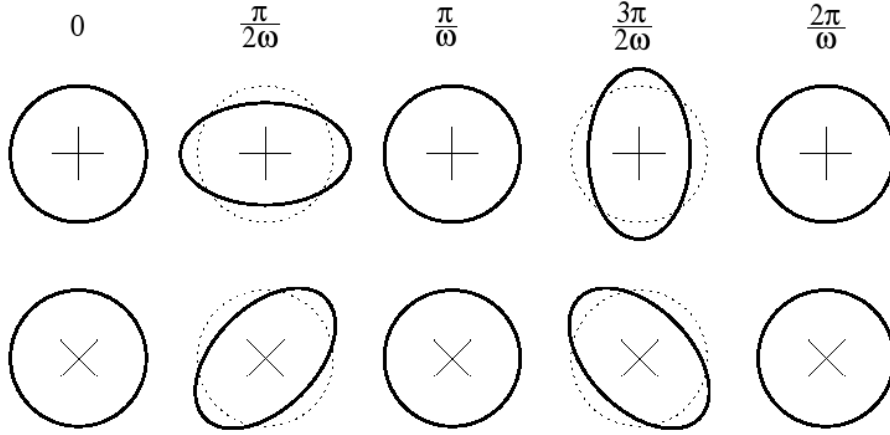
Figure 1.1: The "+" and "×" polarisation of a gravitational wave. The dotted lines indicate the test particles' position in the absence of gravitational wave signal. The phase of the wave is labelled on top.

$$A_{\mu\nu}u^{\nu} = 0 \quad \text{(transverse wave)} \tag{1.7}$$

$$A^{\mu}_{\mu} = 0 \quad \text{(traceless)} \tag{1.8}$$

where u^{ν} is the 4-velocity of the observer. In this representation and considering a wave propagating in the z direction, the metric perturbation $h_{\mu\nu}$ acquires the canonical representation

$$h_{\mu\nu}(\mathbf{x}, t) = \begin{pmatrix} 0 & 0 & 0 & 0 \\ 0 & h_+(\mathbf{x},t) & h_\times(\mathbf{x},t) & 0 \\ 0 & h_\times(\mathbf{x},t) & -h_+(\mathbf{x},t) & 0 \\ 0 & 0 & 0 & 0 \end{pmatrix} \tag{1.9}$$

where h_+ and $h_\times$ are the commonly known as *plus* and *cross* polarisation amplitudes of the gravitational wave.

Sources of Gravitational Waves

When massive bodies move with respect to one another, gravitational waves can be generated and propagate through the surrounding space. If multipoles are used to describe the mass distribution of the body, one finds that the first contribution to the gravitational field must be the quadrupole moment of the source, since the dipole one vanishes due to the conservation of momentum[2]. In analogy with the electromagnetic case, the luminosity that a given source radiates can be calculated.

---

[2]The source's dipole moment d second derivative is the momentum derivative that is conserved if no external force is introduced in the system, $\ddot{d} = \dot{p} = 0$ [63].

As it turns out, it is given by the *quadrupolar formula* [63] in the far field approximation

$$
\begin{aligned}
L &= \frac{1}{5\,c^3} < \dddot{I}_{jk}\dddot{I}_{jk} >, \quad [L] = \frac{\text{erg}}{\text{s}} \\
I_{jk} &\equiv \int d^3x\, \rho \left(x_j x_k - \frac{1}{3}\delta_{jk} r^2 \right)
\end{aligned}
\tag{1.10}
$$

where I_{jk} are the *reduced quadrupole moments*. To get an order of magnitude of the energy released due to this mechanism by massive bodies, a very rough estimate would give us that the Earth in its orbit around the Sun radiates $\sim 10^{-20}\,\text{W}$ via gravitational waves.

It is clear that the expected detectable sources of gravitational waves must be found in extremely massive environments and this yields directly to an astrophysical context. Gravitational wave sources have been historically split into the high frequency and low frequency classification, being the $\sim 10\,\text{Hz}$ region dividing both groups. As explained below, this is due to the seismic noise cut-off that limits the ground based detectors performance.

High frequency sources   Among the first class of sources, one of the candidates to be detected by ground based detectors are rotating neutron stars. These objects can generate gravitational waves due to small ellipticities in their structure. Being highly massive objects spinning at millisecond periods, they appear as suitable sources for ground based detectors. The last upper limit for the detection of this kind of sources is set at $S_h^{1/2} \leq 5.28 \times 10^{-24}\,\text{Hz}^{-1/2}$ at $f \simeq 140\,\text{Hz}$ [1], where $S_h^{1/2}$ is the strain ($h \equiv \Delta\ell/\ell$) rms power spectral density.

Massive objects like binary systems of neutron stars or black holes can also produce gravitational waves in the high frequency range. In such systems, the loss of energy due to gravitational radiation implies the shrinkage of the distance between both bodies. The last epoch of this inspiral process can be particularly bright in terms of gravitational energy released, and thus searches for these signals have been pursued using current detectors data. Results for this search are given as upper values for the rates of these sytems assuming a particular population of binaries. Depending on the source considered these upper rates go from $0.5\,\text{yr}^{-1} \times 10^{-10}\,\text{L}_{\odot,\text{b}}$ to $4.9\,\text{yr}^{-1} \times 10^{-10}\,\text{L}_{\odot,\text{b}}$ where $\text{L}_{\odot,\text{b}}$ is the blue light luminosity of the Sun [3].

Another kind of astrophysical objects suitable for gravitational wave searches in ground based detectors are those where large amounts of matter are displaced in a very short time; typical examples of these processes are supernova explosions. A search for these sources in the lastest scientific data run in the Laser Interferometer Gravitational Wave Observatory (LIGO) detector yielded an upper value of $S_h^{1/2} \leq 1.3 \times 10^{-21}\,\text{Hz}^{-1/2}$ at $f = 153\,\text{Hz}$, which could be related to the equivalent of $8 \times 10^{-8}\,M_\odot$ converted into gravitational radiation at a distance of $10\,\text{kpc}$ [4].

There exist a fourth kind of detectable signal at high frequencies due to a Stochastic Gravitational Wave Background (SGWB). Various physical mechanisms have been proposed for this gravitational equivalent to the Cosmic Microwave Background (CMB): from an amplification of quantum vacuum fluctuations during inflation to phase transition in the early universe, or cosmic

Class	Source	d/pc	f/mHz	$M_1/M_\odot$	$M_2/M_\odot$	$h/10^{-22}$
WD+WD	WD 0957-666	100	0.38	0.37	0.32	4
	WD 1101+364	100	0.16	0.31	0.36	2
	WD 1704+481	100	0.16	0.39	0.56	4
	WD 2331+290	100	0.14	0.39	>0.32	>2
WD+sdB	KPD 0422+4521	100	0.26	0.51	0.53	6
	KPD 1930+2752	100	0.24	0.50	0.97	10
Am CVn	RXJ 0806.3+1527	300	6.2	0.4	0.12	4
	RXJ 1914+245	100	3.5	0.6	0.07	6
	KUV 05184-0939	1000	3.2	0.7	.092	0.9
	AM CVn	100	1.94	0.5	.033	2
	HP Lib	100	1.79	0.6	0.03	2
	CR Boo	100	1.36	0.6	0.02	1
	V803 Cen	100	1.24	0.6	0.02	1
	CP Eri	200	1.16	0.6	0.02	0.4
	GP Com	200	0.72	0.5	0.02	0.3
LMXB	4U 1820-30	8100	3.0	1.4	<0.1	0.2
	4U 1620-67	8000	0.79	1.4	<0.03	.06
W UMa	CC Com	90	0.105	0.7	0.7	6

Figure 1.2: Assured sources for Laser Interferometer Space Antenna (LISA)

strings. On the other hand, a large enough population of unresolved continuous signals, like neutron star binaries, would be also detected as a stochastic background. Searches of a background signal implies the study of the cross correlation between two or more gravitational wave detectors. As an example, a collaboration between the LIGO and the ALLEGRO detectors set an upper value for a background signal to $1.5 \times 10^{-23}\,\mathrm{Hz}^{-1/2}$ at $f = 915\,\mathrm{Hz}$ [2].

Low frequency sources The proposed low frequency gravitational frequency detector LISA has fostered interest in the exploration of gravitational wave sources in the frequency band $0.1\,\mathrm{mHz} < f < 1\,\mathrm{Hz}$. Actually, one of the most relevant properties of the space borne detector LISA is that it has a list of guaranteed binary systems to be detected if the design performance is achieved —these are the *verification binaries* [95]. Among the binary systems, white dwarf binaries are not only expected to contribute as individual sources but the large amount of detectable systems of this kind in our galaxy is expected to produce a *background confusion noise* around $3 - 8\,\mathrm{mHz}$ [17] —see Figure 1.6 (dashed line).

Beyond these white dwarf binary systems, a low frequency gravitational wave observatory like LISA would be able to detect several other more exotic and less understood systems. For instance, Super Massive Black Hole (SMBH) are expected to produce a clear signal in the LISA bandwith.

The detection of such systems would imply the measurement of the black hole parameters to an unprecedent resolution. The foreseen strong signal, together with the low interaction of gravitational waves with the media could allow the measurement of the reduced mass up to $\sim 1\%$ for a $(10^6 + 10^6)M_\odot$ binary at redshift $z = 10$ [18].

This same massive objects could also contribute to another kind of signal in the gravitational wave sky. We refer to the so called Extreme Mass Ratio Inspiral (EMRI), i.e. a stellar black hole object in an inspiral orbit around a massive black hole, e.g. a $10^6 M_\odot$ object. The detection of gravitational waves coming from an EMRI would allow the mapping of the spacetime around the massive object and therefore the study of the strong gravitational field regime. Estimates of the event rates set an order of magnitude of $10^2 \, \mathrm{yr}^{-1}$ expected for LISA, detecting objects up to $z = 1$ [35].

Finally, the low frequency region of the gravitational wave observation band can also be thought as a testing region for the detection of a SGWB. However, current predictions set an upper value below the capabilities of LISA and, if the background is expected to present a flat spectra, the most sensitive ground based observatories will have better probabilities of detecting this cosmological signal.

Gravitational wave detection

The best way to represent equation (1.9) is to consider its effect between two free falling test particles. General Relativity (GR) tells us that, being in free fall, the test particles will follow geodesic curves in the Riemann manifold describing the spacetime. A gravitational wave will perturb this motion as described by the *geodesic deviation* equation [90]

$$\frac{d^2}{d\tau^2}\xi^\alpha = R^\alpha_{\mu\nu\beta}\, U^\mu U^\nu\, \xi^\beta \tag{1.11}$$

where $U^\mu = dx^\mu/d\tau$ is the 4-velocity of either of the two particles, τ the proper time and ξ^α a 4-vector connecting both particles.

Now, if we recover the description of the gravitational wave that led us to equation (1.9), it can be shown that the test particles motion can be readily described with the expression [50]

$$\ell(t) = \ell_0 \left[1 + \frac{1}{2} \left[h_+(t)\cos(2\phi) + h_\times(t)\sin(2\phi) \right] \sin^2(\theta) \right] \tag{1.12}$$

where (θ, ϕ) is the orientation of the vector joining both test masses in the gravitational wave frame, $\ell(t) = \xi^\mu \xi_\mu$ the distance between both particles and ℓ_0 their initial relative distance. The corresponding motion is shown in Figure 1.1.

Two experimental approaches have been followed in order to detect the geodesic deviation expressed in equation (1.12): Acoustic detectors and interferometers. Although differing in detection techniques, both methods share a common limit in the lowest part of their frequency band. Seismic noise degrades the sensitivity of any ground based gravitational wave detector around $\sim 10\,\mathrm{Hz}$. This frequency band separates the 'high frequency' and 'low frequency' bands in gravitational wave
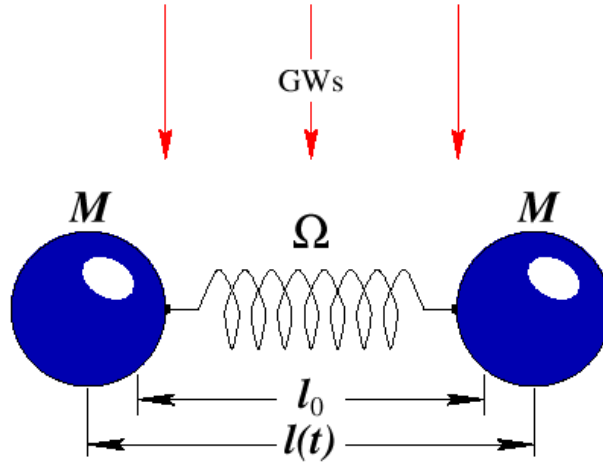
Figure 1.3: The acoustic detection concept. A gravitational wave perpendicular to the spring drives the two masses M at its ends to oscillate at the wave frequency. Resonance amplification is obtained when the latter equals the spring's characteristic frequency, Ω. In a real solid body, the Ω characteristic frequency is replaced by a full resonance spectra.

detection.

Acoustic detectors Historically, the first one implemented by J. Weber was the *acoustic* detector approach. The concept behind these detectors is that the tide induced by a gravitational wave impinging on a solid activates certain oscillating modes of the acoustic spectrum of the body. These resonances can be enhanced and detected using high sensitivity devices, as for instance a Superconducting Quantum Interference Device (SQUID). The main limitation of this technology is that the detection band is limited and therefore acoustic detectors are implicitly narrowbanded detectors with a detection bandwith achieving $\sim 100\,\mathrm{Hz}$ working at $\sim 1\,\mathrm{kHz}$ region.

There is an important representation of this detection technique in different projects worldwide: ALLEGRO [62] in the USA and AURIGA [25], EXPLORER [13], NAUTILUS [14] in Italy. To put some numbers as an example, the NAUTILUS detector consists of a $2300\,\mathrm{kg}$ cylindrical Aluminium bar of $3\,\mathrm{m}$ long refrigerated to $0.1\,\mathrm{K}$. Its resonance frequencies are at 908 and $924\,\mathrm{Hz}$ and the detector maximum burst amplitude sensitivity is of the order $h \sim 10^{-19}$. All the previous detectors use a solid body of cylindrical shape. There are however ongoing projects developing the same concept for the spherical shape which has, among others, the distinctive property of being an omnidirectional detector [50]. Examples of spherical detectors can be found in The Netherlands (MINIGRAIL [29]) and in Brazil (MARIO SCHENBERG [7]).

Interferometric detectors A second approach to detect gravitational waves is to use an interferometer that measures the relative distance between three masses in a Michelson configuration as
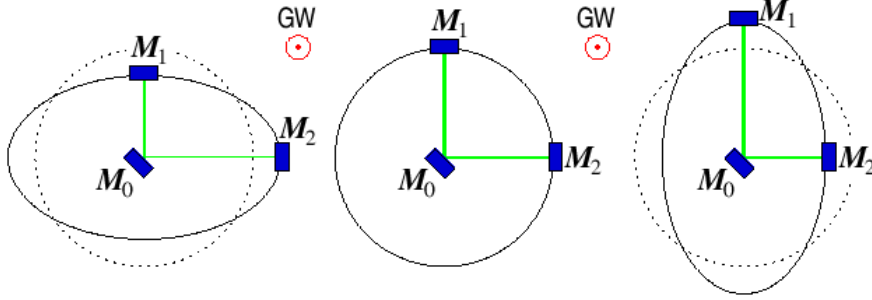
Figure 1.4: Interferometric concept to detect gravitational waves. The incoming wave causes the end masses M_1 and M_2 to oscillate in phase opposition with respect M_0.

shown in Figure 1.4. A gravitational wave crossing the interferometer plane with its propagation vector perpendicular to this plane can be measured as a relative displacement of one mass with respect the other. This approach, although lacking of an omnidirectional sensitivity as a solid sphere would have, presents an important improvement with respect the acoustic detectors, i.e. a broader detection bandwith. It is worth mentioning that the effect measured by an interferometer can not be naïvely assigned to the stretching of one arm with respect the other since the geometric variation caused by the gravitational waves will affect both the interferometer arm and the laser beam, leading to a cancellation of the effect. If the interaction between the electromagnetic field and the gravitational wave is studied [49], it appears that the interferometric signal must rather be assigned to the fact that gravitational wave affects the spacetime and thus the laser beam, with spatial and temporal components, feels the gravitational wave differently from the interferometer arm, only with spatial components. This results in measurable phase shifts, and can be thought as an alternative description to the usual geodesic deviation one.

There are currently various interferometers working in the data acquisition phase, these are: the two LIGO [5] in the USA of 4 and 2 km, VIRGO [19] in Italy with an armlength around 3 km, and also GEO600 [105] in Germany and TAMA [9] in Japan with smaller armlengths of 600 and 300 m respectively.

Although sharing the same design concept, each collaboration has contributed to the field with different techniques. For instance, VIRGO incorporated in the design improved seismic attenuators with respect LIGO that should allow a noise reduction in the low frequency band ~ 1 Hz. The Anglo-German collaboration has focused on the development of new techniques that could be applied in the larger detectors to increase its sensitivity, an example of this could be the *signal recycling* technique. The TAMA detector is also designed as a technology demonstrator that will pave the way to a future cryogenic kilometer-sized detector, known as Large scale Cryogenic Gravitational wave Telescope (LCGT).
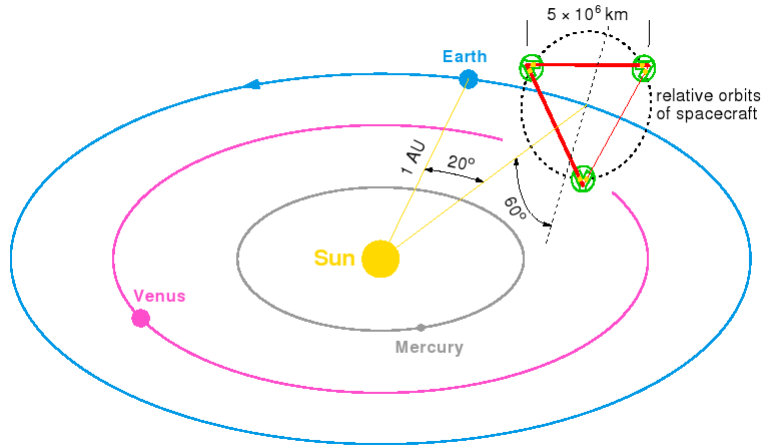
Figure 1.5: LISA orbit scheme

1.2 LISA and LISA Pathfinder

We now focus on the low frequency gravitational observatory Laser Interferometer Space Antenna (LISA). This project is the framework where the present thesis is developed. Actually, it is basically related to the technology probe mission aimed to test the key technologies for LISA. This mission is the LISA PathFinder (LPF) and its main characteristics will also be described in the following.

1.2.1 Gravitational waves detection in space

LISA is a joint ESA-NASA mission, designed as a gravitational wave detector with top sensitivity in the milliHertz band. The main concept behind LISA are three spacecraft hosting two free falling test masses each, and separated from each other 5×10^6 km. Each spacecraft is linked to the other two by means of an infrared (1064 nm) laser beam that allows the precise monitoring of the displacement between test masses at each spacecraft. The cubic test masses act as end mirrors of the interferometer.

The interferometry required for the LISA project implies certain challenges which are worth mentioning. The laser source in one of the spacecraft provides a 1 W laser beam which is sent via a 30 cm telescope to a second spacecraft. Although the laser power is precisely focused, the long way to each second spacecraft provokes the spread of the laser beam in a spot of several kilometers in diameter, and hence the power received by the second spacecraft gets reduced to the 10^{-10} W level. Such a low power is too weak to be returned to the original spacecraft, and thus the solution adopted is to *lock* the frequency of the local oscillator to the incoming light and send a new laser beam mimicking the one arriving, but using the available 1 W power.

In order to detect gravitational waves, the test masses must be in free fall on board the three

spacecraft. This condition must be met at the same time that the distance between spacecraft is maintained, implying that the spacecraft orbits must be carefully defined. The current baseline is shown in Figure 1.5: the barycentre of the triangle formed by the three spacecraft follows the ecliptic 20° behind the Earth; the plane of the triangle is inclined 60° with respect the ecliptic plane and each of the three spacecraft revolve around the Sun in a nearly circular orbit, while following at the same time a counterclockwise rotation of the whole triangular configuration.

A crucial issue regarding the LISA orbits is stability. Interferometer arms in LISA are subjected to fluctuations of the order of 1% of their total length, i.e 5×10^4 km. This difference between armlengths could considerably degrade the instrument performance since this large distance causes an enourmous coupling of laser frequency noise into the interferometric length measurement. However, a technique has been proposed to use the arm's length as a reference length [91]. This is a standard method in ground based detectors, however the 30 s delay due to the photon round-trip introduces a challenge for the control loop that has been proved to be overcome with this new approach [58]. We can also name here a second procedure to reduce the phase noise, this is the Time Delay Interferometry (TDI) [97]: a postprocessing technique that uses independent signals of single interferometers conforming a constellation, like in the LISA case, to cancel phase noise in unequal arms interferometers.

The geodesic free fall of the test masses inside the spacecraft must be guaranteed by the so called Gravitational Reference Sensor (GRS). This is conformed by a set of capacitative sensors surrounding the free floating test mass that senses its relative displacements based on a capacitive measurement [23] that can act both as a sensor or an actuator. The motion of the test mass sensed in this way is used to apply microNewton corrections to the spacecraft by means of Field Emision Electric Propulsion (FEEP) thrusters[3]. This system minimises the disturbances acting directly on the test mass, as for instance cosmic ray showers, as well as those forces applied on the spacecraft, e.g. solar radiation pressure. The required acceleration noise for the LISA mission is set at [17]

$$S_{\Delta a,\text{LISA}}^{1/2}(\omega) \le 3 \times 10^{-15} \left[1 + \left(\frac{\omega/2\pi}{3 \text{ mHz}} \right)^2 \right] \text{m s}^{-2}/\sqrt{\text{Hz}} \qquad (1.13)$$

in the frequency range $0.1 \text{ mHz} \le \omega/2\pi \le 100 \text{ mHz}$. This particular noise budget will be the one that the LPF mission is devoted to study, as explained below.

Summing up, the final sensitivity curve of LISA will be defined by contributions arising from very different physical mechanisms, in brief: the low frequency range will be dominated by spurious forces affecting the test mass motion and thus the GRS performance will have a decisive role in this region. On the other hand, either the local interferometric measurement inside each spacecraft or the spacecraft-to-spacecraft interferometry will set the higher part of the sensitivity curve. Figure 1.6 shows these dependences by observing how the sensitivity curve varies as a function of some of the LISA design parameters.

---

[3]This option is however under study
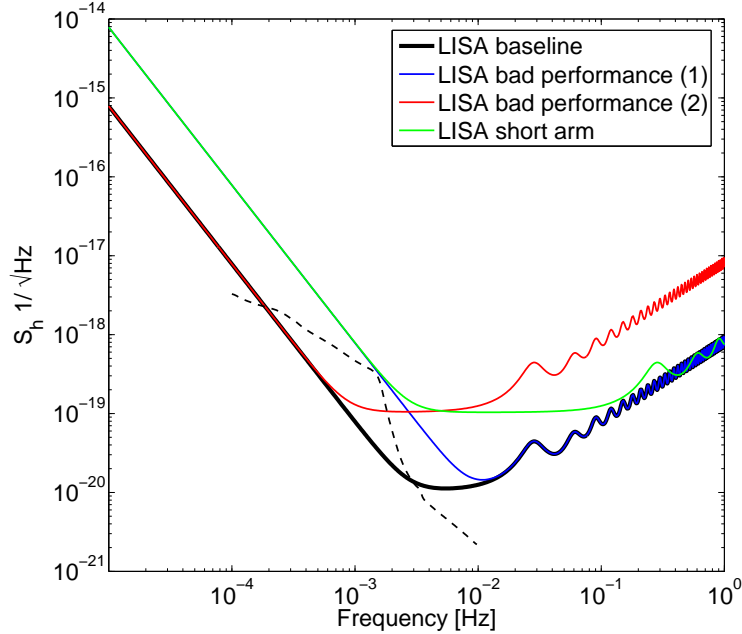
Figure 1.6: LISA baseline sensitivity compared to the sensitivity of the same design reducing a factor of 10 the arm's length (in green) or increasing the acceleration noise (in blue) or the position noise (in red) by a factor of 10 also. The latter acceleration noise budget is the one required for the LPF mission —see section §1.2.2. Sensitivities are compared to the expected white dwarf confusion noise [17] (dashed lines). Curves were obtained with the *Sensitivity Curve Generator* [92].

1.2.2 The LISA Pathfinder mission

The demanding requirements needed for LISA forced the testing of some of its key technologies previous to the final mission approval. The testing mission was born as the *SMART-2* mission although it was later renamed as LISA PathFinder (LPF) since only LISA technology was part of the payload. The starting concept contained two independent experiments: the European LISA Technology Package (LTP) and the American Disturbance Reduction System (DRS), though the latter was dropped from the design leaving only the thrusters and the control software.

The requirement for the LTP experiment is directly derived from the acceleration noise budget for LISA, equation (1.13), relaxing an order of magnitude both the amplitude and the bandwith, giving an acceleration noise requirement [10]

$$S_{a,\mathrm{LPF}}^{1/2}(\omega) \leq 3 \times 10^{-14} \left[1 + \left(\frac{\omega/2\pi}{3 \text{ mHz}} \right)^2 \right] \text{ m s}^{-2}/\sqrt{\text{Hz}} \tag{1.14}$$

in the frequency range $1 \text{ mHz} \leq \omega/2\pi \leq 30 \text{ mHz}$. The main concept to achieve an experimental test of this sensitivity is to squeeze one of LISA's arms to 30 cm length and reproduce the geodesic
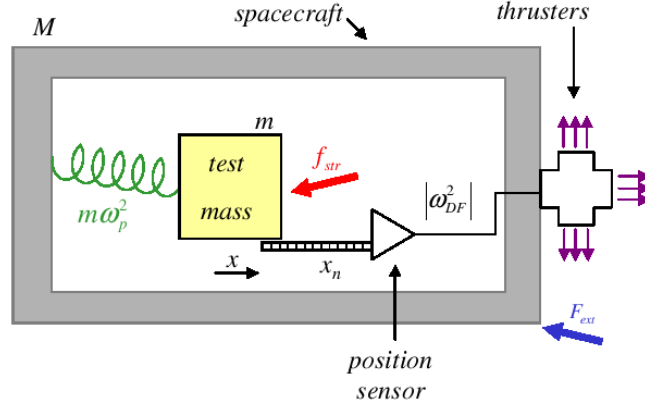
Figure 1.7: The *drag free* principle. The spacecraft (M) shields the test mass (m) from external forces (F_{ext}). To keep centred around the free falling test mass the spacecraft is equipped with position sensors that feed the spacecraft thrusters in a control loop with gain ω_{DF}^2. Sources of disturbances in the control loop are: the sensor displacement noise x_n, position independent (stray) forces f_{str} and the test mass-to-spacecraft residual coupling provoked by any DC force gradient

experiment in a unique spacecraft. In doing so, two of the main concepts of LISA are put to test, namely the *drag-free* control loop performed by the GRS and also the spacecraft-to-test mass interferometry. The spacecraft-to-spacecraft measurement is the one that the LPF mission will not test. Another differences with respect LISA is that since both test masses will be aligned on the same spacecraft, LPF will not be able to follow both test masses in all the sensitive axis.

We can now take a closer look on the implications of equation (1.14) in terms of the LTP working principle. If one considers a spacecraft (mass M) shielding a free floating test mass (m) that, by means of a set of sensors, measures the relative distance between test mass and spacecraft and, at the same time, uses this signal to keep it centred around the free falling test mass, it can be shown that the accelerations on the test mass can be expressed as [42]

$$a = \frac{f_{str}}{m} + \omega_p^2 \left(x_n + \frac{F_{ext}}{M\,\omega_{DF}^2} \right) = \frac{f_{str}}{m} + \omega_p^2 \Delta x \tag{1.15}$$

where

- F_{ext} are forces applied on the spacecraft (thrusters noise also enters this group).

- f_{str} is any stray force (position independent) applied on the test mass. This can be due to unshielded forces (e.g. cosmic rays) but also from the spacecraft itself (e.g. thermal forces).

- x_n is the position sensor noise.

- ω_p is the parasitic stiffness per unit mass that couples the test mass to the spacecraft.

17

Returning to the mission final goal, the demanding condition (1.14) imposes restrictions on the spectral noise density in all variables appearing in (1.15): from stray forces f_{str} to the parasitic stiffness ω_p between spacecraft and test mass or the position sensor noise x_n, all these variables are required to achieve upper limit values in order to reach the LTP acceleration noise requirement [100]. As we will see in next chapter, this will be also true for the requirement on the thermal environment inside the LTP. Since thermal gradients will turn into forces on the test masses, the limit set on f_{str} will directly translate into a requirement for the thermal stability in the LTP.

We will in the following review the basic working principles of the subsystems involved in the LTP measurement: the Gravitational Reference Sensor (GRS), the Optical Metrology Subsystem (OMS) and the Data and Diagnostics Subsystem (DDS).

Gravitational Reference Sensor

The GRS on board the LPF mission is the central part of the drag-free control loop in the LTP. Its conceptual design is based on a capacitive measurement of the distance between a freely falling cubic test mass and a set of electrodes surrounding it, rigidly attached to the spacecraft structure. We will first briefly describe the GRS main components to subsequently be able to understand the working principle.

Test Mass The role of the Test Mass (TM), acting as end-mirror of the interferometer is foreseen to be played by a 46 mm Gold-Platinum alloy cube[4]. The reason behind the material selection must be found in the stringent requirement for the total magnetic moment of the TM, which is of $|\overrightarrow{m}| \leq 2 \times 10^{-8}\,A\,m^2$. The high density obtained with this alloy, around $20\,g\,m^{-3}$, has also been considered an advantage when choosing a suitable material.

Increasing the TM size will always improve the sensitivity measurements both because its greater mass and its higher area available for sensing electrodes — see next section. In the LTP application, requirements on the mass budget come from the caging mechanism[5] which requires the TM not to exceed roughly 2 kg.

Electrode Housing The position sensor is based on a capacitive measurement which allow readout and actuation. For the moment, we will describe the structure and composition of the sensor to then address the working principle.

The central part of the position sensor is the previously described TM, this is surrounded by an array of six pairs of electrodes, each one entering in a capacitive-inductive read-out circuit which allows a detailed monitoring of the TM motion both in its displacement and rotational degrees of

---

[4]Pioneering drag-free satellites, like TRIAD [15], used spherical bodies as TM, however best spheres can only achieve this shape with departures of 100 nm [99] which would translate into a position uncertainty of the same order of magnitude. This error can be reduced if a spherical spinning TM is considered in the design, as for instance in the GP-B mission [93]. Although suppressing surface irregularities, rotation introduces stability and control problems and also electromagnetic effects if the mass is a conducting one (GP-B uses a superconducting sphere).

[5]The caging mechanism is the responsible of holding the test mass during launch and release it in appropiate conditions to allow the drag-free control to acquire control of it.

	Density ρ [kg m^{-3}]	Specific heat C [J kg^{-1} K^{-1}]	Thermal conductivity K [W m^{-1} K^{-1}]	CTE α [10^{-6} K^{-1}]
Molybdenum	10200	251	138	5.3
Sapphire	3980	750	37.5	5 - 6.7
Gold	19300	128	318	8
Platinum	21400	134	69	8.9
Zerodur	821	2530	1.64	0.1-0.02
Optical Window glass	3670	720	0.599	10
CFRP	1600	1200	30	5.5-8.4
Titanium (Ti6Al4V)	4430	526.3	6.7	8.6

Table 1.1: Thermal properties for LTP materials.

freedom. The structure where the electrodes are placed is the *Electrode Housing*, and consists of a hollow cube of approximately 70 mm edge surrounding the TM.

Materials conforming the Inertial Sensor are selected to have a high thermal conductivity in order to prevent thermal gradients. These are the main source of thermal induced noise in the measurement as will be later described. For this reason a metal-ceramic high thermal conductance composite structure has been selected as the choice for the Electrode Housing. Besides thermal reasons, this choice provides also great mechanical reliability, particularly relevant when considering the launch phase, and also for its handling and machining properties. The materials selected for the GRS structure are Molybdenum for electric conducting parts and Sapphire for electrical insulators. In order to avoid thermal induced stress that may perturb the capacitive measurement, thermal expansion coefficients are required to match those materials used in the GRS. This condition is well fulfilled by the Mo-Sapphire couple as shown in Table 1.1.

Bottom panel of Figure 1.8 also shows a characteristic of the Electrode Housing: *the guard rings* are surfaces between different electrodes grounded with the objective to minimise the effect of electric field lines closing onto the neighbour electrode, introducing cross-talk effects. It must be stressed that all sensing and injecting electrodes as well as guard rings will be Au-coated to enhance electrostatic homogeneity.

Capacitive measurement As previously stated, the TM is surrounded by an array of six pairs of electrodes in a capacitive-inductive resonant circuit. By linear combinations of the six readout channels, this geometrical configuration provides the information of all six degrees of freedom of the test mass, allowing also electrostatic actuation on it. The TM is biased at 100 kHz by means of six injection electrodes distributed by pairs: 2 pairs in the z faces and 1 in the y face —see Figure 1.8. Being opposite electrodes part of the same resonant circuit, the TM motion produces a modulation of the capacitances as a consequence of the dependence of these capacitances with the distance separating the electrodes and the TM. This induces a difference of the current flowing through both arms of the bridge —see Figure 1.9, being this one the final signal describing the
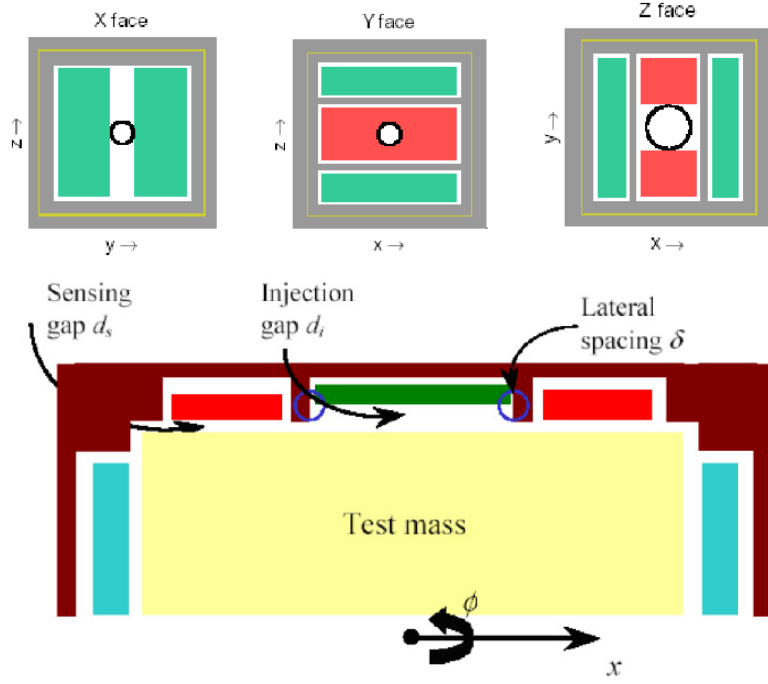
Figure 1.8: *Top:* Electrode housing configuration. Sensing electrodes appear in green and injecting electrodes in red. *Bottom:* Injection electrodes are placed in a recessed configuration which reduces the electrostatic stiffness . Extracted from [99]

TM motion. Along each axis, the sum of the currents produced by the two sensors provides the translational displacement of the test mass with respect to the centre of the electrode housing, while the difference provides the information about the test mass rotation. Moreover, the same scheme can be used to act on the TM by applying voltage differences between the electrodes and TM faces if a correcting force is needed in order to generate a TM motion.

The working principle of the capacitive sensor is based on the dependence of the capacitances of two parallel plates with respect the distance between them. If one plate moves from its position, a force proportional to the displacement appears between both. Being a displacement proportional force ($F = -k\,x$), the constant of proportionality of the force, k, is usually termed *stiffness*, and it can be shown [99] to be described by

$$k_j = -(V_m - V_j)^2 \frac{A_j \epsilon_0}{d_j^3} \tag{1.16}$$

where V_m is the equivalent AC TM voltage taking into account the injection electrodes applied voltage and the equivalent capacitance of the system composed by the test mass and the surrounding electrodes, V_j is the voltage at electrode j, A_j is the overlapping area between electrode and TM, d_j the equilibrium distance between electrode and TM.
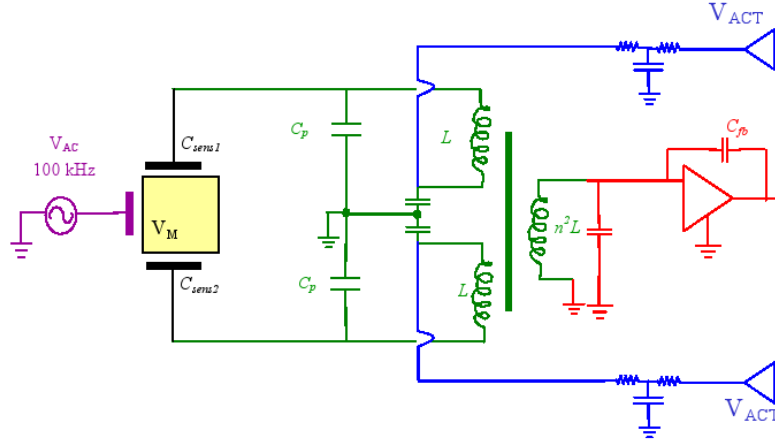
Figure 1.9: Parametric bridge motion readout and actuation. V_{ac} is the ac generator to bias the TM through the purple injection (bias) electrode. C_{sens} are the capacitances between the sensing electrodes and the TM. The capacitances C_p that also includes parasitic capacitances of electrodes to ground are used to set the bridge to resonance. The transformer is a differential transformer coupled to a low noise amplifier used as a current amplifier. V_{ACT} represents the force actuation signals (at $\approx 1\,\mathrm{kHz}$, amplitude modulated between 0 and $\approx 1\,\mathrm{Hz}$). Extracted from [99]

There are numerous possible effects able to affect the capacitive measurement such as patch charges, magnetic impurities, surface imperfections, interaction with test mass charging and other unmodeled effects that can act as potential sources of stiffness and stray forces [20]. Because most of these effects fall off rapidly with the distance, a 4 mm gap in the most sensitive axes is selected compared to the 2.9 mm in the y direction and 3.5 mm in the z direction. The counterpart of this option appears as the necessity to increase the bias to maintain high position sensitivity once a larger gap is introduced between the electrode and the TM. On the other end, the limit in increasing the gap is set by the caging mechanism. The size of the indentation in the z faces must be twice the sensing gap in order to allow for self-centring of the TM during recaging. This sets a limit of 4 mm for all gaps [99].

Among the different possible configurations to distribute sensing electrodes in the housing, the selected design is graphically presented in Figure 1.8. Clearly, x direction sensitivity is maximised placing all injecting electrodes on other directions since the voltage difference between this surfaces and the TM implies a related stiffness increase which diminishes the sensitivity.

Optical Metrology Subsystem

The LTP experiment has a high sensitivity metrology subsystem designed to monitor at picometer resolution the distance between two test masses. Comparison studies between different designs left as a baseline choice, being now implemented, the non-polarising heterodyne Mach-Zender interferometer [37, 99] which we briefly describe in the following.
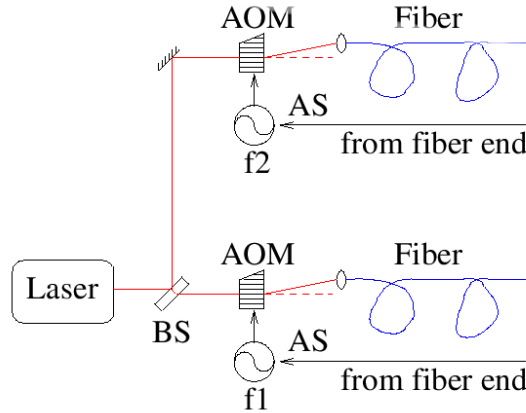
Figure 1.10: Heterodyne interferometry. In the modulation bench the laser beam is split and each resulting beam is frequency-shifted by the AOMs at f_1 and f_2, the recombined beams will produce the signal at the heterodyne frequency, $f_{het} = f_2 - f_1$.

The laser beam has a wavelength of $1064\,\text{nm}$ and the power is approximately of $25\,\text{mW}$ at the end of the optical fiber. The non-polarising choice avoids errors caused for polarised optical elements, for instance polarisation changing due to thermal stress-induced birefringence [99]. The interferometric measurement is based on the Mach-Zender design which differs from the classical Michelson interferometer in that the beams do not double back on themselves at the mirrors and therefore both arms of the interferometer are completely independent. Moreover, this configuration uses two detectors instead of one, as is the case in the Michelson interferometer.

The laser signal generated at the modulation bench applies the principle of *heterodyne interferometry*, based on the generation of a signal at a given frequency, f_{het}, from two other signals that are tuned to differ precisely this f_{het} amount. To do so, in the LTP the laser beam is split into two beams, each of which is frequency-shifted by an Acousto-Optical Modulator (AOM)[6]. The driving frequencies of the two AOM, differ by $1\,\text{kHz}$ ($1.6\,\text{kHz}$ in the Engineering Model, in the AEI-Hannover). When both beams are made to interfere at a beam splitter the resulting photocurrent in a photodiode shows a strong component at the heterodyne frequency.

The measurement principle is thus based in that any pathlength difference between both beams will show up as a phase variation of that heterodyne signal. This phase is measured against a reference beam that is (ideally) not subject to any pathlength variation. Being the relevant signal generated by the subtraction between the perturbed and the reference beam, all common phase-shifting effects that occur in the generation of the two beams (related to fibers, to the AOMs, etc) are suppressed due to this measurement principle. To keep the interferometric measurement

---

[6]These devices introduce a frequency shift in the incoming light by means of sound waves generated in a material. These waves are generated by a piezoelectric transducer attached to a material such as glass. An oscillating electric signal drives the transducer to vibrate, which creates sound waves in the glass. The periodic pattern created by these waves produces a diffraction effect in the incoming laser light which allows, by adjusting the oscillating electric signal, to control the exiting light frequency shift.
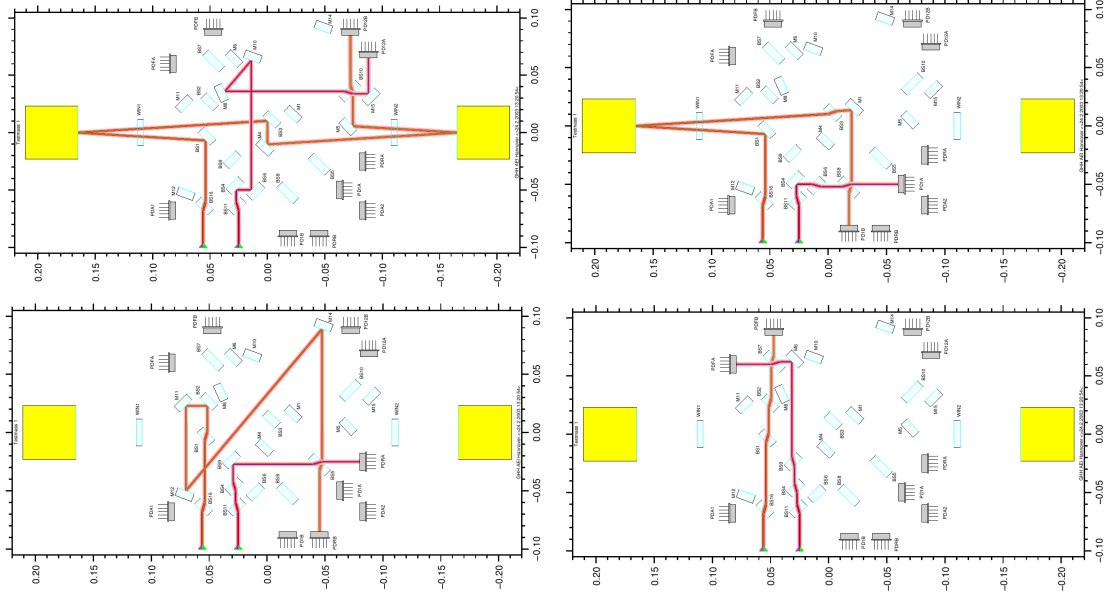
Figure 1.11: From left to right, top to bottom: $x_1 - x_2$ interferometer, x_1 interferometer, $Reference$ interferometer and $Frequency$ interferometer. See text for details.

clean when measuring relevant pathlength variations, i.e. those appearing due to the TM motion, elements conforming the optical bench where the Mach-Zender design is implemented are bonded to the optical bench substrate, made of Zerodur [37].

The technique used to create a monolithic optical bench is the Hydroxide-catalysis technique [31], also known as 'silicate' bonding technique. This method has been previously used in the GP-B mission for the purpose of joining the fused silica pieces forming the star-tracking telescope assembly.

The Optical Bench design appears in Figure 1.11. Four separate interferometers participate in the interferometric measurement: The main scientific measurement corresponds to the pathlength difference measured by the (1) $x_1 - x_2$ interferometer, i.e. the distance between both test masses. The (2) x_1 interferometer provides the distance of one test mass with respect the optical bench and the alignment of that test mass. Both measurements are based, as previously commented, on the substraction of the respective pathlength with respect the (3) $Reference$ interferometer and, finally, the (4) $Frequency$ interferometer, with intentionally unequal pathlengths in order to measure the error introduced by frequency fluctuations, allowing also the subsequential correction.

A point to note is that the laser beatnote is finally measured, in each interferometer, using quadrant photodiodes. Analogously to the GRS situation with the set of electrodes surrounding the test mass, we can take advantage of the configuration to obtain not only distance information but also information regarding the spatial orientation of the test mass.

The final step in the interferometer measuring chain is the phasemeter [38] which samples the

heterodyne signal $f_{het} \equiv 1\,\mathrm{kHz}$ with an output rate of $f \equiv 100\,\mathrm{Hz}$ which is delivered to the Data Management Unit (DMU) for the final processing step. This data treatment will be performed in the flight model by a dedicated hardware (FPGA) [101].
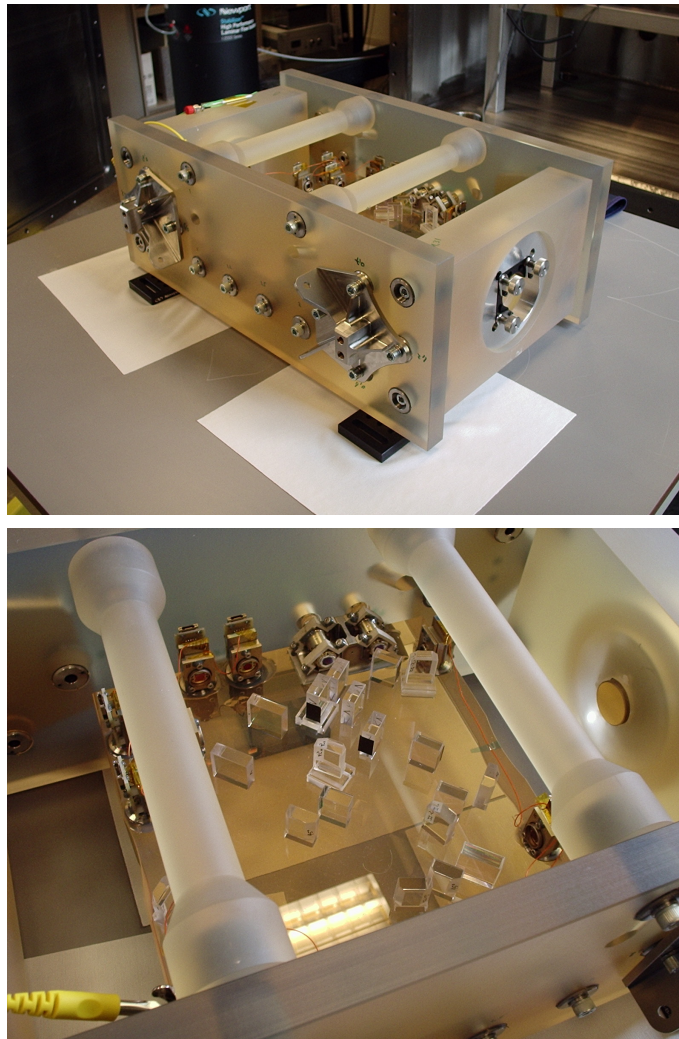
Figure 1.12: The Optical Bench Engineering Model lateral (top) and top (bottom) view. The latter shows the optical layout on the Optical Bench together with the fiber injectors (top right part of the Optical Bench) and two photodiodes at their left. The golden circle on the right is the mirror acting as a dummy test mass. Courtesy of A.F. García Marín

Diagnostics

The LTP is designed as a technology readiness mission with the main scope of probing the drag free technology required for LISA and is thus an experiment from which information that will be needed to achieve the more demanding LISA goal can be extracted.

The Diagnostics Subsystem has a very important role in this last part since it is designed to identify and characterise those noise sources that affect the main scientific measurement. The list of items conforming the DDS is

1. *Diagnostics items.* These are a number of sensors, with their associated electronics, which are intended to monitor various disturbances happening inside the LPF

   - Temperature Sensors. There are **23** distributed trough the LTP Core Assembly (LCA)
   - Heaters. There are **14**, distributed in the Electrode Housing, the Optical Window and the suspension struts.
   - Magnetometers. There are **4** of fluxgate type surrounding the LTP, outside of the thermal shield.
   - Coils. There are **2**, each one attached to one vacuum tank and both aligned with the line joining the test masses.
   - Radiation Monitor. Only one, attached to the spacecraft's shear walls.

2. *Data Management Unit (DMU)* [73]. The LTP computer. It is responsible for driving and control of the diagnostics items, and for the acquisition and onboard processing of phasemeter data. It has three main components, each one duplicated as a resource against failure.

   - Power Distribution Unit (PDU)
   - Data Acquisition Unit (DAU)
   - Data Processing Unit (DPU)

We will now overview the main characteristics of the Diagnostics items, a more detailed description can be found in [12, 52].

Magnetic diagnostics   The test masses onboard the LPF are two 1.96 kg cubes of an Au-Pt alloy. The reason behind this choice is, as previously commented, a compromise between weak magnetic properties and mechanical resistance. The trade-off between both criteria leads to a pair of cubic masses with very low magnetic response (the expected values for the test masses are $|\chi| < 10^{-5}$ and $|m| < 10^{-8} \, \text{Am}^2$). Even the foreseen suppression of the magnetic characteristics, the LTP acceleration noise requirement, equation (1.14), imposes a rather demanding magnetic cleanliness for the LTP environment —see Table 1.2.

The role of the magnetic diagnostics is to monitor the magnetic field by means of the magnetometers array onboard the LTP and extrapolate the value of the magnetic field and magnetic field

Magnitude	Requirement
DC Magnetic field	$10\,\mu\text{T}$
DC Magnetic field gradient	$5\,\mu\text{T/m}$
Magnetic field fluctuations	$650\,\text{nT}/\sqrt{\text{Hz}}$
Magnetic field gradient fluctuations	$250\,(\text{nT/m})/\sqrt{\text{Hz}}$

Table 1.2: LTP magnetic requirements

gradient at the test masses locations in order to be able to evaluate the magnetic noise contribution to the test mass acceleration. It is precisely the distance between magnetometer and test mass that makes the diagnostics task specially hard since the magnetic field is generated by a long list of magnetic sources inside the spacecraft (50 approx.), and only 4 fluxgate magnetometers are available. Several analysis techniques are been studied to solve this problem, see for instance [11, 61].

The magnetic subsystem will also provide a pair of magnetic coils to be attached to the LTP vacuum chambers enclosing the test mass. These devices will be able to apply high Signal-to-Noise Ratio (SNR) magnetic signals that will be used to determine *in-flight* the magnetic properties of the test mass.
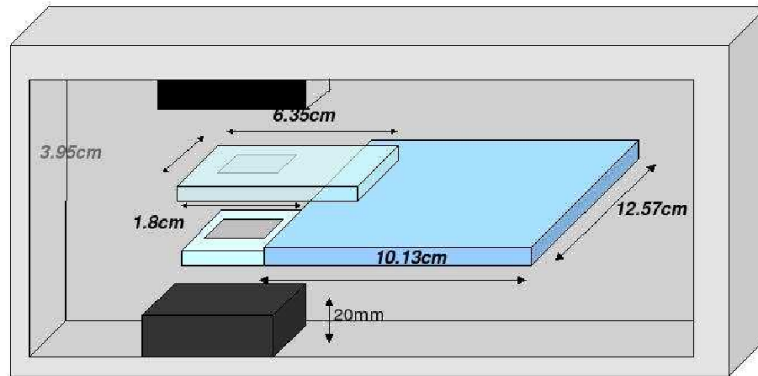
Figure 1.13: Radiation Monitor scheme. Two PIN diodes in telescopic configuration inside a shielding structure.

Radiation Monitor Because of the capacitive measurement used to sense the test mass motion, the GRS is sensitive to charge variations of the test masses. In the Lagrange point 1 (L1) where the experiment will take place there are two envisaged sources of charging on the test masses: Galactic Cosmic Rays (GCR) and Solar Energetic Particles (SEP). Both are composed mainly by protons and a smaller fraction of He nuclei and heavier nuclei respectively, but differ in its energy spectra. Therefore, the LTP needs a particle counter in order to characterise the particle shower contribution to the noise performance of the experiment. A property needed for the Radiation Monitor is the capability to distinguish GCR from SEP, implying that is must be able to evaluate

the energy spectra of the incoming shower. A second condition to be fulfilled is that the detector must characterise the particles arriving in the test mass which, due to the spacecraft shielding, are those with energies above $\sim 100\,\mathrm{MeV}$.

The concept of the particle counter designed to reach the above conditions is based on two PIN diodes, each of which can count individual particle hits. Photons are absorbed while protons and heavier nuclei can exit through the opposite side of the diode. A telescopic configuration of these diodes allows the discrimination of the energies of the incident particles based on their energy deposition. The particle counter is placed inside a metallic box which has an equivalent stopping power as the one of the spacecraft with respect the test mass —see Figure 1.13.

Thermal diagnostics This thesis is devoted to this subject. The reader is referred to the next chapter for a description of the Thermal Diagnostics Subsystem onboard the LTP and the rest of the chapters for related topics.
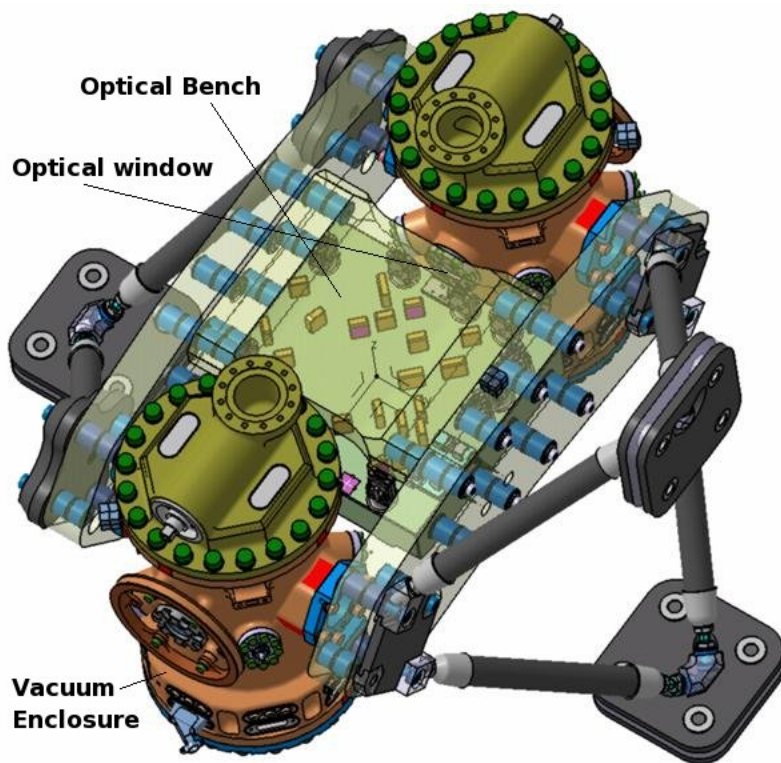
Figure 1.14: Layout of the LTP Core Assembly, as of 13-October-2006.

Chapter 2

Thermal Diagnostics

The LISA Pathfinder mission is devoted to pave the way to gravitational wave astronomy in space or, in more specific terms, to low frequency gravitational wave detection. In order to reach this objective, it must develop some technologies at a given sensitivity level where the scientific case assures that the detection will be undoubtedly achieved. However, the detection of gravitational waves refers to the LISA project which aims to reproduce the same geodesic deviation measurement that the LPF will undergo but separating both masses $5 \cdot 10^6$ km. The LTP experiment on board the LPF will reach, roughly in order of magnitude, the requirement in terms of acceleration but a much lower value when considering strain sensitivity, precisely due to the squeezing of the LISA arms. The LTP must therefore be considered as a null-type experiment, i.e., an experiment where the no detection of signal or, in better terms, the suppression of all perturbing agents is considered the main priority.

If we thus assume this framework, noise will immediately appear as the main interesting process to understand and characterise. In our particular case, we will be referring to noise as a stochastic process represented in a time series which will be our instrument output datastream.

The scope of the experiment requires to deal with the noise figure of the experiment and compare it with the design figure, the one that must be achieved based on the design being followed. Therefore, in a null-type experiment, the design phase builds up also a noise model which sets the experiment limits to be reached a posteriori. The noise model may be based, as this is the case in the LTP case, in previous experimental experience which helps to define the processes setting the floor noise and to parametrise it by means of proper characterisation experiments.

Among the different kinds of noise sources we will distinguish those intrinsically related to the experiment dynamics from those intrinsically related to an external agent. An example of the former would be the shot noise taking place at the photodiodes while test mass displacements due to the magnetic field will enter in the second class. Under this classification the noise model can be expressed as

$$S(\omega) = \sum_i S_i(\omega) + \sum_k |h_k(\omega)|^2 \, S_k^{(ext)}(\omega) + (cross\ terms) \qquad (2.1)$$

where the first term gathers instrumental noise and the second disturbances contributions. The latter has been split into the noise term $S_k^{(ext)}(\omega)$ as measured by the diagnostics items and the transfer functions, $|h_k(\omega)|^2$, translating the external agent noise to noise contribution to the experimental main datastream.

When running the experiment this noise model is put to test and thus the main output stream (interferometric in our case) is required to measure the noise level, but the disturbances (those related with external agents) need also be monitored in order to fully reproduce the noise model and probe its validity. At this point the diagnostics[1] acquires its relevance. In the LTP the main disturbing forces arises from magnetics, thermal and charged particles showers, and thus the corresponding sensors are distributed across the LTP.

A first step for the diagnostics is thus to translate its measurements into equivalent noise on the main measurement via the noise model. Despite of the monitoring process just described, the diagnostics can acquire an active part in the experiment as testers of the noise model. The main problem with the noise investigations is that contributions coming from different agents can not be distinguished. Since these processes are setting the noise floor level, there is no possibility for our instrument to measure it separately. The adopted solution is to include diagnostic apparatus (heaters and coils in the LTP) able to actively increase the power of a particular noise agent. Because we are measuring in general small effects, we will consider that the coupling factor relating the disturbance with the measurement is independent of the applied power and thus with an applied stronger signal we will clearly determine the relation between both. This way, we are taking advantage of the diagnostics items to determine the noise model, reducing the uncertainty of its parameters.

The framework used to evaluate the noise model will be the system approach. The methodology is based on the description of the problem in terms of an input/output relation expressed as a *transfer function* that gathers the dynamics of the system under study. This function translates a given input time series into an output time series as well. The system approach will be thoroughly considered in Chapter 8 where it will be directly applied to a real data set.

In this chapter we will be mainly focusing on the description of those instruments affected by temperature disturbances, also describing which are the relevant effects to be considered by the noise model. From this set of parameters conforming the noise model we will be able to derive a requirement for the temperature stability inside the experiment that must guarantee that temperature fluctuations will not spoil the main scientific goal. At the same time, this will translate in a noise level to be reached by our temperature sensors, which need to have a margin in its working range wide enough to sense any deviation from the requirement. The achievement of this sensitivity level will be the scope of Chapter 5.

---

[1]from the Greek $\delta\iota\alpha\gamma\nu\omega\sigma\tau\iota\kappa\acute{o}\varsigma$ [diagnostikós], able to distinguish

2.1 Thermal effects

As previously stated, thermal diagnostics are built upon a noise model which must take into account all those disturbance effects that may couple temperature into displacement noise either via direct displacement of the test mass or via fake signals registered at the phasemeter due to thermoptical effects. Although not always being the case, disturbances in the GRS are usually related to effects from the first kind whereas thermal effects affecting the OMS will be always of the second kind.

The spurious accelerations generated by these effects will be finally compared with the LPF acceleration requirement, equation (1.14), that we rewrite here

$$S_{a,\text{LPF}}^{1/2}(\omega) \le 3 \times 10^{-14} \left[1 + \left(\frac{\omega/2\pi}{3 \text{ mHz}} \right)^2 \right] \text{m s}^{-2}/\sqrt{\text{Hz}} \tag{2.2}$$

in the frequency range $1 \text{ mHz} \le \omega/2\pi \le 30 \text{ mHz}$.

2.1.1 Noise effects inside the Gravitational Reference Sensor

Temperature differences between the walls of the electrode housing cause differential pressures on opposite faces of the test masses, which in turn result in net forces on them, hence in noise in the drag-free measurement.

Three different mechanisms have been identified whereby temperature fluctuations distort the LTP readout: radiation pressure, radiometer effect and outgassing. We will give a quantitatively estimate of their respective contributions to temperature fluctuation noise, together with a brief description of other temperature related effects that can perturb the drag-free measurement.

Radiation pressure

A body at any (absolute) temperature T emits thermal radiation. This exerts pressure on any surfaces the radiation hits. According to standard electromagnetic theory, such pressure is given by

$$p_{\text{e.m.}} = \frac{4}{3} \frac{\sigma}{c} T^4 \tag{2.3}$$

where $\sigma = 5.67 \times 10^{-8} \text{ Wm}^{-2}\text{K}^{-4}$ is the Stefan-Boltzmann constant, and c is the speed of light. Thus, if there are temperature fluctuations around the test mass, a noisy net force will appear on it —see Figure 2.1 for a graphical display. The effect can be easily quantified making use of equation 2.3:

$$\Delta p_{\text{e.m.}} = \frac{16 \sigma}{3 c} \alpha_{\text{e.m.}} T^3 \Delta T \tag{2.4}$$

where Δp, ΔT make reference to differences of pressure and temperature between the sides of the test mass and $\alpha_{e.m.}$ is the view factor parameter which takes into account the geometry of the problem. Appendix A shows the computation of this value which, for the case of interaction between test mass and electrode housing walls, is estimated to be $\alpha_{\text{e.m.}} \simeq 0.68$. Associated
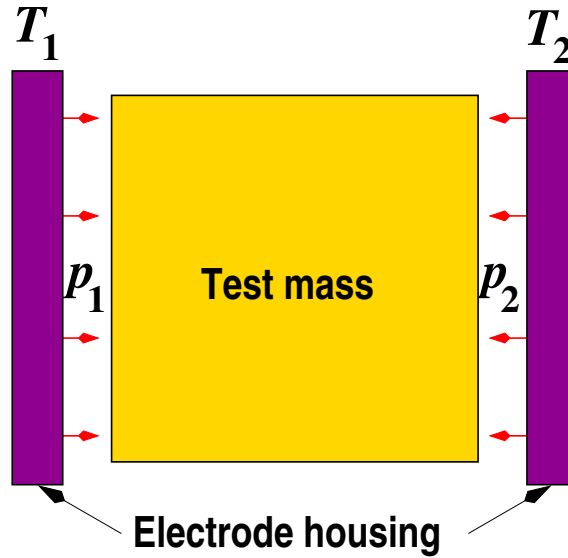
Figure 2.1: EH scheme

acceleration noise is hence obtained multiplying the above by the test mass surface area, A_{TM} and dividing by its mass m_{TM}:

$$\Delta a_{\mathrm{e.m.}} = \frac{16\,A_{\mathrm{TM}}\sigma}{3\,m_{\mathrm{TM}}c}\,\alpha_{\mathrm{e.m.}}\,T^3\Delta T \tag{2.5}$$

Radiometer effect

The radiometer effect has widely appeared in discussions related to experiments aiming to test the Equivalence Principle [66, 65, 81] such as the STEP [106] or the MICROSCOPE [98] missions.

The radiometer effect takes its name from the Crookes's lightmill radiometer [2]. This effect happens in rarefied gas atmospheres, where the gas particles have a mean free path well in excess of the dimensions of the containing vessel, so that equilibrium conditions do not happen when pressure is uniform, but rather when the ratios of pressure to square root of temperature equal one another.

This can be better understood if we consider two vessels at different temperatures T_A and T_B connected through a hole, a flow of gas molecules from the hotter to the colder receptacle will be established until equilibrium is reached. We can thus consider equilibrium will be achieved when the number of molecules per unit time passing from A to B is the same as the rate going from B

---

[2] "It was Reynolds in 1879 who first proposed the right explanation after a first proposal of Maxwell who was delighted to see a demonstration of the radiation pressure as predicted by his theory of electromagnetism. However, radiation pressure should make the lightmill turn in wrong way, opposite to the radiometer effect. Maxwell refereed Reynolds paper and submitted a paper to the Royal Society giving credit to Reynolds explanation but criticising his mathematical treatment. Reynolds was greatly incensed to view how Maxwell paper criticising his work was published even before his own work but Maxwell's death that same year ended with the controversy." From [36].

to A,

$$n_A \, \bar{v}_A = n_B \, \bar{v}_B \qquad (2.6)$$

where n is the number of particles per unit volume and v the average speed of the gas molecules, expressed in terms of the gas molar mass m and the pressure p as

$$
\begin{aligned}
n_i &= \frac{p_i}{K_B \, T_i} \\
v_i &= \sqrt{\frac{3 \, K_B \, T}{m}}
\end{aligned}
\qquad (2.7)
$$

Replacing these expressions in (2.6), we can obtain the pressure dependence in terms of temperature [47]

$$\frac{p_1}{\sqrt{T_1}} = \frac{p_2}{\sqrt{T_2}} \qquad (2.8)$$

Taking the derivatives at both sides, the effect can be expressed as

$$\Delta p = \frac{1}{2} \frac{\Delta T}{T} p \qquad (2.9)$$

Returning now to the LTP conditions, the test mass acceleration associated with the radiometer effect can be, in a first approximation, related to the gradient between opposite faces obtaining the following expression

$$\Delta a_{\mathrm{radiometer}} = \frac{1}{2} \frac{p \, A_{\mathrm{TM}}}{m_{\mathrm{TM}}} \frac{\Delta T}{T} \qquad (2.10)$$

This is the basic equation of the radiometer usually considered to describe the radiometer effect in the LTP case. However, as in the radiation pressure case, the original expression lacks from a geometrical factor taking into account the particular distribution of interacting surfaces in the GRS. The previous derivation of the effect considered two vessel at different temperature and the condition to achieve equilibrium between both, a more detailed description would have to include angular dependences. The reader can find a brief description of a theory for the radiometer effect containing angular dependences in Appendix B.

Outgassing

In high vacuum conditions, the interaction of molecules with the walls of the containing vessel plays an important role in the level of vacuum which can be achieved. The rarefied conditions where the bouncing takes place implies that the process does not statistically follow an elastic collision. The group of interactions in which the gas is retained by the solid (or liquid) receives the name of *sorption* and includes two mechanism: adsorption and absorption. The opposite mechanism, i.e. when the gas molecules are released from the material, are consequently known as *desorption* or

outgassing [80].

In order to understand the difficulties that outgassing poses on the GRS subsystem it will be useful to briefly describe the phenomena taking place during these processes. The *adsorption* process is an activation mechanism. Thus, a molecule impinging on the surface can assume an equilibrium energy at the lowest potential state of the potential energy if an energy barrier is overcome. Since the forces are attractive, work is done in adsorbing molecules and heat is generated, being thus an exothermic process. The amount of heat differs depending on the process. If the adsorption is purely physical it involves Van der Waals forces and the maximum attainable adsorption energy is approximately 0.3 eV/molecule. However, if chemical processes take place the adsorption similar to the formation of a chemical compound with transfer of electrons and the energy of adsorption can be much greater ≈ 12 eV/molecule. If the molecule finally enters the material in much the same manner as a gas dissolving in a liquid, the molecule is considered to be *absorbed*.

Outgassing process is therefore dependent on pressure, the shape of the material, the kind of surface and, the most important for this study, on temperature. If the temperature raises in one side of the Electrode Housing, molecules from that side will have more energy to overcome the potential barrier and a net flux will be established, pushing the test mass to the colder face of the electrode housing. Moreover, an important consequence of the outgassing process is that it affects the global pressure level and therefore the radiometer effect which is directly proportional to the pressure. It is therefore of great interest to model and parametrise this contribution.

However, the outgassing process is harder to evaluate in terms of well established principles as the previous effects. The usual way to model outgassing is to consider it as an the activation process, therefore the outgassing rate Q can be expressed as [80, 81]

$$Q(T) = Q_0 \, e^{-E_{act}/K_B \, T} = Q_0 \, e^{-\Theta/T}, \quad [Q] = \frac{\mathrm{Pa\,m}}{\mathrm{s}} \tag{2.11}$$

where Q_0 is a constant factor and Θ is the activation temperature strongly depending on the gas and the host material but considered to be allocated on the range $[3000\,\mathrm{K}, 30000\,\mathrm{K}]$ producing thus a strong temperature dependence.

As before, we can take advantage of equation (2.11) to derive a relation describing the outgassing effects in the GRS environment with respect to temperature gradients between both faces of the electrode housing. This can be shown to be expressed by [21]

$$\Delta a_{out} = \frac{Q(T) \, A_{\mathrm{TM}}}{C_{eff} \, m_{\mathrm{TM}}} \frac{\Theta}{T^2} \Delta T \tag{2.12}$$

where now the geometric dependence is included in the C_{eff} factor, which stands for the *effective conductance* of the molecular flow path around the test mass and through the holes in the GRS.

Once the expression for the pressure difference is found, we now face the materials properties question. Materials are parametrised in what respects outgassing using three parameters:

- *Total Mass Loss (TML)* measures the difference of weight of the sample before and after a baking process.

- *Collected Volatile Condensed Materials (CVCM)* measures the difference between the weight of a clean collector and of the collector having condensed materials after the baking of the sample, providing the mass of condensables.

- *Water Vapor Regained (WVR)* this value is the amount of water readsorbed/reabsorbed in 24 hours while the sample is exposed to 25 ℃, and 50% relative humidity. It is given as a percentage of the starting mass.

A complete list of materials used in space applications classified in terms of these parameters is freely provided by NASA [64].

The issue has also attracted attention of people from other space missions [65, 66], and further experimental work appears to be necessary to reliably assess the impact of this phenomenon. Partial evidence has however been gathered that outgassing might be in practice the dominant thermal effect in the LTP [21].

Thermal distortion

Thermal distortions of the electrode housing due to thermal expansion are sources of noise to be considered in the design of the GRS. The effect to be considered in this case is twofold since the expansion of an electrode will obviously affect the relative distance between test mass and electrode, i.e., converting into equivalent displacement noise but it will also induce a change in the capacitance between test mass an electrode, i.e. converting into effective acceleration noise in the sensor [27, 99].

The effect is complex due to the dependence on the geometry of the spacecraft and on materials used. A detailed study of this effect requires a dedicated thermal and structural model [76]. However, first estimations seem to show that this noise source has a negligible effect. For instance, assuming a temperature stability $S_T^{1/2} \simeq 2 \times 10^{-4}\,\mathrm{K}/\sqrt{\mathrm{Hz}}$, a 1 kg test mass, 5 cm of distance to the test mass and a thermal expansion coefficient of $2 \times 10^{-5}\,\mathrm{K}^{-1}$ the acceleration noise obtained is $2 \times 10^{-16}\,\mathrm{m\,s}^{-2}/\sqrt{\mathrm{Hz}}$ [89, 94], below the noise budget requirement (2.2).

Residual gas impacts

Residual gas inside the GRS can induce noisy motion of the test masses. The effect is however driven by the pressure or temperature average value instead of thermal fluctuations as the rest of effects treated in this section. Being however a thermal related effect, we name it here for the sake of completeness.

To get a rough estimate of the effect of random impacts of molecules in the test mass, we consider an acceleration described as [89]

$$
\begin{aligned}
a &= \text{(number density)} \cdot \text{(impact rate)} \cdot \text{(average velocity)} \\
&= n \cdot \left(\frac{n \, \bar{v} \, A_{TM}}{3} \right) \cdot \bar{v}
\end{aligned}
\tag{2.13a}
$$

where the molecules average mean velocity, $\bar{v}$, and the number density n are

$$
\bar{v} = \sqrt{\frac{3 \, K_B \, T}{m}}
\tag{2.13b}
$$

$$
n = \frac{p}{K_B \, T}
\tag{2.13c}
$$

Substituting these expressions in equation (2.13a), the following expression for acceleration noise due to residual gas impacts is obtained.

$$
a = \left(\frac{p \, A_{TM}}{m_{TM}^2} \right)^{1/2} (3 \, K_B T \, m)^{1/4}
\tag{2.14}
$$

As expected, the effect is not dependent on temperature gradients across the electrode housing but on global magnitudes such as temperature or pressure in the GRS environment. The allocated budget for this noise effect is $S_a^{1/2} \sim 1 \cdot 10^{-15} (\mathrm{m/s^2})/\sqrt{\mathrm{Hz}}$

Total temperature fluctuation noise in the GRS

Having enumerated the thermal processes that may couple temperature disturbances to test mass motion in the GRS we can now proceed to set a limit on temperature gradient which ensures this forces to be below the acceleration goal or, more precisely, set a limit ensuring that these forces do not exceed the allocated noise budget.

Outgassing, the radiometer effect and radiation pressure fluctuations are of course totally correlated and hence the spectral densities of acceleration and temperature in the *GRS* are related by

$$
S_{a, \text{ tf GRS}}^{1/2}(\omega) = \frac{A_{TM}}{m_{TM}} \left[\alpha_{e.m.} \frac{16}{3} \frac{\sigma}{c} T^3 + \alpha_{radio} \frac{1}{2} \frac{p}{T} + \frac{Q(T)}{C_{eff}} \frac{\Theta}{T^2} \right] S_{\Delta T, \text{ GRS}}^{1/2}(\omega)
\tag{2.15}
$$

Nominal conditions in the LTP are the following [3]:

$$
\begin{array}{ll}
A_{\mathrm{TM}} = 4.6 \times 10^{-2} \text{ m} & \Theta = 3 \times 10^4 \\
m_{\mathrm{TM}} = 1.96 \text{ kg} & Q(\mathrm{T}=293\,\mathrm{K}) = 1.4\,\mathrm{nJ/s} \\
T = 293 \text{ K} & C_{eff}|_{GRS} = 4.3 \times 10^{-2}\,\mathrm{m^3/s} \\
p = 10^{-5} \text{ Pa} &
\end{array}
$$

which give

---

[3]Numerical values for the outgassing parameters are extracted from on ground results in the torsion pendulum [21]. These values could change for the flight model since the foreseen baking process is expected reduce the outgassing flow coming from the walls of the Electrode Housing.

$$S_{a,\,\text{tf GRS}}^{1/2}(\omega) \quad = \quad (a_{rad} + a_{radio} + a_{out})S_{\Delta T,\,\text{GRS}}^{1/2} \tag{2.16}$$

$$\simeq \quad [18 + 9 + 40] \times 10^{-12} S_{\Delta T,\,\text{GRS}}^{1/2}(\omega)\,\text{ms}^{-2}/\sqrt{\text{Hz}} \tag{2.17}$$

the thermal feedtrough factor is thus in the order of magnitude $\sim 100\,\text{pN/K}$ [21]. It must be noted that, as previously stated, these effects are matter of current research and that the precisely determination of the related coupling factors is to be done in flight in the final LTP experiment conditions.

2.1.2 Noise effects inside the *OMS*

Temperature disturbances affecting the OMS will induce pathlength variations on the interferometer that will appear on the final interferometric readout as fake test mass displacements. The requirement for the OMS performance is set to [100]

$$S_{x,laser}^{1/2} \leq 9 \times 10^{-12} \left[1 + \left(\frac{f}{3\,\text{mHz}} \right)^{-4} \right]^{1/2} \frac{\text{m}}{\sqrt{\text{Hz}}} \tag{2.18}$$

It is thus necessary to ensure that any thermal related effect does not translate into a contribution exceeding (2.18). While it is not difficult to characterise how individual components are influenced by thermal effects, to assess the behaviour of the fully integrated optical metrology is a more complicated task. We will therefore first consider the physical temperature related effects affecting the OMS and then proceed to estimate its contributions to the interferometer readout taking into account those locations on the OMS that are envisaged to be sensitive to thermal changes.

Physical effects

The first effect we can expect from temperature gradients in an interferometer is that thermal expansion affects differentially to both interferometer arms. The effect is readily explained with the expression

$$dx = L\,\alpha\,dT \tag{2.19}$$

where L is the nominal length of the interferometer arm and $\alpha = \frac{1}{L}\frac{dL}{dT}$ is the thermal expansion coefficient. Although expression (2.19) is simple, the evaluation of the effect can become a complicated task because of the complex geometry covered by the laser beam or by the temperature gradient profile that may cause differential expansions at different points.

A second effect to be considered is the imprint that temperature fluctuations may cause on individual optical elements. In this case not only the thermal expansion mechanism needs to be considered but also proper optical effects may disturb the laser pathlength. In order to quantita-

tively understand this mechanism, let's consider a laser beam impinging on a plate of thickness L and refractive index n. The pathlength variation that this optical element adds to the laser beam can be computed as the difference between the pathlength with and without the slab. If, for the sake of simplicity, normal incidence is assumed the resulting pathlength difference can be written down as

$$s = n \cdot L - L \tag{2.20}$$

where the pathlength without the slab is considered to be L since $n = 1$. Taking the derivative with respect the temperature in (2.20) will show which are the dependences that we shall take care of for the OMS thermal diagnostics,

$$\frac{ds}{dT} = L \left(\frac{dn}{dT} + \alpha(n - 1) \right) \tag{2.21}$$

where $\alpha = \frac{1}{L} \frac{dL}{dT}$ is the coefficient of thermal expansion. Moreover, it is convenient to translate pathlength variations to phase since this will be our final goal. Taking into account the relation between the phase measured and the pathlength

$$\phi = \frac{2\pi}{\lambda} s \tag{2.22}$$

where λ is the laser wavelength, we get [57]

$$\frac{d\phi}{dT} = \frac{2\pi L}{\lambda} \left(\frac{dn}{dT} + \alpha(n - 1) \right) \tag{2.23}$$

This is thus the figure of merit to be evaluated in those OMS locations sensitive to temperature disturbances. From equation (2.23) it appears that there are two thermal effects that will couple the interferometric readout to temperature gradients inside the LTP. These are:

- Index of refraction dependence with temperature of optical components depends on temperature.

- Temperature changes cause dilatation (and contractions) of optical elements, which in turn cause light's optical path to change accordingly. If an optical element is in contact with a material with different thermal expansion coefficient, then stress effects can induce pathlength differences as well.

These effects need to be evaluated separately depending on the location since materials and the interaction with the laser beam differs for each compound.

OMS critical locations

Optical Bench   The optical elements attached to the bench form the four interferometers on which the metrology subsystem of the LTP is based. At the same time, the bench has ten pho-

todiodes that will be dissipating $\approx 5\,\mathrm{mW}$. These are, apart from the diagnostics items, the only thermal active parts inside the LCA.

However, the material selected for the optical bench manufacturing, Zerodur, ensures that power fluctuations of the photodiodes will not be detected by the interferometer given its low Coefficient of Thermal Expansion (CTE) — see values from Table 1.1. For instance, a quick analysis shows that the dissipated power of one photodiode in the optical bench will increase its temperature $\approx 1 \times 10^{-7}\,\mathrm{K}$, i.e. a negligible amount [99] when measured as pathlength difference.

Even so, first estimations seem to point out that temperature related effects can be neglected if a temperature stability of $S_T^{1/2} \leq 10^{-4}\,\mathrm{K}/\sqrt{\mathrm{Hz}}$ can be ensured [27].

Optical Window   Is the interface between the test masses and the Optical Bench: laser beams must bounce off the test masses to monitor their positions by precision interferometry, hence a transparent window is necessary for the light to make it to the interior of the VE.

The OW is a plane-parallel plate and is therefore a potential source of noise: random variations of its optical properties may result in corresponding optical path fluctuations, which distort the laser light phase, hence the optical Metrology readout. Great care must be taken when manufacturing this critical component of the LTP and, once manufactured, characterisation of its behaviour duly performed.

The Optical Window is subjected to both thermal effects previously enumerated. Thermal gradients will change the pathlength of the laser beam going through it but at the same time this optical element has a peculiar property which differences it from the rest: is the only non bonded optical element. The glass separating the vacuum enclosure from the optical bench will be clamped into a Titanium ring and therefore thermal fluctuations on the metal could induce more disturbing effects

We will treat in detail the Optical Window problem in Chapter 8 but, before that, we can make a fast estimate of the effect of the coupling of the laser beam with thermal fluctuations on the optical window based on the properties of the glass, being this the *OHARA S-PHM52* glass. If the data-sheet properties are used to calculate the thermal related path-length variations in the optical window glass due to changes in the refractive index, the result is that $d\phi/dT$ is $\sim 21 \times 10^{-3}\,\mathrm{mrad/K}$ [57].

From this coupling coefficients, a first estimation on the temperature stability requirement can be obtained. If the optical layout in Figure 1.11 is taken into account, we must consider that the laser beam passes four times through an optical window (two times for each window in its path from the Optical Bench to the Test Mass and viceversa) and thus the overall coefficient becomes $\approx 4 \times 21 \times 10^{-3}\,\mathrm{rad/K}$. As an example, a budget of $9\,\mathrm{pm}/\sqrt{\mathrm{Hz}}$ ($\approx 50\,\mu\mathrm{rad}/\sqrt{\mathrm{Hz}}$) of equation (2.18) would lead to a required thermal stability of $S_T^{1/2} \leq 6 \times 10^{-4}\,\mathrm{K}/\sqrt{\mathrm{Hz}}$ in the measurement band.

Struts   The LCA is connected to the thermal shield by means of 8 Carbon Fiber Reinforced Plastic (CFRP) struts. Being the only conductive link to the external temperature environment, they are considered as critical items in the thermal design.

Although not being directly part of the OMS subsystem, temperature leaks through the struts could be sensed by the interferometer as displacements due to stress on the optical bench which makes it to be considered as a part of the OMS thermal diagnostic subsystem. Due to the complex coupling between temperature evolution, structural properties and interferometric sensing it is difficult to predict the response of the interferometer readout to these disturbances. As before, the low expansion coefficient of the material puts a hard limit on the possible effects of thermal dilatation due to struts.

Total temperature fluctuation noise in the OMS

Significant progress has been made since the early design proposals —see reference [10] and following articles in that issue of *Classical and Quantum Gravity*—, and improved materials and designs are now available. Altogether, it appears that

$$S_{T,\,\mathrm{OMS}}^{1/2} \simeq 10^{-4}\,\mathrm{K}/\sqrt{\mathrm{Hz}} \tag{2.24}$$

is a sensible requirement which should comfortably guarantee the performance of the optical bench against temperature fluctuations in flight —see [99], Chapter 12, and [16]. Like before, the noise level (2.24) is estimated to account for about 10 % of the total LTP acceleration noise, equation (2.25).

2.2 Total temperature fluctuation noise budget for the *LTP*

Random temperature fluctuations in the LTP introduce noise in the system through various channels and mechanisms, as we describe and quantitatively assess in this section. Proper characterisation of these effects will help us set the limits of temperature fluctuations compatible with LTP full science performance.

As a rule of thumb, the total contribution of temperature fluctuation noise to the total acceleration noise, equation (2.2), should not exceed 10 %. We thus require that

$$S_{a,T}^{1/2}(\omega) \le 3{\times}10^{-15} \left[1 + \left(\frac{\omega/2\pi}{3\ \mathrm{mHz}}\right)^2\right]\,\mathrm{m\,s^{-2}}/\sqrt{\mathrm{Hz}} \tag{2.25}$$

for frequencies within the LTP MBW. This assumption is in fact somewhat conservative, as the Project Engineers have estimated that more than twice this value is actually compliant with the overall LTP noise budget [102]. We shall however adopt equation (2.25) as reference to ensure we are playing on the safe side.

Estimates so far indicate that both GRS and OMS noise are very accurately in the order of

$$S_T^{1/2}(\omega) \le 10^{-4}\,\mathrm{K}/\sqrt{\mathrm{Hz}}\,, \quad 1\,\mathrm{mHz} \le \omega/2\pi \le 30\,\mathrm{mHz} \tag{2.26}$$

Noise in the GRS should be mostly uncorrelated with noise in the OMS, and they are of

a different nature, anyway: while temperature *gradient* fluctuations across the test masses are responsible for GRS thermal disturbances, *local* temperature fluctuations affect the OMS.

The above argument does not however preclude the fact that GRS and OMS temperature fluctuations will each contribute to the total LTP noise budget —this is often termed noise *apportioning* in the technical jargon [100]. The zero-correlation hypothesis means that both kinds of noise add quadratically. We are thus reassured that equation (8.13) is a sensible requirement for the temperature fluctuations which can be tolerated in the LTP. Let us however stress that we still can count with some margin, as acceleration noise due to temperature fluctuations has been taken as a conservative 10 % of the total acceleration noise.

2.3 Temperature diagnostics items distribution

Temperature diagnostics items have to be distributed through the LCA. Figures 2.2 to 2.3 show the current baseline distribution of temperature sensors and heaters in the LTP experiment.

This distribution takes into account the thermal effects above described. For instance, four sensors in couples of two in each x axes faces of the GRS allows the detection and characterisation of gradients in this direction where the capacitive sensors maximise its sensitivity. The same number of heaters guarantees the application of the diagnostics philosophy described, i.e., applying high Signal-to-Noise ratio thermal signals to enhance the test mass motion due to thermal effects. It must be pointed out that although physically independent, both heaters on the same GRS face are jointly connected and thus can not be switched on separately.

Thermal disturbances in the Optical Window will be characterised by a set of three sensors, two lateral and one a the top together with two lateral heaters following with the same diagnostic philosophy.

Possible thermal leaks arriving at the LCA through the struts will be sensed by temperature sensors attached to them. However, not all of them will be sensed since the initial structure of the LTP had only six struts and thus six sensor and heater pairs were allocated. The addition of two more struts left short of sensors and heaters in two of the eight struts.

Finally four sensors are distributed on the Optical Bench. In this case there is no heater to induce shocks, the reason being the high power required to induce a thermal response in the Zerodur.
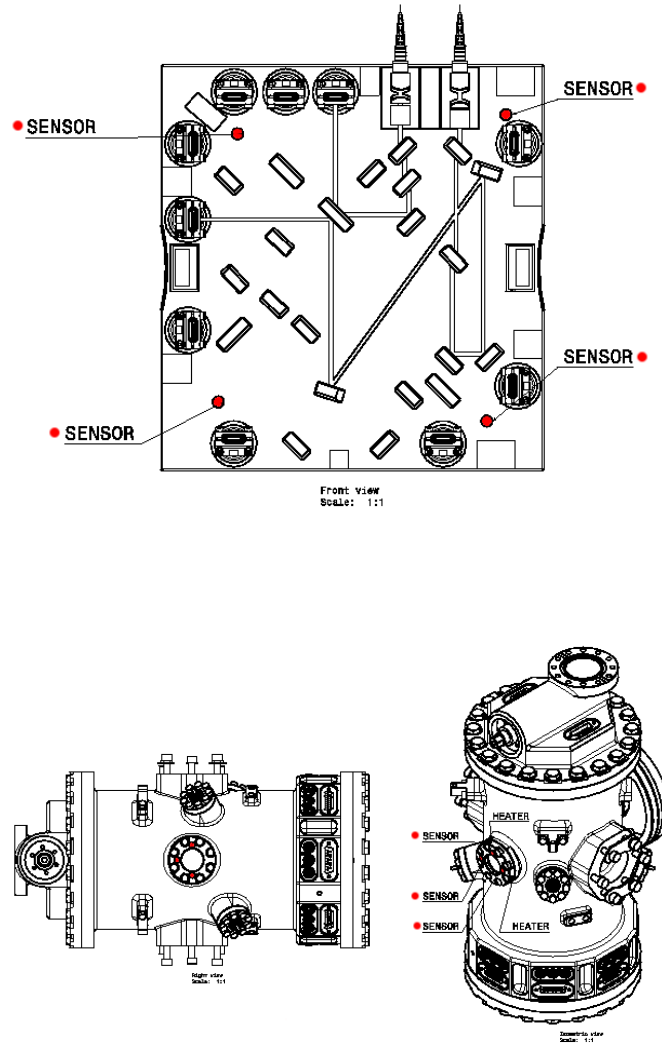
Figure 2.2: *Top*: Scheme of the distribution of thermal diagnostics items through on the Optical Bench. This proposal has been modified, the current baseline is to displace these sensors to the lateral sides of the Optical Bench to prevent any interaction of the sensors' wiring with the laser beam. *Bottom*: Scheme of the distribution of thermal diagnostics items in the Vacuum Tank enclosing the Test Mass. Three sensors (in red) and two heaters (in green) are distributed surrounding the Optical Window.
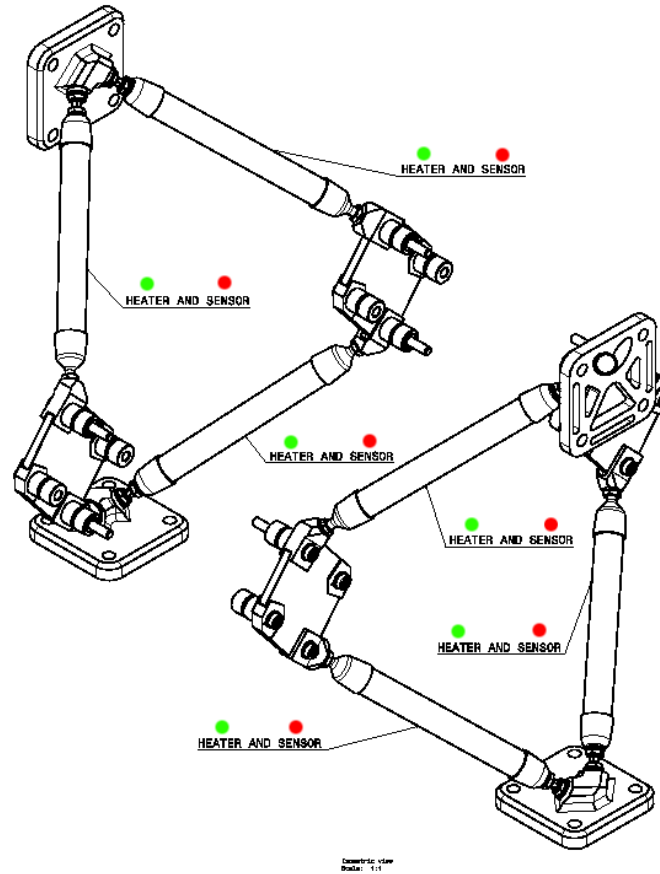
Figure 2.3: Scheme of the distribution of thermal diagnostics items in the LCA struts. Due to the isometric view, only those Struts with thermal diagnostics items are shown. There are however two more of them not shown in the figure.

II. Temperature subsytem qualification

" Caminante, no hay camino,
se hace camino al andar. "

Proverbios y Cantares
Antonio Machado

Chapter 3

Thermal analysis tools

We will start this Chapter reviewing a standard technique in engineering when dealing with thermal problems, namely the thermal analogy to electrical circuits. This methodology is of standard use in thermal design. It allows a clear and fast idea of the thermal magnitudes involved in the problem. Since we will be facing the thermal design problem in Chapter 4, where we will be interested in describing the properties of a thermal insulator, it will be useful to first briefly describe some concepts not only to recover it from the literature [44] but also to fix a nomenclature which usually leads to misunderstandings.

We will therefore sequentially pass from the simplest assumption to increasing levels of complexity in resolving thermal problems. Our final step will be the resolution of the full Fourier's equation in frequency domain to obtain a thermal transfer function describing the thermal fluctuations inside a given volume once fixed the initial and boundary conditions. This result will be of particular interest in Chapter 4 when designing a thermal insulator in the low frequency regime.

3.1   Thermal resistance overview

In most applications, the thermal analysis to be performed on a system is basically restricted to its steady state approximation. Under this condition, we are not interested in the non-stationary evolution of the thermal process, the assumption is made that the system has gone through a first transient regime and has finally reach a steady solution.

We will herein consider the steady state approximation in order to obtain thermal expressions describing the *thermal resistance* of a given system. The electrical analogy will show to be specially fruitful in these cases and therefore we will take profit of it to study thermal phenomena. This will be better understood following an example.

Let's consider a slab where a constant heat flux, $\dot{Q}$, is established between its two edges at a distance L. We will assume that all the flux flows in the x direction confined to an area A. In these conditions, Fourier's law relates flux and temperature gradient in the following manner,

$$\dot{Q} = -k\,A\,\frac{dT}{dx} \tag{3.1}$$

Straightforward integration leads to

$$\dot{Q} = \frac{T_1 - T_2}{L/k\,A} \tag{3.2}$$

where T_1 and T_2 refer to temperatures at both edges. A simple analogy can be traced from this expression with Ohm's law $I = V/R$ considering the temperature difference as a driving potential in the same way voltage acts in the electric case. We can therefore define a *thermal resistance* as $R \equiv L/K\,A$.

The usefullness of this parameter is clearly found when considering more complex or composite structures. If we, for instance, apply the same reasoning previously followed to a system composed of two adjacent slabs and compute the temperature gradient the relation that appears can be split into two terms, each one with a clear analogy in electrical terms.

$$\begin{aligned}
\dot{Q} &= \frac{T_1 - T_3}{L_A/K_A\,A + L_B/K_B\,A} \\
&= \frac{\Delta T}{R_A + R_B}
\end{aligned} \tag{3.3}$$

As shown in Figure 3.1 the relation between heat flux and temperature gradient in the steady regime can be easily written down if we consider the thermal resistances in series in the electric analogy. This approach leads directly to the second expression in equation (3.3), with all the geometric information included in the thermal resistance parameter, R.

Once derived this result, most of the thermal steady state problems can be split up in simple geometries and solved by means of the analog thermal circuit, these are the so called *thermal networks* [44]. Table (3.1) summarises thermal resistance expressions for simple common geometries which can be used for this purpose. Naturally, different geometries imply different dependence of the thermal resistance with the geometrical variable: from proportional to the length in the slab case to the difference of inverse length in the hollow sphere case. In the cylinder and the sphere case, hollow objects had to be considered in order to impose the constant temperature condition in the inner face.

3.1.1 The lumped capacitance method

The thermal resistance concept shows to be a useful concept in thermal design. However, its main limitations reside in the steady state condition, i.e., the time independent behaviour. Because we will finally be interested in thermal fluctuations and its power spectra representation we will in this section go through the next step in thermal analysis which is to introduce time dependencies.

Following the same previous electrical analogy we will need to introduce a *thermal capacitance* which enables a time dependent analysis. The standard method to do so in thermal engineering
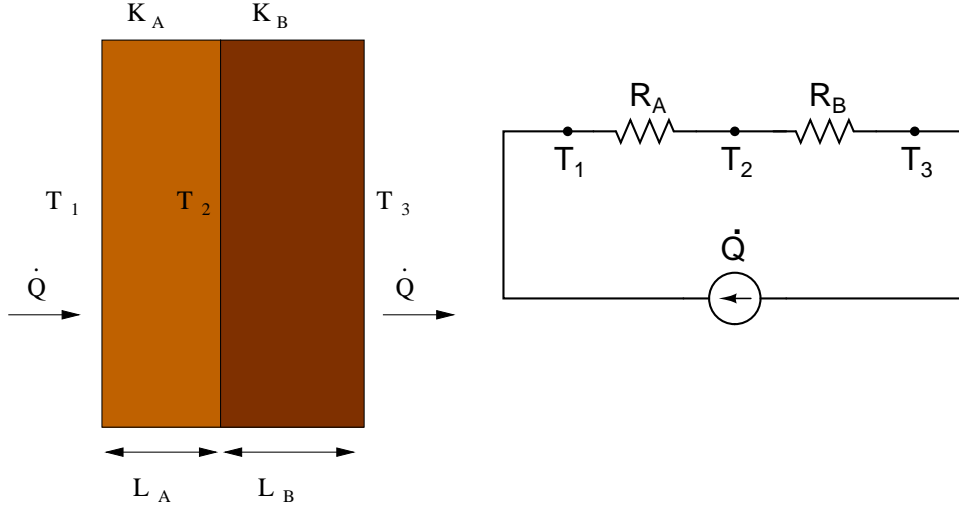
Figure 3.1: Graphical representation of the electrical analogy to thermal problems.

is the *lumped capacitance method*. The main hypothesis on which this method is based is that the temperature in the solid is spatially uniform at all times, which directly implies the suppression of temperature gradients across the volume. This may be the case if thermal resistance inside the body is lower than the resistance between the body and its surroundings. Although this may not be the case in our final application, we will consider it as valid here to work out the expressions.

In this framework we can not consider Fourier's law because the uniform temperature condition will imply infinite thermal conductivity. Instead, an energy balance equation is used in this approach, this relation can be generally expressed as

$$ -h\,A(T(t) - T|_{t\to\infty}) = \rho V C \frac{dT}{dt} \tag{3.4} $$

where h is the *heat transfer coefficient* $[\mathrm{Wm^{-2}K^{-1}}]$, A the area crossed by the heat flux, ρ the density, V the volume and C the heat capacity. In equation (3.4) the *rhs* is the energy stored by the body whereas the *lhs* is the energy being supplied by the media. As a consequence of the uniform temperature assumption, no spatial dependencies appear in the equation and the time dependence can be easily solved leading to

$$ \theta(t) = \theta(0) \exp\left[-\left(\frac{h\,A}{\rho V C}\right)t\right] \tag{3.5} $$

where $\theta(t) = T(t) - T|_{t\to\infty}$.C Now, expression (3.5) defines a time constant for the thermal process which, recovering the electrical analogy, can be interpreted as a discharging time constant of a RC circuit

Geometry	Thermal resistance [K/W]
Slab (length L, section A)	$\dfrac{L}{K\,A}$
Hollow cylinder (length L, radius $r_2 > r_1$)	$\dfrac{\ln(r_2/r_1)}{2\pi LK}$
Hollow sphere (radius $r_2 > r_1$)	$\dfrac{1}{4\pi K}\left(\dfrac{1}{r_1} - \dfrac{1}{r_2}\right)$

Table 3.1: Steady thermal conduction resistances for common geometries

$$\tau_T = R_T C_T = \left(\frac{1}{hA}\right)(\rho VC) \qquad (3.6)$$

The capacitance here introduced provides an information of the *thermal inertia* of the solid. The response of the system to thermal inputs becomes faster reducing either the capacitance (the mass or heat capacity) or the thermal resistance (inversely related to contact conductivity). An increase of either parameter will result in a longer timescale to reach the thermal equilibrium.

A noteworthy point to introduce here is to consider the implication of the electrical analogy when switching to frequency domain analysis. This must be our final goal so it is interesting to start tracing some consequences with this first simple model.

If the capacitor analog is taken in full consideration, we can try to translate also its frequency domain interpretation to the thermal case. In doing so, we would have a low-pass filter with time constant $\tau_c = R{\cdot}C$, hence meaning that thermal changes with timescale $\tau < \tau_c$ entering this system will be suppressed (more suppressed as τ gets shorter) as well as variations of longer periods than the cut-off, $\tau > \tau_c$, will survive through the system. This interpretation will be greatly clarified in the following sections and we will be finally using it as a thermal insulator design tool (cf. § 4.1.4).

The lumped capacitance approximation is therefore a good description as far as we consider the uniform temperature condition acceptable. There is however a condition which sets the limit where this approximation is valid, the standard methodology to quantify the viability of the lumped capacitance method is to introduce the dimensionless *Biot number* which can be understood as the ratio of the body thermal resistance and the contact thermal resistance from body to the environment. The Biot number is defined as the ratio of thermal conductance resistance inside the solid to thermal contact resistance to the environment, which can be expressed as [44]

$$Bi \equiv \frac{hL}{K} = \frac{L/KA}{1/hA} = \frac{R_{cond}}{R_{cont}} \qquad (3.7)$$

where Bi is the Biot number. The uniform temperature condition can thus be considered to be fulfilled for situations where $Bi \ll 1$, in other terms, where the body thermal resistance is

much lower than the contact resistance. The threshold to divide both regimes is usually taken in the literature [44] as $Bi = 0.1$. If this condition does not apply we are forced to face the spatial gradient term of the Fourier equation, as we will see in next section.

3.2 Thermal transfer function

After exploring the steady state condition and the uniform temperature condition we need now to consider a more general analysis. The model herein studied will be based in the assumption that heat flows through the body only by thermal conduction. Being our final application a solid body, convection or radiation mechanisms are not considered to be relevant for the problem. No other special conditions are imposed on the solution. Under such general framework we must deal with the Fourier heat equation.

We will present two different approaches to solve this problem. Our first attempt will be to solve the Fourier equation in time domain and study the solution properties and then compare it to the solution obtained by considering the Fourier equation in the frequency domain. As we will see, the latter approach will show advantages with respect to the technical complexity, leading with less effort to the type of solution we will be interested in.

Our main problem will turn out to be the boundary condition defining the geometry of the problem which we will consider in a first attempt to be a spherical monolithic body. This seems to be the easiest choice that we shall use to go through the method without being worried about technical complexities that may arise in other geometries. After comparing both solutions, the time and the frequency domain one, this constraint will be relaxed in order to obtain solutions to a variety of geometries.

The time dependent solution will allow a description of great interest for our application: the evolution of temperature disturbances inside the body. However, it will turn out that fluctuations around an equilibrium state will be better described in terms of the Fourier transform and, as we will see, this will lead to the *transfer function* approach, where transfer function must be understood as the relation between temperature fluctuations in a given point of the body with respect to the environmental temperature fluctuations.

3.2.1 Spherical time domain solutions

Let then $T(\mathbf{x}, t)$ be the temperature at time t of a point positioned at vector $\mathbf{x}^1$ relative to the centre of the sphere. Fourier's partial differential equation reads

$$\rho C \, \partial_t T(\mathbf{x}, t) = \nabla \cdot [K \, \nabla T(\mathbf{x}, t)] \tag{3.8}$$

where ρ, C, K are the density, the specific heat and thermal conductivity, respectively. The problem needs specific initial and boundary conditions that will uniquely determine the solution.

---

[1]Through all this chapter we will be dealing with three dimensional functions. The notation convention adopted will be to denote by the vectors with bolded variable, i.e. $\mathbf{x} = (x, y, z)$.

These are chosen to be

$$
\begin{aligned}
\text{Boundary conditions :} \quad T(\mathbf{x} = \mathbf{x_c}, t) \ &< \ \infty & \text{(3.9a)} \\
T(\mathbf{x} = \mathbf{x_b}, t) \ &= \ T_0(\mathbf{x} = \mathbf{x_b}, t) & \text{(3.9b)} \\
\text{Initial conditions :} \quad T(\mathbf{x}, t_0 = 0) \ &= \ 0 & \text{(3.9c)}
\end{aligned}
$$

An analyticity condition is imposed at the centre and the temperature at the surface of this body is assumed to be known, $T_0(\mathbf{x} = \mathbf{x_b}, t)$. Because we will be mainly interested in fluctuations around an equilibrium value, a zero initial condition is fixed considering this initial moment as an arbitrary time after a first transient behaviour is overcome, we are thus assuming that $t_0 \gg \tau$ in equation (3.9c), where τ refers to the system transient timescale.

The boundary condition can be described in terms of a series of spherical harmonics as follows

$$
T_0(\mathbf{a}, t) = \sum_{l,m} b_{lm}(t) Y_{lm}(\theta, \phi) \tag{3.10}
$$

where $b_{l,m}(t)$ are the multipole components of $T_0(\mathbf{a}, t)$. The solution of this problem is exposed in Appendix C.1 in terms of the Sturm-Liouville orthogonal function theory. The expression for the temperature evolution on a given point $\mathbf{x}$ of the sphere is given by

$$
T(\mathbf{x}, t) = \sum_{n,l,m} Q_{nl} \, X_{nlm}(\mathbf{x}) \frac{1}{\tau_{nl}} \int dt' \, e^{-(t-t')/\tau_{nl}} \, b_{lm}(t') \tag{3.11}
$$

where

- Q_{nl} are coefficients depending on the radius and the physical properties ρ, C, K

- $X_{nlm}(\mathbf{x})$ is a set of orthonormal eigenfunctions in the sphere, solutions to the Sturm-Liouville problem

$$
\frac{K}{\rho C} \nabla^2 X_{nlm}(\mathbf{x}) = -\frac{1}{\tau_{nl}} X_{nlm}(\mathbf{x}) \tag{3.12}
$$

with homogeneous boundary conditions. They can be factorised as

$$
X_{nlm}(\mathbf{x}) = R_{nl}(r) Y_{lm}(\theta, \phi) \tag{3.13}
$$

splitting the dependencies into radial and the spherical harmonics contribution.

- τ_{nl} are characteristic time constants determined by the eigenvalue equation (3.12) and the boundary condition, equations (3.9).

A remarkable property of (3.11) is that the sphere acts as a series of *low-pass filters* applied on the temperature fluctuations acting on the surface on the sphere. Each multipole component

$b_{lm}(t)$ is weighted by the impulse response function $K_{nl}(t) = \tau_{nl}^{-1} e^{-t/\tau_{nl}}$, i.e., a linear low-pass filter with time constant τ_{nl}. This is more clearly seen in the frequency domain representation, Fourier-transforming equation (3.11),

$$\tilde{T}(\mathbf{x}, \omega) = \sum_{n,l,m} Q_{nl} \, X_{nlm}(\mathbf{x}) \frac{1}{\tau_{nl}} \frac{\tilde{b}_{lm}(\omega)}{1 + i \, \omega \, \tau_{nl}} \tag{3.14}$$

The external perturbation is thus suppressed by a series of low-pass filters with increasing time constant [53]. We can define a cut-off frequency for this filter considering its lowest frequency contribution, the first order frequency is —see equation (C.17) in Appendix C.1,

$$\omega_c = \frac{\pi^2 K}{\rho \, C a^2} \tag{3.15}$$

which relate all geometric values and material properties into a characteristic factor of the insulator. As expected, a higher degree of attenuation to external temperature perturbations requires either increasing the radius, the density or the thermal capacity of the material used or, alternatively reducing the thermal conductivity.

This way, we recover the frequency domain insight we first sketched in § 3.1. In this framework we naturally obtain a set of timescales τ_{nl} describing the properties of a solid volume as a thermal low-pass filter. We must therefore consider a solid volume not as a simple RC low-pass filter but as an infinite sum of them with decreasing time constants.

The comparison with the lumped capacitance approach leads us to interpret this infinite sum of filters as the consequence of the inclusion in the analysis of the spatial derivative, since the lumped capacitance method was based on the assumption that temperature was homogeneously distributed in the solid, meaning $\vec{\nabla} T = 0$. As seen when studying this case, this approximation yields directly to a unique time constant in the problem. However, as shown in equation (3.14) this characteristic parameter splits up into an infinite series when the spatial derivative is considered.

At this point, the series of τ_{nl} time constants acting as filter poles appears as the eigenvalues of the equation (3.12). When dealing with frequency domain expression we will find more concise expressions relating these series of parameters with the geometry of the problem.

Isotropic boundary conditions

Until now we have obtained a solution for the general spherical problem. In order to work out explicitly the expression previously derived, we will fix our attention in a less general problem. Let's consider the sphere in an isotropic temperature bath,

$$T_0(\mathbf{r} = \mathbf{a}, t) = B(t) \tag{3.16}$$

which directly translates into only monopole fluctuations in the harmonic expansion

$$b_{lm}(t) = \sqrt{4 \, \pi} B(t) \, \delta_{l0} \, \delta_{m0} \tag{3.17}$$
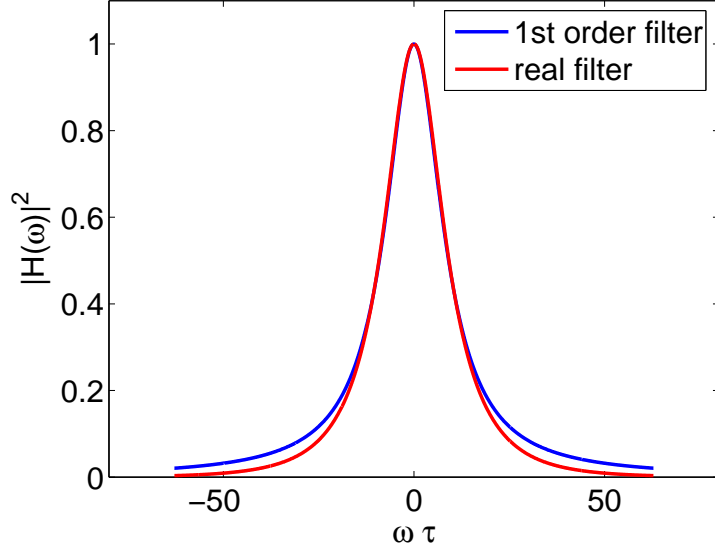
Figure 3.2: The isotropic real solution of the thermal transfer function is compared to a first order filter of equivalent time constant.

leading to the following temperature distribution

$$\widetilde{T}(\mathbf{x}, \omega) = 2 \sum_{n=1}^{\infty} (-1)^n \frac{\sin(n\pi r/a)}{n\pi r/a} \frac{\widetilde{B}(\omega)}{1 + i \frac{\omega\tau}{n^2\pi^2}} \tag{3.18}$$

This Fourier series is better analysed if the action of the spherical body contribution is separated from the external temperature dependence. If we write the previous relation as $\widetilde{T}(\mathbf{x}, \omega) = \widetilde{K}(\mathbf{x}, \omega) \widetilde{B}(\omega)$ all the relevant information about the thermal suppression is contained in $\widetilde{K}(\mathbf{x}, \omega)$ to which we shall refer as *transfer function* because it relates the input thermal signal from the environment —$\widetilde{B}(\omega)$— to the thermal response inside the body —$\widetilde{T}(\mathbf{x}, \omega)$. Following Appendix C.2, we can express the $\widetilde{K}(\mathbf{x}, \omega)$ function at the centre of the sphere as

$$\widetilde{K}(0, \omega) = \frac{(1+i)\beta}{\sinh(\beta)\cos(\beta) + i \cosh(\beta)\sin(\beta)}, \quad \beta \equiv \left| \frac{\omega\tau}{2} \right|^{1/2} \tag{3.19}$$

A closed transfer function expression is finally obtained for the monolithic spherical body. The methodology has however allowed us only to solve it in closed form at the centre of the geometry and some analytical development has been necessary. Figure 3.2 shows how this solution differ from a first order filter of equivalent time constant, the exponential decay makes the real filter to suppress much more efficiently thermal fluctuations at the filter tails. This fact is clearly understood as a consequence of the superposition of an infinite number of linear filters with decreasing time constant values.

3.2.2 Spherical frequency domain solutions

With the time domain we have been able to describe temperature fluctuations inside an spherical insulation body. The solution explicitly described in Appendix C.1 requires to solve a Sturm-Liouville problem. This should not be a problem if we are able to cope with the resulting Fourier series. For instance, in the spherical insulator the sum of the resulting Fourier series came up as a limit of an analytical equality (cf. Appendix C.2). However, this fortunate match may turn into an impossible task when facing more complex problems. This may be the case for the next level in complexity situations we will find interesting to solve, as multiple layer objects and non-spherical geometries.

An alternative procedure to solve this problem is through integral transforms. In § 3.2.1, we found the Fourier representation to be very useful in order to understand the physical meaning of the solution. We can now go a step further and use the frequency domain representation as the most natural choice to solve our problem. Since our final goal is the description of thermal fluctuations inside the insulator body and to set a limit for the expected fluctuations coming from external disturbances in the Measuring BandWidth (MBW), the integral transform method to solve Partial Differential Equations (PDE) will show suitable for this purpose.

Integral transform methods allow to deal with PDE algebraically switching to a new domain, frequency in our case, where partial derivatives acquire generally simpler dependences. The main disadvantage when working out PDE solutions with the integral transform method is to antitransform the solution to obtain the time dependent expressions. We can, however, get through this difficulty by realising that the transformed solution is in fact our final solution since it describes the filter properties of our insulator body and therefore we do not need to antitransform to extract the relevant information. As shown below, this will make easier the solving procedure and hence provide a method to solve geometries of increasing complexity.

We will compare this methodology solving the heat equation in a spherical monolithic body with a known external temperature bath, equations (3.8) and (3.9a-3.9c). Fourier transforming the heat equation we obtain

$$i\omega\rho C\,\tilde{T}(\mathbf{x},\omega) = \nabla \cdot [K\nabla\hat{T}(\mathbf{x},\omega)] \tag{3.20}$$

If we consider a single layer of a material with constant conductivity, equation (3.20) can be recast in the form

$$(\nabla^2 + q^2)\widetilde{T}(\mathbf{x},\omega) = 0 \tag{3.21}$$

where the initial condition (3.9c) has been used to remove the initial value appearing as a result of the Fourier transform of the time derivative. Equation (3.21) is of the Helmholtz kind with its characteristic parameter q defined in terms of the properties of the material.

$$q^2 = -i\omega\frac{\rho C}{K} \tag{3.22}$$

Now, we can write down the general solution for this equation taking into account the spherical symmetry of the problem which sets the eigenfunctions to be used, i.e., the spherical Bessel functions, $j_l(z)$ and $y_l(z)$, for the radial equation and the spherical harmonics $Y_{lm}(\theta, \phi)$ for the angular solution —see [6], leading to

$$\widetilde{T}(\mathbf{x}, \omega) = \sum_{lm} [A_{lm}(\omega) \, j_l(q\,r) + B_{lm}(\omega) y_l(q\,r)] Y_{lm}(\theta, \phi) \tag{3.23a}$$

where the radial functions are defined as

$$j_l(z) = z^l \left(-\frac{1}{z} \frac{d}{dz} \right)^l \frac{\sin z}{z} , \quad y_l(z) = -z^l \left(-\frac{1}{z} \frac{d}{dz} \right)^l \frac{\cos z}{z} \tag{3.23b}$$

The determination of the expansion coefficients is straightforward for the case being studied since convergence of the solution at the centre of the sphere, condition (3.9a), requires $B_{lm} = 0$ due to the divergence of $_l(z)$ at $x = 0$. The second boundary condition, equation (3.9b), fixes the environment temperature and hence sets an expression for the A_{lm} coefficient. Recalling the spherical expansion of the surface temperature, equation (3.10), now in the frequency domain

$$\widetilde{T}_0(\mathbf{r} = \mathbf{a}, \omega) = \sum_{l,m} \widetilde{b}_{lm}(\omega) Y_{lm}(\theta, \phi) \tag{3.24}$$

leads to the following simple identification valid at all orders in the spherical decomposition

$$A_{lm}(\omega) = \frac{\widetilde{b}_{lm}(\omega)}{j_l(q\,a)} \tag{3.25}$$

If we now, as previously stated, define the transfer function as the expression relating the temperature disturbance inside the body to the environmetal temperature fluctuations, $\widetilde{T}(\mathbf{x}, \omega) = \sum_{lm} \widetilde{K}_l(\mathbf{x}, \omega) \widetilde{b}_{lm}(\omega)$ we end with a concise description of the sphere's thermal behaviour,

$$\widetilde{K}_l(r, \omega) = \frac{j_l(q\,r)}{j_l(q\,a)} \tag{3.26}$$

which expresses the information first obtained in the time domain solution in (3.14). With this direct method however we are able to evaluate the transfer function at any point inside the body whereas the cumbersome series we faced in the time domain could only be solved in the limit $x \to 0$.

We will naturally recover equation (3.19) when evaluating the transfer functions at the centre for the case of isotropic thermal perturbations as shown next.

Isotropic boundary conditions at the surface

The conditions simplifying the problem which help us find an analytical solution for $\widetilde{K}(0, \omega)$ will be recast here in order to prove the identity of both solutions if the same situations are considered. Indeed, at the centre of the sphere equation (3.26) translates into

$$\tilde{K}_l(0,\omega) = \frac{1}{j_l(q\,a)} \tag{3.27}$$

Isotropic disturbances need now to be considered. As a result of this approximation, we only need to consider the monopole term of the series leading to

$$
\begin{aligned}
\tilde{K}_0(0,\omega) &= \frac{1}{j_0(q\,a)} \\
&= \frac{q\,a}{sin(q\,a)}
\end{aligned}
\tag{3.28}
$$

if we now expand the solution taking into account the complex number nature of the parameter q defined in equation (3.22) we finally obtain the original expression for the transfer function at the centre of the sphere subjected to an isotropic thermal bath, equation (3.19), which we recover here

$$\tilde{K}(0,\omega) = \frac{(1+i)\beta}{\sinh(\beta)\cos(\beta) + i\,\cosh(\beta)\sin(\beta)}\,, \quad \beta \equiv \left|\frac{\omega\tau}{2}\right|^{1/2} \tag{3.29}$$

A noteworthy corollary of this method is obtained if we compare both methodologies. In Appendix C.2 , $\widetilde{K}(0,\omega)$ was derived as the limit of a Fourier series given that a closed expression could not be easily obtained by analytically summing the expression. Once we now the solution derived directly in the frequency domain we can recover the generic form of the sum and find a closed solution for the sum by identifying both results, this will lead to the following solution —the full series is treated in (C.32),

$$2\sum_{n=1}^{\infty}(-1)^n \frac{sin(n\pi r/a)}{n\pi r/a}\frac{1}{1+i\frac{\omega\tau}{n^2\pi^2}} = \frac{j_0(q\,r)}{j_0(q\,a)}, \qquad q = \frac{(1+i)}{2}\sqrt{\omega\frac{\rho C}{K}} \tag{3.30}$$

This identification can be of particular interest when considering complex geometries or even in the case when non-isotropic disturbances are taken into account.

3.2.3   Multilayer insulation

In many cases a simple geometry as the one previously studied is not of interest because it does not reflect a real situation. In particular, following the electrical analogy to thermal problems, thermal insulators are often designed as a RC low pass circuit. In order to stress the insulation effect, two different bodies are used to build the insulator: a low conductivity material (R-contribution) to isolate, and a massive body contributing to the thermal capacitance (C-contribution). Or, in other terms, if a massive body is inserted inside a thermal low-conductivity shell, the external heat arriving at the core will clearly imply lower temperature increases if these are described as $\Delta T = Q \cdot (m\,C)^{-1}$, thus inversely proportional to the thermal capacitance, $m\,C$.

Two comments are in order at this point. First, both materials in the previous description

have their own R and C contribution but their global behaviour as a unique body can be easily understood if we neglect the resistance of the massive body and the mass of the low conductivity material as made above. In second place, it must be also noticed that the RC model is a simplified model to provide guide but it does not describe the filter tails, as seen in §3.2.1.

In a more practical sense, an inner massive core is even desirable for manufacturing or for handling reasons. If we consider the insulator being constructed in this way as a thermal bench to perform calibration and characterisation experiments we shall stress two properties of the inner massive core that will be interesting for our purpose: 1) homogenise the temperature inside the insulator and 2) prevent from self-heating effects which could be of relevance if the sensor used in the test were attached to a low conductivity material.

A multilayer body can pose a difficult mathematical problem if one seeks to obtain a time domain solution for the temperature field inside the insulator body, even of considerable difficulty if only restricting ourselves to the isotropic solution at the centre. We will thus herein describe which are the main advantages of the frequency approach which can make easier this task.

Let's consider a multilayer thermal insulator; we can imagine an n-shell spherical configuration of different materials having $n-1$ interfaces at the fixed radii $a_1, a_2, \ldots a_{n-1}$. The general solution is a function defined at each of the n regions

$$T(\mathbf{x}, \omega) = \sum_k T^{(k)}(\mathbf{x}, \omega)[\theta(r - a_{k-1}) - \theta(r - a_k)] \tag{3.31}$$

with $\theta(x)$ the step function. Each $T^{(k)}(\mathbf{x}, \omega)$ function acquires the form of the general spherical solution at each of these spherical shells

$$\widetilde{T}^{(k)}(\mathbf{x}, \omega) = \sum_{lm} \left[A_{lm}^{(k)}(\omega)\, j_l(q_k\, r) + B_{lm}^{(k)}(\omega) y_l(q_k\, r) \right] Y_{lm}(\theta, \phi) \tag{3.32}$$

We will need to solve Fourier's equation in each shell. This set of equations can be abbreviated as

$$\left(\nabla^2 + q_k^2 \right) \widetilde{T}^{(k)}(\mathbf{x}, \omega) = 0 \;, \quad a_{k-1} \le r \le a_k \tag{3.33}$$

We must therefore determine the coefficients of the expansion based on the boundary coefficients which determine the problem. For the case under study both equations fixing the outer temperature field (3.9a) and imposing convergence of the solution at the centre (3.9b) first used in the homogeneous problem are conserved, and we will add the corresponding interface matching conditions. Continuity of the temperature field and temperature gradient are thus imposed at each interface k,

$$\widetilde{T}^{(k-1)}(r = a_k, \omega) = \widetilde{T}^{(k)}(r = a_k, \omega) \tag{3.34}$$

$$K_{k-1} \frac{\partial \widetilde{T}^{(k-1)}}{\partial r}(r = a_k, \omega) = K_k \frac{\partial \widetilde{T}^{(k)}}{\partial r}(r = a_k, \omega) \tag{3.35}$$

whence a linear system of equations is defined. The number of coefficients to be determined is $2n$ for each (l, m) pair, where n is the number of layers. We can thus proceed to evaluate the $2n \times 2n$ system of equations,

$$\mathbf{M} \cdot \mathbf{C} = \mathbf{E} \tag{3.36}$$

where $\mathbf{C}$ is the vector of coefficients to be determined, $\mathbf{C} = \{A_{lm}^{(1)}, B_{lm}^{(1)}, \ldots, A_{lm}^{(n)}, B_{lm}^{(n)}\}$, $\mathbf{E}$ gathers the boundary condition which in our case is zero except for the last layer, where the external temperature fluctuation is imposed $\mathbf{E} = \{0, 0, \ldots, B(\omega)\}$ and $\mathbf{M}$ is the $2n \times 2n$ matrix

$$\begin{pmatrix} j_l(q_1\, r) & y_l(q_1\, r) & 0 & 0 & \cdots & 0 \\ K_1\, \partial_r j_l(q_1\, r) & K_1\, \partial_r y_l(q_1\, r) & -K_2\, \partial_r j_l(q_2\, r) & -K_2\, \partial_r y_l(q_2\, r) & \cdots & 0 \\ 0 & 0 & j_l(q_2\, r) & y_l(q_2\, r) & \cdots & 0 \\ 0 & 0 & K_2\, \partial_r j_l(q_2\, r) & K_2\, \partial_r y_l(q_2\, r) & \cdots & 0 \\ 0 & 0 & \vdots & \vdots & \ddots & 0 \\ 0 & 0 & 0 & \cdots & j_l(q_n\, r) & y_l(q_n\, r) \end{pmatrix} \tag{3.37}$$

where the first and the last equations represent conditions (3.9a) and (3.9b) referring to the conditions imposing convergence at the center of the body and fixing the external temperature fluctuations respectively. We have thus reduced a complicated PDE problem to the resolution of an algebraic system of equations affordable by the standard Cramer's rule. The solution is described by the coefficients which can be generally written as

$$A_{lm}^{(k)} = \frac{\eta_l^{(k)}}{\Delta_l} \quad k = 1, \ldots, n \tag{3.38a}$$

$$B_{lm}^{(k)} = \frac{\nu_l^{(k)}}{\Delta_l} \quad k = 1, \ldots, n \tag{3.38b}$$

being $\eta_l^{(k)}$ and $\nu_l^{(k)}$ the characteristic determinants corresponding to each coefficient and Δ_l the determinant of the system of equations.

Although being a simple methodology, the resolution of the transfer function directly in frequency domain leads to a complex analytical solution which can be hardly interpreted without simplifications. In these conditions this method shows its great convenience if we notice that the time domain solution will imply the Fourier antitransform of the expression just derived. Indeed, to finally recover a time domain solution we are forced to evaluate the integral

$$
\begin{aligned}
T(\mathbf{x},t) &= \frac{1}{2\pi} \int_{-\infty}^{\infty} d\omega \, e^{+i\,\omega\,t} \, \widetilde{T}(\mathbf{x},\omega) \\
&= \sum_{k} \frac{1}{2\pi} \int_{-\infty}^{\infty} d\omega \, e^{+i\,\omega\,t} \sum_{lm} \frac{\eta_l^{(k)}}{\Delta_l} \, j_l(q_k\,r) + \frac{\nu_l^{(k)}}{\Delta_l} \, y_l(q_k\,r) \quad (3.39)
\end{aligned}
$$

The residue theorem [24] is usually invoked in order to evaluate this expression. In doing so we will find that our solution is described as a sum over the poles of the function, i.e, those ones defined by the solutions in equation (3.38), but we are now in situation to write down this series since we know explicitly its analytical form. The time domain solution will be thus defined as a sum over the values fulfilling the equation $\Delta_l = 0$ which from equation (3.37) can clearly be a difficult series from where to extract zeros in a precise manner. The frequency domain approach is therefore an elegant way to work out this complicated problem.

3.2.4 Application to Cartesian coordinates

The method previously discussed has shown to be a useful solution and we have been able to find an expression for the transfer function of a homogeneous sphere. Our next step will be to consider other simple geometries which can help us to analyse simple thermal problems in terms of its corresponding transfer functions. In particular we will centre our attention into Cartesian coordinates to see how this solution differs from the spherical case.

Naturally, the main argument developed in §3.2 is not changed here, the only variation we need to introduce refers to equation (3.23a) where we chose a general solution according to the geometry of the problem. Before that, we will briefly summarise the starting point which will be the same regardless of the system of coordinates, we refer obviously to Fourier's equation,

$$
\rho C \, \partial_t T(\mathbf{x},t) = \nabla \cdot [K \, \nabla T(\mathbf{x},t)] \quad (3.40)
$$

which we aim to solve considering, for the sake of simplicity, considering a cubic geometry surrounded by an isotropic bath, expressed in the cartesian coordinate system as

$$
\begin{aligned}
\text{Boundary conditions}: T(x=0,t) = T(x=L,t) &= T_0(t) \quad &(3.41\text{a}) \\
T(y=0,t) = T(y=L,t) &= T_0(t) \quad &(3.41\text{b}) \\
T(z=0,t) = T(z=L,t) &= T_0(t) \quad &(3.41\text{c}) \\
\text{Initial conditions}: \quad T(\mathbf{x},t_0=0) &= 0 \quad &(3.41\text{d})
\end{aligned}
$$

taking advantage of the symmetry of the problem, we can split the solution in three equivalent problems from which we will can build the final solution by virtue of the superposition principle. Each of this will be composed by a cube with two opposite faces at temperature $T_0(t)$ and the rest

maintained at zero.

In order to solve each of this split problems we will switch to the frequency domain to take advantage of the algebraic simplicity gained with the Fourier transform. Assuming an homogeneous and isotropic thermal conductivity through the medium, we can write down Fourier's equation as

$$(\nabla^2 + q^2)\widetilde{T}(\mathbf{x}, \omega) = 0, \qquad q^2 = -i\,\omega\frac{\rho C}{K} \tag{3.42}$$

this must be solved with the boundary conditions correspondent to one of the three subproblems into which we have reduced our initial problem. For instance, we consider the cube with y and z faces at zero and x faces at $T_0(t)$,

$$
\begin{aligned}
\text{Boundary conditions}: \widetilde{T}(x = 0, \omega) = \widetilde{T}(x = L, \omega) &= \widetilde{T}_0(\omega) & \text{(3.43a)} \\
\widetilde{T}(y = 0, \omega) = \widetilde{T}(y = L, \omega) &= 0 & \text{(3.43b)} \\
\widetilde{T}(z = 0, \omega) = \widetilde{T}(z = L, \omega) &= 0 & \text{(3.43c)} \\
\text{Initial conditions}: \qquad\qquad T(\mathbf{x}, t_0 = 0) &= 0 & \text{(3.43d)}
\end{aligned}
$$

Equation (3.42) with the previous conditions (3.43) has the solution (cf. § 15.11 in [24])

$$\widetilde{T}_x(\mathbf{x}, \omega) = \frac{16\,T_0(\omega)}{\pi^2}\sum_{n=0}^{\infty}\sum_{m=0}^{\infty}\frac{\sinh(l(L-x)) + \sinh(lx)}{\sinh(lL)}\frac{\sin((2m+1)\pi y/L)}{(2m+1)}\frac{\sin((2n+1)\pi z/L)}{(2n+1)}$$

$$\tag{3.44a}$$

with

$$l^2 = \frac{(2\,n+1)^2\pi^2}{L^2} + \frac{(2\,m+1)^2\pi^2}{L^2} + q^2 \tag{3.44b}$$

If we now add the three equivalent solutions that solve the same problem for x, y and z axes (which are easily obtained applying condition (3.43a) to the y and z axes respectively) we will end with the full solution

$$\widetilde{T}(\mathbf{x}, \omega) = \widetilde{T}_x(\mathbf{x}, \omega) + \widetilde{T}_y(\mathbf{x}, \omega) + \widetilde{T}_z(\mathbf{x}, \omega) \tag{3.45}$$

and from this the transfer function, defined as $\widetilde{T}(\mathbf{x}, \omega) = H(\mathbf{x}, \omega)\widetilde{T}_0(\mathbf{x}, \omega)$, of thermal perturbations inside a cubic insulator is readily obtained

$$
\begin{aligned}
H(\mathbf{x}, \omega) \;=\; & \frac{16}{\pi^2} \sum_{n=0}^{\infty} \sum_{m=0}^{\infty} \frac{\sinh(l(L-x)) + \sinh(lx)}{\sinh(lL)} \frac{\sin((2m+1)\pi y/L)}{(2m+1)} \frac{\sin((2n+1)\pi z/L)}{(2n+1)} \\
& + \frac{\sinh(l(L-y)) + \sinh(ly)}{\sinh(lL)} \frac{\sin((2m+1)\pi z/L)}{(2m+1)} \frac{\sin((2n+1)\pi x/L)}{(2n+1)} \\
& + \frac{\sinh(l(L-z)) + \sinh(lz)}{\sinh(lL)} \frac{\sin((2m+1)\pi y/L)}{(2m+1)} \frac{\sin((2n+1)\pi x/L)}{(2n+1)} \quad\text{(3.46a)}
\end{aligned}
$$

with

$$
l^2 = \frac{(2\,n+1)^2 \pi^2}{L^2} + \frac{(2\,m+1)^2 \pi^2}{L^2} + q^2, \qquad q^2 = -i\,\omega \frac{\rho C}{K} \quad\text{(3.46b)}
$$

We have here reproduced the maximal symmetric problem, extensions to parallelepiped can be easily obtained from the current solution.

3.3   Thermal frequency sweep

We have previously analytically derived a thermal transfer function describing the relation between the inner temperature fluctuations with respect to the fluctuations of the external layer of an insulator body. The problem has been solved for simple geometries where we can take advantage of the body symmetries to solve the equations. This can be a major drawback in most real cases if complex geometries take part in the design.

In this section we provide a more flexible analysis tool to solve geometrical complex problems. The method is based on a numerically evaluation of the thermal response of a given body for a fixed frequency value [69]. By repeating this procedure for successive frequencies, a complete description of the system through the MBW is afforded.

3.3.1   Theoretical motivation

Our previous analytical study showed how a thermal insulator can be treated as thermal low-pass filter when analysing the problem in the frequency domain. We will now be interested to switch to time domain in order to compare to numerical simulations. However, our final purpose remains to be the frequency domain description and thus to evaluate the transfer function. This implies that the best suited input signal to test the system in our numerical simulations is a sinusoidal signal at a fixed frequency ω_0 because in such a case we will be exciting a unique frequency mode in the Fourier picture.

In order to express this concept, we can generally describe a system by the relation between the output response with respect to a given input. In the digital processing terminology we could use the notation [78]

$$
y[n] = h[z]\, x[n] \quad\text{(3.47)}
$$

where $x[n]$ and $y[n]$ are the input and output digital values respectively and $h[z]$ the transfer function collecting the dynamic information of the system, the later is described as an operator in the z variable where the convention $z^{-1}x[n] = x[n-1]$ is assumed. We thus decide to test the system with a sinusoidal input starting at some point $n = 0$, the input signal becomes

$$x[n] = Ae^{i\omega_0 t n} \quad n \geq 0 \tag{3.48}$$

Systems subjected to finite duration input signals show two different behaviours: a transient response, $y_{trs}[n]$ that decays at long time scales and a steady-state signal, $y_{ss}[n]$ that can be understood as the input sinusoidal signal with a reduced amplitude given by the transfer function value at the test frequency $H(\omega_0)$,

$$
\begin{aligned}
y[n] &= y_{ss}[n] + y_{trs}[n] \\
&= H(\omega_0)\,Ae^{i\omega_0 t_s n} + y_{trs}[n]
\end{aligned}
\tag{3.49}
$$

A remarkable property of the output obtained in this operation is that the steady-state response do not change the frequency with respect to the input applied. As an example, the first order difference equation

$$y[n] = ay[n-1] + x[n] \tag{3.50}$$

shows a response of the type ($\S 4.4.2$ in [78])

$$y[n] = \underbrace{\frac{A}{1 - a\,e^{-i\omega_0 t_s}}e^{i\omega_0 t_s n}}_{y_{ss}[n]} + \underbrace{a^{n+1}y(-1) - \frac{A\,a^{n+1}e^{-i\omega_0 t_s(n+1)}}{1 - a\,e^{-i\omega_0 t_s}}e^{i\omega_0 t_s n}}_{y_{tr}[n]} \tag{3.51}$$

when the input signal is as in (3.48). Here, we have split the steady and the transient response as in equation (3.49) to show both terms contributing to the response. The transfer function can be directly obtained from this expression as

$$H(\omega_0) = \frac{1}{1 - a\,e^{-i\omega_0 t_s}} \tag{3.52}$$

Now, from these results we notice that if we are interested in determining the transfer function of this system from a thermal simulation of its response, we need to test the system with a sinusoidal input at long time scales (long enough to overcome the transient phase). In this region $t \gg \tau$, the transfer function at the frequency of the input signal $H(\omega_0)$ can be obtained as the amplitude of the $y[n]$ response signal multiplied by the amplitude of the input signal — see first term in (3.51).

A systematic way to deal with this problem is to fit the response to a function able to extract this parameters from the thermal evolution obtained from the thermal simulation. The trial function used in our case is defined as follows
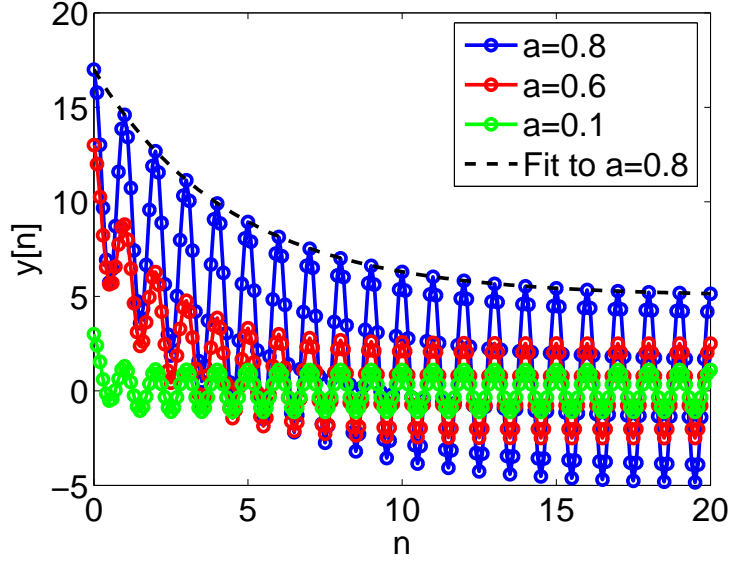
Figure 3.3: Graphical representation of the response of a first-order difference equation to a sinusoidal input —equation (3.51)— considering different values for the difference equation parameter. The fit to get the steady amplitude of the response is also shown, see text for details.

$$y[n] = p_1 + p_2 e^{-n\, t_s/p_3} \tag{3.53}$$

and in order to obtain the amplitude we need to apply it to the peak values of the response obtained as shown in Figure 3.3. This way, the p_1 parameter retrieved from the fit can be directly associated with the transfer function since it contains the value of the amplitude at $t \to \infty$, i.e.

$$p_1 = y_{ss}[n \to \infty]|_{max} = A\, H(\omega_0) \tag{3.54}$$

The interpretation of the p_2 is not straightforward and will be generally related to a complicated expression depending on the equation behind the process. Finally, the p_3 can not be related explicitly to a parameter in the analytic expression but it gives us the information of the timescale of the process and thus can be considered and *effective* time constant.

3.3.2 Methodology

If we now assume the previous properties derived from the output as valid for all type of low-pass thermal systems excited by a sinusoidal thermal signal of fixed frequency we can therefore define a method to evaluate its transfer function from the obtained output. The methodology will be thus

i) Create a finite elements model of our system under study

ii) Apply a sinusoidal signal of fixed frequency ω_0 and amplitude $T = 1\,\text{K}$ to the selected node J

$$T_J[t] = 1 \cdot \sin(\omega_0\, t) \tag{3.55}$$

iii) Fit results on different node (K) peak values

$$T_{K,max}[t] = p_1 + p_2 e^{-t/p_3} \tag{3.56}$$

iv) Get transfer function of node K with respect temperature fluctuations at frequency ω_0 at the input node, J

$$G_{KJ}(\omega_0) = p_1 \tag{3.57}$$

This method will be applied in §4.1.2 to complement the analytical approach in the design of a thermal insulator, and is also currently being applied to the LCA thermal model with the purpose of obtaining thermal transfer function between different points of the model.

Chapter 4

Thermal test bench design

The DDS on board the LPF mission must provide information to help understand the performance of the LTP experiment in its scientific run case. Several diagnostics items conform the DDS but all them share a common objective, i.e., the noise apportioning. To this end, two independent measurements are required: First, a controlled disturbance that enhances the coupling of a given noise source with what we will consider the main scientific data stream, interferometer phase for instance. With a suitable data analysis, this experiment must provide a good functional dependence of the noise source with the main scientific data.

Once this noise relation is known, the diagnostics sensors set needs to monitor the environmental variables not only to prevent from possible non-valid data streams due to an excess of disturbances taking place, but also to determine which is the contribution to the total noise budget coming from different sensors.

In this chapter we will focus our attention on the monitoring phase of the procedure. The foreseen noise related physical phenomena has been reviewed in Chapter 2, and we will herein consider the thermal sensitivity requirement for the thermal Front-End Electronics (FEE) derived there as the goal to be reached by the temperature subsystem, assuming that the achievement of this condition will imply that the noise contribution due to thermal effects will be, accordingly to the mission budget, roughly a 10% of the total noise budget.

The full FEE prototype will be put to test in a second design phase in Chapter 5. The scope will be to demonstrate the fulfilment of the temperature requirements. However, a major problem appears since to evaluate noise contributions arising from temperature FEE, but not related with environmental perturbations, requires a thermal test bench able to isolate the temperature measurement devices to a noise level below our measurement goal. Being below our measurement noise level, our temperature floor noise can not be directly measured so we will need to base our design in a strong thermal analysis of the insulator both analytically and numerically and, afterwards, in a suitable testing of the insulator, reporting the fulfilment of the desired properties.

4.1 Thermal test bench design

Besides noise related to temperature, random fluctuations can also enter the measurement process due to sensors or electronics effects. The test to be performed must guarantee that any hardware related fluctuation in the temperature read out process will be below a Power Spectral Density (PSD) level which is the one we are interested to measure. This level has been previously defined to be the temperature PSD of $10^{-4} \mathrm{K}/\sqrt{\mathrm{Hz}}$ (cf. §2.2) in the MBW and this leads consequently to the requirement for the temperature FEE considering a prescription of an order of magnitude reduction of the noise floor in order to be able to clearly discriminate related fluctuations. We rewrite here the following requirement for the noise level fluctuations associated FEE,

$$S_{T,\mathrm{FEE}}^{1/2}(\omega) \leq 10^{-5}\,\mathrm{K}/\sqrt{\mathrm{Hz}} \quad 1\,\mathrm{mHz} \leq \omega/2\pi \leq 30\mathrm{mHz} \tag{4.1}$$

But if the FEE is to be put to test we now face the same problem of setting an acceptance criteria for the thermal cleanliness of the test environment. It seems logical to apply the same solution as before and require a minimum of an order of magnitude decrease of environmental temperature fluctuations in the test bench location. Hence, we will need a thermal insulator able to screen temperature fluctuations to a level given by

$$S_{T,\mathrm{Bench}}^{1/2}(\omega) \leq 10^{-6}\,\mathrm{K}/\sqrt{\mathrm{Hz}} \quad 1\,\mathrm{mHz} \leq \omega/2\pi \leq 30\mathrm{mHz} \tag{4.2}$$

The test must provide a sufficiently stable bench, able to prevent the temperature gauges in the temperature subsystem from any possible environmental thermal fluctuations. Achieving this quiet environment will be the unique manner to guarantee that the thermal sensing subsystem is not introducing random fluctuations by its own, above the proper environmental temperature fluctuations.

The concept idea of the insulator is displayed in figure 4.1: an interior metal core of good thermal conductivity is surrounded by a thick layer of a poorly conductive material. The inner block ensures thermal stability of the sensors attached to it, while the surrounding substrate efficiently shields them from external temperature. The concept behind the design is clearly a *thermal RC* low pass filter if we consider the external layer acting as the R (low conductivity) and the inner core representing the C contribution (high density). In the following, the thermal transfer function formalism will be applied to this specific problem.

4.1.1 Insulator transfer function

Once the problem has been posed we now proceed to the design phase, our interest will be focused on the definition of the thermal insulator taking advantage of the formalism to arrive to a specific solution which must guarantee (4.2). The free parameters which must therefore be fixed by the analysis are the dimensions and the materials to be used.

Based on the methodology described in section 3.2, an analytical expression for our proposed insulator can be fully obtained in the frequency domain. For the sake of conciseness, the compu-
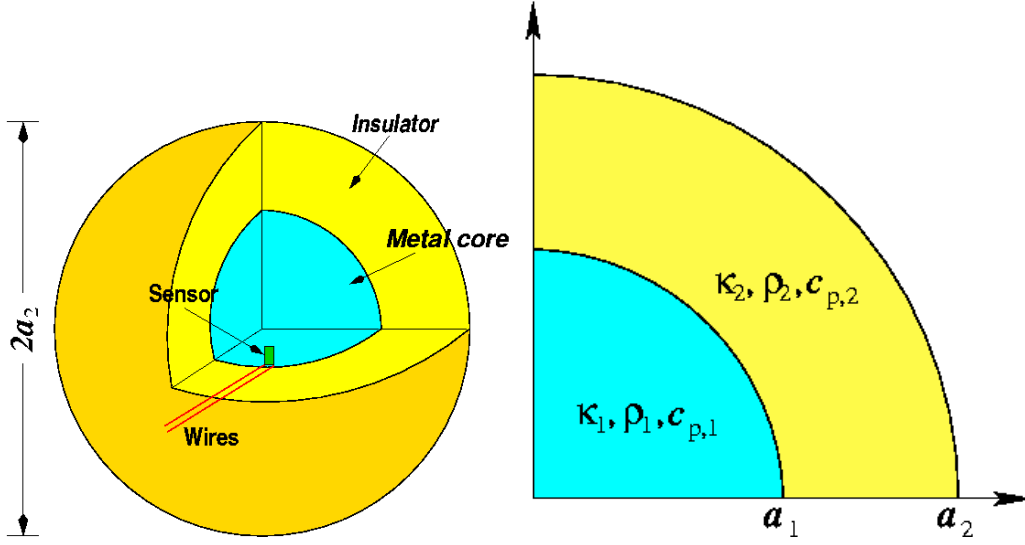
Figure 4.1: Thermal insulator design concept. *Left:* diagram, including sensor placement principle. *Right:* cut view, with notation convention.

tation of the thermal fluctuations inside a double layer spherical body is reported in Appendix D where the reader can find the algebraic derivation in full detail. We will stick here to the isotropic case, hence the transfer function takes only into account the monopole contribution, $l = 0$ and $m = 0$, which leads to equation (D.23) rewritten here

$$H(r, \omega) = \begin{cases} \xi_0(\omega)\, j_0(q_1 r) \,, & 0 \leq r \leq a_1 \\ \eta_0(\omega)\, j_0(q_2 r) + \zeta_0(\omega)\, y_0(q_2 r) \,, & a_1 \leq r \leq a_2 \end{cases} \tag{4.3}$$

where

$$q_j = \left(\omega\, \frac{\rho_j\, C_j}{2\, K_j} \right)^{1/2} (1 - i), \qquad [q] = \mathrm{m}^{-1}, \qquad i = \sqrt{-1} \tag{4.4}$$

This is a low-pass filter transfer function —even though the cumbersome frequency dependencies involved in the expressions above do not make it immediately obvious. The $3\,\mathrm{dB}$ cut-off angular frequency for this filter defines a time constant τ by $1/\tau \equiv \omega_{\mathrm{cut-off}}$, which correspondingly is a complicated function of the insulator's physical and geometrical properties.

In order to gain some insight into the equations, we can work out the solution at the centre of the body. This way, we get rid off the radial dependence and obtain an expression as a function of dimensions and materials properties, as was our first intention.

$$H_c(\omega) = \frac{K_2\, a_1\, a_2\, q_1\, q_2}{K_1\, \sinh(q_2\, (a_2 - a_1))\, F_1(a_1) + K_2\, \sinh(q_1\, a_1)\, F_2(a_2)} \tag{4.5a}$$

where q_j has previously been defined in (4.4) and the functions $F_1(r)$ and $F_2(r)$ are given by,
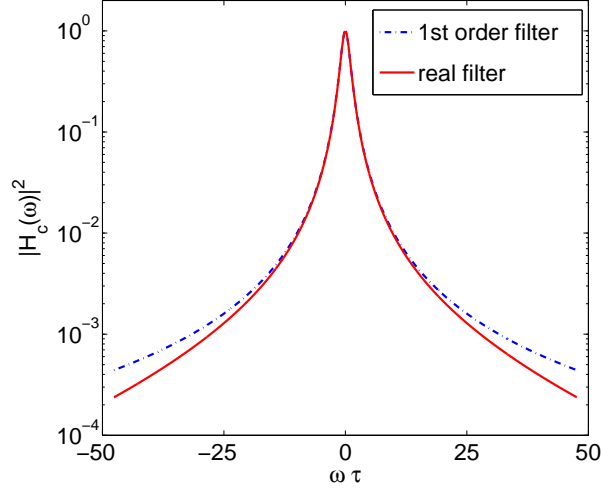
Figure 4.2: Frequency response at the centre $(r = 0)$ of a spherical thermal insulator —as given in equation (4.5)—, along with the frequency response of a low-pass filter of order one and same frequency cut-off, $\omega_{\text{cut-off}} = 1/\tau$

$$F_1(r) = r\,q_1\,\cosh(q_1\,r) - \sinh(q_1\,r) \tag{4.5b}$$

$$F_2(r) = a_1\,q_2\,\cosh(q_2\,(r - a_1)) + \sinh(q_2\,(r - a_1)) \tag{4.5c}$$

Despite the cumbersome aspect of expression (4.5) to describe a thermal problem, the same equation can be found in classical thermal literature – see [24], as a mid step solution when applying the Laplace Transform to solve thermal problems. In our case, however, equation (4.5) contains all the relevant information and therefore the costly antitransformation is not necessary.

Figure 4.2 shows graphically the situation: the solid curve plots the square modulus of $H(r = 0, \omega)$, where the cut-off $1/\tau$ is shown as the 3 dB abscissa. For comparison, the figure also shows (broken curve) a low-pass filter of the first order with the same frequency cut-off, i.e., $|H_{\text{1st order}}(\omega)|^2 = (1 + \omega^2\tau^2)^{-1}$.

The high frequency roll-off of the real filter (in red) is seen to drop below the first order counterpart (in blue): the latter clearly has a slow slope at high frequencies, $|H_{\text{1st order}}(\omega)| \sim (\omega\tau)^{-1}$, while the former can be shown to follow a much steeper, exponential curve. Given that

$$j_0(z) = \frac{\sin z}{z} \;, \quad y_0(z) = -\frac{\cos z}{z} \tag{4.6}$$

for any *complex* argument z, and that q has equal real and imaginary parts, according to (4.4) it is easy to verify that, at high frequencies, $H(r, \omega)$ has exponential roll-off tails:

	Density ρ [kg m^{-3}]	Specific heat C [J kg^{-1} K^{-1}]	Thermal conductivity K [W m^{-1} K^{-1}]	Cut-off frequency ω_c [Hz]
Aluminium	2700	900	250	10^{-3}
Copper	8920	385	401	$1.2{\times}10^{-3}$
Dry Air	1.16	1012	0.02	$1.6{\times}10^{-4}$
Polyurethane	35	1000	0.04	$1.1{\times}10^{-5}$
Nylon	1500	1000	0.25	$1.6{\times}10^{-6}$
Teflon	2000	1000	0.25	$1.2{\times}10^{-6}$
Concrete	2300	837	1.8	$9.2{\times}10^{-6}$
Wood	420	2720	0.15	$1.3{\times}10^{-6}$
Glass	2800	800	0.81	$3.6{\times}10^{-6}$
Water	1000	4186	0.58	$1.3{\times}10^{-6}$

Table 4.1: Thermal properties for some common materials with its correspondent frequency as defined in (3.15) if they were used in a 1 m radius spherical insulator. Materials are split into conductors, insulators and common building materials for comparison.

$$|H(0,\omega)| \sim \omega\tau\, e^{-\sqrt{\omega\tau}} \quad \text{when} \quad \omega\tau \gg 1 \tag{4.7}$$

As already mentioned in this section, to test the temperature sensors and electronics we need a very strong noise suppression factor in the LTP frequency band. Inspection of figure 4.2 and equation (4.5) readily shows that high damping factors require such frequency band to lie in the filter's tails. The thermal insulator should therefore be designed in such a way that its time constant are high enough compared to $(2\pi\tau)^{-1}$. The exponential roll-off in the transfer function shown by (4.7) makes the filter actually feasible with moderate dimensions.

4.1.2   Numerical analysis

In this section we consider the application of the Thermal sweep formalism (cf. §3.3) to obtain useful numbers for the implementation of a real insulator device which complies with the needs of the experiment.

There are a wide range of selectable materials for our purpose, Table 4.1 shows the thermal properties for some of them. As previously stated, the insulator requires a core which shall provide the massive part and an outer low conductivity material to screen environmental temperature fluctuations. The final selection: an Aluminium core surrounded by a layer of polyurethane was made based mainly in cost and handling terms[1].

Aluminium is a good heat conductor and is easy to work with in the laboratory; polyurethane

---

[1]It is worth mentioning the peculiar properties that water offers under these considerations. Provided its high thermal capacitance, an insulator with an inner core of water would allow a low cut-off frequency and therefore, a high suppression factor at high frequencies. Nonetheless, handling would introduce many more problems than working with a metal and the liquid medium could induce errors and uncontrolled disturbances to the final temperature measurement, which is the final goal.
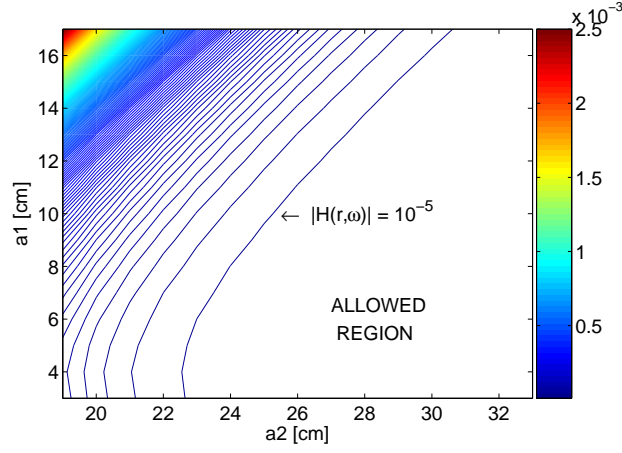
Figure 4.3: Map of the amplitude suppression of an external thermal fluctuation inside a double layer spherical insulator built as an Aluminium core surrounded by a polyurethane layer. The suppression is expressed in terms of the dimensions of both layers. Lines show steps of 10^{-5} in amplitude suppression.

is a good insulator and is also convenient to handle, as it can be foamed to any desired shape from canned liquid. Other alternatives are certainly possible, but this appears sufficiently good and we shall therefore stick to this specific choice.

The choice of dimensions for the insulating body must of course ensure that the minimum requirement, equation (4.2), is met. For this to be reached, a primary consideration is the size of the ambient temperature fluctuations in the site where the experiment is made. Dedicated measurements in our laboratory showed that [54]

$$S_{T,\ \mathrm{room}}^{1/2}(\omega) \simeq 10^{-1}\,\mathrm{K}/\sqrt{\mathrm{Hz}}\ , \quad 1\,\mathrm{mHz} \le \omega/2\pi \le 30\,\mathrm{mHz} \tag{4.8}$$

We therefore need to implement a device such that $|H(r < a_1, \omega)| \le 10^{-5}$ throughout the MBW. Dimensions for both the Aluminium core and the polyurethane layer fulfilling this purpose can be obtained by replacing the materials properties in expression (4.5).

The figure of merit is graphically expressed in Figure 4.3 as a function of both dimensions a_1 and a_2 at the lower end of the LTP frequency band (i.e., 1 mHz). Given the requirement (4.2) and the environmental condition (4.8), we have labelled the region $H_c(10^{-3}\,\mathrm{Hz}) \le 10^{-5}$ as the *allowed region*, meaning that any two points (a_1,a_2) of this region represents a valid solution for our scope. Although sensors are implanted for test on the surface of the aluminium core, evaluating the transfer function at the centre is a useful choice because temperature gradients in the Aluminium core are highly suppressed. We can thus take $H_c(\omega)$ as good indicator of the thermal screening at the sensors location —this will be better shown in § 4.1.4 when plotting the insulator thermal transfer function. It is also a simplifying assumption to take the transfer function value at 1 mHz, but it turns out that at higher frequencies the thermal damping is stronger —see Figure 4.2—

74

which clearly sets $H_c(1\,\mathrm{mHz})$ as the limiting value for our design guideline. Figure 4.3 also shows a remarkable property of the insulator concept. If one fixes a given polyurethane layer and increases the inner metal core the insulation capability decreases, the maximum efficiency of the design is found when following the maximum gradient line in Figure 4.3, thus increasing the polyurethane while decreasing the metal core, without exceeding a given minimum, seems the optimal criterion to reach a maximum suppression.

However, we still need to include another consideration referring possible contribution to thermal noise of the wires connecting FEE with the sensors inside the Aluminium core to finally set the insulators dimensions, this will be clarified in §4.1.4. However, before this discussion we will move to the comparison of the analytical results just derived to the results of thermal simulations applying the methodology described in §3.3, which may help not to demonstrate, which would require experimental input, but to test our design before the implementation phase.

4.1.3 Simulation comparison

The methodology followed in this section will be that described in §3.3 in order to sample the thermal transfer function at different points in frequency domain. We will herein apply this evaluation procedure to the insulator design just solved analytically. This cross-check will allow to confront both methods solving an easy problem. A coincidence in the result will give us confidence about the numerical methodology.

Geometrical design and mesh generation of the insulator has been developed using the FEM-LAB [26] software which is based in Finite Elements Method (FEM) for the numerical resolution and allows also for post processing after the thermal analysis is done. The resolution is performed in a model which consists in an inner core of aluminium surrounded by an insulator material as shown in Figure 4.4. The total amount of elements used for the simulation was 9272. Given the low gradients which we will be applying to the problem and the easy geometric design, a higher resolution mesh will not be necessary in our application.

The numerical approach requires to stick to a fixed dimensions choice regardless of our final decision about the final dimensions. Here we will consider a solution which fits in the allowed region in Figure 4.3, that is the case for

$$a_1 = 125\,\mathrm{mm}$$
$$a_2 = 300\,\mathrm{mm} \tag{4.9}$$

where we are considering Aluminium and polyurethane as the components of the insulator. As motivated in §3.3, after the meshing process is done, a sinusoidal fluctuation is applied to external boundary of the polyurethane. Using this fluctuation as a input for our system, we can evaluate the transfer function by plotting how this sinusoidal behaviour is suppressed into the insulator at different frequencies.
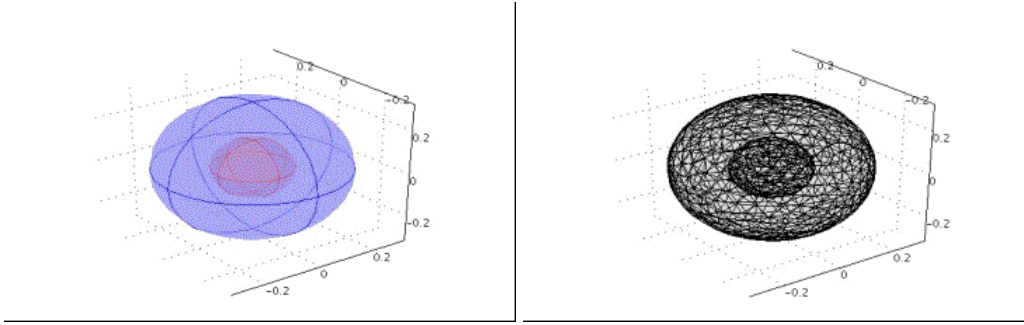
Figure 4.4: *Left:* Geometrical design of the insulator. *Right:* Generated mesh.

For a given external fluctuation, the insulator will suppress that external input by a factor that will depend on the frequency of the signal applied. Higher frequencies will be suppressed more efficiently than lower ones producing a low-pass filter effect for thermal fluctuations. If we compute this effect at different frequencies for a unitary input we will directly obtain the transfer function for this system, i.e., the relation between the system's output and the input applied.

Moreover, we can also obtain information not only from the temporal stationary zone but also from the initial steps of our simulation, which contains the transient regime. The insulator design studied here behaves as a low-pass filter which can be mainly characterised by the dimensions and the thermal properties of the materials being used. By fitting the initial transient behaviour to a typical exponential law we can obtain the system time constant. This parameter characterises insulator in the same way that an electrical low-pass circuit is characterised by the ratio $\tau = RC$, where R is resistance and C capacity.

In order to determine these parameters 6 FEM models with different frequency input have been evaluated. The data obtained for each one is fitted using a typical decay exponential law:

$$T(t) = A + B \cdot e^{-t/C} \tag{4.10}$$

where $T(t)$ is the temperature at the centre of the geometry and A,B and C the parameters to be fitted. Given the sinusoidal behaviour of our signal, only the maximal values for each period are fitted to the curve. With this choice, the A parameter on the fitting function acquires the significance of temperature fluctuations suppression on the asymptotic limit and hence it can be directly associated with the system transfer function for the input frequency applied (only when a unitary input is applied as it is in our case). This identification has other advantages. First, it allows us to evaluate the transfer function even though the time series obtained from the simulation may not arrive to the stationary regime. Thus, a lot of computation effort can be saved using this approach. And finally, by applying fit equation we can also evaluate the amplitude suppression high frequency models where the sinusoidal will be hardly observed and the main part corresponds to the transient behaviour.
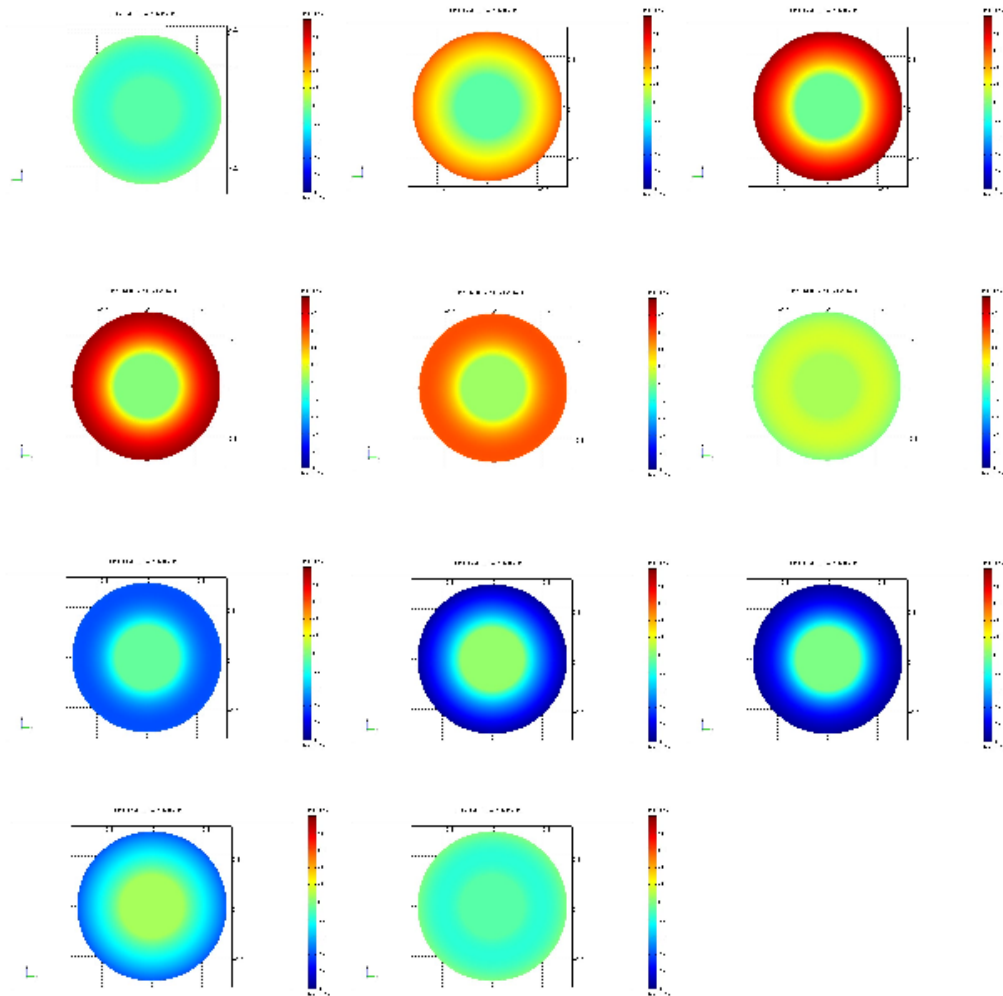
Figure 4.5: Complete cycle for a $1\,\mathrm{K}$ perturbation of applied in a frequency $10\,\mu\mathrm{Hz}$. The complete sequence lasts for 27 hours. Temperature range is [-1,1] in order to observe the external perturbation full period.

Fit constants	Value	Fit constants	Value
	MODEL $f = 1\,\mu\text{Hz}$		*MODEL* $f = 0.4\,\text{mHz}$
A	0.644 ± 10^{-3}	A	$8.83 \times 10^{-5} \pm 3 \times 10^{-7}$
B	0.504 ± 10^{-3}	B	$0.00216056 \pm 8 \times 10^{-7}$
C	188220 ± 1	C	188529 ± 100
	MODEL $f = 10\,\mu\text{Hz}$		*MODEL* $f = 1\,\text{mHz}$
A	$0.083 \pm 4 \times 10^{-3}$	A	$2.0520 \times 10^{-6} \pm 10^{-10}$
B	$0.084 \pm 1 \cdot 10^{-3}$	B	$0.000865835 \pm (2 \times 10^{-10})$
C	186888 ± 5000	C	188230 ± 0.1
	MODEL $f = 0.1\,\text{mHz}$		*MODEL* $f = 2\,\text{mHz}$
A	0.00375 ± 10^{-5}	A	$4 \times 10^{-8} \pm 10^{-8}$
B	$0.00865 \pm 3 \times 10^{-5}$	B	$4 \times 10^{-4} \pm 10^{-8}$
C	188246 ± 1	C	188321 ± 10

Table 4.2: Fit values of the thermal response for different models.

Figure 4.5 shows a sequence of a complete cycle of the external perturbation for a given frequency fluctuation of $10\,\mu\text{Hz}$, and a temperature variation amplitude of $\Delta T = 1\,\text{K}$. Aluminium core fluctuations are not observed in this sequence due to the long temperature scale range used, which in this case is $2\,\text{K}$, fixed by the external air shell fluctuation . However, if only the aluminium core is plotted, one can observe its fluctuations with an amplitude given by the A parameter.

The time constant will be determined by the C fitting parameter and the B parameter its a contribution to the initial temperature value which has no relevant information in our study. Results for this set of models are shown in Table 4.2 from where we can extract the envisaged parameters.

Before facing the interpretation of results, some care must be taken on the origin or parameter errors. There are two main error sources for our set of parameters. The first one arising in the simulation process and controlled by the convergence factor parameter of the simulation. Clearly, if we are to claim a given amplitude suppression coefficient we need at least the equivalent simulation precision if we do not want our results to be dominated by numerical error. Secondly, model parameters appear after an exponential fit process and hence parameters will be assigned an error value. The latter will be the one driving the parameter error given that we will consider that in each simulation the convergence factor is set below the required precision compute the suppression factor.

It appears from Table 4.2 that the C parameter converges for all the models and thus gives us some confidence that the parameter is well determined following this approach. The statistical mean of the different models for this parameter is

$$C = 188100 \pm 800\,\text{s} \tag{4.11}$$
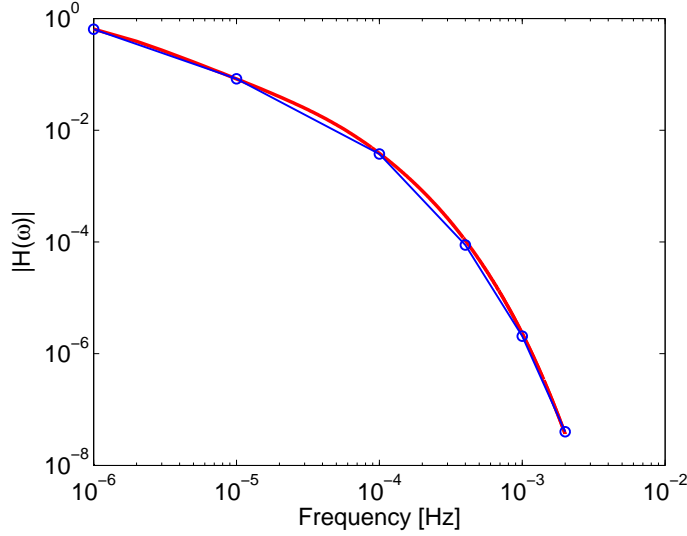
Figure 4.6: Transfer function derived by means of thermal simulation compared with the analytical solution. Errorbars for the former are of the size of the marker.

which gives as the typical response time of the insulator. A high value, as the one obtained, must be expected if we take into account that the response time is directly related in a standard low pass filter with the pole position of the transfer function. Since we are designing a filter with high suppression factor at low frequencies, a high settling time needs also to be expected.

The parameter B can not be directly related to a physical magnitude because it is generally related to a complicated function depending on the material and geometry under study. Contrarily, after our analysis the A parameter seems to be well defined and, as expected, shows a low pass filter behaviour when plotted as a function of the frequency. As a consistency check, we have plotted in Figure 4.6 the comparison of the filter derived from the thermal simulations with the analytical solution for an Aluminium-polyurethane two layer sphere, equation (4.5), with dimension given by (4.9).

The matching between both filters derived in analytical and numerical form reassures us about both methodologies applied on the thermal design. It lacks however an experimental verification which finally *probes* in first place the approach followed until this point for the thermal design and which will also serve as a verification test for the temperature diagnostic subsystem.

Before considering the experimental setup we need to include a possible source of temperature noise in our test bench, i.e., thermal leakage reaching the temperature sensors through the connecting wires. We come to this point next.

Figure 4.7: Wires thermal noise contribution scheme

4.1.4 Thermal leakage

A point to take into account in the design of a suitable test bench for thermal diagnostics is not only to assure a good enough thermal isolation at the MBW but also to prevent the design from thermal leaks. Based on the thermal insulator design previous discussed, the main path of temperature fluctuations from the environment 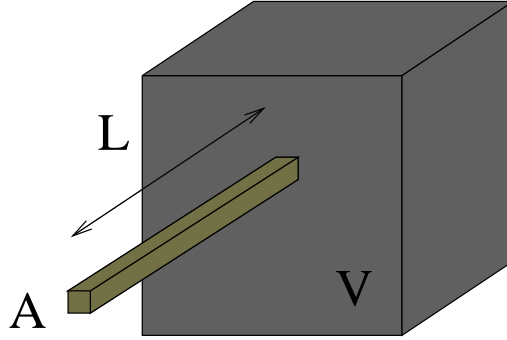to reach the inner part of the insulator are through the electric wires connecting the temperature sensors. Given its high conductivity, special care must be addressed to these wires which may degrade the high stability conditions which the insulator is designed to reach.

We can however find an upper value for the thermal contribution of sensors' wires deriving a transfer function which translates external temperature fluctuations to temperature fluctuations of the inner block [72]. The simple model herein described is based on the assumption that all the heat flux generated by the temperature difference at both edges of the wire is effectively used to increase the inner mass temperature, i.e., no lateral flux losses are considered. The high insulation material surrounding the inner core, where the wires will be nested, reinforces that this condition may be accomplished. Moreover, in the derivation we will suppress any spatial derivative in the temperature equations, the approximation will consequently lead to a lumped capacitance method like description, implying a linear filter (cf. § 3.1.1). As we know from the analytical solution for the insulator, this is not the case for thermal real problems and the approximation is only valid if a low thermal gradient is assumed. A more detailed model will require a full resolution of the thermal equations subjected to the wire geometry.

To derive this simplified model, let's consider a mass ρV of the insulator being continuously heated by a wire of length L and section A, as the one shown in Figure 4.7. The mass will therefore increase its temperature following the law

$$q = \rho\, C\, V\, \frac{dT}{dt} \tag{4.12}$$

where C stands for the specific heat of the body being heated and V refers to its volume. Since we are interested to characterise the insulator in the frequency domain, we will rewrite this
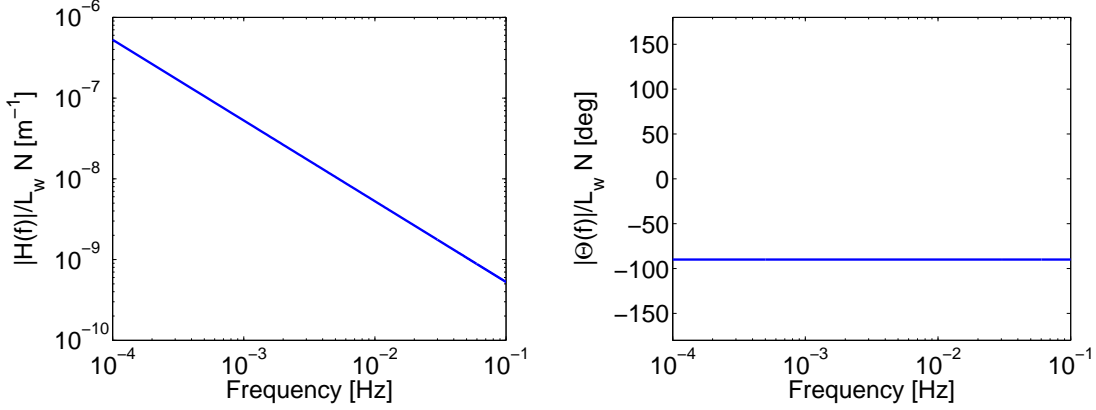
Figure 4.8: Wires temperature noise contribution Bode diagram per unit of wire's length and number of wires used.

expression as

$$S_q^{1/2} = \rho \, C \, V \, S_T^{1/2} \omega \qquad (4.13)$$

On the other hand, this heat flux is related to the difference of temperatures at both ends of the wire by Fourier's law,

$$q = K \frac{A}{L}(T_2 - T_1) \qquad (4.14)$$

where K is the conductivity of the material composing the wires. Following the same scheme as before, this expression becomes

$$S_q^{1/2} = K \frac{A}{L} \sqrt{S_{T_2} + S_{T_1}} \qquad (4.15)$$

We can now rearrange both equations, equations (4.13) and (4.15), to obtain an expression relating temperature fluctuations in the mass provoked by temperature fluctuations arising at the external end of the wire. Assuming that the temperature fluctuations at the external end of the wire are much greater than fluctuations at the inner end, $S_{T_2}^{1/2} \gg S_{T_1}^{1/2}$, this relation reads

$$S_{T_{in}}^{1/2} = \frac{\pi}{\omega} \frac{r_w^2 \, K_w}{L_w \, (\rho_C \, C_C \, V_C)} S_{T_{out}}^{1/2} \qquad (4.16)$$

where r_ω is the radius of the wire. In equation (4.16) subindex C refers to properties of the body and subindex w refers to properties of the wire. As clearly seen from this expression, temperature noise contribution from wiring can be avoided increasing the inner body mass or, alternatively, by lengthening the wires if the mass of the inner body is fixed.

Another factor rescaling the transfer function appears when more than one wire is considered. In this case, we will consider all noisy contributions from N different cables totally correlated. If

81

equation (4.16) is expressed as $S_{T_{in}}^{1/2} = H_w(f) S_{T_{out}}^{1/2}$, we end with

$$H_w(f) = \frac{N}{2\,i\,f} \frac{r_w^2\,K_w}{L_w\,(\rho_C\,C_C\,V_C)} \tag{4.17}$$

Although this might not be the case for all situations, the hypothesis must be considered a worst case description since temperature contributions are, under this assumption, linearly added.

Application to the insulator case

Equation (4.17) is plotted as a Bode diagram in Figure 4.8, where the f^{-1} slope is clearly seen and the phase plot shows a constant $-\pi/2$ delay through all the band. We can thus proceed with this analytical solution in the same way that lead us in § 4.1.2 to the definition of suitable dimensions for the insulator. Analogously to the definition of suitable dimensions for the insulator we can reproduce a two dimensional map of fluctuations amplitude suppression in terms of the wires' length and inner core volume. If we recover the external temperature condition, equation (4.2) and the environmental condition (4.8), we will clearly require again the suppression level given by $|H(a_1,\omega)| \le 10^{-5}$ and thus define the *allowed region* for a given wires' length once we have fixed the inner core volume
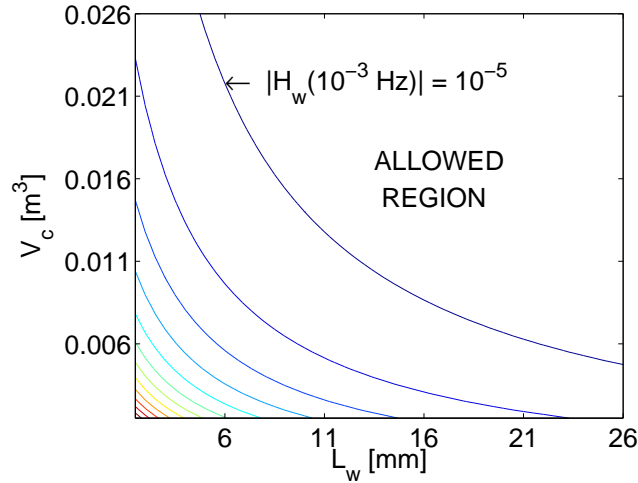
Figure 4.9: Map of the amplitude suppression for a given external thermal fluctuation inside a Aluminium volume due to temperature fluctuations heating the volume through 40 thin Copper wires. Map suppression is given in terms of wires' length and volume of the Aluminium body. Lines show steps of 10^{-5} in amplitude suppression.

Typical parameters are used for the numerical evaluation. We have considered the case of an Aluminium core linked to the external perturbation by means of a Copper wire. Materials properties for both can be found in Table 4.1. With this prescription the only parameters needed to evaluate expression (4.17) are the radius of the wire, taken to be $r_w = 0.1\,\text{mm}$, and the number

of wires arriving in the inner core which is $N = 40$, taking in care our particular setup, described in § 5.5.

Figure 4.3 shows this fluctuations amplitude suppression map when sampling the dimensions parameter space. As expected, increasing the wires' length or the inner core volume in our design implies a suppression of temperature fluctuations inside the Aluminium core. With all these elements at hand we can now define our thermal test bench.

4.2 Thermal bench description

The step towards the final test requires now to specify suitable dimensions for the bench. These must be extracted from analytical expressions once provided a requirement to be reached. This information must be therefore implemented carefully because of the stringent requirement needed to correctly test the temperature subsystem. This section is devoted to both design and implementation phase, leaving the results analysis for the next section.

4.2.1 Design

With the previous design conditions at hand a conservative choice was taken. To ensure a sufficient thermal suppression inside the volume an overdimensioned insulator was chosen. Also, due to manufacturing reasons, the spherical shape was replaced by the more common cubic geometry. This fact shall not change our design baseline since the main properties and screen capability of the insulator is set by its mass rather than by geometric properties. We thus will work with the spherical description previously derived using as dimension parameters the equivalent radius that a sphere will need to have in order to occupy the same volume as the cubic solution used.

The solution adopted was finally an inner core composed of three Aluminium slabs (260mm × 260mm × 80mm each) surrounded with polyurethane layer of 330 mm width —details can be found in § 4.2.2. The equivalent spherical shape will be formed with two layer with its respective radius given by

$$a_1 = 15.7 \, \text{cm} \quad a_2 = 57 \, \text{cm} \tag{4.18}$$

Figure 4.10 shows different insulators configurations in what respects thermal disturbance suppression. The thermal insulation achieved by the polyurethane is clearly seen as a decreasing line in the loglog diagram extending all through the outer polyurethane region. The inner core is distinguished by a plateau of nearly constant amplitude suppression driven by the high thermal conductivity of the Aluminium which tends to homogenise all this region to a fixed $H_{Al}(\omega)$ value. An outstanding detail appearing in the profile is the sharp decay at the interface Aluminium-polyurethane. The reason of this behaviour may be found in the thermal gradients that are established between both materials if the perturbation reaching this interface has power enough to raise a gradient between both. Since both upper panels in Figure 4.10 are evaluated for an external perturbation at 1 mHz, the cause of the sharp cut at the interface between both materials

a)

b)

c)
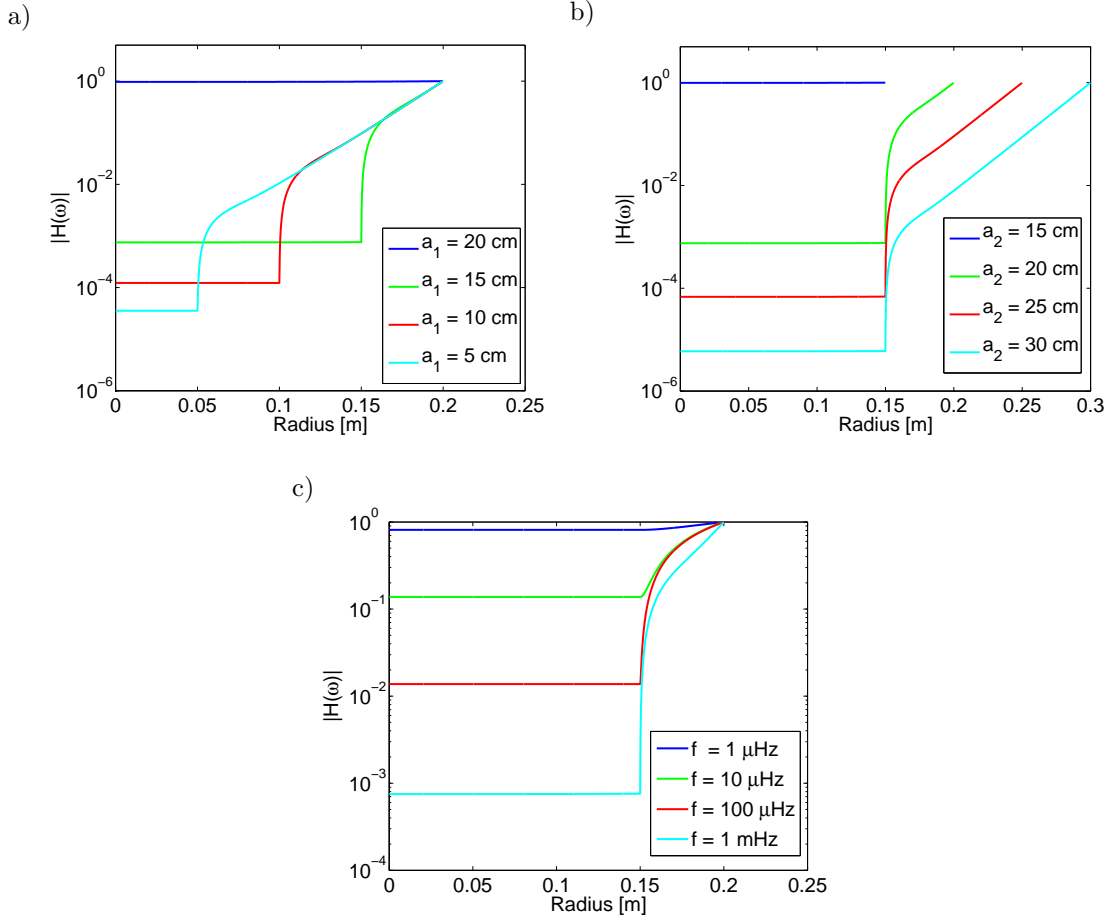
Figure 4.10: Thermal insulator transfer function profiles *a)* Fixing the outer polyurethane layer to 20 cm, the inner core is expanded in 5 cm steps. The profile of temperature suppression is shown at $f = 1\,\mathrm{mHz}$ *b)* Fixing the inner Aluminium core to 15 cm the outer layer is expanded in 5 cm steps, also at $1\,\mathrm{mHz}$. In both panels *a)* and *b)*, the blue line represents the solution for an homogeneous, i.e. one layer, insulator. *c)* Setting the dimensions to $(15\,\mathrm{cm}, 20\,\mathrm{cm})$, the thermal bench suppression temperature profile is evaluated for different environmental temperature frequencies.

is better understood considering Figure 4.10 *c)*, where the transfer function is evaluated for fixed dimension values at different frequencies.

As previously seen in Figure 4.3, the final level of suppression can both be achieved by means of enlarging either the inner or the outer component. Both panels 4.10 *a)* and 4.10 *b)* seems to show a similar scaling of $H(\omega)$ in the plateau reached at the inner Aluminium when either increasing the inner core dimension or the outer layer.

Finally, we must take into account the wires' contribution to build the final insulator thermal transfer function. To minimise this contribution, it was decided to lengthen the path from the external face to the final connection with the sensors attached to the Aluminium core. Setting a
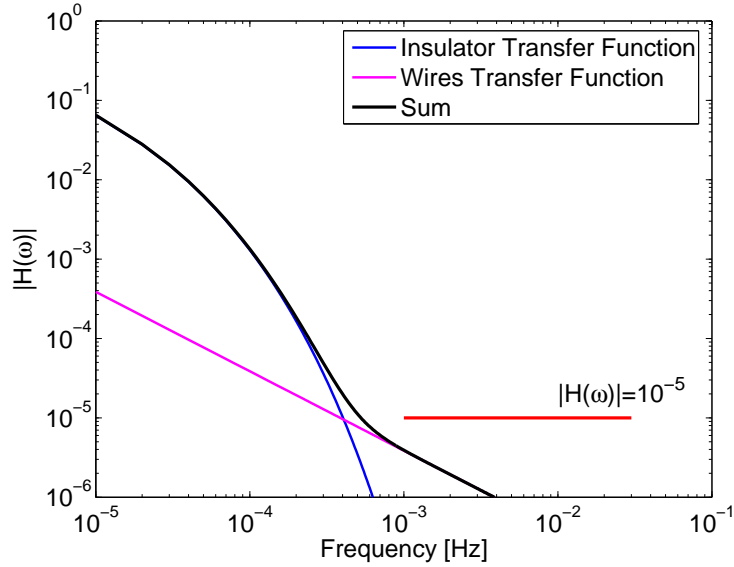
Figure 4.11: Insulator thermal transfer function. The required suppression factor in the MBW appears in red.

wires length $l_w \simeq 50$ cm should place our design, following Figure 4.3, in a situation able to reach the required level of temperature fluctuations in the inner Aluminium core. This is shown in Figure 4.11 where the final predicted thermal transfer function for this design is shown. The comparison with the required suppression factor leads us to conclude the viability of the selected design.

4.2.2 Implementation

The design process led to a definition of the insulator to be used. The next step was to implement the design in a thermal test bench including the temperature sensors to be put to test. The manufacturing of the thermal test bench was performed in NTE[2] premises during July 2004. To ensure the achievement of the insulation goal, a monolithic design was followed, i.e., the insulator could not be opened after being built. Thus, the set of sensors introduced in it could not be replaced, the bench is designed hence as a destructive test. A second non-destructive design is now being used to test the Flight Model sensors [85].

The inner body of the insulator and the one providing the main mass is composed by three stacked Aluminium slabs (260mm × 260mm × 80mm each) as the ones shown in figure 4.12. Eight holes were drilled on the middle slab: 7 holes of 3.5 mm and 8 mm depth and an eighth of 9 mm and 8 mm depth, the latter to be used for the reference resistor. Thermal grease (Dow Corning 340) was used to ensure good thermal contact between the sensors and the Aluminium body. Also to prevent from stresses that could take out place the sensors, its wires were fixed with glue (Araldit)

---

[2]http://www.nte.es

a)

b)

c)

d)
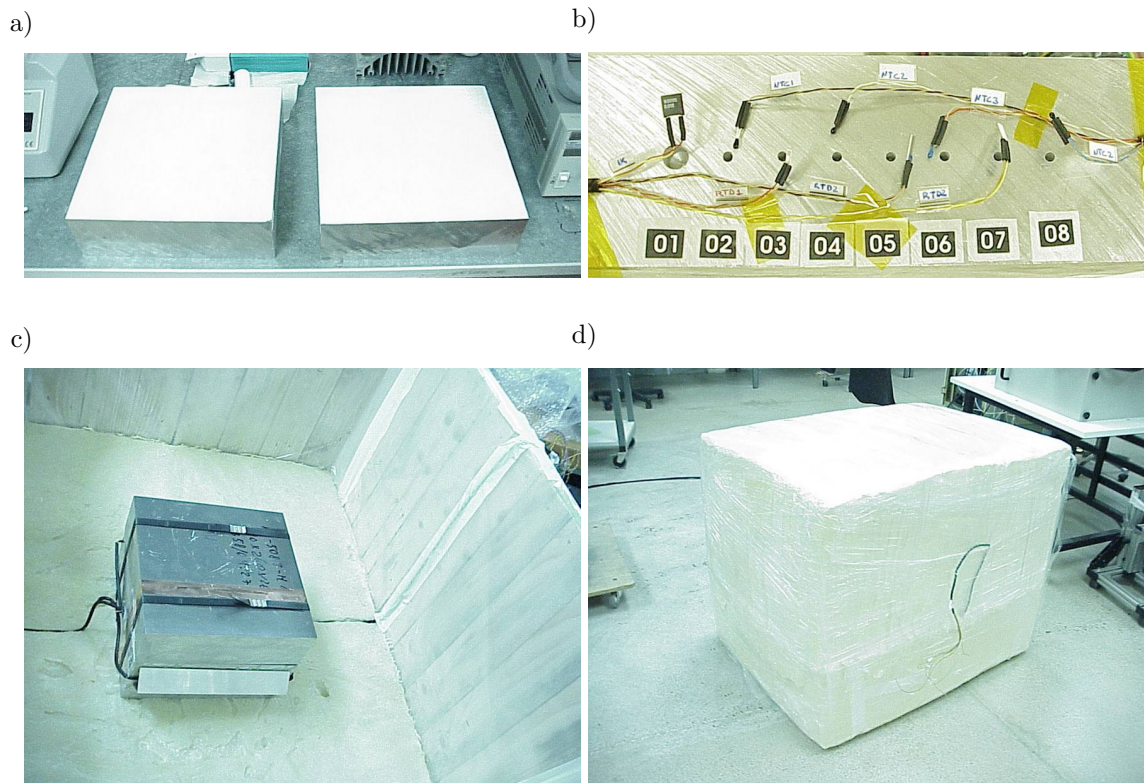
Figure 4.12: *a)* Two of the three Aluminium slabs used to compose the inner mass of the insulator. *b)* Distribution of temperature sensors on a side slab. NTC sensors occupy odd-numbered holes whereas Platinum sensors were inserted in even-numbered holes. Position #1 is left for the reference sensor. *c)* The inner Aluminium core inside the mould. *d)* The final insulator covered with plastic film.

to the Aluminium.

An Aluminium L-shaped cover glued to the Aluminium block protected the wiring and sensors from possible damages during the polyurethane grow up. All three blocks were stacked introducing thermal grease between them to facilitate thermal conduction. A Copper tape bracing the Aluminium core provide grounding to the lateral blocks. Finally, slings were used to avoid displacements of the blocks during the polyurethane grow up.

The polyurethane shell covering the Aluminium block was implemented as a first 330 mm layer where the metallic core was accommodated. Polyurethane was grown in a wood box acting as a mould. After this first layer, the metallic core was placed in the middle to be finally covered with polyurethane filling the mould. Figure 4.12 shows a mid step and the final appearance of the thermal bench when the wood box is removed and the outer surface is protected with plastic.

Chapter 5

Experimental qualification test

The present Chapter is devoted to the description of the qualification test of the temperature FEE once all the suitable thermal analysis tools have been developed and applied to the definition of test bench that ensures, at least from an analytical point of view, the achievement of the requirements.

Our first step goes through the design of an accurate electronics, able to theoretically reach the level of sensitivity taking into account not only the low level of temperature disturbances that needs to be monitored in flight but also that the mission MBW sets a technological challenge which requires testing electronics down to very low frequency band, where 1/f noise usually dominates the instrumental behaviour. At the same time, the selection of suitable sensors requires a trade-off between sensitivity and stability to reach the required instrumental noise level during long time periods.

First, a brief description of the thermal FEE will be given in order to stress some of the design clues on which it is based. We will then directly pass to the implementation of the test. Once the insulator has been fully described in Chapter 4 we will just need to describe the final implementation to then proceed with the results and corresponding data analysis.

5.1 Temperature subsystem description

The temperature subsystem on board the LTP plays a central role in what respects the demonstration of the drag-free technology, especially if we take into account the low frequency regime where the experiment is designed to work. Temperature disturbances can exert forces on the test mass, or in other temperature sensitive positions, with relaxation times long enough to enter in the MBW. On the other hand, thermal forces affecting the test mass will be surface forces whereas any magnetic or charged related disturbance applied on the test mass will affect the whole body.

5.2 Requirements

The temperature requirement budget is set by the LTP goal noise budget [100], rewritten here

$$S_{\Delta a,\text{LTP}}^{1/2}(\omega) \leq 3 \times 10^{-14} \left[1 + \left(\frac{\omega/2\pi}{3\text{ mHz}} \right)^2 \right] m\,s^{-2}/\sqrt{\text{Hz}} \tag{5.1}$$

in the frequency range $1\,\text{mHz} \leq \omega/2\pi \leq 30\text{mHz}$. This expression gives the global noise budget from which an apportioning has distributed its affordable contributions to different LTP subsystems [99]. This is translated into a temperature noise level delimited by

$$S_{T,\text{LTP}}^{1/2}(\omega) \leq 10^{-4}\,\text{K}/\sqrt{\text{Hz}} \quad 1\,\text{mHz} \leq \omega/2\pi \leq 30\text{mHz} \tag{5.2}$$

Although this requirement is partly design-given, the thermal contributions of different effects to the total noise budget can be outlined on the basis of the expected effects affecting the metrology measurement. We refer the reader to Chapter 2 for a description of such effects and their implication in the temperature stability requirement onboard the LTP.

We now pose the question: which is the level of noise we can accept in the temperature measurement system —which includes sensors, wires and electronics— if we are to diagnose temperature variations below the level (5.2)? Clearly, the answer to that question depends on how accurately those fluctuations are to be measured. The stability requirement equation (5.2) is already rather demanding of itself, so we do not expect thermal fluctuations to be much smaller. With this in mind, to request the measuring system to be about one order of magnitude less noisy than the maximum noise level to measure seems a sensible option:

$$S_{T,\text{FEE}}^{1/2}(\omega) \leq 10^{-5}\,\text{K}/\sqrt{\text{Hz}} \quad 1\,\text{mHz} \leq \omega/2\pi \leq 30\text{mHz} \tag{5.3}$$

This has in fact become a mission top level requirement —see [100], section 6.2. There are two groups of reasons which support it:

- Equation (5.2) defines the *maximum* acceptable level of temperature noise in the LTP. If this is satisfied, which of course must, then actual fluctuations will be less than that. Requirement (5.3) then sets a 10 % discrimination capability for the measuring device, a standard approach which is certainly compatible with better performance.

- LISA is more demanding than LPF as regards thermal stability. Actually, LISA requires an order of magnitude less temperature fluctuation noise than LTP [99]. If we require (5.3) for LTP then we are in a position where analysis of thermal sources of noise of relevance for LISA can be identified and tagged for improvement, at least in the overlapping frequency band of both missions. This prospect is in line with the very concept of LPF as a precursor mission.

Absolute versus differential temperature measurements in flight

The above arguments, and specially the first, can perhaps be criticised in terms of: why not perform *differential* measurements? This might relax the very demanding requirement in equation (5.3), in the sense that it would only apply to differential rather than absolute temperature measurements in flight.

While it is true that certain thermal disturbances depend on temperature *gradients* across the test masses —like the radiometer effect and radiation pressure gradients— there are others which do not —mostly those related to the optics. One could accordingly split up the temperature gauges into two classes, but this does not seem a particularly sensible choice, since the best device would obviously be the one to use in all cases, anyway.

A space mission like LPF does not allow to fix hardware design inefficiencies once it has been launched. The choice of making applicable the requirement stated in equation (5.3) to *all* temperature measurements, whether differential or absolute, seems thus not advisable to relax: some margin is necessary to cope with unforeseen sources of error.

5.3 Sensors

In this section the available thermal devices identified as previously interesting candidates for the LTP diagnostic temperature subsystem are briefly described. A wide variety of technologies is available as temperature sensors, however the selection performed in [82] took into account which among those solutions are suitable for our application.

A major difficulty to choose a particular technological solution is to assure that a space-qualified analog device is manufactured, this restriction is considered for any component being integrated on the spacecraft but is particularly restrictive for temperature sensors since these devices are usually used as diagnostics but not at the precision level required for this application. The space-qualified list of products sets a first important sieve that will be complemented by stability and precision reasoning, leading to a final solution reached after experimental testing.

The temperature sensors herein described are Resistance Temperature Detector (RTD) and Negative Temperature Coefficient (NTC) sensors.

5.3.1 Resistance Temperature Detectors

Temperature variations can be detected using materials which change their resistivity when subjected to temperature variations. This are called RTD but since the most common material used for this application is Platinum, they are also usually know as Platinium Resistance Thermometer (PRT). The variation on the electrical resistance of the conductor is not related to an increase of the number of electrons available for conduction but based on the vibrations of the atoms around their lattice equilibrium positions. A temperature raise in these bodies translates into an increase of the random thermal vibrations of the atoms around its equilibrium positions, reducing the mean free path of the electrons and consequently increasing its electrical resistance.

	Platinum	Copper	Nickel	Molybdenum
α [K^{-1}]	3.85×10^{-3}	4.3×10^{-3}	6.81×10^{-3}	3.79×10^{-3}
Range [°C]	[-200,850]	[-200,260]	[-80,320]	[-200,200]

Table 5.1: Characteristics of RTD sensors for different constitutive materials.

The following phenomenological description is usually adopted

$$R(T) = R_0(1 + \alpha_1 T + \alpha_2 T^2 + \cdots + \alpha_n T^n) \tag{5.4}$$

where R_0 is the resistance at the reference temperature and T is the variation with respect this reference value. Typical values for this coefficients [74] are $\alpha_1 \approx 3.9 \times 10^{-3}$ K^{-1} and $\alpha_2 \approx -5.8 \times 10^{-7}$K^{-1} from where the standard relation $\alpha_1/\alpha_2 \approx 10^3$ can be deduced. Indeed, RTD sensors are generally treated as linear thence using only the first two terms in (5.4).

There are different materials used as RTD such as Platinum, Copper, Nickel and Molybdenum. Among these the most sensitive are the Nickel sensors but their working range is shorter than the rest. The ones showing better performance are the Platinum sensors, among which the $100\,\Omega$ sensor (Pt100) is one of the most commonly used. In these sensors tolerance in the nominal value of the resistance is of the order 0.1% to 1%.

5.3.2 Thermistor

Thermistors is the abbreviation for "thermally sensitive resistor". As the RTD, thermistors are resistive materials with a dependence of their resistive value with temperature, however this dependence is of a different nature as the one arising in the RTD since thermistors are not conductors but semiconductors. The temperature dependence appears here due to the dependence on the number of electrical carriers with the temperature. When temperature increases there are more carriers available and therefore the resistivity decreases, yielding a negative temperature coefficient of the sensor. This property can be tuned by means of doping techniques, highly doped materials can acquire metallic properties with a positive temperature coefficient (Positive Temperature Coefficient (PTC)) in a limited temperature range.

Thermistors are manufactured mixing and synthesising oxides doped with metals, the most commonly used are Manganese, Nickel, Cobalt, Iron and Copper. The resistive element is inserted, after the synthesis, into an epoxy or glass shell.

This device exhibits an exponential dependence of its resistance with temperature, the most commonly used law expressing this dependence is the *Steinhart-Hart equation* [74]

$$\frac{1}{T} = A + B \ln(R) + C \left(\ln(R)\right)^3 \tag{5.5}$$

where R is the resistance value of the thermistor at a temperature T; the parameters A,B and C are constants coefficients characterising the thermistor. An approximate error around 0.01 ℃ in

a 100 ℃ range can be achieved using equation (5.5).

Their high sensitivity makes thermistors a good option but the main disadvantage that these devices suppose is their repeatability. Given that the semiconductors are subjected to artificial ageing process to increase their stability, they can show an important dispersion when using different NTC to sense a same value. It will not be a major drawback for our application if the sensor is not accurate in the determination of the nominal temperature value since the hard requirement of the LTP thermal diagnostics fall on the fluctuating behaviour of the sensor and electronics at low frequencies. However, if the sensor shows dispersion in the spectral domain we will need to ensure that the sensitivity plus the dispersion region falls below the requirement, equation (5.3).

5.4 Temperature Front End Electronics

The stringent requirements assumed for the LTP thermal diagnostics set an important challenge for the design of the FEE. Not only the acquisition by means of suitable electronics circuitry needs to be designed and tested accordingly but any device used in the design has to be qualified for space use. Moreover, power and mass are always crucial parameters in space applications, susceptible to be reduced. Hence the design must be optimal in these parameters.

Temperature sensors will be distributed through the LCA as previously described in section 2.3. The criterion to distribute the thermal items is, in general, to locate them in thermal sensitive locations which can introduce noisy measurements via thermal effects. Therefore the inclusion of the sensors must be carefully addressed. A requirement is set for this reason to the power dissipated by the sensors [51]

$$P \leq 10 \, \mu\text{W} \tag{5.6a}$$

A collaboration UPC-IEEC has been working in the design of a FEE able to fulfil the noise temperature requirements level with the limiting conditions previously sketched. The final description of the system can be found in [79, 86]. We will in the following briefly describe the main characteristics of the chosen solution.

The signal conditioning circuit is divided in three main blocks: the bridge circuit, the Multiplexer (MUX) and Instrumental Amplifier (IA), and the Programmable Gain Amplifier (PGA) and low pass filter, Figure 5.1.

A Wheatstone bridge is used as the signal conditioning circuit. For each sensor, four different resistors form the bridge, one branch defined by R_{ref} and $R_{\text{ref,i}}$, and the second branch conformed by R_{ref} and $R_{\text{sens,n}}(T)$, being the later the sensing element. The resultant output voltage is

$$v_0(T) = V_{\text{bridge}} \left(\frac{R_{\text{ref,i}}}{R_{\text{ref,i}} + R_{\text{ref}}} - \frac{R_{\text{sens,n}}(T)}{R_{\text{sens,n}}(\text{T}) + R_{\text{ref}}} \right), \quad i = 1, \dots 6 \quad n = 1, \dots 4 \tag{5.7}$$

As an interesting feature of the Wheatstone bridge, it allows centring the zero output for different temperature scale configurations. This is the so called deflection method [74] which leads

91
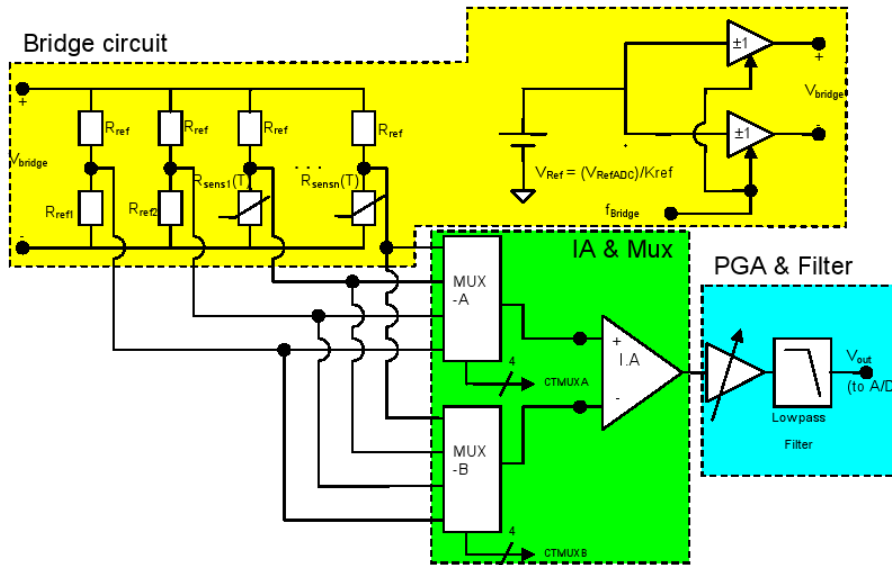
Figure 5.1: Block diagram of the signal conditioning circuit. Two multiplexers select the two branches of the Wheatstone bridge: MUX-A chooses a given sensor and MUX-B fixes one of the possible references that defines the temperature scale. The design also allows to measure differential temperatures between two sensors replacing the reference resistance by a second temperature sensor.

in our application to six scales centred at: 12, 15, 20, 22.5, 25 and 27.5 ºC. The adoption of these scales is directly related to the high sensitivity and resolution needed, and to maintain the output of the bridge as close to zero as possible to minimise the effect of gain errors along the measurement chain. Each scale is related to a R_{ref} value which is selected by one MUX.

As previously stated, the bridge is powered with an AC square signal. The bridge with the sensor to measure is selected with two multiplexers (MUX-A and MUX-B) connected to the IA inputs. The signal is amplified with a constant gain by the IA and an additional programmable amplifier allows selecting two different gains. After amplifying, the signal is low-pass filtered to reduce the noise bandwidth below to a half of the Analog-to-Digital Converter (A/D) sampling frequency.

The bridge is continuously powered to prevent from variable errors in the self heating term, the selected feeding signal is an AC square bridge, the reason being that 1) the AC signal reduces the offset voltages at the bridge output and 2) the square shape implies a constant power applied to the sensor which reduces the second harmonic signal in the output spectrum due to self-heating.

The monitoring of the temperature environment on board the LTP, and specifically in those places where high temperature couplings are expected, requires a total amount of 24 sensing devices distributed through the LCA [51]. A dedicated FEE for each sensor is an unreliable solution due to mass and power limitations hence a solution of a FEE for four sensors was established introducing

Component	Model
Reference resistance	Vishay
Multiplexer	DG408 1:8
IA	AD624

Table 5.2: Components used in the FEE design

the second MUX switching between four different sensors, $R_{TS}(T)$.

Each branch of the Wheatstone bridge is connected to a input of the IA, therefore we get an amplification of the bridge output by a constant factor, fixed at 200.

After the amplification, a low-pass filtering is implemented in the sampling procedure to prevent from aliasing effects. There exists however a constraint on the cut-off frequency of the filter because of the settling time it imposes on the sampling process. Each time the polarity of the bridge is changed or another channel is selected the filter has to settle to a new value. The shorter the bandwidth we are considering, the longer the settling time will be. Thus, it is necessary to introduce a delay after a change in the input to acquire the signal sampled by the A/D. After the sampling, the output signal will be integrated to reduce the noise. A trade-off between a shorter bandwidth and more samples acquired in the A/D yields to a cut-off frequency of 500 Hz and a 10 ms of settling time. It can be shown [79] that with the referred setting time the error is minimised to the pK range.

The signal digital processing enters once the A/D samples the signal. The sampling frequency is 38.4 kHz. Each sample at the end of the chain consists of $M = 3456$ samples of which only $N = 3072$ are averaged and translated into A/D counts.

These parameters yield to an integrating time of 80 ms with zeros at each 12.5 Hz (the 50 Hz interference and its harmonics are zeroed) and an equivalent resolution of 27.5 bits (16 $\log_2 N$).

After the integration the signal is downsampled a factor M changing the polarity of the bridge circuit every M inputs. The final signal is obtained averaging the difference between two consecutive samples. This operation is represented by a transfer function that suppresses the noise contribution at DC, which is the frequency domain expression of the frequency transposition by the bridge's square modulation.

5.4.1 Noise analysis

Temperature fluctuations can enter in the data acquisition chain in many steps of the process. We will herein summarise the expected dependencies of the FEE blocks just described. The temperature coupling of each device is one of the most important coefficients to take into account in the design. It is here generally termed as Temperature Coefficient (TC) and labelled with the symbol α ($[\alpha] = \mathrm{K}^{-1}$). Hence α_X is the coupling factor of the given device X to temperature. This convention is also applied to temperature sensors, defining what its sensitivity or TC as

Block	Noise Dependence	TC limiting value $[\text{K}^{-1}]$	Solution Used $[\text{K}^{-1}]$
$S_{T,b}^{1/2}(T,\omega)$	$\dfrac{S_{v_o}^{1/2}(T,\omega)}{\frac{R_2}{R_2+R_{TS}(T)}\,\alpha_{TS}(T)[P_{TS}R_{TS}(T)]^{1/2}}$	$\alpha_R \leq 2\times 10^{-6}$	$\alpha_R = 0.6\times 10^{-6}$
$S_{T,IA}^{1/2}(T,\omega)$	$\alpha_{IA}\,S_{v_o}^{1/2}(T,\omega)$	$\alpha_{G_{IA}} \leq 3.5\times 10^{-6}$	$\alpha_{G_{IA}} = 3.5\times 10^{-6}$
$S_{T,MUX}^{1/2}$	N_c	–	$N_c = 4$
$S_{T,A/D}^{1/2}(T,\omega)$	$\dfrac{\Delta}{2^{16}}\,FS\,\dfrac{1}{\sqrt{f_s/2}}\,\dfrac{1}{G_{IA}\,s_b(T)}$	$\alpha_{G_{A/D}} \leq 35\times 10^{-6}$	$\alpha_{G_{A/D}} = 7\times 10^{-6}$

Table 5.3: Temperature FEE noise contributions

$$\alpha = \frac{1}{R_{TS}(T)}\frac{d\,R_{TS}(T)}{dT} \tag{5.8}$$

Table 5.3 gathers the expressions for the FEE noise contributions [86]. A common rule can be used applying this expressions to define upper values for the TC of each of those devices conforming the FEE: it must be always satisfied that

$$\frac{\alpha_X(T)}{s_b(T)}S_{T,FEE}^{1/2} \leq S_{T,system}^{1/2} \tag{5.9}$$

Considering $S_{T,FEE}^{1/2} \leq 10^{-5}\,\text{K}/\sqrt{\text{Hz}}$ yields to the limiting parameters appearing in Table 5.3 which were driving factors for the design and component selection. From these, some interesting conclusions can be extracted from the bridge noise contribution $S_{T,b}^{1/2}(T,\omega)$:

- the greater the dissipated power in the sensor the lower the temperature spectral noise density.

- the greater the relative sensor sensitivity the lower the temperature spectral noise density.

- changing the nominal value of the sensor does not reduce or increase the temperature spectral noise density.

These rules, among other considerations, has been considered in the designing process of the Thermal FEE.

5.5 Experiment setup

In this section we describe the details of the experimental setup used to test the LTP temperature FEE. In the previous chapter we showed how the internal core was drilled to allocate a total amount of 16 sensors. Figure 5.2 shows which is the distribution of the sensors inside the Aluminium core. Since the test bench was built as a destructive probe, both kind of sensors, RTD and NTC, were decided to be included in the same bench. Both types were distributed homogeneously through the holes to prevent from differences in the measurements that could be assigned to their position more
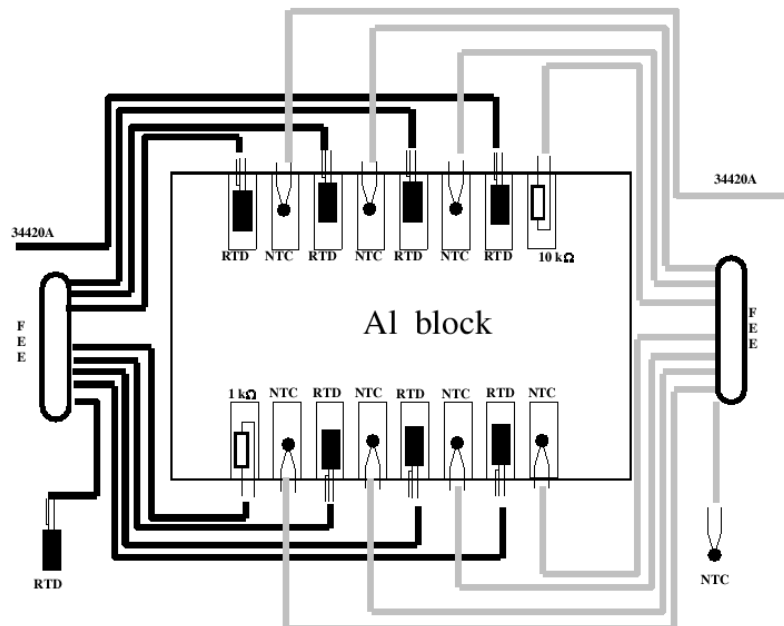
Figure 5.2: Distribution of sensors inside the insulator. Two different possibilities are shown labelled in black and grey wires depending if the sensors being tested are RTD or NTC sensors respectively.

than differences in the sensors themselves. Besides the sensors put to test inside the Aluminium, two reference probe were introduced in the Aluminium core. The role of these resistances, which are not temperature dependent, is to monitor fluctuations that are induced by the temperature FEE itself, setting the noise floor level. Because temperature fluctuations can not affect them, with these sensors inside the aluminium we are able to disentangle temperature related noise with any other sources arising at some point of the measurement chain. Furthermore, there are two more reference sensors, one of each type, sensing external environmental perturbations that will help understand the screening power of the insulator.

Two possible setup configurations share the same thermal test bench. We will refer to *Configuration 1* when measuring with the NTC and *Configuration 2* the one using the RTD sensors. If we thus summarise all the temperature items conforming the test, we end with:

- CONFIGURATION 1

    - 7 NTC sensors (YSI44006)

    - 1 Reference sensor (Vishay S102J $10 \, k\Omega$)

    - 1 Environmental sensor (Betatherm 10K3A5421)

- CONFIGURATION 2
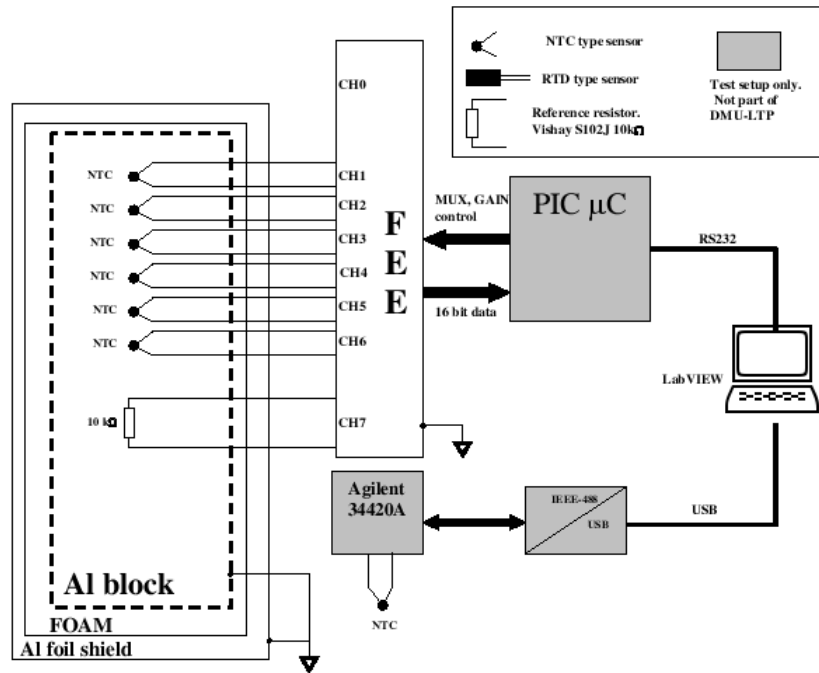
Figure 5.3: Setup for the performance test experiment.

- 7 RTD sensors (4 LabFacility DM507 and 3 IST P1K0.520.7W.B.010)

- 1 Reference sensor (Vishay S102J 1 kΩ)

- 1 Environmental sensor

The procedure to perform the temperature test needs to be split in two different runs due to the setup design just described above [54]. In the first run, Test 1, 4 NTC-type sensors[1] were measured in addition to the 10 kΩ reference sensor also placed in the Aluminium block. The environmental sensor was a NTC-type sensor measured by an Agilent multimeter. The diagram for this experiment is shown in Figure 5.3

In the second run, Configuration 2, 4 RTD-type sensors were measured in addition to the 1 kΩ reference resistor. Data from the environmental sensors were acquired by the Agilent multimeter. RTD-type sensors were measured using 3 wires, except for the outside one where a 4-wires connection was used.

---

[1]The reason to use only four channels of the FEE must be found in the final FEE design. Although the prototype allows to multiplex a total amount of 8 channels, the final design sets a maximum of four channels. See for instance [79]

5.6 Results

The experiment was expected to provide two different outputs. First, to ensure that the thermal insulator was correctly described by the analytical transfer function previously derived – see § 4.1.4. Once the required thermal stability was ensured inside the insulator, the performance of the FEE could be tested and the fitness of NTC or RTD sensors for our final purpose could be experimentally discussed.

Both experiments required opposite environmental conditions and therefore they were undertook in very different conditions. The thermal insulator characterisation requires a strongly perturbed environment in order to be able to clearly bring out the transfer function provoked by the insulator whereas the performance test demands a quiet and stable environment. Data used for the first test was acquired in the NTE clean room and the later was instead tested at the Universitat Politècnica de Catalunya (UPC) Faraday chamber.

5.6.1 Insulator test

A low frequency thermally perturbed environment is hardly found in other situation than leaving the test bench subjected to daily and human related perturbations, i.e. placing the test bench in an office with direct solar light contact. However, contrary to what was expected it turned out that NTE clean room had even more disturbance power in the MBW than if it had been exposed to daily trends, the reason was the active temperature control that ensured the room thermal stability. In order to establish the temperature to a given value, the activation cycle driving this control produced a strong ripple of about $1\,°C$ in 45min scale time, thus generating important disturbances in the low frequency band. Initial performance test campaigns at this location ended with non-compliant temperature noise level in the MBW [56].

An example of the data acquired in the clean room appear in Figure 5.4, in this case a five days time series starting with an abrupt temperature step followed by the active temperature control ripple is shown. The high suppression inside the insulator is also clearly seen. If this data set is analysed in the Fourier domain, the dynamics of this temperature fluctuations can be extracted in a more suitable framework and therefore its physical cause can be better understood. Figure 5.4 compares the analytical prediction of equation (4.5) with two experimental runs: the black curve corresponds precisely to a five days time series showed previously and the grey curve represents a data stream a month long with largely varying thermal conditions outside the insulator [55]. These curves are relatively clean below $10^{-4}\,Hz$ but they tend to approach unity at higher frequencies, which is an indication that electronics noise is dominant in that band: indeed, system readouts inside and outside the insulator tend to equal each other (transfer function nearing unity) while real temperature fluctuations obviously do not.

Thicker lines are fits to the data in the lower frequency band, the solid is the exact prediction of the model, while the dotted is a first order filter fit, and the dashed one is a second order filter fit. The last two are provided as examples that the data can also be adjusted by simpler models in restricted data regions yet indicating that the actual behaviour of the insulator follows a trend
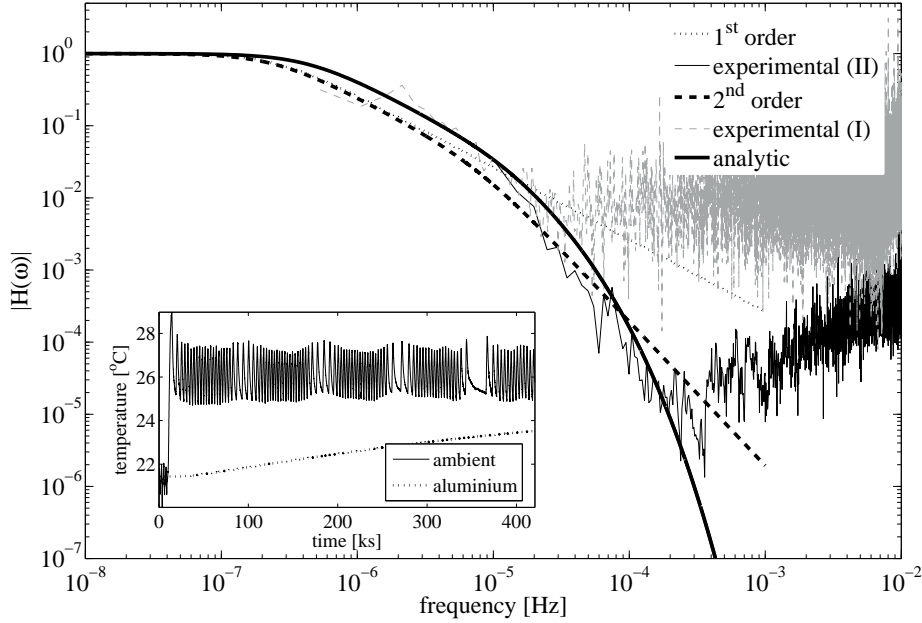
Figure 5.4: Results for the insulator test. Details can be found in the text.

with steeper negative slope towards higher frequencies.

Because the scope of these test runs was precisely to evaluate the response of the insulator against a strong perturbative background, the LTP MBW, being above 10^{-3}, is not covered by these data. However the fact that the models predictions are followed quite well at low frequencies is reassuring, in that we can expect filter suppression factors of 10^6 and more in the MBW. This is simply because we do not expect the transfer function to bounce back up again at high frequencies.

With this results we are thus quite confident about our test bench design, the next step is to place the insulator in a quite and stable environment which will give us some insight about temperature fluctuations in the MBW.

5.6.2   Front End Electronics performance test

A suitable environment to test the FEE performance was found in the Faraday chamber, located in a underground at UPC premises. No active temperature control was considered in this test in order to achieve the required temperature stability.

Temperature was measured in two different and sequential runs. Configuration 1 and Configuration 2 previously described were used to undertake the experiment and thus to compare both technologic available solutions for the FEE temperature sensors. The detailed data analysis treatment of the performance test can be found in [87].

Configuration 1 results are shown in Figure 5.5. The black line corresponds to the PSD of the
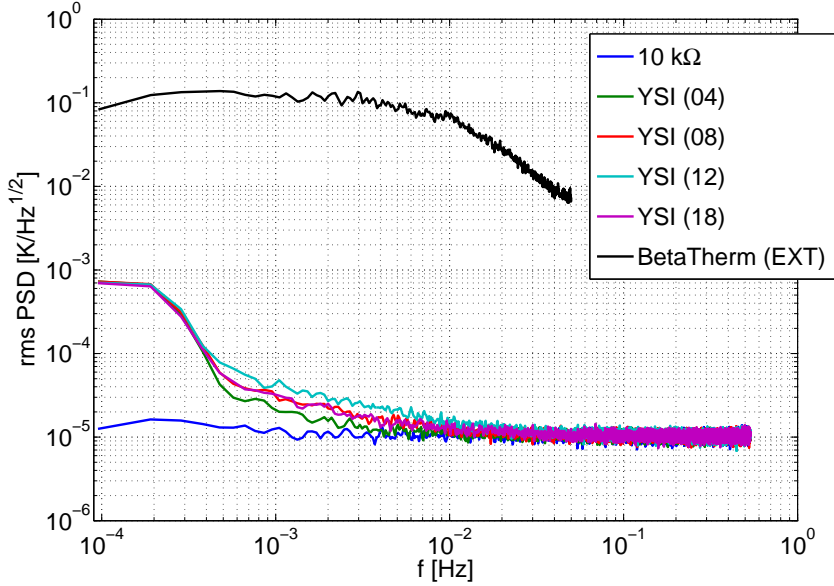
Figure 5.5: Configuration 1 performance test results

sensor measuring environmental temperature fluctuations. From this noise level we can consider the Faraday chamber as a good enough thermal environment for the performance test purpose since the temperature fluctuations noise level is of $S_T^{1/2} \simeq 0.1\,\mathrm{K}/\sqrt{\mathrm{Hz}}$ at $1\,\mathrm{mHz}$ and decreasing at higher frequencies. The blue curve corresponds to electronics noise since it is obtained as the PSD of the data stream acquired from the reference sensor inside the insulator.

Finally, the rest of curves trace the sensors measurements inside the Aluminium block. A first remarkable property is a considerable variance between different NTC sensors. The reason of this uncertainty must be found in the manufacturing processes – see 5.3.2, in particular the ageing processes to which the semiconductors are subjected. However, the main problem that this data set seems to pose refers to the low frequency behaviour of the sensors. As clearly seen in Figure 5.5, despite the variance of the thermistors, the noise level at the low end of the MBW can be set into the interval $S_T^{1/2} = [1.2, 4.1] \times 10^{-5}\,\mathrm{K}/\sqrt{\mathrm{Hz}}$. Measurements are therefore slightly above the FEE temperature requirement

A systematic spurious contribution adding noise to the readout in the MBW was identified being the 16-bit A/D the origin of the problem, in particular due to quantification errors induced mainly by the Integrated NonLinearity (INL) problems of the A/D — see [79], section 2.2.1.2. This error source is directly related to the numerical value of the data being acquired, in our particular case the noisy term decreases for decreasing values of the temperature slope and thus, in the worst case, can be prevented setting a acceptable maximum slope as a requirement. However, this is not considered a baseline approach and technologic solutions exists for this problem, for instance: a Sigma-Delta A/D (these devices do not show INL problems) or including a dithering voltage at
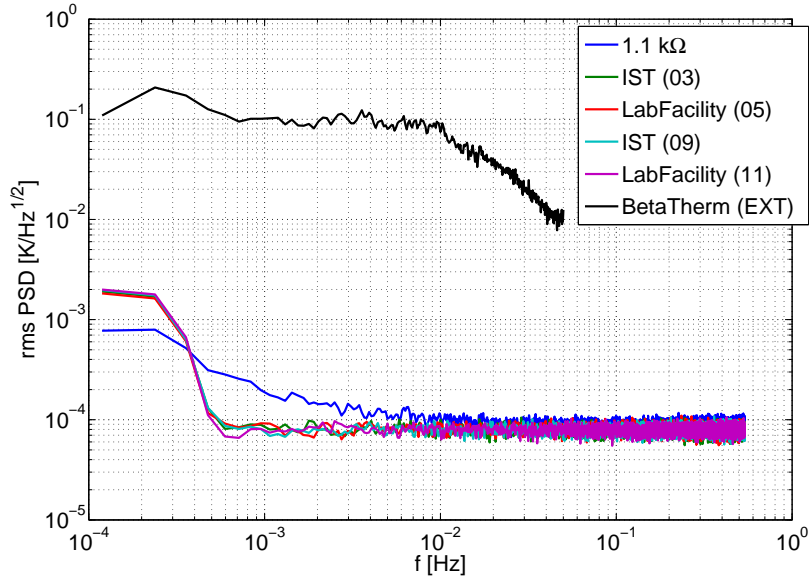
Figure 5.6: Configuration 2 performance test results

the A/D input.

Configuration 2 results are shown in Figure 5.6. The black line corresponds to the PSD of the sensor measuring environmental temperature fluctuations. The floor noise clearly gets worse using this data set: $S_T^{1/2} \simeq 7 \times 10^{-5}\,\mathrm{K}/\sqrt{\mathrm{Hz}}$, the reason being the linear dependence of Platinum sensors to temperature changes compared to the more drastic exponential of the NTC's. On the other hand, RTD sensors show a flat spectrum all along the MBW proving a high long term stability, even at the milihertz scale and even more important, the repeatability of the measurement is highly increased with this sensors. Contrary to the first set of measurements performed with the Configuration 1 setup, RTD sensors put to test show a minimum variance in its noise levels, as shown in Figure 5.6.

Although sharing the same electronic measurement chain, the INL problems related to the A/D do not appear in Figure 5.6. Indeed, when measuring temperature fluctuations at the required sensitivity of tens of microkelvin, the Johnson noise appears as the dominant contribution. Consequently, those effects present in the case of the NTC's can not be appreciated since we are now at higher noise levels, as clearly seen when comparing Figure 5.5 and Figure 5.6 floor noise levels.

III. Heaters and Data Analysis

" Y el que no confunde, se confunde. "

Niebla
Miguel de Unamuno

Chapter 6

Thermal diagnostics experiments description

An experimental approach is clearly needed for the diagnostics purposes. In Chapter 5 the thermal Front End Electronics was experimentally tested focusing on the evaluation on the sensitivity performance of the device. In that case, we were not facing a diagnostic experiment, the final scope was rather to probe the thermal sensitivity goal, $S_T = 10^{-5}\,\mathrm{K}/\sqrt{\mathrm{Hz}}$ in the MBW. Thus, it must rather be considered an instrumentation qualification, as we named then, than a diagnostic experiment.

On the contrary, we will in this Chapter address the problem of thermal diagnostics and its experimental realisation. Unfortunately, the description will not be comprehensive since we could only thermally characterise the Optical Metrology Subsystem, and therefore we will stick to this subsystem. The experiments consist in the simultaneous measurement of both phase and temperature with the aim of reproducing the mission conditions in the most trustworthy way possible. This includes, for instance, attaching methods of thermal items to its locations or the use of different acquisition systems in parallel.

In Chapter 2 we reviewed some of the identified thermal effects expected to induce thermal noise in various locations of the LTP. There are three relevant parts affecting the Optical Metrology Subsystem with respect to its coupling to thermal disturbances: the Optical Bench, the LCA Struts and the Optical Window. The first could be directly studied by means of the Optical Bench Engineering Model. Although the Engineering Model has not any strut which allows to study effects of a heat shock applied on it, the heat loads were applied to the Optical Bench flanges, i.e the mechanical part linking the Zerodur of the Optical Bench to the Struts — see below for more details. This way, some of the effects taking place in the interferometer phase due to thermal leaks from the outer environment could be reproduced and enhanced with the heaters.

Finally, three Optical Window prototypes were also subjected to thermal pulses. The significance of this part of the LTP design together with the relative ignorance of the effects that a

glass clamped into Aluminium braces could induce in the measurement led to a more systematic and deep study of this part during the campaign. The representative amount of data obtained with these experiments allowed a careful data analysis process yielding a system identification methodology that will be described in Chapter 8.

The aim of this Chapter will be to provide the experimental details as well as a phenomenological description of the results obtained. The processing of these results, either to extract information regarding the heater sizing and characterisation or related with data analysis and noise model determination will be left for Chapter 7 and Chapter 8 respectively.

6.1 Setup description

A crucial element for the characterisation was the conditioning of the interferometric signal. The heterodyne signal was produced in an optical bench, as described in §1.2.2 [37, 38]. The optical fibers collecting the light of the two outputs were directed to a vacuum tank flange, whence directly connected to the Engineering Model fiber injectors.

The vacuum tank had a cylindrical shape with an approximate volume of 950 l. The vacuum system lied in two independent vacuum pumps and a sensor, the models used for the experiment were:

- Scroll Pump Franklin Electric Mod.1301007453. Power: 3/4 hp

- Turbo Pump Pfeiffer Typ. TPH170. Volume flow rate: 170 l/s

- Vacuum Sensor Leybold Vakuum GmbH Typ. ITR90, Nr.12094.

both vacuum pumps acting on the tank were connected in series. On the bottom plate there were two fiber-optical feedthroughs and about 100 electrical feedthroughs.

Light arriving at the photodiodes on the Engineering Model optical bench was acquired via a phasemeter fulfilling the sampling properties to be accomplished by the final flight model [38]. The second acquisition subsystem, the one in charge of the temperature sensors, was the temperature FEE described in Chapter 4. This way, we are not only reproducing the experiment in the best way we can but we are also obtaining the data as much in the same format as possible and thus we will need to face some data conditioning problems, e.g. resampling, that will necessarily appear in the final experiment.

In what respects the thermal diagnostics items used for the test were, equally as for the above test equipment, those models resembling the ones to be used in-flight. After the experiments reported in Chapter 5, the baseline sensor selection has been the NTC sensors. Among the different models, a glass encapsulated model has been chosen for its enhanced stability. Moreover, the selected sensor has a surface probe shape which facilitates the attaching process, guaranteeing better temperature monitoring.

In the heaters side, the best choice found in the market for an application as the one required for our purpose, which require low power but a certain flexibility to be attached to different surfaces
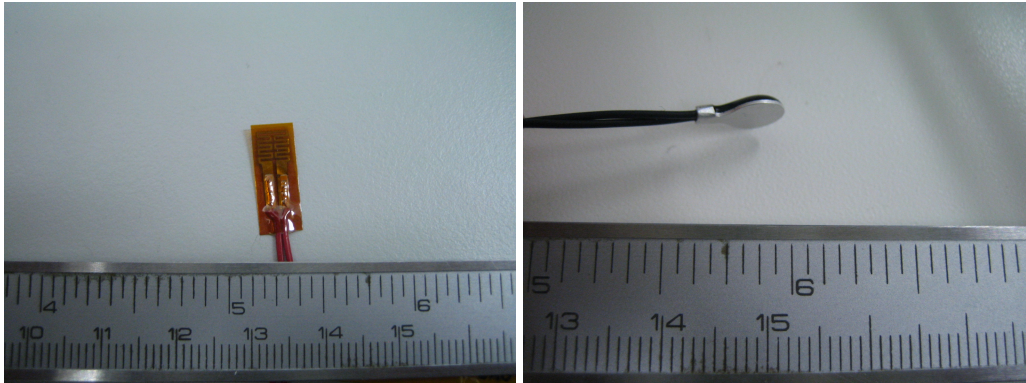
Figure 6.1: Left: 5.3 Ω MINCO heaters. Right: Glass encapsulated Betatherm sensor

with different shapes, was the Kapton (or polyamide like) heaters. Different sizes, implying different resistances, were used in the experiments depending on the allocation

Heaters' experiments stood out two setup problems: first, the thermal radiation of the heater was, in our first experiments, clearly visible through the sensors located at different points. This raised up the need of a screening of these effects in order to clearly calibrate the heat effect on the interferometer due to thermal conduction. A radiation screening layer was achieved using Aluminium foil tape around the heater. In second place, the attaching method of the heater needed to be also carefully examined since it had to fulfil both thermal and vacuum requirements. The solution was found in the Pressure Sensitive Adhesive (PSA) film, which entered into the list of materials space qualified with a low outgassing rate[1].

Next list summarises the main items used for the tests:

- *Heaters*:MINCO HK5565R5.3L12AU (5.3 Ω), MINCO HK5303R70.2L12A (70.2 Ω)

- *Sensor*: BetaTherm G10K4D853 Glass Encapsulated NTC Thermistor (10 kΩ nominal resistance)

- *PSA film*: 3M Adhesive Transfer Tape

- *Aluminium tape*: 3M Aluminium Foil tape

Figure 6.1 shows some of the items used for the thermal test performed on the Engineering Model and the Optical Window prototype.

6.2 The Optical Bench Engineering Model

The Optical Bench holds the interferometer layout on board the LTP, it is built based on the silicate bonding technique [31] which allows the construction of a monolithic interferometer. The main

---

[1]http://outgassing.nasa.gov
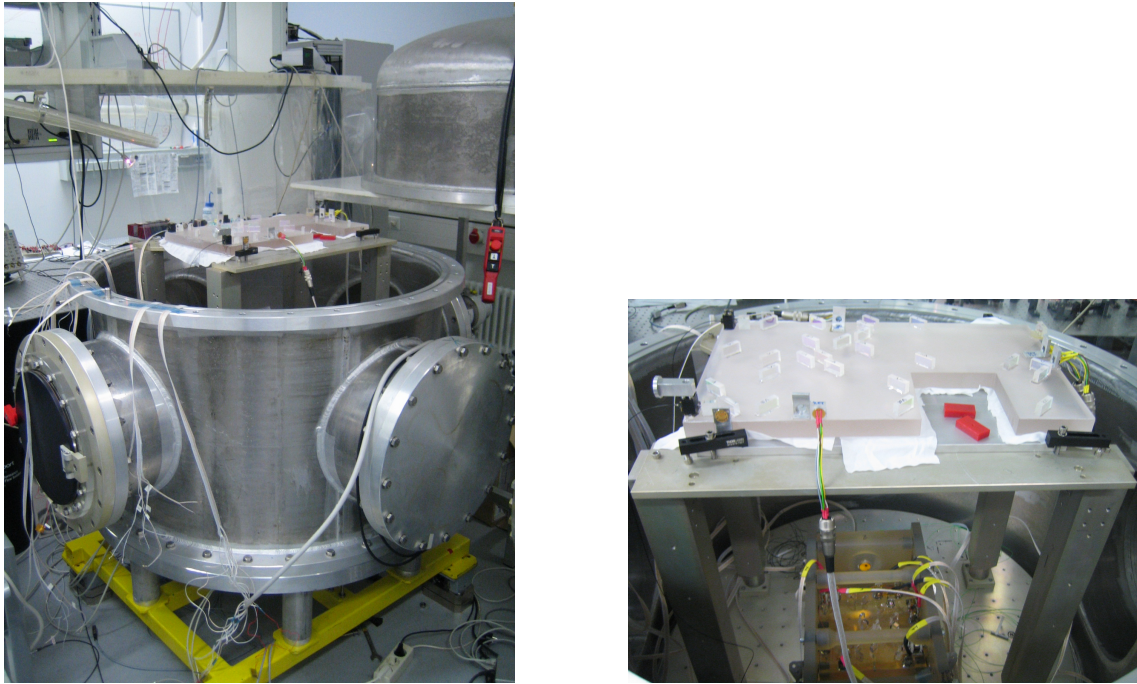
Figure 6.2: *Left:* Outside view of the vacuum tank with the optical test bench inside. *Right:* EM inside the vacuum tank on the bottom part below the optical test bench.

characteristic of this bench were already discussed in § 1.2.2 and references therein. We will in the following do not enter in more technical detail about the operation of the interferometer and try to describe the setup upon which the experiments were performed. A final point to stress is that the Engineering Model had successfully passed, before the thermal campaign, a performance test [39] and therefore must be considered a reliable model. This ensures that thermal data obtained on it are representative of the final experiment, if not in environmental conditions, at least in the structural ones.

6.2.1   Optical Bench heating

A set of four heaters are envisaged to be attached to the Optical Bench as a part of the thermal diagnostic subsystem. Although they were initially planned to be attached on the four corners, the current baseline is to attach them to the lateral sides to prevent from possible interactions of the sensors with the laser beam or any of the elements of the interferometric setup.

Contrary to the rest of locations, Optical Bench sensors do not have nearly heaters to enhance the thermal signal in that location. The extremely stable properties of the Zerodur seem to point out that thermal disturbances will hardly introduce noise effects in the phasemeter readout. However, the lack of heat input in these locations will make more difficult their related data analysis, the reason being that without a clear heat input we do not have a direct way to establish
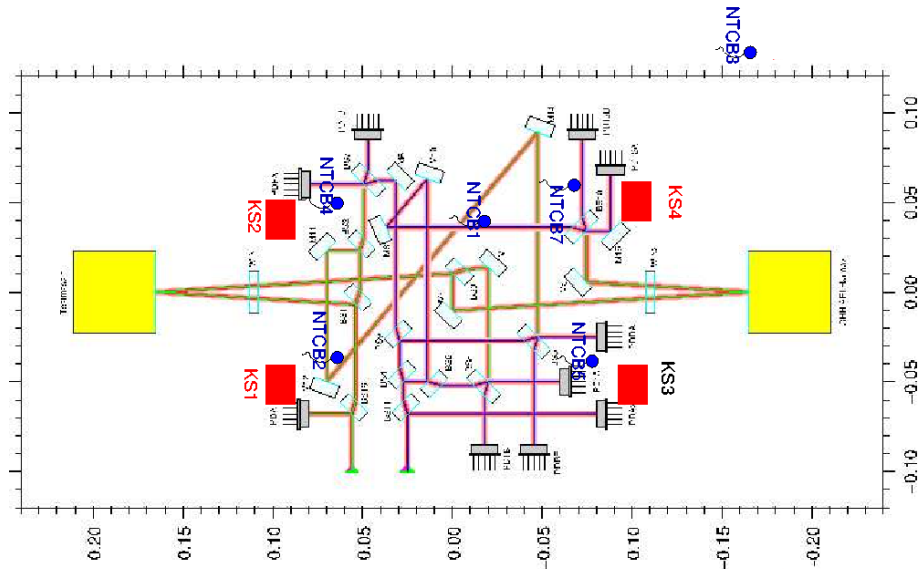
Figure 6.3: Scheme of diagnostics items distribution in the Optical Bench test configuration. Red squares mark heater position and blue dots sensor position.

a relationship between the temperature at a given point and the interferometric behaviour, i.e. a transfer function. Even if the related thermal effects are easy to understand since they are basically related to the coefficient of thermal expansion of the Zerodur, the complex geometry traced by the laser beams makes it difficult to understand the whole effect. The results reported here must be therefore considered a qualitative description of the effects that could take place in the Optical Bench due to thermal stresses.

A global scheme of the Optical Bench with the laser beam layout is shown in Figure 6.3, in the same picture the sensors and the heaters, in blue and red respectively, used in the experiment are schematically distributed through the Engineering Model as they were in the experiment. The heaters used for this test were the $5.3\,\Omega$ heaters, which are shown in Figure 6.1, left panel. In Figure 6.4 a detail of the configuration is shown. The NTC appears on top of the Bench, each one near a photodiode. Heaters attached to the lateral side can not directly seen because of the Aluminium tape covering them.

Test results

There a two kind of results that can be derived from the described setup. In first place, the measured data allow us to thermally characterise the Optical Bench by simply comparing the input power with the temperature increase achieved, regardless of the interferometric output. In second place, we can consider the interferometric output in order to try to determine any correlation
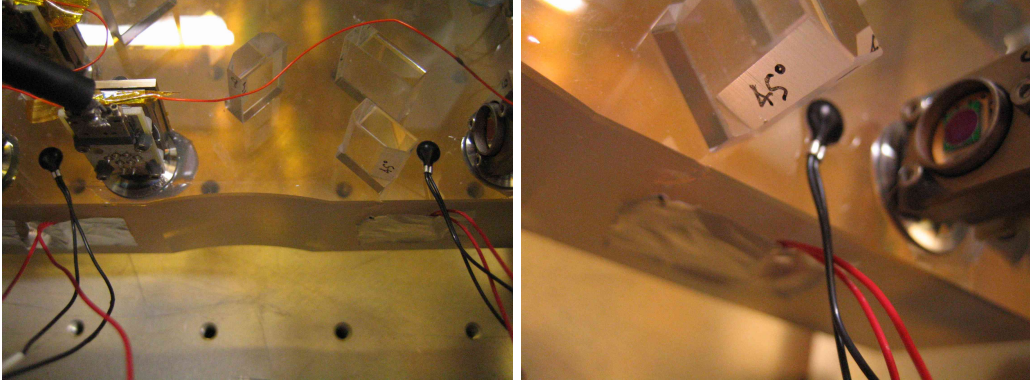
Figure 6.4: Detail of the Optical Bench test setup. *Left:* Two electrode and heater couple are shown attached to both corners of the Optical Bench. *Right:* A heater and sensor couple in one corner. The former is covered by Aluminium tape. The sensor is attached between a beamsplitter and one of the photodiodes.

between temperature and phase increase.

By applying heat pulses and measuring temperature increments on the closest sensor to the heater one can obtain a thermal response characterisation for the OB. Given the low conductivity of the OB plate, these values can only be used to estimate temperature increase for local heat impact.

Table 6.1 reports on typical values obtained from the experiment. As shown there, we can extract a *thermal resistance*, R_{th}, factor relating heat input with the obtained temperature increase. This should be defined as

$$\Delta T = R_{th}\,P \tag{6.1}$$

However, as was shown in §3.1, the thermal resistance defined in this way can only be applied in the steady state and it can be used, under this condition, to characterise the thermal behaviour of the system. In our case, equilibrium is not reached so the ratio between power and temperature increase does not achieve a constant value. Instead, the constant parameter characterising the system should be defined in this case as the thermal response per unit time,

$$\Delta T = Q_{th}\,P\,\Delta t \tag{6.2}$$

where we have labelled this parameter as Q_{th}. If values on Table 6.1 are substituted in the equation and the statistical mean is computed, the result obtained is

$$Q_{th} = (3 \pm 1) \times 10^{-3}\,\mathrm{K\,W^{-1}s^{-1}} \tag{6.3}$$

This parameter thus describes the temperature rise in a temperature sensor on the Optical Bench provided the duration of the pulse and the power applied in the closest heater.
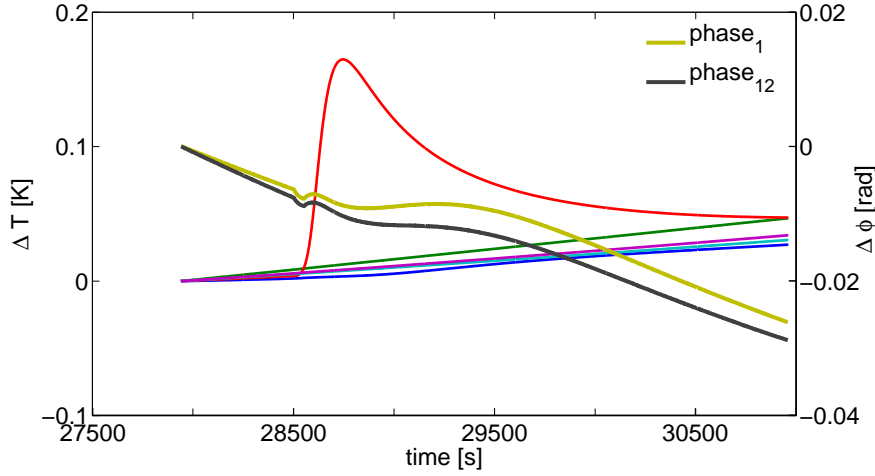
Figure 6.5: Optical Bench interferometric response to a 1 W heat pulses during 50 s applied on KS1 location —see Figure 6.3. The x_1 and x_{12} interferometers are labeled and the rest of curves correspond to sensors on the Optical Bench. The red curve is the sensor closest to the heater source.

As previously stated, a second class of conclusions can be obtained with our experimental results if now the interferometric readout is taken into account. Figure 6.5 and 6.6 show the phase evolution for the same heat shock on three different locations, corresponding to KS1, KS2 and KS4 heaters on Figure 6.3, on all cases a 50 s pulse of 1 W was applied. The first evident result that we obtain by inspection of Figures 6.5 and 6.6 is that the interferometer responds differently depending on the heat application point. When heating the Bench, the complex geometry drawn by the laser beam shows up in different responses of the laser readout depending on the heat location point. Moreover, it is difficult to disentangle the thermal contribution from the phase response since the four interferometers conforming the Optical Bench can be affected by the thermal shock. As an example, Figures 6.5 and 6.6 show the evolution of the interferometer measuring the distance between the Optical Bench and the test mass 1 (interferometer x_1) and the interferometer measuring the difference between both test masses (interferometer x_{12}), the latter being linearly dependent on the former.

As clearly seen in these panels, the phases of both interferometers can appear completely correlated as in Figure 6.5, which probably means that the interferometer being affected is x_1 and this dependence is being transmitted to the x_{12} interferometers. But they can also show different behaviours which may be difficult to correlate one with the other, as in Figure 6.6.

Also, a relevant property to be considered for data analysis purposes is the long time scale responses shown by the Optical Bench system. A marked decorrelation in time is clearly observed between the phase response and the temperature sensor located closest to the heat source — see for instance the 500 s peak delay between purple and black curve in Figure 6.6 (top).
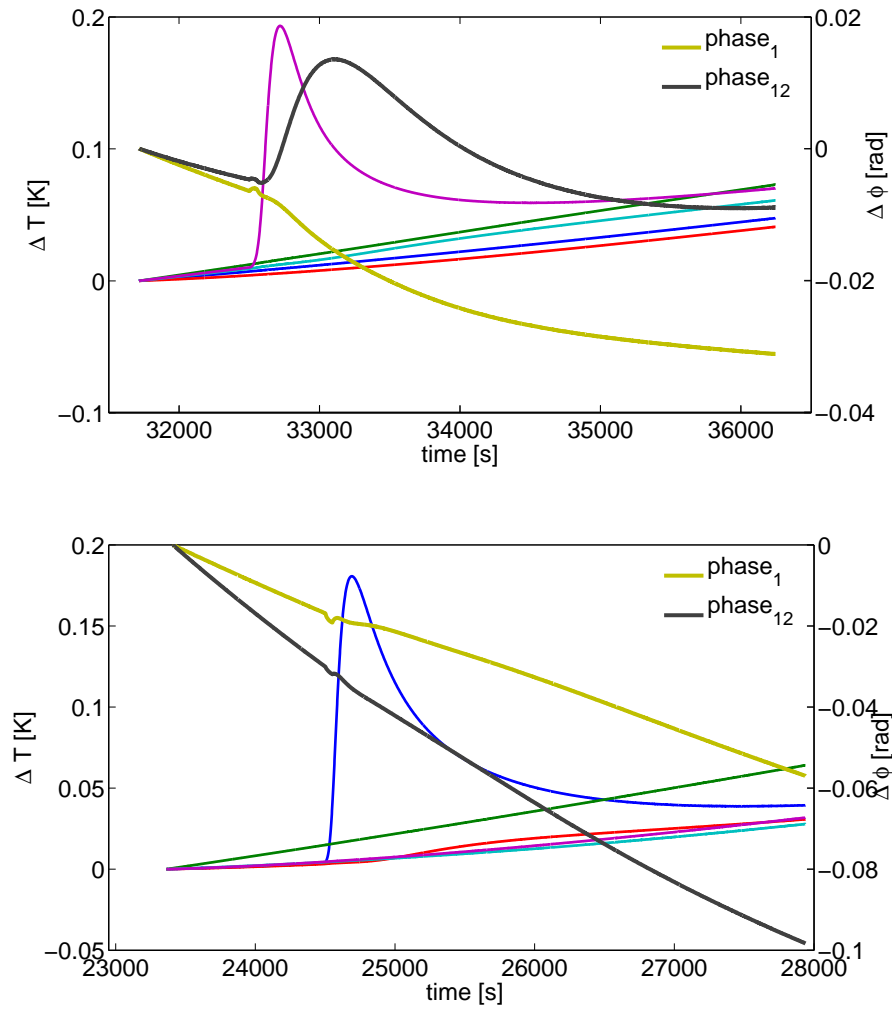
Figure 6.6: Optical Bench interferometric response to a 1 W heat pulses applied during 50 s on KS2 (top) and KS4 (bottom) case —see Figure 6.3. Responses of both interferometers x1 and x12 are labelled, the rest of curves correspond to temperature sensors distributed as in Figure 6.3. Only the sensor closest to the heater being activated (purple and blue line respectively) shows a clear response to the heat pulse, the rest of sensors show the usual linear trend.

Heater	Power [W]	Heating time [s]	Phase maximum [mrad]	ΔT	Peak delay [s]
	0.5	50	0.24	0.048	248.49
	1	50	0.30	0.092	208.12
KS1	2	50	3.03	0.176	275.04
	0.5	100	1.38	0.088	243.97
	0.5	200	2.31	0.167	166.36
	0.5	50	1.31	0.040	257.16
	1	50	1.47	0.083	255.68
KS2	2	50	3.23	0.159	256.64
	0.5	100	1.44	0.079	223.75
	0.5	200	2.00	0.152	145.53
	0.5	50	4.23	0.045	283.73
	1	50	11.25	0.094	283.8
KS4	2	50	20.31	0.180	281.42
	0.5	100	9.80	0.089	247.92
	0.5	200	17.40	0.168	173.36

Table 6.1: Optical Bench phase and interferometric response

The observed behaviour endorses the conclusion that the heat shock is affecting the Optical Bench in a different region from the one being monitored by the sensor and thus, if the interactions is to be modeled, long timescale correlations between the temperature and the laser beam through the Zerodur must be considered.

The correct characterisation of the OB interferometer output in terms of temperatures gradients generated along the bench requires a detailed data modelling able to extract the physical relevant parameters from the data delivered by the experiment. Some methodologies for this purpose will be treated in Chapter 8.

A first order of magnitude estimation of the impact on the interferometric output can only be derived by a peak comparison of both temperature and phase evolution, taking into account the temperature of the sensor closest to the heater being used. Table 6.1 gathers these values for different heating profiles. A time delay between phase and temperature peak is also added to emphasise the fact that both peak values are decorrelated and thus the rad/K factor obtained by means of the ratio between both parameters can not be directly associated with a physical mechanism but must be considered, we recall, a first estimate of the thermal sensitivity of the Bench.

From the previous table a different thermal sensitivity can be observed at different locations on the OB, when applying heat pulses the temperature peaks remain on the same range for each heater but the phase response shows significant variations. Differences between each location are stressed when comparing the statistical mean of the data in Table 6.1. The heater located in the diagonally opposite corner with respect the fiber injectors — KS4 in the notation displayed in Figure 6.3, shows an enhanced influence on the interferometer. These differences are summarised

Heater	Coupling factor [mrad/K]	Thermal response [K/W s]
KS1	10 ± 6	1.7 ± 0.2
KS2	20 ± 7	1.6 ± 0.5
KS4	100 ± 10	1.8 ± 0.7

Table 6.2: Optical Bench thermal coupling factors.

in Table 6.2.

The different coupling coefficient must not be related to differences in temperature increase as registered by the sensors since, as seen in Table 6.1, sensors in different locations on the Bench response equally to a heat pulse of identical characteristics. The cause of the discrepancies must be rather found in the particular geometry conformed by the optical elements distributed through the Bench. If, for instance, thermal dilatation is considered to be the only effect responsible of the behaviour observed, a unique parameter would be driving the effect, this should be the CTE ($\alpha \simeq 0.1 \cdot 10^{-6}\,\mathrm{K}^{-1}$ for the Zerodur) and thus values in Table 6.2 would mean that we are observing the same effect taking place at different distances with respect the temperature sensor registering the temperature evolution. In order to translate this interaction via the Zerodur's CTE to a coupling factor we can rearrange the equation of thermal dilatation in the following manner,

$$\frac{\Delta L}{\Delta T} = \left(\frac{2\pi}{1064 \times 10^{-7}\,\mathrm{cm}} \right) \alpha \cdot L = 0.006 \left[\frac{L}{1\,\mathrm{cm}} \right] \mathrm{mrad/K} \qquad (6.4)$$

In this order of magnitude estimation, Table 6.2 could be understood as the effect of thermal dilatation at different lengths. However, our assumption has been to consider that the effect is uniquely determined by the thermal dilatation of the bench between two fixed points. It might also be the case that the effect is the sum of different dilatation effects between various points or even that other effects than the thermal dilatation applies. For these reasons, our estimation in equation (6.4) must be considered merely a rule of thumb description of the effect.

Another point that shall be stressed from the current available results is that only the closest sensor to the heater is able to sense the heat shock. This evidence, that is basically showing the low thermal conductivity of the Zerodur, implies that temperature sensors on the Bench will hardly map the temperature around its location. This is not case, for instance, for the Electrode Housing sensors which rapidly sense temperature disturbance at other points of the housing given the high conductivity of the structure. Figure 6.5 and 6.6 show this property plotting all the sensors used in the setup, the initial value of each curve is subtracted from all points to get a common origin.

Finally, a few words can be added about a small effect detected during the experiments. As shown in Figure 6.7, the phase shows a fast bounce at the beginning of the heating sequence. This is not related to a temperature effect as sensed by the temperature sensors since the closest sensor to the heater does not show a similar behaviour, it is just starting to feel the effect of the heat shock when the phase appears to bounce up and down. However, this small effect is directly proportional in time to the pulse heat applied —Figure 6.7, see zoomed plot. This dependence seems to point out a possible relation with thermal radiation
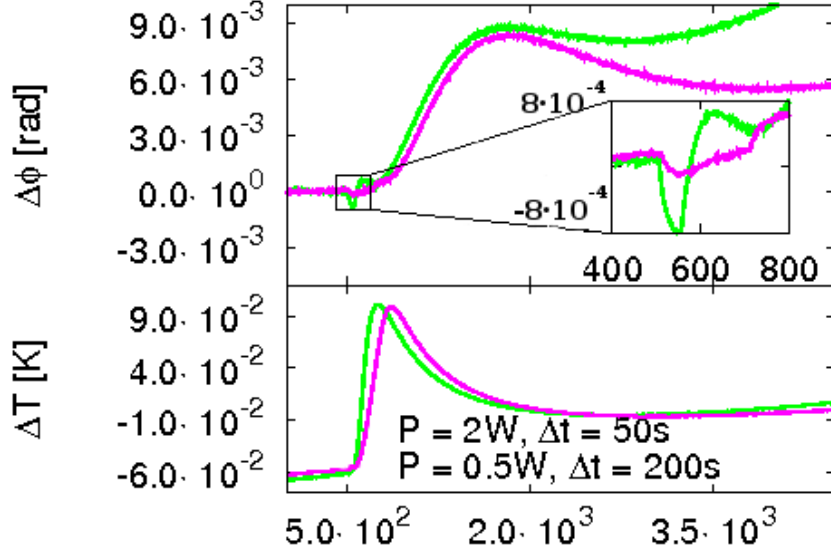
Figure 6.7: Optical Bench interferometric response to heat pulses. *Top:* Phase response. *Bottom:* Temperature as measured by the closest sensor to the location where heat is applied.

Even though the heaters were covered to prevent these effects, the Aluminium tape used must be only considered a first protective layer since this will also radiate once it is heated. The main problem raised by the thermal radiation is to find which optical element, responsible for the phase bouncing mechanism, is being heated. In our setup, the most probable candidate seems to be the mirror acting as dummy test mass in the Engineering Model. This is directly facing the heaters since the latter are attached to the Optical Bench lateral side. An order of magnitude estimation of the temperature gradient required for this effect to be undertook on the mirror could help us to discern the reliability of this effect to explain the phase bouncing. Substituting approximate values of the mirror on the Engineering Model ($\alpha \simeq 5 \times 10^{-6}\,\mathrm{K}^{-1}$, $L \simeq 2\,\mathrm{cm}$ for the mirror width) and the phase shift observed in Figure 6.7 ($\Delta\phi \simeq 0.7\,\mathrm{mrad}$) in the thermal dilatation equation we can find

$$\Delta T = \frac{1064\,\mathrm{nm}}{2\pi}\frac{\Delta\phi}{\alpha \cdot L} \simeq 1.2\,\mathrm{mK} \tag{6.5}$$

The required thermal gradient is thus attainable based on the heat power applied $\sim 1\,\mathrm{W}$ and the considerably short distance between heater and mirror, of a few centimetres. Without probing our hypothesis, the result in equation 6.5 gives us some confidence on thermal radiation as an explanation of the observed bouncing effect.

We can not go further from the estimation in what respects the thermal radiation hypothesis for the phase effect of Figure 6.7. The confirmation would be good news for the LTP because it will directly rule out this noise source for the experiment since, in the final experiment, the role

115
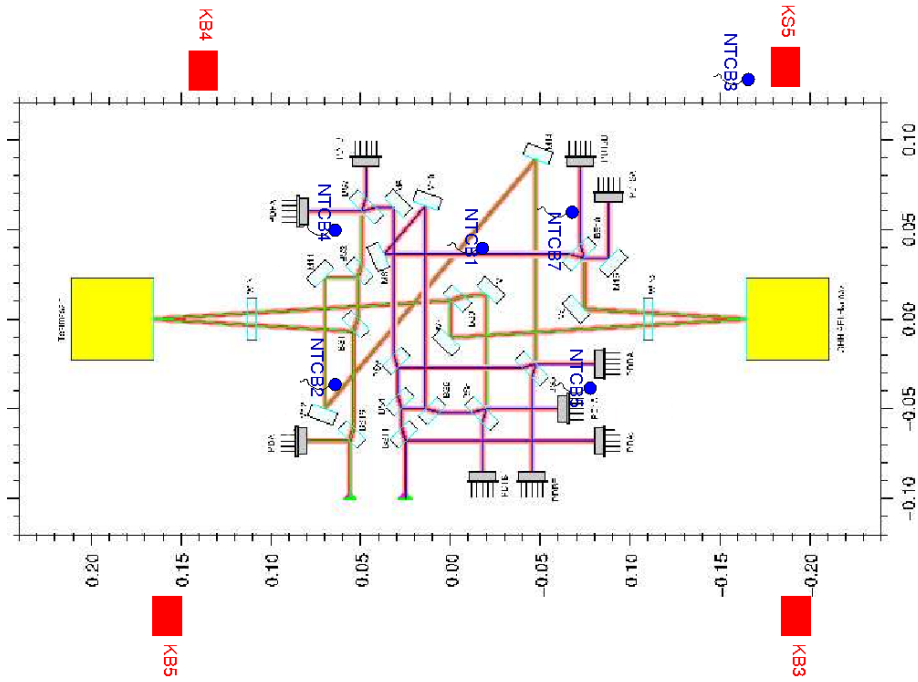
Figure 6.8: Flange test configuration. Red squares mark heater position and blue dots sensor position

played by the dummy mirror is carried out by the test mass inside the vacuum enclosure.

It could be argued that radiation coming from heaters attached to the Optical Bench will not be a problem because these heaters are not part of the final design, as explained before. However, this same effect is also present in experiments carried out at the Optical Bench flange, near the struts location where a set of heaters will be located. Even though experiments in the Bench may not be relevant for the mission, it can give some pieces of information to analyse experiments in other locations which will be part of the LTP diagnostic operations as is the case of the Optical Bench flange, discussed next.

6.2.2 Flange heating

The Optical Bench Engineering Model allowed various configurations of heaters and sensors distributed through it. We took advantage of this possibility to explore the effect of an induced thermal disturbance applied in the flange of the Optical Bench. These parts, four in total, will be the only conductive path thermally linking the LTP experiment with the thermal shield surrounding the LTP Core Assembly and, by extension, to the outer environment.

During the mission flight, the connection between the thermal shield enclosing the LCA and the flanges of the Optical Bench is done by means of the so called struts. These are CFRP cylinders subjecting the experiment to the inner walls of the thermal shield. In the current baseline there are eight of these subjections, although in the previous structural design six of these were planned
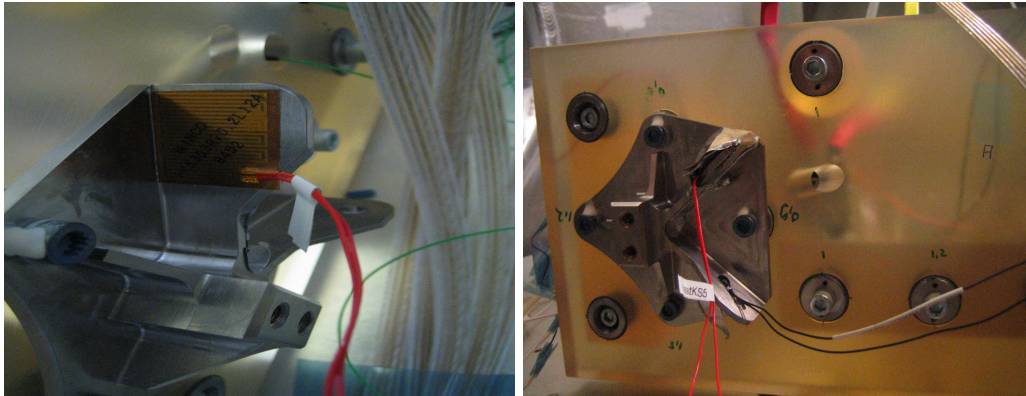
Figure 6.9: *Left:* Heaters attached to upper part on flange. *Right:* Heaters attached to upper part on flange (with red wires) covered with aluminium tape and sensor on the lower part of flange (black wires).

in order to generate an isostatic subjection. However, in the current design, it seems preferable a harder subjection system than an isostatic one though the later may introduce some undesired structural stresses.

The diagnostics subsystem provides six sensors and six heaters, according to the initial baseline. The principle of actuation being the same as the rest of locations where heaters are foreseen to be attached, i.e. to estimate a transfer function due to thermal effects by applying high Signal-to-Noise Ratio thermal pulses and also to monitor the thermal environment during science mode, when no controlled disturbance is applied and the instrument is working in the most stable environment that the spacecraft can provide.

As stated at the beginning of the section, the Optical Bench Engineering Model offered a unique opportunity to study possible effects of a thermal disturbance in the flange. It must be noticed, however, that the results obtained in this manner can not be directly translated to the LTP because of the fact that the heaters in the LTP will be located on the struts, not in the flange. The approach must be thus to use the Engineering Model to describe the phase response to a given heat pulse. The translation of the heat power applied on the flange to the equivalent heat power to be applied on the struts is a problem delimited within the framework of the LCA thermal model, described in Chapter 7.

A detail of the setup used during the experiment is shown in Figure 6.9. Kapton heaters were used in this location in the same way as in the Optical Bench setup, described in the last section. The only difference is that heaters used in the new experiment will be of greater resistance $(70.2\,\Omega)$, thus allowing the application of a greater power. To reduce possible thermal radiation effects, heaters were covered with Aluminium tape as shown in Figure 6.9, right panel. Temperature sensors were attached to the lower part of the flange.

Temperatures were monitored using the LTP temperature Front-End Electronics described in section §5.4. Sensors chosen were surface type NTC, both heaters and sensors were fixed by means

of PSA film. All measurements were performed at $P \simeq 10^{-3}$ mbar vacuum level.

Test results

As before, results can be split into temperature and phase responses to heat pulses. The former does not add any information different than the one that could be obtained with the thermal model. Table 6.3 gathers some of the values obtained during the experiments. In order to compute the temperature peak time (Δt), the initial time $t = 0$ is considered to be at the start of the heat pulse.

Power [W]	Heating time [s]	Temperature peak time [s]	ΔT [K]
1	50	565	0.12
1	100	582	0.24
2	100	571	0.32
2	200	634	0.62
2	500	832	1.49

Table 6.3: Thermal values obtained applying heat pulses to the flange.

In this case, the fact that the flange is a metallic piece turns into a faster response than when dealing with the Optical Bench, as seen in Figure 6.10. The steady state is not reach due to the short duration of the pulses but we can define the same parameter as in the Optical Bench case, equation (6.2), collecting the information in Table 6.3, which leads to

$$Q_{eq} = (1.9 \pm 0.4) \times 10^{-3} \, \mathrm{K \, W^{-1} \, s^{-1}} \tag{6.6}$$

From this number, a first conclusion can be stated. If compared with the same value characterising the Optical Bench, equation (6.3), it shows a very similar result with the one obtained in (6.6). Since both values refers to very different systems in what respects their thermal behaviour the similitude of both parameters needs to be associated with the setup conditions: whereas the sensors in the Optical Bench plate is near the heat application point — Figure 6.4, the flange setup experiment sensors were located in the lower flange part and the heaters in the upper part which turned out into a bad characterisation, even the high thermal conductivity of the itanium flange.

Table 6.3 summarises some results of different runs related to the thermal response of the Engineering Model flange when heat pulses were applied, to a better characterisation of the thermal response the maximum temperature increase time is also given. Here, we can not proceed in the same way as in the Optical Bench experiment. As seen in Figure 6.8, the setup provides us with only a temperature sensor in one flange, therefore we will take this characterisation as a pattern and we will assume that it is valid for the rest flanges.
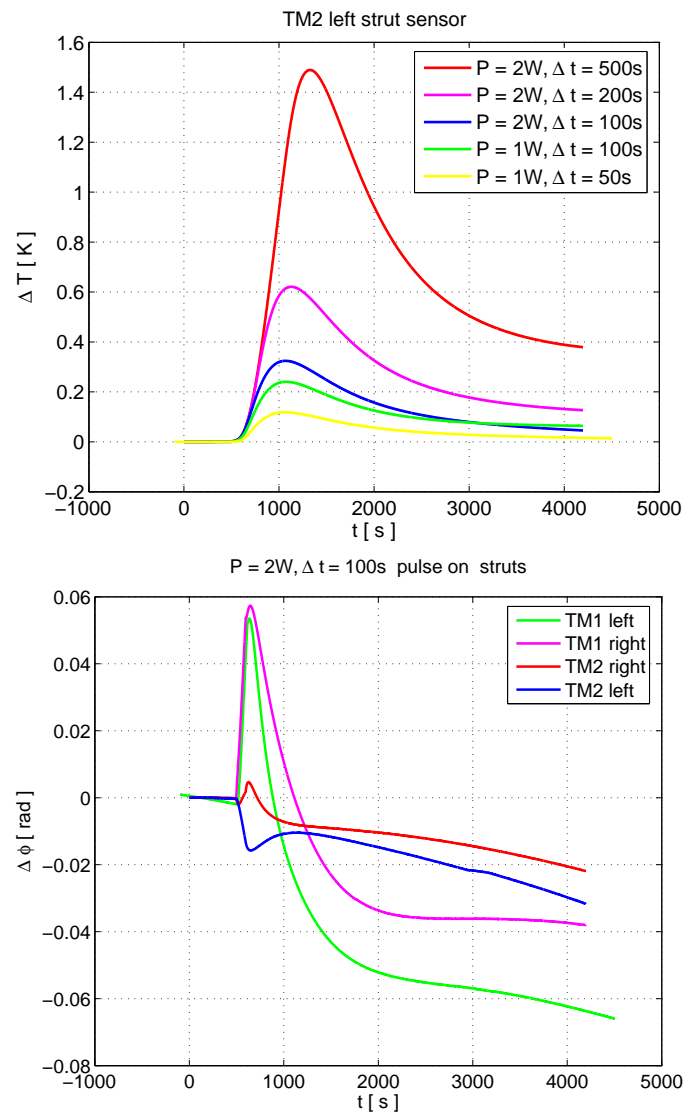
Figure 6.10: *Top:* Temperature increase in flanges when applying heat loads. *Bottom:* Phase response when heating in the four Engineering Model Flanges.

Heater	Power [W]	Heating time [s]	Phase maximum [mrad]
KS5	1	50	-3
	1	100	-12
	1	200	-11
	2	100	-11
	2	200	-27
	2	500	-57
KB4	2	100	59
	2	200	100
	2	500	114
KB5	1	50	25
	1	100	44
	1	250	98
	1	500	136
	2	100	58
	2	500	171
KB3	2	100	7

Table 6.4: Optical Bench phase and interferometric response.

The results of the phase response under the same experiments can be included in the similar reasoning considered in the last section but with some changes. For instance, a difference in the phase response is also observed depending on the heat source location, as when dealing with heat pulses on the Optical Bench. This suggests that we could identify the same physical process in both situations, i.e. if we were considering that the location-dependent responses in the Bench are due to the complex laser beam path, we could also consider this effect to happen in the current discussion. However, this can not be proved from our data and may be difficult to argue since temperature sensors distributed on the Bench do not sense the heat pulse.

Another piece of evidence of the underlying physics appears when comparing the features of the phase response for both cases: the Optical Bench and the flange. Whereas the former showed a small sharp fast response during the heat pulse and a smoothed delayed second response —see Figure 6.5 and 6.6, in the second case the response is a faster and sharper one but the main difference is that the phase is highly sensitive to the thermal shock. That is, for instance, the case in Figure 6.10 where heat pulses of 2 W are seen to induce a ~ 60 mrad response. In the Optical Bench a ~ 10 mrad was hardly achieved with a heat pulse of the same duration and power applied. This fact seems to rule out the possibility of explaining the effects of the phase response in both the Optical Bench and flanges under a unique physical mechanism.

In the same line of reasoning, if we first detected a small bounce during the heater activation time in the Optical Bench case, we observe now that the measured response of the laser happens exactly during this activations time. To stress the effect, in Figure 6.11 the phase increase is shown with the temperature increase and the heat applied in the strut, the correlation between the phase and the heat pulse is clearly displayed. In fact, phase appears to be correlated with the heat pulse
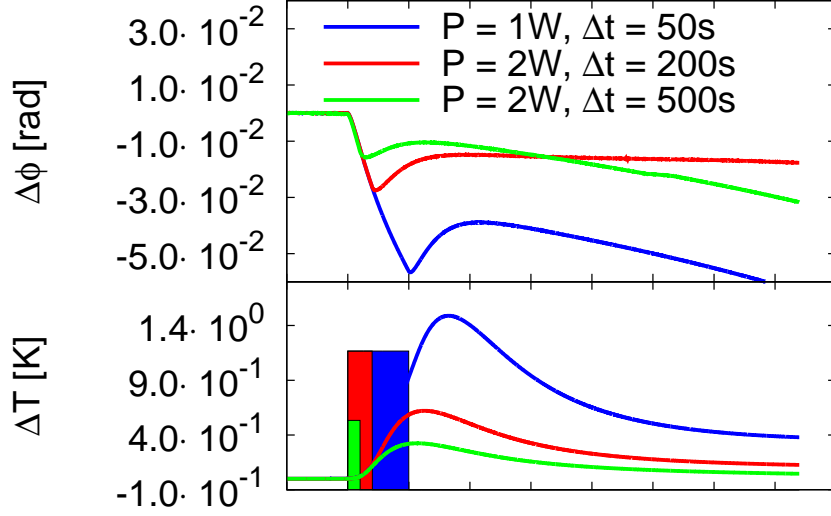
Figure 6.11: Interferometric response to heat pulses applied on KB3 location —see Figure 6.8.
Top: Interferometer output at different powers. *Bottom:* Temperature increase as measured by
the sensor in the Flange. Heat input is also displayed as coloured steps.

more than with the temperature response.

This high sensitivity response of the flanges to thermal shocks can be appreciated in Table 6.5.
It must be taken into account that, from the previous discussion on the Q_{th} parameter the rad/K
factor might be corrected because of the underestimation of the temperature increase. A correction
factor of ~ 20 (cf. §7.3) should be applied if we consider results in the LCA thermal model. This
factor smooths the problem but, on the basis of current data, struts still remain to be a possible
source of thermal induced noise.

Heater	Coupling factor [mrad/K]
KS5	-30 ± 10
KB4	110 ± 50
KB5	180 ± 60
KB3	21

Table 6.5: Flange coupling factor.

6.3 The Optical Window

The current baseline of LISA Pathfinder and LISA includes vacuum tanks containing the test
masses which act as end mirrors for the interferometer. Presence of such tanks, or vacuum enclo-
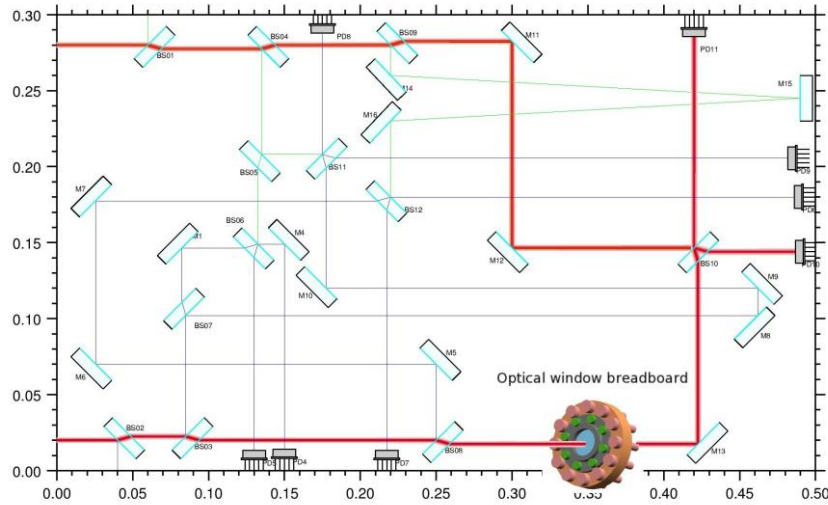
Figure 6.12: Schematic of the interferometric measurement concept.

sures (VE), force the inclusion of a transmissive element interfacing between the interior of the VE and the optical bench outside. This optical element is the Optical Window.

In the experiment two different prototype OWs were tested. Both were manufactured following the same baseline as the one to be applied in the final LTP flight model. The main element of the window is a very low thermal expansion coefficient glass, chosen in order to minimise thermal related losses and fluctuations. The glass used is the *OHARA S-PHM52* and is clamped between two titanium rings, fastened by means of titanium bolts. Two Helicoflex sealings prevent gas leakage in space conditions.

The OW is expected to induce thermal related noise in the Metrology subsystem. In order to quantify its contribution to the total noise budget a set of thermal diagnostics items were attached to the Optical Window prototypes. They are shown in Figure 6.13, left panel: two Kapton heaters attached to the titanium flange lateral surface, and four glass encapsulated thermistors attached in pairs to the titanium flange and on the athermal glass surface, for precision temperature measurements. These diagnostics items were all glued to their attachment points with Pressure Sensitive Adhesive (PSA) tape, of similar characteristics to the one to be used in flight. The temperature sensors on the glass will actually not fly with the LTP. They will however provide relevant information to implement real mission data analysis procedures and methods, for which only the titanium temperature data will be available.

During the experiment, the window was leaning vertically on a PVC two-rail structure —see Figure 6.13, right panel—, which impeded any high conductivity thermal contact with the rest of the hardware. Although not directly affecting the thermo-optical interaction studied here, the OW will be part of the VE in the real LTP, thus a higher thermal conductance is to be expected, and therefore a faster suppression of thermal gradients is foreseen during mission operations.
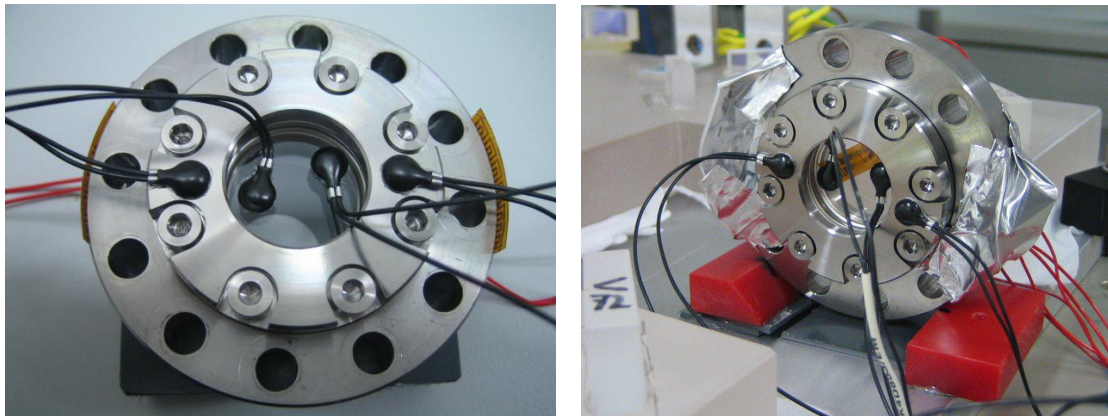
Figure 6.13: The OW (left), with the plane-parallel plate inside the titanium flange, heaters on the lateral surface of the latter (pale brown foils) and two pairs of NTC temperature sensors (black beads with wires). On the right, mounting of the OW on rails for measurements. Note heaters are covered with aluminium foils: this is to prevent undesired heating of other components by heaters' emission of thermal radiation.

The complete set-up (i.e., the glass plus its mounting structure and the just mentioned diagnostics items) was inserted as a transmissive element in a dedicated optical bench, as seen in Figure 6.12. The heaters were covered with aluminium foil to reduce thermal radiation effects (Figure 6.13, right). For the same reason, the window was introduced in a copper box leaving only a narrow opening for the laser beam to go through. As seen in the schematic of Figure 6.12, the beam traverses the OW only once. This will not be the case in the real LTP, where the laser will go twice through each window, instead, but the one passage configuration used here simplifies the OW thermal characterisation without information losses. All the experiments were performed under low pressure conditions at a $P \simeq 10^{-3}$ Pa vacuum level.

The Optical Window was subject to various heat pulses comprising a wide range of duration length and powers in order to calibrate the required power for the thermal test to be performed in-flight. The data here reported gather 25 experiment runs on two different prototypes, applying heat pulses from 100 mW to 2 W ranging from 10 s to 100 s of application time. All experiments were performed at room temperature, which falls within the expected range of working temperatures of the LTP experiment during operations, required to be between 10 ^{o}C and 30 ^{o}C. Figure 6.14 shows a typical response data plot, with indication of the temperature sensor readings and the interferometrically registered phase shifts corresponding to a specific heat signal input —see the figure caption for the details.

Two different data acquisition systems were used in the experiment: the interferometric data were acquired via the LTP phasemeter prototype [38], whereas the thermal diagnostics data were acquired using the LTP FEE prototype [56, 79]. Both acquisition systems had previously successfully passed tests of compliance with mission noise budgets.
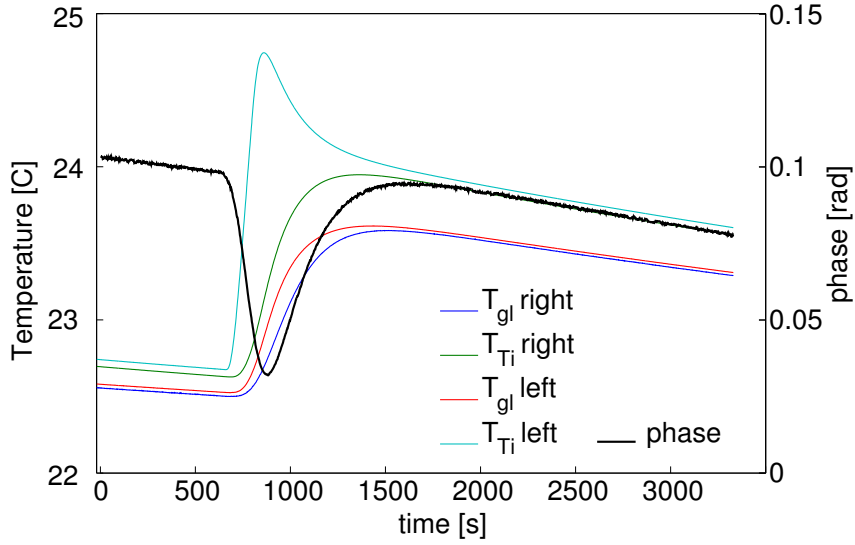
Figure 6.14: Phase (black curve) and various temperature sensors' responses (coloured curves) to a 2 Watt heat pulse applied during 100 seconds. Legend indications correspond to the thermometers shown in Figure 6.13.

Test results

Plot in Figure 6.14 shows a typical response of the interferometer when a heat pulse is applied to the Optical Window. The setup allows the characterisation of the window using data from four different temperature sensors. This time, all of them show the imprint of the heat shock.

Contrary to some effects we have found in other locations, the response here observed clearly relates to the temperature as registered in the sensors distributed through the window and among the different sensors, specifically to the one close to the heater being switched on. Naturally, this should be our first guess if we restrict our criterion to the correlation of peak values of the phase with the peak values registered by the temperature sensors.

Following the same scheme applied in the rest of heaters locations, we provide in Table 6.6 a sample of the results obtained during the experiments. The degree of freedom that our setup allowed to change was to heat the Optical Window from either of the two heaters attached at the laterals sides of the window or to switch both at a time. Results are then split in this way. As expected, both unilateral heating show a similar response and the one using both heaters roughly showed a doubled response with respect the first case.

Both parameters describing the thermal response —we have previously defined it as Q_{th}— and the coupling between temperature and the phase — the rad/K factor— can be computed here as well. Table 6.7 gathers the statistical mean of the collected values.

In what respects the thermal response, the one obtained from the Optical Window is approximately one order of magnitude greater than the obtained in other locations, reflecting the fast response and the good thermal link between the heater and the sensor on the titanium ring. This

Heater	Power [W]	Heating time [s]	Phase maximum [rad]	ΔT_{Ti} [K]
H.left	2	10	-0.007	0.218
	2	50	-0.033	1.074
	2	100	-0.064	2.090
	1	10	-0.004	0.110
	1	50	-0.018	0.539
	1	100	-0.034	1.045
H.right	2	10	-0.007	0.218
	2	50	-0.035	1.070
	2	100	-0.066	2.090
	1	10	-0.005	0.114
	1	50	-0.019	0.553
	1	100	-0.035	1.074
H.left+H.right	1+1	10	-0.008	0.156
	1+1	50	-0.036	0.730
	1+1	100	-0.067	1.450
	0.1+0.1	1000	-0.016	0.584
	0.5+0.5	10	-0.005	0.066
	0.5+0.5	50	-0.018	0.325
	0.5+0.5	100	-0.034	0.655
	0.05+0.05	1000	-0.015	0.696

Table 6.6: Thermal and optical response for different heating pulses on the Optical Window.

value, though a good setup characterisation, can hardly be extrapolated to the final flight experiment. As described in the last section, the Optical Window prototypes were standing on top of two PVC rails and therefore thermal conductivity links of the Optical Window to the environment were highly suppressed. The opposite situation will indeed happen onboard the satellite. Being the Optical Window a part of the vacuum enclosure, it will be clamped to the titanium components and thus any thermal gradient will be rapidly propagated and therefore suppressed.

Regarding the rad/K coupling factor, the thermal load applied on the Window is likely to produce two kind of pathlength variations: those induced by purely thermal effects and those related to stress effects. Among the first ones, we will need to consider, for instance, the change of the refraction index with temperature and the pathlength increase due to the glass thermal expansion. On the stress side, forces acting on the glass are able to induce pathlength variations due to various effects which are hard to model and even more difficult to understand since they will always appear disguised by thermal effects. The only parameter provided by the manufacturer quantifying the interaction between stress and pathlength interaction is the photoelastic coefficient β. However, it must be noticed that β does not describe the change in the refraction index due to stress, $dn/d\sigma$, but the appearance of birefringence due to stress, that is the change of the propagation velocity of light in the different axes of the material. Although not being directly related, both parameters range in the same order of magnitude [57] and the latter is usually used

Heater	Coupling factor [rad/K]	Thermal response [K/W·s]
H.left	$(-32 \pm 2) \times 10^{-3}$	$(10.7 \pm 0.2) \times 10^{-3}$
H.right	$(-34 \pm 5) \times 10^{-3}$	$(10.7 \pm 0.3) \times 10^{-3}$
H.left + H.right	$(-47 \pm 16) \times 10^{-3}$	$(13 \pm 3) \times 10^{-3}$

Table 6.7: Thermal and optical response statistical mean.

for order of magnitude estimations of this effect.

A thorough analysis of the Window has been undertaken in the framework of the Data Analysis methodology to be applied to the LTP Diagnostics Data. As a result of these studies, which took the Optical Window as the central system under study, the modelling of the Window phase response to thermal disturbances has been developed and this process has led to a careful estimation of the previously announced effects taking into account all the involved physical parameters. This description is linked to the Data Analysis methodology and uses concepts developed in that framework, for instance differences of the coupling parameter with respect to frequency, that do not fit in the current phenomenological approach. The reader is referred to Chapter 8 for an estimation of these effects in a more rigorous context.

Chapter 7

Heaters sizing

In this chapter we will focus our attention on the thermal diagnostic elements that the LTP experiment will use during in flight operations to test and investigate thermal effects in different locations of the LCA.

We have already discussed in previous chapters the purpose of this thermal shocks and the reasons to choose the selected locations of the heaters, we will here leave these arguments apart and centre ourselves on the technical problem. We will need to address, in first place, the required power that these items must deliver to a given specific thermal sensitive place in order to produce a high enough response of either the OMS or the GRS, depending on the location. In fact, an even more relevant question to solve in terms of design purposes and the one driving the study herein developed is the question of the maximum power to be supplied by these heaters, which really sets a limiting criterion for the process of hardware selection.

Our starting point in doing so is the Top Level requirements [100] which set a required value for the thermal gradients to be established in these locations.

Location	Requirement
Optical Window	$10\,\text{mK}$
Inertial Sensors	$100\,\text{mK}$
Struts	$100\,\text{mK}$

Table 7.1: Top Level requirements for the controlled thermal disturbances induced by heaters in the LTP

These requirements are based on an estimation of the interaction between the locations in table 7.1 and the thermal gradient. These could be readily translated to power requirements by means of the thermal response parameter that we have been computing in Chapter 6 from experimental data.

However, our approach has been to base our criterion in the Signal-to-Noise ratio induced by the thermal signal in the interferometer data. The main advantage of using this criterion is that we

127

are considering the whole effect taking place due to thermal disturbance, and we do not need even to understand it in detail although this will be our final goal. On the other hand, if experimental data is not available we need to base our sizing computation in a model of the interaction where we must introduce the undergoing physics.

Both approaches will be applied in the following section. We will take advantage of the experiments on the Optical Bench and the Optical Window, performed in the AEI, to size the heaters in these locations. The case of the Inertial Sensor will need to be studied by means of simulations on the LCA thermal model.

Finally, with the heaters of each location being characterised we will be able to address their hardware implementation. A few words will be said about the hardware solution adopted in each case, as well as some problems detected when considering its interaction with the satellite, such as for instance gluing or magnetic cleanliness.

7.1 LTP thermal model

In the following chapter we will be referring to the LTP thermal model. Before entering those particular applications where thermal simulations are required, we will need to sketch the main properties and principles of work of our simulation tool. Although we might refer to it in the following as the LTP thermal model, the software we will be dealing with only models those items inside the thermal shield in the LTP, i.e. the scientific instrument, which is known as LCA [34].

7.1.1 Thermal simulation principles

Solving thermal problems in complex geometries requires the use of numerical techniques which enable the transformation of the continuous partial differential equation into a discrete problem that can be afforded by means of numerical techniques by nowadays computers. This discretising process is based on the so called *Lumped Parameter Method* —see § 3.1. This methodology has its conceptual origin in the electrical analogy of thermal problems in which temperature equates to voltage and heat flow to current flow.

Mathematically, the lumped parameter method can be seen as a means of deriving a first-order finite-difference approximation to the governing differential equation. The power of the method lies in replacing the spatial partial derivative of the PDE by a set of discrete *nodes* that will be used to compute finite differences. With this transformation the problem will be best suited to be solved numerically. The lumped parameter is thus appropriate to solve thermal problems in complex geometries, where other methods may be inappropriate.

We can state the general equation for a lumped parameter problem by applying heat balance to a given node i. If we suppose a network of n nodes $N_1, N_2, \cdots N_n$ where the temperature of the node N_i is T_i, its capacity C_i and contains an internal heat source Q_i, the heat balance can be expressed as

$$C_i \frac{dT_i}{dt} = \sum_{i \neq j} K_{ij} \left(T_j - T_i\right) + \sum_{i \neq j} R_{ij}(T_j^4 - T_i^4) + Q_i \qquad (7.1)$$

where K_{ij} is the linear conductance between nodes i and j (which may represent conduction, convection or other process commonly considered as linear, like evaporation or condensation) and R_{ij} is the radiative exchange constant. Equation (7.1) reduces to

$$0 = \sum_{i \neq j} K_{ij} \left(T_j - T_i\right) + \sum_{i \neq j} R_{ij}(T_j^4 - T_i^4) + Q_i \qquad (7.2)$$

in the steady state. This is therefore the system of equations to be solved by means of iteration methods [8] which differs depending on the definition of the problem as steady state or transient and also in stability and speed criterion.

7.1.2 Software implementation

The software used is the standard European Space Agency thermal analysis tool used to support the design and the verification of space thermal control systems: ESATAN (ESA Thermal Analysis Network tool) is a software package for the prediction of temperature distribution in engineering components and systems using the thermal network analysis technique. It enables the user to specify his problem in the thermal network quantities of nodes, conductances and material properties, together with the sequences of solutions required to obtain the steady-state or transient temperature distributions. It also has a batch edit facility which permits previously defined network models to be incorporated into a model and changes to be carried out if required.

ESATAN is written entirely in Fortran 77, the user is thus able to introduce Fortran routines in the code but the usual way to work in ESATAN is the Mortran language, a superset of Fortran, in which the main functions and definition statements are implemented. The structure of an ESATAN model is split into Data Blocks, containing the definition of the model, topology, parameters and properties; and the Operations Blocks which gather the information about the operations to be performed on the model defined in the Data Blocks during the solution.

The information about the thermal model in the Data Blocks consists mainly in the definition of *nodes* and *conductors*. The former contains all the properties relevant to the thermal problem needed to define a node entity, i.e. density, conductivity, capacity and volume among others, while the conductors establish the relation between two different entities, this can be due to conduction or to radiation, for instance. The information about the geometry of the problem is included in the conductors definition since the thermal resistance concept used in the thermal networks takes into account in its definition the geometry of the body (cf. § 3.1).

We can get a more deep understanding of ESATAN by describing the definition of its thermal conductances, providing specific definitions for the parameters K_{ij} and R_{ij} in equation (7.1). We will describe the definitions of linear conductors and radiation conductors. ESATAN however is able to define a third class of conductors used for fluid simulation where the temperature changes

are also driven by the mass displacement. These will not be reviewed here.

GL conductance   In the ESATAN nomenclature, conduction is parametrised by the GL conductors, which can also account for other linear couplings, e.g. convection. These conductors represent the rate of heat transfer Q_{ij} between nodes i and j at temperatures T_i and T_j

$$Q_{ij} = h\,(T_i - T_j) \tag{7.3}$$

where h is the GL conductance.

GR conductance   The radiative conductors represent the rate of heat transfer Q_{ij} between nodes i and j at temperatures T_i and T_j

$$Q_{ij} = \sigma\varepsilon_i\,\alpha_j\,A_i\,F_{ij}(T_i^4 - T_j^4) = \sigma\,h\,(T_i^4 - T_j^4) \tag{7.4}$$

where σ is the Stefan-Boltzmann constant, ε_i is the emissivity of node i, α_j is the absorptivity of node j, A_i is the area of node i and F_{ij} is the view factor from node i to node j. The value of the GR conductor is $h = \varepsilon_i\,\alpha_j\,A_i\,F_{ij}$.

It should be recognised that ESATAN does not derive network models from specified geometries: that task must be performed by the user. The role of ESATAN is to handle, check, and solve the network models that the user has devised to represent his problem. In current case, the geometry definition is developed by Carlo Gavazzi Space (CGS) with the Thermica[1] software. As an example, in Figure 7.1, some details of the model with those parts where thermal diagnostics elements modelled are displayed.

7.2   Inertial sensor

As commented in previous chapters, the thermal diagnostic subsystem on board the LTP foresees to introduce controlled thermal disturbances in the GRS subsystem. To this end, four heaters are planned to be attached to the electrode housing as schematically showed in Figure 7.3.

The role of the heaters in the electrode housing is to generate temperature gradients through the housing structure. As reviewed in Chapter 6, there exists a considerable amount of thermal effects that can perturb the test mass geodesic motion in these conditions. These effects will be directly related to the temperature gradient between opposite sides of the electrode housing and hence, in this case, a thermal modelling has been used to set the required power as well as to evaluate possible heating strategies.

It is important to note that in developing this study our conclusion will be based on the foot of two assumptions:

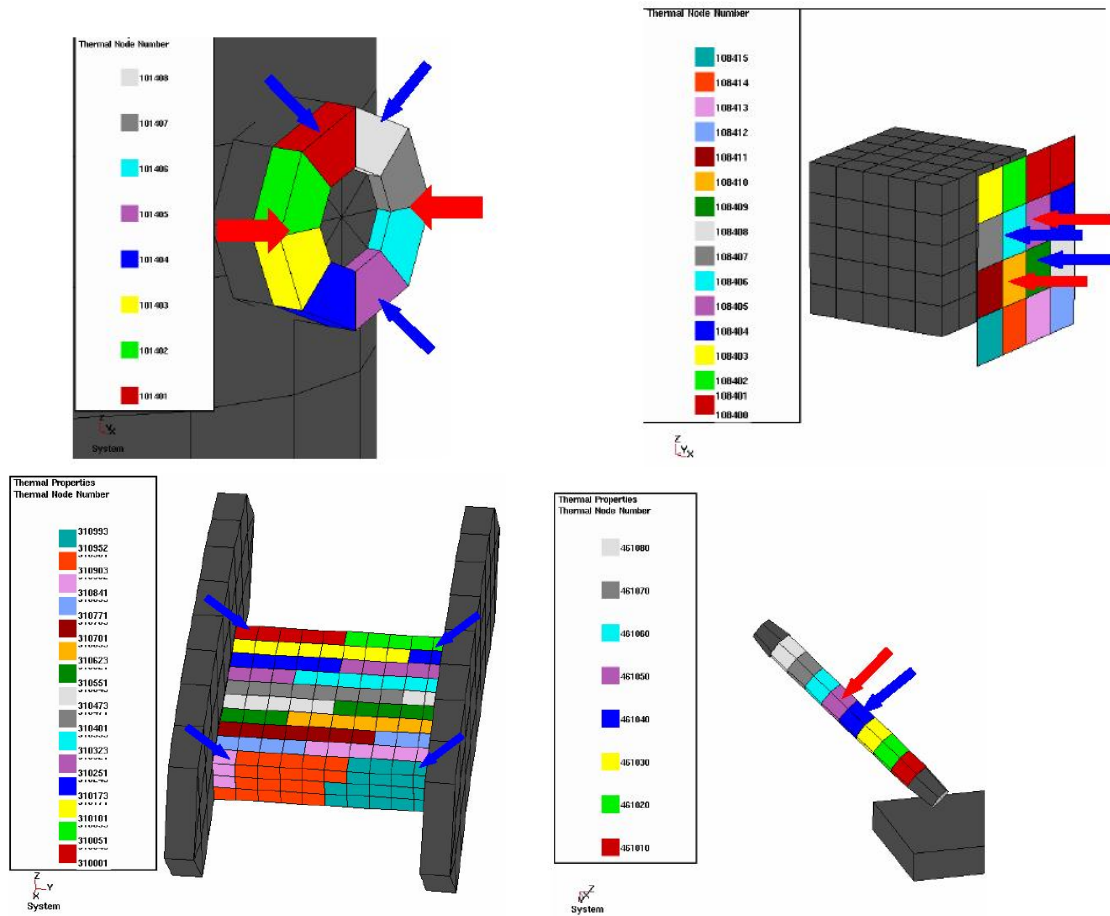[1]http://www.sinda.com/thermica_home.htm

Figure 7.1: Details of some of the locations of the LCA thermal model where thermal items are introduced in the model. From top to bottom, left to right: the Optical Window, the Electrode Housing, the Optical Bench and the Struts. Red arrows show locations were heaters are introduced in the model while blue arrows show temperature sensors locations in version 8.0.

131

- The LCA thermal model reproduces reliably the temperature behaviour through the housing

- Temperature gradients are translated into force on the test mass by means of feedthrough coefficients, related with various thermal effects.

Clear enough, any change in any of these features would rescale the numbers obtained below. In fact, this has been exactly the case for both of them. The precise measurement of the feedthrough coefficients are matter of current experimental research and will also be part of the experimental schedule of the LTP mission. Because of its relevance with respect the performance of the LISA mission there exist a considerable amount of literature dealing with the evaluation of these parameters, both from an analytical point of view [89, 94] or with an experimental approach [22, 21, 77], not always showing good agreement.

Regarding the second assumption in what we will base our study, i.e. the reliability of the thermal model, it may be helpful to give a brief historical description of the development of the thermal model with respect the thermal diagnostics modelling.

R_{ct} [K/W]	333.3
C $[J/kg/K]$	950
Heater mass [g]	1.0
Contact area $[\text{cm}^2]$	0.5^2
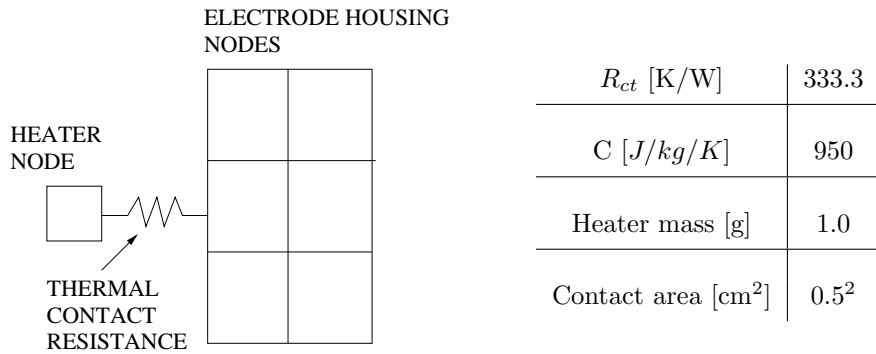
Figure 7.2: Heater modelling scheme with the parameters used in the simulation

The starting point is the version 6.0 of the LCA thermal model. Results in this version led to first results which seemed to point out a long transient response on the thermal gradient suppression [67]. However, these turned out to be related to the software modelling and in the version 6.1 the thermal gradients disappeared at long timescales, as first expected [33].

Moreover, since the thermal model did not include any of the thermal items it was necessary to introduce them in the model. The straightforward way to introduce thermal shocks was to heat preexisting nodes, however this was not suitable for our main interest since the thermal properties of the heater and its interaction with the attaching surface (the attaching area, the thermal contact resistance, etc.) played an important role in the heaters sizing. The solution adopted was to introduce independent thermal nodes acting as diagnostics items [68]. This way, a more realistic modelling was achieved since the heat source was linked to the electrode housing wall by means of a parameter including the information about the contact area and the thermal resistance contact between the heater and the surface —Figure 7.2 shows typical parameters used for the modelling.
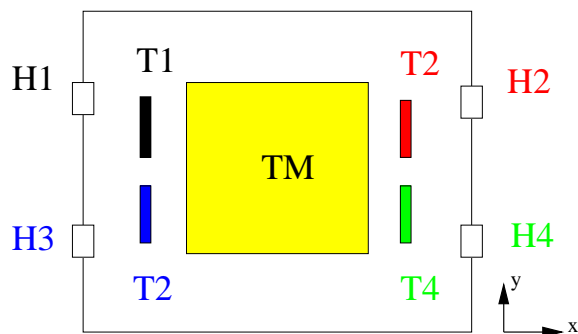
Figure 7.3: Scheme of diagnostics items on the electrode housing

This approach was finally included as a part of the thermal model in version 8.0 [34], the available one at the time of writing.

In order to fix the required power and pulse duration, as in the previous case, a SNR study can be performed. In general, a higher SNR is expected for higher powers and longer pulse duration (lower frequencies), however the lower limit of the MBW sets a maximum of 500s for the pulse duration. The reason being that, as explained before, a full period of the triangular signal comprises a sequential activation of heaters at both sides of the EH.

In conclusion, due to the dependence on the thermal model just described the methodology used to characterise the heaters on the Inertial Sensor has thus been necessary, as far as possible, model independent in order to incorporate each new model income in a flexible way. We will describe this methodology in the following sections.

7.2.1 Activation schemes

Thermal coupling between the test mass and the surrounding electrodes is tested by applying a train of heat pulses to those positions of the electrode housing previously defined. Given that the thermal coupling must be characterised in the MBW, a suitable activation period will lead to a periodic force applied on the test mass with the main frequency inside the MBW.

To take advantage of the four heaters and in order to optimise the power required to produce an observable, heaters are switched on in pairs. This choice allows two different configurations depending on the set of heaters switched on at any given time. We describe both in the following although only the first will be really of interest for the mission, the second one is considered since it allows a direct comparison with results with the torsion pendulum [22].

- **Activation scheme 1 (Net force)** if heaters on the same face of the electrode housing are switched on at the same time then a gradient between opposite faces of the electrode housing is generated.

- **Activation scheme 2 (Net torque)** alternate switching on of heaters placed diagonally opposite positions will produce a net torque on the test mass, observable by the GRS.
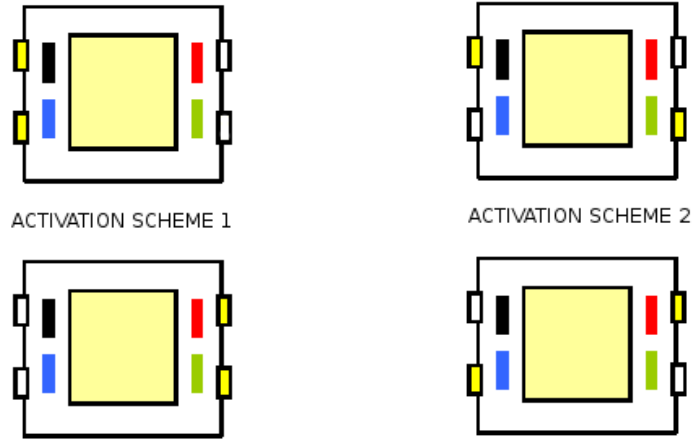
Figure 7.4: Electrode housing heaters activation schemes

The described activation scheme implies two heaters to be switched on at a time. To prevent from possible confusion each independent heater is called *physical heater*, whereas each pair of heaters switched on at a time are called *logical heater*, i.e, physical heaters H1 and H3 in Figure 7.3 are considered as a unique logical heater in activation scheme 1. When not specified otherwise, the term *heater* refers to a physical heater throughout this section.

When testing these activation schemes in the LCA thermal model, temperature evaluated on an electrode shows a constant slope increase during the time that the heater associated with its electrode, e.g. electrode T1 with heater H1 in Figure 7.3, is switched on. An important feature of this response is that the slope of the temperature increase appears to be linear with respect the power applied. This property will be used below when defining the *heater efficiency*, we shall for the moment stick to the linear trend that the heater action induces on the electrode temperature, regardless of its relation to the power applied.

Since the thermal effects are mainly dependent on the ΔT variable, we will take it as the figure of merit characterising our heating scheme. Either computed as $\Delta T = T_1 - T_2$ or as $\Delta T = T_3 - T_4$, the final result will be the same in Activation scheme 1 given the symmetry of this heating procedure. Based on previous studies [67], our choice was to use $\Delta T_l = (T_1 + T_3) - (T_2 + T_4)$ since this parametrisation contains the whole information about the full set of heaters.

Moreover, defined in this way, ΔT_l is proportional to the longitudinal displacement of the test mass due to thermal effects. For instance, if computed with the *Activation scheme 2*, ΔT_l vanishes. We would have therefore to use a different parametrisation to characterise the torque applied to the test mass under this heating scheme. This will be given by $\Delta T_t = (T_1 + T_4) - (T_2 + T_3)$, directly proportional to torque forces as can be easily recognised in Figure 7.3

It must be noted, however, that the discussed heating schemes and the data analysis described below are not intended to set a diagnostic analysis procedure. The scope is, on the contrary, more focused in the design of an efficient diagnostic subsystem. Diagnostic analysis requires more
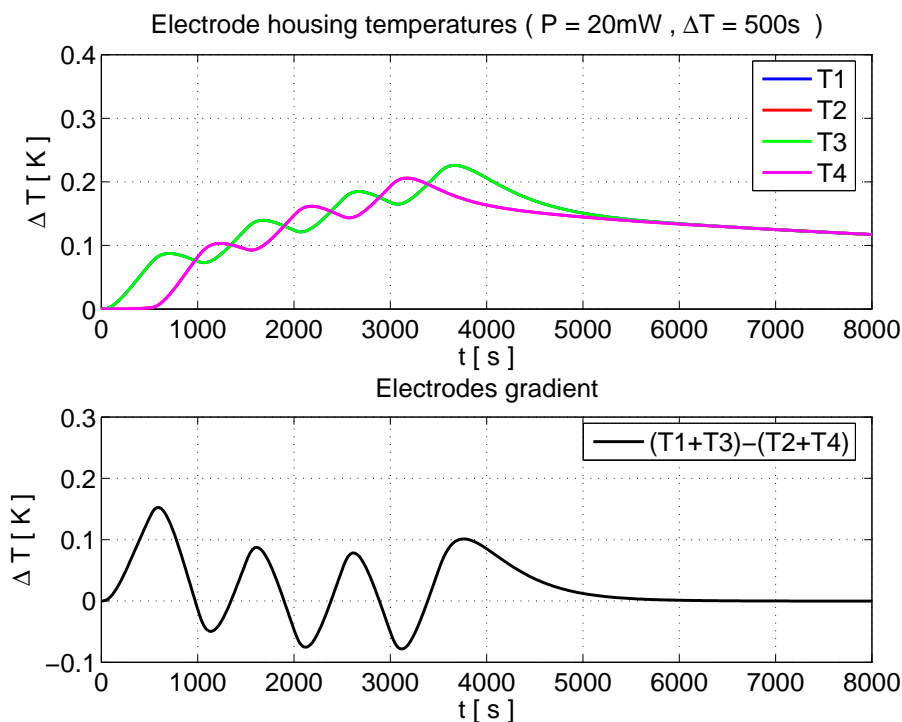
Figure 7.5: Top: Electrodes temperature for a complete heaters cycle. Bottom: Difference between opposite electrodes. Labels follow schema on Figure 7.3

complex considerations about data, such as those included in Chapter 8.

7.2.2 Analytical approach: triangular signal

Let's now turn to the ΔT_l signal defined above. The LCA thermal model allows us to compute this value from the thermal nodes describing the electrodes on the GRS. According to results displayed in Figure 7.5, the subtraction just described in the previous section leads to a nearly triangular signal. The temperature rippling on the electrodes due to heaters alternation is accentuated when subtracting temperature on both sides, leading to a clearer signal.

In order to reach a flexible methodology we will take advantage of this particular feature of the thermal signal in the Inertial Sensor. If we assume our signal to be a triangular signal, we can switch to an analytical approach and build a table of SNR values. Making use of an analytical description we are able to parametrise the thermal signal in a set of values describing its frequency, amplitude and total duration. These parameters will be the unique link to the thermal model or the feedthrough coefficients variation. This way, any change in any of those will be easily introduced in the computation to obtain an updated SNR table.

The signal describing the forced impinged on the test mass, $\Delta T_l(t)$ is described, in this framework, by a sum of triangular shape signals

135
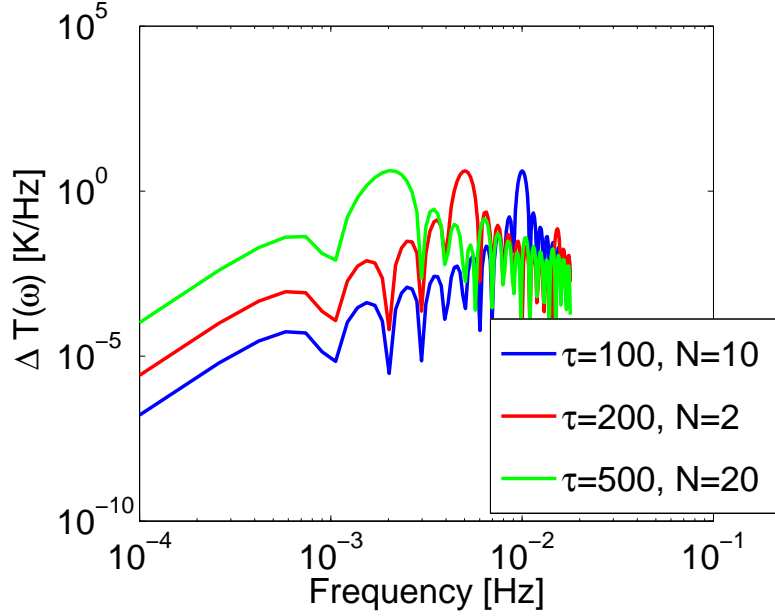
Figure 7.6: Thermal signal in the frequency domain as computed with equation (7.6). The amplitude of the signal is fixed at $A = 10 \, \mathrm{mK}$.

$$\Delta T_l(t) = \sum_{k=1}^{N} \Delta T_k(t) \tag{7.5a}$$

where

$$\Delta T_k(t) = \begin{cases} \frac{2A}{\tau} t + \left(\frac{3}{2} - 2\,k\right) A & (k-1)\,\tau < t < \left(k - \frac{1}{2}\right)\tau \\ -\frac{2A}{\tau} t + \left(2\,k - \frac{1}{2}\right) A & \left(k - \frac{1}{2}\right)\tau < t < k\,\tau \end{cases} \tag{7.5b}$$

where A and τ are peak-to-peak amplitude and the period of the signal, respectively. The Fourier transform for this signal can readily be obtained from the above expression

$$|\Delta \widetilde{T}(\omega)|^2 = \frac{A^2}{\tau^2 \omega^4} \sin^2\left(\frac{N\,\tau\,\omega}{2}\right) \left[\tau\,\omega - 4\tan\left(\frac{\tau\omega}{4}\right)\right]^2 \tag{7.6}$$

which will be useful for numerical integration. Figure 7.6 shows the signal in frequency domain considering different parameters. As graphically represented in this panel, if we fix the total integration time, low frequency signals have a broader spectrum and therefore a higher SNR when integrated.

A feature which can be easily incorporated into the description is a linear trend increase of the temperature gradient.

$$\Delta T(t) = \alpha\,t + \sum_{k=1}^{N} \Delta T_k(t) \tag{7.7}$$

This can show to be useful in thermal systems where large time constants can induce long transients in the temperature evolution. In such a case, if a constant gradient is established between both electrode housing sides, a net DC force would be applied upon the test mass and this clearly will be transformed into a higher power at low frequencies in the spectrum representation [67]. This must, however, not be the case for the GRS, since it is designed to efficiently smear out any temperature gradient.

7.2.3 Computing signal to noise ratio

In order to set the required power for the heaters we need a criterion to make our selection. The standard choice to size the input signal applied into a system is to take into account the effect produced on it by means of the induced signal. In the case under study, our input signal is the temperature increase, and the system response we are interested to provoke is the displacement of the test mass by means of thermal effects. We shall thus consider the force that we are producing on the test mass as the figure of merit to size the effect of the heaters.

To go ahead with this procedure requires to use the feedthrough coefficients related to the thermal effects described in Chapter 2. The most relevant turned out to be the radiation pressure, the radiometer effect and the outgassing coming from the electrode housing walls. Experiments have shown that the overall feedthrough coefficient is given by [21]

$$\frac{\Delta F}{\Delta T} = \frac{\Delta F_{e.m.}}{\Delta T} + \frac{\Delta F_{radio}}{\Delta T} + \frac{\Delta F_{outgas.}}{\Delta T} \approx 100\,\mathrm{pN/K} \tag{7.8}$$

where the force differences are from side to side of the test mass and ΔT is defined as the difference between the temperature of two opposite electrodes. Here we are following the opposite way than in the diagnostic analysis problem — for instance in Chapter 6 — since parameters in equation (7.8), or an equivalent description, are those we aim to determine via the diagnostics items. However, we are taking it as previously determined in order to evaluate the required power to test this thermal signals in-flight.

The above translates into a force signal

$$|\widetilde{F}(\omega)|^2 = (100\,\mathrm{pN/K})\,|\widetilde{T}(\omega)|^2 \tag{7.9}$$

We must now compare this signal to the background noise expected on the LTP, which can be evaluated by the requirement on acceleration noise, translated to force [100]

$$
\begin{aligned}
S_F(\omega) &= m_{TM}^2 \cdot S_a(\omega) \\
&= m_{TM}^2 \cdot \left[2.8 \times 10^{-14} \left[1 + \left(\frac{f}{3\,\mathrm{mHz}} \right)^2 \right] \right]^2 \mathrm{N^2/Hz}
\end{aligned}
\tag{7.10}
$$

This will allow us to evaluate the required power to achieve a given Signal-to-Noise ratio in the sensing signal. We recall here the expression

$$
(SNR)^2 = \int_{MBW} \frac{d\omega}{2\pi} \frac{|\Delta \widetilde{F}(\omega)|^2}{S_F(\omega)}
\tag{7.11}
$$

where $\Delta \widetilde{F}(\omega)$ contains the dependence in the power applied with the heaters, as previously seen. Hence, we will find the heaters power by requiring on expression (7.11) that SNR > 50.

Substituting equations (7.9) and (7.10) in equation (7.11) we can compute a grid of SNR values selecting plausible values for the amplitude of the signal applied and the expected integration time.

ΔT [mK]	$N \cdot \tau = 3000\,\mathrm{s}$			$N \cdot \tau = 6000\,\mathrm{s}$		
	$\tau = 100\,\mathrm{s}$	$\tau = 500\,\mathrm{s}$	$\tau = 1000\,\mathrm{s}$	$\tau = 100\,\mathrm{s}$	$\tau = 500\,\mathrm{s}$	$\tau = 1000\,\mathrm{s}$
1	0	7	4	0	8	6
5	1	28	26	4	39	37
10	7	56	52	9	78	74
20	13	113	104	17	156	145
40	26	223	206	37	314	291

Table 7.2: SNR for signals of different peak to peak amplitude (ΔT) and period (τ), $N \cdot \tau$ meaning the total integration time.

Values in Table 7.2 are expressed in terms of peak to peak value of the thermal gradient signal. The translation of these values in terms of heaters power depends on thermal modelling and it is mainly characterised by the heaters efficiency considered next.

7.2.4 Power to temperature efficiency

Once the criterion has been fixed and the table of possible values built, our next step needs to be the translation of the temperature increases into heater's power since this is our final control parameter. To this end, we will use a property previously sketched. As shown in §7.2.2, the action of the heater applied on the housing is a constant slope increase of the temperature in the electrode close to the heater being switched on. But even more relevant for our purpose is the fact that there exists a linear relation between the power and this contant slope, we have already used this relation from temperature to power in Chapter 6 where we called it the thermal response, Q.

Applied to the problem of the Inertial sensor, this parameter has a twofold importance. In first place, it allows the translation of the temperature gradients into heater's power and consequently

Power [mW]	Physical heater efficiency [μK/s]
5	74
20	302
40	604
100	1520

Table 7.3: Physical heater efficiency on the electrode housing

can be used to pass from an applied heater power to a SNR obtained as sensed by the GRS or the OMS. But, on the modelling side, this parameter tells us about the thermal model and can be used, following our methodology, to detect variations between different version of the LCA thermal model.

The thermal response is defined by means of the relationship between power applied and the temperature increase slope, which can be expressed as

$$\frac{\Delta T}{\Delta t} = Q\,P, \qquad [Q] = \frac{\text{K/s}}{\text{W}} = \text{K/J} \tag{7.12}$$

Q is the thermal response and clearly allows us to characterise the thermal response of the GRS regardless of the geometry. We will determine the Q parameter in the Inertial Sensor by means of thermal simulations varying the power applied to each of them. The following values for the temperature slope in the electrode close to the heater are obtained in the LCA thermal model, from which the Q factor can be derived, fitting these values with equation (7.12)

$$Q = 15 \times 10^{-3} \frac{\text{K}}{\text{s\,W}} \tag{7.13}$$

This value thermally characterises the interaction between the EH and the heaters. It depends on geometrical and material properties as well as the way EH heaters are modeled in the thermal model. Any change on these parameters will have an impact on this value and therefore in the relation SNR to heaters power. For instance, first results from the thermal model lead to an overestimation of the power required for the heaters due to a software related error [67]. The amendment of this error was easily carried out thanks to a direct comparison of the Q value using both models. Indeed, the correction of this value, which was of three orders of magnitude, was directly translated into a reduction in the same amount of the required power to be applied to the electrode housing, yielding the actual reported values.

In order to achieve a SNR of 50 when applying 500 s heat pulses, a 10 mK peak to peak gradient signal is required, see Table 7.2. Following equation (7.12), this gradient can be produced with 1.3 mW per heater. However, the maximum power required is established by fixing the same peak to peak gradient at higher frequencies, i.e., a 10 mK peak to peak gradient between electrodes with a 30s period will require, following (7.12), 22 mW per physical heater ($\sim$ 50 mW per logical heater). Although this value should be the one required to be the maximum power for the heaters in the Electrode Housing, the definition of this value was done with a different estimation of the feedthrough factor. In that case, the effect of outgassing was considered to be negligible
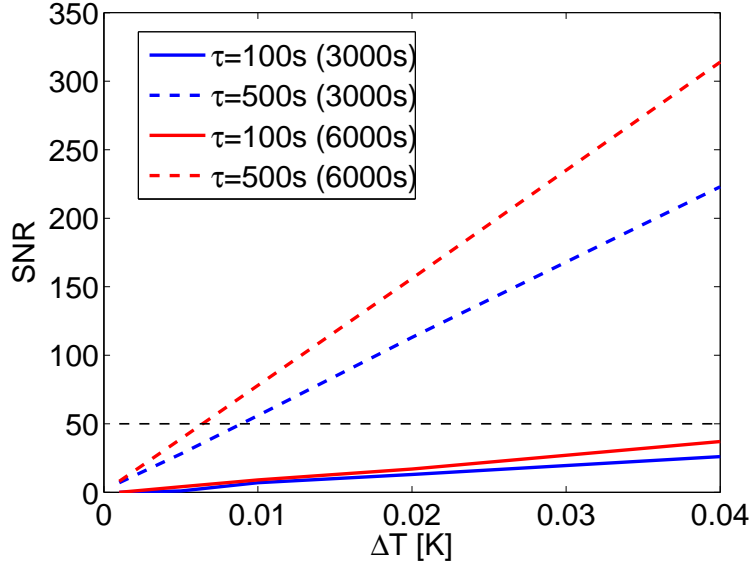
Figure 7.7: SNR curves. Dashed lines correspond to doubling the integration time. The black dashed line sets the required SNR to be reached with the induced thermal signal.

compared to the radiometer effect and the radiation pressure leading to a feedthrough factor $\Delta F/\Delta T \simeq 50\,\text{pN/K}$, roughly a half of the one now considered in equation (7.8). As a consequence a higher power was needed to get the same SNR thus resulting in the required $45\,\text{mW}$ per physical heater ($90\,\text{mW}$ per logical heater) appearing in the DDS industrial document specification [45].

This same relation but in terms of the temperature gradient between electrodes is shown in Figure 7.7. Given a temperature gradient —ΔT— and a duration of the pulse —Δt— fixed, the SNR is computed for two integration times: $3000\,\text{s}$ and $6000\,\text{s}$. From these results, it appears that with the chosen parameters a signal of $\Delta t = 100\,\text{s}$ does not fulfil the SNR $= 50$ requirement for any of the values of ΔT (meaning also heater power) displayed in the graph. The requirement is however reached for $\Delta T \simeq 8\,\text{mK}$ for the $\Delta t = 500\,\text{s}$ and an application time of $6000\,\text{s}$ or with $\Delta T \simeq 10\,\text{mK}$ if the total application time is set to $3000\,\text{s}$.

Power [mW]	SNR
0.13	9
0.65	39
1.3	78
2.6	156
5.2	315

Table 7.4: SNR in terms of physical heater power for $500\,\text{s}$ heater activation time and an integration time of $6000\,\text{s}$. The total power applied is $2 \times$ Power, being two heaters switched on each time.

7.2.5 Radiation view factor

The LCA model can also be used for other kinds of studies around the Inertial Sensor. We can use the thermal model not only to simulate thermal evolution of the thermal network if a heat input is applied, as we have been doing to this point, but we can also extract from the model relevant physical parameters.

Specifically, we can obtain from the thermal model an estimation of the radiation pressure to which the test mass will be subjected during the heating experiments. This is of particular interest since we can take advantage of the geometry and the information about the materials introduced in the model to evaluate the radiation that the enclosing environment will emit to the test mass. This contribution is what we have been referring to as the thermal radiation feedthrough coefficient and, to date, the best estimate sets a value for this specific contribution of [21]

$$\frac{\Delta F}{\Delta T}|_{rad} \simeq 9\,\mathrm{pN/K} \tag{7.14}$$

which corresponds to a nominal contribution of the effect considered to be of $\frac{\Delta F}{\Delta T}|_{rad} \simeq 27\,\mathrm{pN/K}$ which needs to be corrected by factors taking into account the geometry and material absorptivity, given by $\kappa_{RP} \simeq 0.32$.

The LCA thermal model is therefore a unique tool to evaluate thermal effects in the flight model. On the other hand, it must be noticed that we will be dealing with a modelling subject to eventual future changes. As commented above we shall focus on the methodology to extract this information that can be applied regardless of the modelling details and changes.

In order to evaluate the radiation pressure contribution we will take advantage of the GR conductors defined in the ESATAN LCA model. To review the meaning of these parameters, they are defined between two nodes i and j of a thermal network as

$$GR = \varepsilon_i\,\alpha_j\,A_i\,F_{ij} \tag{7.15}$$

where ε_i is the emissivity of node i, α_j is the absorptivity of node j, A_i is the area of node i and F_{ij} is the view factor from node i to node j. Nodes i and j need obviously to be radiatively linked in the model and, in such a case, the GR conductor gathers all the information regarding the geometry and the materials involved. These parameters can be internally computed by ESATAN once all the information regarding geometry and materials properties have been introduced.

Our approach to estimate the radiation pressure will be to evaluate the heat flux interchange between nodes on one of the surfaces of the test mass with respect each node facing this surface on the inner surface of the electrode housing, including the electrodes and the guard rings. For each couple of nodes we will compute the flux as

$$Q_{ij} = GR_{ij}\,\sigma\,(T_j^4 - T_i^4) \tag{7.16}$$
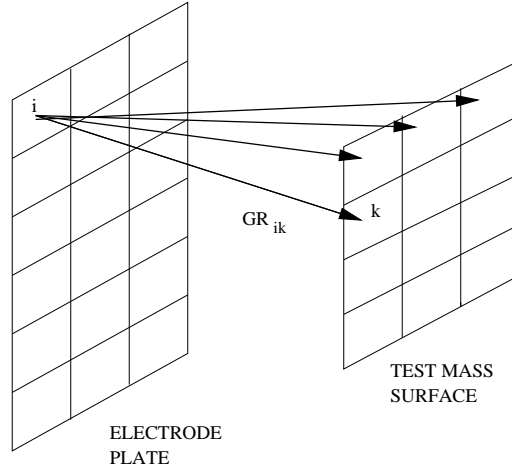
and from this value the pressure as

Figure 7.8: ESATAN LCA thermal model is used to compute radiative conductances from the electrode plates and the guard rings to the test mass surface facing them.

$$P_{ij} = \frac{4}{3}\frac{1}{c}Q_{ij} \qquad (7.17)$$

We can naturally proceed in the same manner for the opposite side of the test mass and then sum both terms contributing to the test mass motion. In doing so, we are evaluating thermal radiation in a differential way, i.e. considering temperature gradients across the surface of the Electrode Housing. Instead of applying a unique feedthrough factor we are taking into account the contributions from each node which do not only depend on geometric factors but also on the temperature of the node at each time.

The comparison of the results obtained following this methodology and the ones based on experimental results obtained in the torsion pendulum [21] leads to a discrepancy of roughly an order of magnitude which will imply that the effective feedthrough as derived by the thermal model would be $\frac{\Delta F}{\Delta T}|_{rad} \simeq 0.4\,\mathrm{pN/K}$, compared to the $\frac{\Delta F}{\Delta T}|_{rad} \simeq 9\,\mathrm{pN/K}$ measured in [21].

As stated above, several factors among the modelling issues could be responsible of this discrepancy. On the other hand, the experimental study leading to the result in equation (7.14) considers a geometrical correction factor that includes the effect of radiation coming from Y and Z walls and also the shear effect of photons impinging on the lateral sides. These effects, not considered in our study, could explain a few per cent of the discrepancy between both values. It is however unlikely that these lateral effects could explain the main discrepancy between both values.

7.3 Struts

The optical ench and the LTP experiment will be subject to the thermal shield enclosing them by means of eight CFRP struts. These are considered thermal sensitive elements among the experiment design since they are the only conductive link connecting the experiment with the

external environment. Any heat flux crossing them could produce thermal induced stresses or other effects that may degrade the experiment performance.

The diagnostics subsystem provides six heaters and six temperature sensors for this location in order to characterise and monitor any effect related with temperature fluctuations in the struts. We have previously seen in § 6.2.2 some experimental test that showed indeed certain dependence of the interferometer with respect thermal shocks applied, not in the struts which were not part of the Engineering Model being tested, but on the Optical Bench flanges. However, as discussed there, with the current available data we can not relate the observed effect with a determined physical effect and thus is rather difficult to translate these results to the final flight model. Furthermore, the most probable effect we were able to assign was thermal radiation and, if that was the case, those results will not be applicable in the flight experiment.

In these conditions we must stick to the most basic heater's requirement, which is established in [100] and has been quoted at the beginning of this chapter in Table 7.1, that is: heaters attached must be able to induce a heat shock of 100 mK as sensed by the closest sensor. This requirement is shown to be fulfilled with the current design in the top panel of Figure 7.9, where the thermal model is used to evaluate the effect of the heaters in the struts. Temperature increases an order of magnitude above the requirement are easily achieved with typical values for the heaters power.

Temperature gradients in the Optical Bench can be also computed from the thermal model, this can be of interest to evaluate possible thermal induced stresses in the Bench which could be detected by the interferometer. Bottom panel of Figure 7.9 refers to this issue and, as shown there, the expected effects are of few millikelvins from side to side of the Bench and the timescale of the thermal response is of ~ 7000 s.

In order to obtain these curves, a simulation without any heat input is first computed. We then subtract this *zero* contribution to the results of the simulations where heaters are switched on. This way, we are confident that the gradients observed are provoked by the heaters action and are not due to the effect of other sources like the photodiodes in the Bench, which are also modeled and represent a constant heat input.

We can take advantage of the thermal model to compare the temperature evolution curves obtained from simulations with the experimental results acquired in the Engineering Model. To this end, we need to induce a thermal shock not in the strut but on the Optical Bench flange and evaluate the temperature increase in this location. This is done in Figure 7.10 for two different heat pulses. A factor ~ 2 discrepancy is obtained between experimental and simulation results.

Finally, a last correction factor can also be studied with the model. If we assume the interferometric response observed in § 6.2.2 as a valid description for the flight model, we might be interested to connect the results obtained when heating the Optical Bench flange with those that the heat applied on the struts may produce. The only piece of information we need to know is how much is suppressed a thermal increase in the flange with respect the one on the struts if the heat input is applied in this last location. Figure 7.11 represents this situation and the rough value obtained for this temperature suppression is ~ 20, meaning that, according to the LCA model, a heat shock inducing a 1 K temperature increase in the strut will turn into a ~ 50 mK increase in
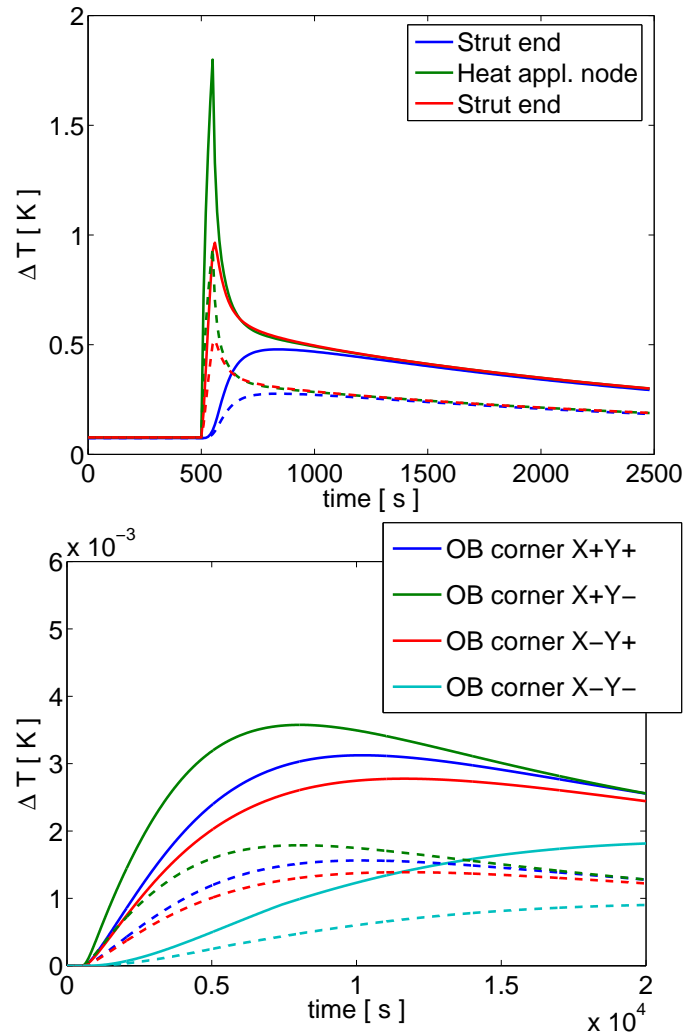
Figure 7.9: LCA thermal model simulation of the temperature increase due to heaters on the struts. *Top:* Temperature increase in the struts for a 50 s pulse of 2 W (solid lines) and 1 W (dashed lines). The two strut ends and the node where the heater is attached to are plotted to observe thermal gradients appearing in the struts. *Bottom:* Temperature increase in the four Optical Bench corners when heating a strut. Solid and dashed lines represents respectively a 50 s pulse of 2 W and 1 W, as before.

the flange. Naturally, this coefficient depends on the duration of the heat pulse, the value here reported corresponds to the range of heat pulses' duration around 50 s.

Even the strong suppression that such a value implies, the power assigned to heaters' struts has shown to be well above the requirements. Temperature increases as the ones observed in §6.2.2 could be obtained, according to these results, by means of heat shocks in the struts. However, we can not assure that the interferometric response will be the same that the ones obtained experimentally since, as explained above, we lack a reliable physical interpretation of the experimental
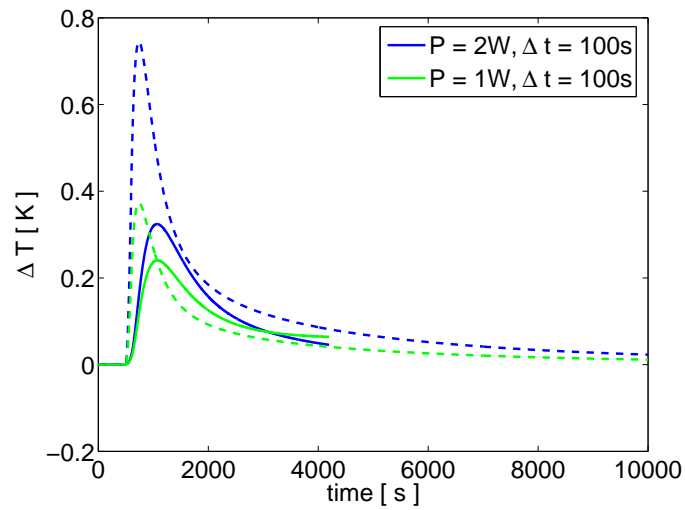
Figure 7.10: Comparison between experimental results (solid lines) and thermal simulations (dashed lines) when heating the Optical Bench flanges.
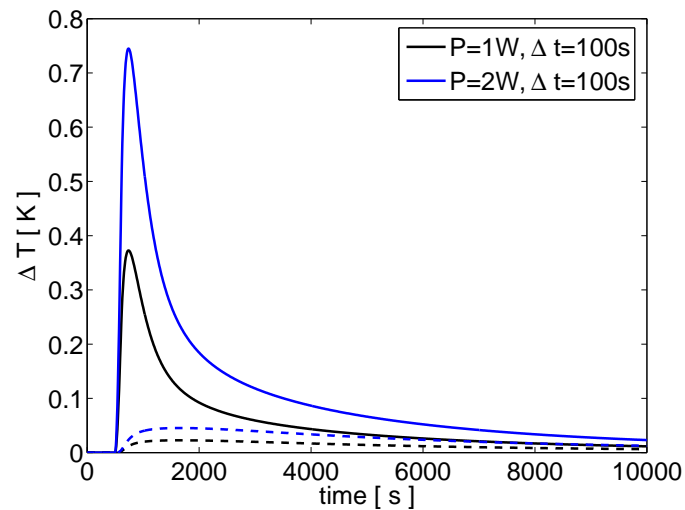
Figure 7.11: Comparison between temperature increase in the Optical Bench flange (dashed lines) and the struts (solid lines) when heating the latter.

results obtained.

7.4 Optical window

The Optical window is the optical interface between the inertial sensor inside the vacuum enclosure and the Optical Bench. Being the only non-bonded optical element fixed on a metallic structure, temperature fluctuations could produce a significant noise contribution to the interferometric read
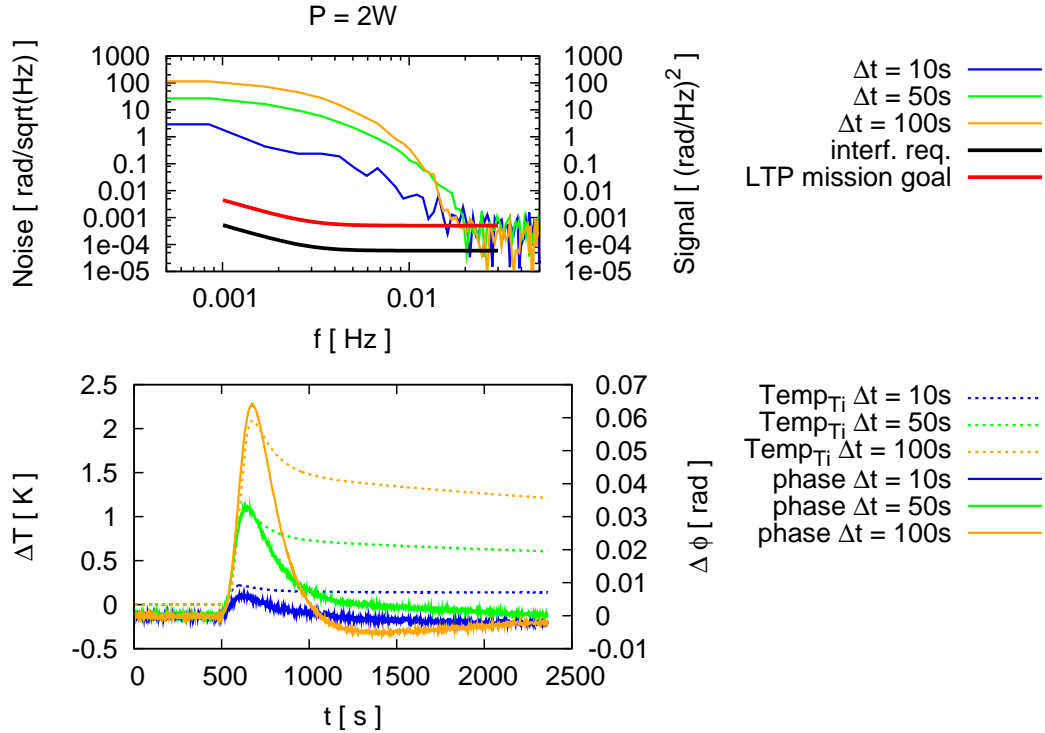
Figure 7.12: Top: Thermal signals FFTs compared to noise budgets. Bottom: Correlation between phase and temperature for different heating times

out, which needs to be identified for a subsequent removal.

For this reason a set of diagnostics items attached to this location are envisaged to be part of the LTP thermal diagnostics subsystem. This set consists of two heaters attached to the lateral sides and three sensors attached to the front side, facing the Optical Bench. More details on the thermal items distributions can be found in § 2.3.

In this case we can take advantage of the experimental results obtained at the laboratory, this save us having to use feedthrough coefficients as in the GRS case. Indeed, the effects we are here considering are those ones coupling temperature to phase variations, as reviewed in § 2.1.2.

The experiment setup, detailed in § 6.3, uses Optical Window prototypes manufactured by CGS using the same techniques to be used in the flight model. Two Kapton heaters are attached at both lateral sides of the window and four sensors are attached at the front side, two on the titanium ring and two in the glass surface. All items are symmetrically distributed on the window in order to perform the experiments in a redundant setup.

7.4.1 Signal-to-Noise ratio analysis

For the Optical Window heater's sizing problem we can recover the Signal-to-Noise ratio procedure in § 7.2.3. To evaluate the SNR we recover the expression (7.11) and also expression (7.10) remains

unchanged for the noise curve $S(\omega)$ of the instrument. However, we do not have, in the Optical Window case, an analytical representation of the signal provoked by the heaters as was the case for the GRS. Since now we are following an empirical approach, the SNR integral must be numerically evaluated using the interferometric signals obtained from the window as the input signal.

With this purpose, a systematic heating scheme was followed when dealing with the Optical Window prototype. This led to a wide set of data, good enough to enable the reconstruction of a SNR table as the one showed in the GRS case, Table 7.5.

The first step was necessarily to Fourier transform the interferometric data obtained when heating the window with different power step signals, and also with different duration lengths, as shown in Figure 7.12. Once both contributions, the one coming from the signal and the one arising from the noisy behaviour, are taken into account in equation (7.11) the SNR values are obtained for each case. Values in Table 7.5 are averaged over different runs and using different OW breadboards in order to give a full representative value.

P [W]	Pulse duration [s]		
	10	50	100
2	36 ± 5	140 ± 20	260 ± 30
1	23 ± 9	66 ± 2	123 ± 7
1+1	32 ± 8	122 ± 18	262 ± 50
0.5+0.5	17 ± 2	65 ± 1	121 ± 7

Table 7.5: SNR values averaged over different heating pulse profiles applied on the OW

The set of values obtained in this way are shown in Figure 7.13 as a function of the power applied. If the duration length of the thermal shocks remains fixed and the power applied is changed, the SNR values obtained seem to point to a linear relation between SNR and power, as shown in Figure 7.13. The established relation allows us to determine the SNR that will be obtained if any other power, in this limited range, is applied to the heater. SNR lines built in this way set our required power if one traces a horizontal line at SNR = 50. We have also extended the analysis to the error bars that appear due to the averaging we have previously done to different runs. They show the dispersion of our values which tend to increase at higher power values, probably due to the fact that in this region thermal effects are emphasised and different contributions could be mixed in the SNR computation. Analogously, we can extrapolate the SNR curves for longer applications times, this is shown in Figure 7.13 in purple.

From the analysis above, we can set an upper value for the required power to get a signal with SNR > 50. This condition can be reached with a $0.4\,\mathrm{W}$ signal lasting $100\,\mathrm{s}$. It is important to note that, as in the GRS case, periodic signal like a pulse train, could also be applied. Hence, the signal pulse just described must be considered the maximum required for the diagnostic purpose, provided that periodical application would lead to the same SNR but requiring less power.
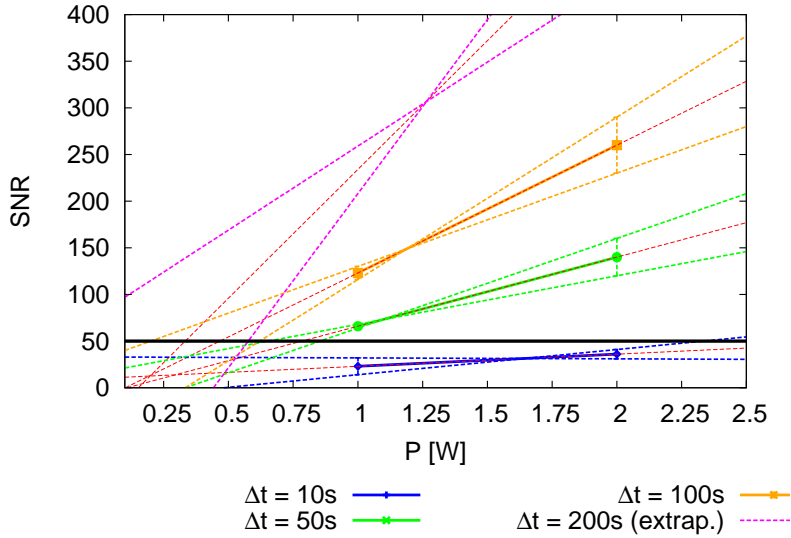
Figure 7.13: Optical SNR values for heat pulses applied on the OW. Red lines show the best fit to average values whereas coloured lines extrapolate the error bars.

7.4.2 Thermal modelling

Thermal modelling has in this case a double purpose. First, we must take into account the differences between the laboratory experiment realisation and the final LTP experiment on board the LTP. The main drawback of the results obtained on the laboratory experiment is that the Optical Window was there nearly thermally isolated, the only conductive contact being its PVC support, while the final window will be mounted in the titanium structure conforming the vacuum enclosure. Thermal simulations were performed in the LCA thermal model to obtain a comparison with the final design concept. An example of the results is shown in Figure 7.14.

A second test that the thermal model can help us to check is the possible effect of the heat pulse on the Optical Window on other sensitive locations. The higher powers that we are now considering are, by orders of magnitude, the heaviest thermal loads on the LCA and thus care must be taken for the thermal behaviour of a so highly stable environment as the LCA will be. Moreover, non controlled thermal effects on other locations would clearly spoil the thermal test experiment since the relation between the heaters input and the observed output would not be due only to the particular location being heated but other contributions will appear and thus our transfer function estimation will be contaminated with effects arising in other locations of the spacecraft.

To take into account these effects, we computed the ΔT_l —defined in § 7.2.1— on the electrodes once a high power thermal shock was applied on the Optical Window. Results show that the expected gradient between electrodes is well below acceptable values. As seen in Figure 7.14, there is a factor 10^{-4} suppression which implies that, according to § 7.2.3, the induced electrode housing (EH) signal will not cause a disturbing contribution. Even more, this spurious effect will be delayed with respect to the original one, i.e, the one applied on the Optical Window, and therefore even if
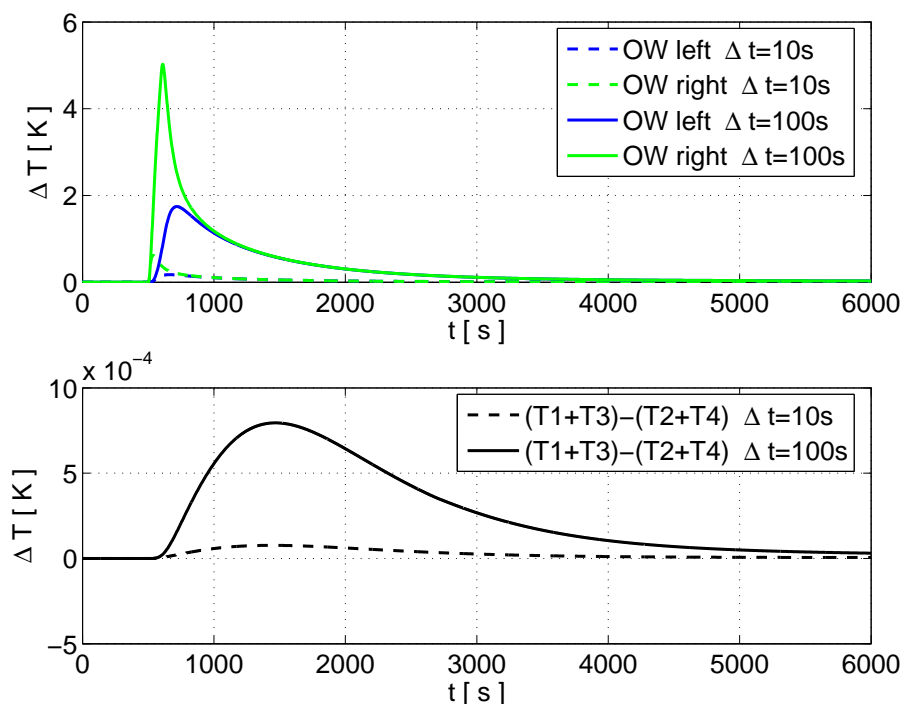
Figure 7.14: Optical Window heating impact on Inertial Sensor

heating the Optical Window affects the test mass motion, both effects could be easily disentangled.

7.5 Heaters on the LTP

From the previous studies we end with a table of values defining a power requirement that must be supplied by the diagnostic heaters in various locations through the LCA. Table 7.6 summarises the previous discussion

Location	Power [W]	Attaching surface
Inertial Sensor	0.045	Molybdenum
Optical Window	1	titanium
Struts	2	CFRP

Table 7.6: Heaters power summary

The power values derived from this study are the ones assumed as requirements for the hardware implementation [45]. We have also added the information regarding the attaching surface since this is of relevance when choosing a hardware model and, as we shall see, it will have implication when considering the attaching glue.

In the following we will focus on hardware related issues. Apart from the one just commented
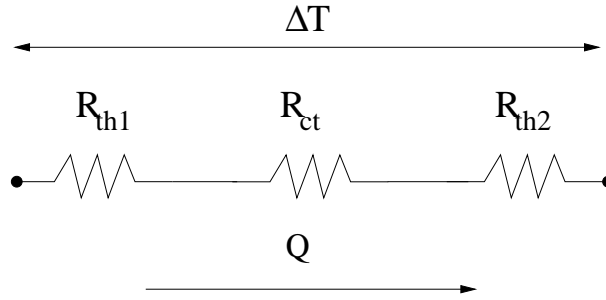
Figure 7.15: Thermal model for the thermal contact resistance

about the attaching glue, magnetic cleanliness or the selection of a suitable heater given the environmental conditions will also be treated.

Glue contact resistance

A problem related with the heating process is the selection of a suitable glueing material. Since we are facing the characterisation of heat sinks, the selected glue must fulfil high conductivity properties. This is not a demanding requirement given that a thermal conductive glue is a standard product in engineering. But we must also ensure that this material has a low outgassing profile, has undergone a space qualification process and, at the same time, is a thermal conductive material to prevent from charging processes that may disturb the GRS capacitive-based measurement.

In order to estimate the correct thermal interface between thermal diagnostic items and attaching points the simplified model described in Figure 7.15 can be considered. In the steady-state condition, Figure 7.15 can be translated in terms of Fourier's law,

$$Q = \frac{\Delta T}{R_{th1} + R_{ct} + R_{th2}} \tag{7.18}$$

where Q is the heat flux, R_{th} stands for the usual *thermal resistance* (in [K/W]) dependent on material thermal properties ($R_{th} = \frac{L}{K\,A}$ for a slab of conductivity K, area A and length L) and R_{ct} is the *thermal contact resistance* related to the conditions of the experiment set-up, i.e. surface flatness, surface roughness, material thickness or attaching pressure. It is defined as [40]

$$R_{ct} = \frac{1}{h_c\,A} \tag{7.19}$$

where A is the area of contact and h_c is the *contact coefficient* (in [W/K $\cdot$ m^2]). From equation (7.18) an upper value can be derived for the thermal contact resistance if the assumption is made that this factor must be negligible with respect to the other terms in (7.18)

$$R_{ct} \ll R_{th1} + R_{th2} \tag{7.20}$$

This is the general expression which must be ensured in any case. However, more specific

ADHESIVE	TML	CVCM	CURE TIME	CURE TEMP.[°C]	WVR
C-868-1 ONE COMPONENT silver filled epoxy/f	0.08	0.00	1 h	170	0.07
DUPONT 5504A silver filled epoxy	0.05	0.00	1 h	160	–
TECKNIT 72-00002 silver filled silicone	0.02	0.00	48 h	121	–
UNISET C-940-1 silver filled polyimide	0.06	0.00	10 min	170	0.05
UNISET C-940-1 silver filled polyimide	0.02	0.00	1 h	170	0.01
UNISET C-940-4 ONE COMPONENT silver filled polyimide	0.08	0.00	10 min	170	0.05

Table 7.7: products fulfiling outgassing requirements of the LTP experiment.

values can be obtained if the application is better determined. For instance, if the sensor/heater is attached to a highly conductive material (as in the IS or OW case), its thermal resistance will be smaller than the sensor/heater, $R_{th1} > R_{th2}$, and hence (7.20) can be simplified to

$$R_{ct} \ll R_{th1} \tag{7.21}$$

If now, the sensor thermal resistance measured in [84], $R_{th1} \simeq 100$ K/W, and the contact area of the thermistor, $A = 11.3 \times 10^{-5}$ m^2 are considered as standard values, the requirement can be translated into

$$\frac{1}{h_c} \ll 11.3 \times 10^{-3} \frac{\text{m}^2 \, \text{K}}{\text{W}} \tag{7.22}$$

However, this value is only representative of the OW and IS cases, where thermal diagnostic items are attached to metal surfaces with high thermal conductivity. When considering low thermal conductivity materials, as in the OB case, expression (7.20) must be applied.

In what respects the outgassing properties, we can take advantage of the low outgassing materials list provided by National Aeronautics and Space Administration (NASA)[2] to create a table of products fulfilling our vacuum requirements [88]. These are presented in Table 7.7.

Magnetic cleanliness

The LTP is highly sensitive to magnetic disturbances and therefore strong magnetic requirements are imposed on any item that enters in the design. Any magnetic field exceeding the requirement could affect the test mass motion and therefore spoil the experiment.
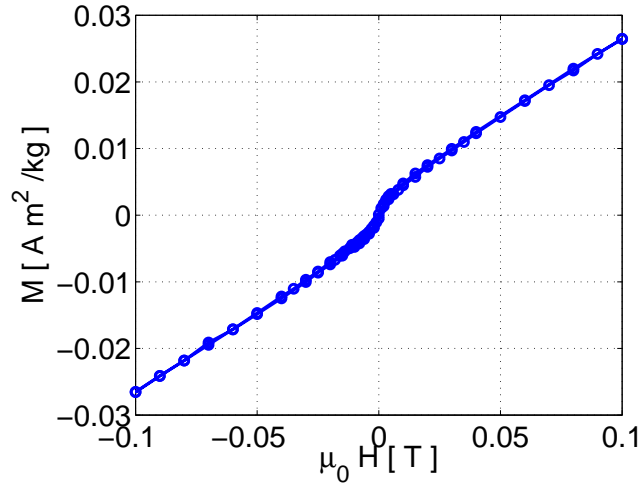
---

[2]http://outgassing.nasa.gov

Figure 7.16: Magnetisation curve for a sample of the heater electrical circuit material

Heaters fully enter the category of items that might be considered problematic for the magnetic cleanliness. There are two characteristics that support the classification in these terms: First, they are located near the test mass and second, the heaters are usually built from an electrical circuit that dissipates power as a function of the applied voltage and its internal resistance. Unfortunately, the most common materials used to build electrical circuits have ferromagnetic properties, e.g iron or nickel, which obviously implies a high risk for our purpose. Indeed, a solution of these characteristics can not be considered for the electrode housing (not only due to magnetic considerations but also due to vacuum conditions, heaters as the ones used in section § 6.1 can not be accepted). An alternative achieving both vacuum and magnetic requirements has been explored and will be discussed in next section.

The next location in order of demanding conditions are the Optical Window heaters. These are outside the vacuum enclosure and therefore conditions on the vacuum are relaxed, allowing to consider the possibility of polyamide heaters. Moreover, if we can prove that the magnetic requirement is fulfilled in this position we can safely assume that the requirement will also be achieved at the last location were heaters are to be attached, the struts.

Heaters used for space applications are not usually magnetically characterised or, at least, not at the level of precision required for the LTP. In order to base our decision on a solid criterion, heaters of the same kind as the ones foreseen to be used in the flight model were subject to magnetic characterisation. The process undertaken was to extract a sample of the heater electrical circuit and measure its magnetic moment at room temperature. The equipment used to this end was the Quantum Design MPMS XL SQUID magnetometer of the Serveis Científicotècnics de la Universitat de Barcelona, managed by Dra. N. Clos.

Results of the measurement, using a $\sim 17\,\mathrm{mg}$ sample, are shown in Figure 7.16. The sample showed two different behaviours in the region $|H| < 5\,\mathrm{mT}$ and $|H| > 5\,\mathrm{mT}$ respectively. Whereas

the latter is a typical paramagnetic curve, the former, which is really the one of our interest shows a soft ferromagnetic response with the typical enhanced susceptibility of these materials. Given the mass of the sample, the remnant magnetic moment can be found to be of the order $m \simeq 1.7 \times 10^{-8} \mathrm{Am}^2$. If the simple dipole approximation is used to compute the magnetic field in the test mass a $B \sim 0.1 \, \mathrm{nT}$ is obtained, some orders of magnitude below the magnetic requirement on the test mass location [100]. However, a detailed evaluation of this effect is needed to confirm the fulfilment of magnetic requirements not only on the magnetic field but also on the magnetic field gradient.

Hardware implementation

After describing some of the problems to be considered in the heaters selection process we are now in conditions to finally summarise the characteristics of the heaters on the LTP.

- *Optical Window:* heaters on the Optical Window will be of polyamide type with a resistance of $45 \, \Omega$ and a maximum power of $1 \, \mathrm{W}$.

- *Struts:* heaters on the Struts will be of polyamide type with a resistance of $44 \, \Omega$ and a maximum power of $2 \, \mathrm{W}$.

- *Inertial Sensor:* heat will be induced in the Inertial Sensor by means of thermistor acting as heaters [84]. Maximum power in this location will be of $45 \, \mathrm{mW}$.

Another point to be taken into account when considering hardware issues is the connection layout. Given that diagnostics items are connected to the DMU via the DAUs, all diagnostics items need to be grouped in sets of four. This is not a major problem in its own but the limitation that makes the wiring crucial is that the DAUs are not redundant. We need thus to distribute the diagnostic items among the DAUs minimising the loss of information available in case of failure. Two possibilities can be adopted *a priori*: to maximise the information in one Inertial Sensor, meaning to group items around test mass 1 and test mass 2 in different DAUs or, on the other hand, to maintain control on items characterising the thermal environment around both test masses but with a limited capability. The latter has been finally adopted for the LTP and the derived wiring scheme can be found in [83].

Another characteristic of the diagnostic subsystem is that when heaters are switched on the power arriving at any location will not be a strictly continuous signal but it will be multiplexed at high frequencies. This will allow to use both independent logical heaters in each Inertial Sensor in order to heat the whole electrode housing homogeneously. This may be suitable if, for instance, thermal experiments are to be performed at different nominal temperatures in order to distinguish thermal effects that have a different dependence on the absolute temperature.

Simulations on the thermal model applying discontinuous heat input showed a decrease of the SNR proportional to the duty cycle assumed for the input cycle. For instance, a duty cycle of 50 leads to a SNR decrease of a factor 2 since half of the energy is not being supplied to the system.

Chapter 8

Diagnostics Data modelling

In this last section our aim will be to focus on the methodology that we shall use to analyse the thermal diagnostics data during in flight operations of the LPF mission. Far from being an exhaustive treatment of the different subsystems, our guideline to build this methodology has been an extensive data set of thermal test runs on a single location: the Optical Window.

However, the only part of the analysis which is clearly related to this specific location is the discussion of the physical interpretation of the results (cf. § 8.5), the rest of the chapter refers to the methodology to deal with diagnostic data in general and, in this sense, the chapter represents an end-to-end simulation of the diagnostics data analysis problem: from the data acquisition and conditioning to the noise apportioning.

As previously commented, diagnostics have both to estimate as precisely as possible the parameters of the noise model and determine the contribution of the noise sources to the instrument noise curve. The first scope requires a brief overview of parameter estimation theory which will also help to set a notation for the rest of the chapter. Next, a *data-based* noise model will be built and subsequently, its contribution to the noise curve established. With the *data-based* nomenclature we mean that results reported herein have been derived from the experimental data to the physical interpretation of the model and the effects involved in it, not the opposite way. The fact that the methodology starts from the data and has allowed us to, in principle, arrive to a physical model endorses the idea that this procedure may also be suitable to deal with diagnostics data in other locations.

8.1 Thermal diagnostics estimation problem

The diagnostic data analysis problem in the LTP naturally fits into a parameter estimation problem. In general terms, the starting point is a set of data points $\mathbf{X_K} = \{x_1[1], x_1[2], \ldots x_1[N];$ $x_2[1], x_2[2], \ldots x_2[N] \ldots x_K[N]\}$ representing input data acquired by diagnostic items, in this case, K temperature sensors distributed across the LCA. A second set of data $\mathbf{Y_R} = \{y_1[1], y_1[2], \ldots y_1[N];$

$y_2[1], y_2[2], \ldots y_2[N] \ldots y_K[N]\}$ is also obtained in the diagnostic process, which corresponds to the response of the system being characterised. This is also considered to be a multiple set of R different datastreams, although we will be working in this Chapter with a unique output variable, i.e. the phase data coming from the optical metrology subsystem. In this situation we will be interested in a set of parameters $\mathbf{\Theta_M} = \{\theta_1, \theta_2, \ldots \theta_M\}$ that relates the two previous data sets given a proposed model,

$$\mathbf{Y_R} = H\left(\mathbf{X_K}; \mathbf{\Theta_M}\right) \tag{8.1}$$

where $H\left(\mathbf{X_K}; \mathbf{\Theta_M}\right)$ is the noise model containing the information of the contribution of different noise sources to the instrument performance. In general, it will be a function of the input data and the parameters we wish to estimate.

The diagnostic problem can be stated as to estimate the $\widehat{\mathbf{\Theta}}_\mathbf{M}$ parameters

$$\widehat{\mathbf{\Theta}}_\mathbf{M} = G\left(\mathbf{Y_R}; \mathbf{X_K}; H\left(\mathbf{X_K}; \mathbf{\Theta_M}\right)\right) \tag{8.2}$$

These parameters will depend on the data set under study but they will also acquire different numerical values depending on the noise model being evaluated. We need then to consider both the data and the modelling as equally relevant for the diagnostic purpose.

8.1.1 Least Squares

The Least Squares approach is a standard methodology used in estimation problems. In the following we briefly describe this approach and how it is implemented in the case of a linear model. If the dependence of the model in the parameters is non-linear, iterative numerical techniques are required to solve the problem.

Expression for Linear Least Squares

A situation of particular interest is when the dependence with the $\mathbf{\Theta}$ parameters can be assumed to be linear. In such a case the Least Square Estimator can be computed analytically. Since we will be applying this expressions in the following sections we will show here the main equations.

The Least Squares Estimator is found minimising

$$\chi^2(\mathbf{\Theta}) = \sum_{n=1}^{N} \sum_{k=1}^{M} (y[n] - \theta_k\, x_k[n])^2 \tag{8.3}$$

or, in matrix notation

$$\chi^2(\mathbf{\Theta}) = (\mathbf{Y} - \mathbf{H}\,\mathbf{\Theta})^T (\mathbf{Y} - \mathbf{H}\,\mathbf{\Theta}) \tag{8.4}$$

If we consider one output variable composed by N values, K input variables with the same length and a model with M parameters to be determined, then $\mathbf{Y}$ is a $1 \times N$ vector, $\mathbf{\Theta}$ a $1 \times M$

vector and $\mathbf{H}$, sometimes known as *observation matrix* [46], contains all the input data, i.e a $K \times N$ matrix.

Now, minimising the Least Squares error

$$\frac{\partial \chi^2(\mathbf{\Theta})}{\partial \mathbf{\Theta}} = -2\mathbf{H}^T\mathbf{Y} + 2\mathbf{H}^T\mathbf{H}\mathbf{\Theta} \tag{8.5}$$

the *normal equations* are found

$$\mathbf{H}^T\mathbf{H}\mathbf{\Theta} = \mathbf{H}^T\mathbf{Y} \tag{8.6}$$

and the estimator is directly derived

$$\widehat{\mathbf{\Theta}} = (\mathbf{H}^T\mathbf{H})^{-1}\mathbf{H}^T\mathbf{Y} \tag{8.7}$$

As previously stated, there is no statistical description of $\widehat{\mathbf{\Theta}}$ since no statistical assumption has been made on the data. The goodness in data description is solely described by the $\chi^2(\mathbf{\Theta})$ of which the minimum value will be given by

$$\chi^2(\mathbf{\Theta})|_{min} = \chi^2(\widehat{\mathbf{\Theta}}) = \mathbf{Y}^T(\mathbf{Y} - \mathbf{H}\widehat{\mathbf{\Theta}}) \tag{8.8}$$

Least Squares estimator is completely described by equations (8.3) and (8.7), in particular the latter defining the estimator will be the one used in the following approaches.

Numerical estimation

When the model being evaluated by the least squares approach is non-linear or, in general, can not be solved by analytical expression the function $\chi^2(\mathbf{\Theta})$ must be minimised by means of numerical methods. This is usually done according to

$$\widehat{\mathbf{\Theta}}^{i+1} = \widehat{\mathbf{\Theta}}^i + \alpha\, f(i) \tag{8.9}$$

There are various methods implementing this process whose main difference is the function selected as the *minimising direction* $f(i)$. For instance, one widely applied criterion is to use the function

$$f(i) = \frac{\partial^2 \chi^2(\mathbf{\Theta})}{\partial \mathbf{\Theta}^2} \tag{8.10}$$

where $\partial^2_{\mathbf{\Theta}}\chi^2(\mathbf{\Theta})$ is the Hessian matrix. These are the so called *Newton methods* and there are also various subclasses which differ in the way the Hessian matrix is estimated. For a more thorough description we refer to [48] and the MATLAB System Identification Toolbox which will be the tool that we shall use when dealing with these problems.

8.2 Fitting the data to models

The data set upon which the analysis will be developed consists in 25 data runs performed on two different Optical Window prototypes. Heat pulses from $100\,\mathrm{mW}$ to $2\,\mathrm{W}$, ranging from $10\,\mathrm{s}$ to $100\,\mathrm{s}$ of application time were applied to this optical element. As described in §6.3, four sensors were simmetrically attached to the window: two in the glass and two in the titanium flange.

Once the data set is chosen we can adapt our previous nomenclature to our particular setup. The variables involved will be

$$
\begin{aligned}
\mathbf{Y} &= \{\phi(t)\} \\
\mathbf{X} &= \{T_{Gl,L}(t), T_{Gl,R}(t), T_{Ti,L}(t), T_{Ti,R}(t)\}
\end{aligned}
\tag{8.11}
$$

where the subindex Gl/Ti refers to the temperature acquired by sensors attached to Glass /Titanium and L/R indicates whether they were attached to the Left/Right side, respectively. This will be the nomenclature followed from now on. As previously commented, we will base our analysis on a unique output variable: the interferometer phase, $\phi(t)$.

The main purpose of this section is to give account of the *measured* interferometer output data in terms of the also measured temperature data. While in this experiment both are of course ultimately caused by the heaters' signal, our interest focuses on the temperature *vs.* phase relationship, as we need to quantify the magnitude of temperature fluctuations noise during science operations in flight [51].

To serve this purpose, we adopt model fitting techniques. Two approaches will be proposed, and discussed in the ensuing section: a direct linear regression fit of the interferometric data to the temperature read-out coming from sensors on the titanium flange and those on the OW glass itself, and an *ARMA* model using only temperature readout from the titanium temperature sensors. The latter is of particular interest, since it is not foreseen that temperature sensors be attached to the glass surface in the real LTP.

8.2.1 Data conditioning

Before we attempt to fit the data to a useful model, some data pre-processing is required.

The temperature and phase acquisition data systems reside on different hardware and software, and deliver the respective time series data for analysis at sample rates which are different as well: temperature data are sampled at $f_{s,T} = 0.65\,\mathrm{Hz}$, whereas phase data are sampled at $f_{s,\phi} = 32.4\,\mathrm{Hz}$, instead. Downsampling and resampling thus needs to be applied to the latter in order to make meaningful sense of data fitting algorithms. To avoid aliasing effects at downsampling phase, suitable low pass filters are applied. This is however not enough to have matched sampling times in both time series, so an additional interpolation algorithm is used for properly matched resampling.

In addition, each data segment is de-trended prior to model fitting. The removed trend is evaluated from the first 500 seconds previous to the heat input signal begins. This way we get rid

of environmental drifts and spurious trending effects.

8.2.2 Direct Linear Regression

Our first attempt to model the Optical Window will be to explore a linear model which relates proportionally the phase response to the available temperature information, we will call it Direct Linear Regression (DLR).

$$\phi(t) = p_1\, T_{\text{Ti}}(t) + p_2\, T_{\text{Gl}}(t) \tag{8.12}$$

where $T_{\text{Ti}}(t)$ is the temperature read by the thermometer on the titanium flange closest to the activated heater, and $T_{\text{Gl}}(t)$ that of a thermometer on the OW glass. The parameters p_1 and p_2 are to be estimated by a least squares algorithm, which was shown in §8.1.1 to have an analytical solution for the case under study. Substituting the model (8.12) into the least square expression (8.3), we get

$$\chi(p_1, p_2)^2 = \sum_{n=1}^{N} \left\{ \phi[n] - p_1\, T_{\text{Ti}}[n] - p_2\, T_{\text{Gl}}[n] \right\}^2 \tag{8.13}$$

Here, $\phi[n]$ is the n-th sample of the measured phase, and $T_{\text{Ti}}[n]$ and $T_{\text{Gl}}[n]$ the corresponding temperature samples. Thus, for example,

$$\phi[n] \equiv \phi(n\Delta t) \;, \quad T_{\text{Ti}}[n] \equiv T_{\text{Ti}}(n\Delta t) \;, \tag{8.14}$$

etc., where the *sampling time* Δt has been set to $\Delta t \equiv 1/f_{\text{s},T}$, as discussed in §8.2.1 above. Finally, N is the number of analysed samples of each read-out.

The minimisation of equation (8.13) will give us the *least squares estimates* $\widehat{p}_1$ and $\widehat{p}_2$ of the parameters p_1 and p_2, respectively. An example of this procedure is shown in Figure (8.1). We report on the results of this analysis in §8.3.

8.2.3 *ARMA* model fit

Although the linear regression method shows to perform quite acceptably well, there is a clear motivation to find a model able to fit the data independently of the glass temperature readings, since the latter will not be available in flight.

In this section we take a different approach to fit phase data to titanium only temperature readings. We shall now assume that the relationship between these magnitudes can be expressed by a *dynamical* equation [70]. The main concept behind this hypothesis is, in some sense, to try to evaluate the information that the glass temperature is carrying by means of the titanium temperature only. This implies that we must provide the model with some flexibility in order to include this new degree of freedom.

To serve this purpose, our approach will be based in the *system identification* methodology [28,
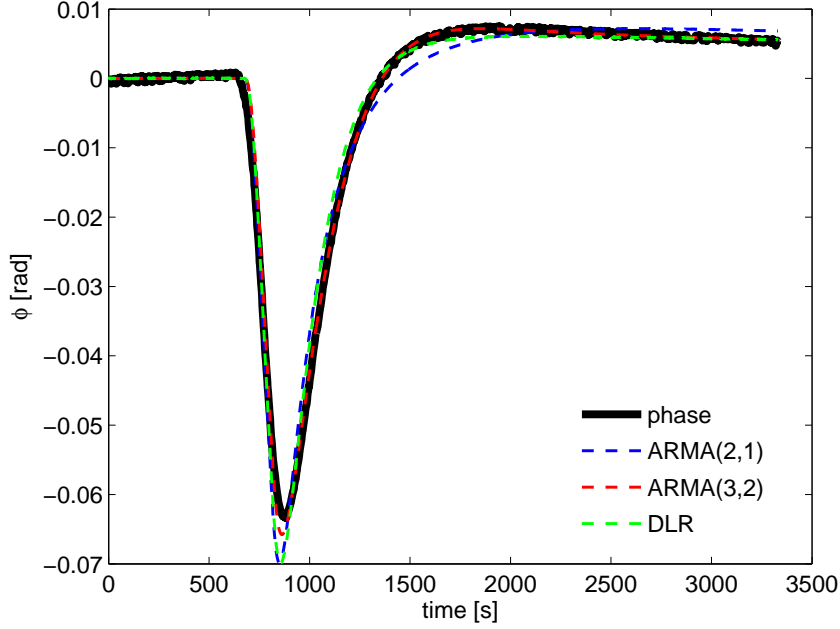
Figure 8.1: Example of fit results for two different models.

32, 48]. In this framework the system under study is represented as a black box between an input and an output variable, $T_{Ti}(t)$ and $\phi(t)$ respectively in our case. In the more general situation, a white noise variable $e(t)$ is introduced in the model with the intention of characterise an eventual noisy contribution. If all the contributions are taken into account, the following description is obtained

$$\phi[n] = G(q, \boldsymbol{\theta_G})\, T_{\text{Ti}}[n] + H(q, \boldsymbol{\theta_H})e[t] \tag{8.15}$$

where q represents the *shift operator*:

$$q\, x[n] = x[n+1]\ , \quad q^{-1}\, x[n] = x[n-1] \tag{8.16}$$

and with $G(q, \boldsymbol{\theta_G})$ and $H(q, \boldsymbol{\theta_H})$ being the transfer functions that contain the dynamical description of the model. These transfer functions are usually represented as rational functions of polynomials

$$
\begin{aligned}
G(q, \boldsymbol{\theta_G}) &= \frac{\alpha_0 + \alpha_1\, q^{-1} + \cdots + \alpha_r\, q^{-r}}{1 + \beta_1\, q^{-1} + \cdots \beta_s\, q^{-s}} &\text{(8.17a)}\\[2mm]
H(q, \boldsymbol{\theta_H}) &= \frac{\gamma_0 + \gamma_1\, q^{-1} + \cdots + \gamma_p\, q^{-p}}{1 + \psi_1\, q^{-1} + \cdots \psi_s\, q^{-s}} &\text{(8.17b)}
\end{aligned}
$$

Different models can be implemented following this procedure [48]: *ARX*, *ARMAX*[1], *OE (Output-Error)* or *BJ (Box-Jenkins)* are some of the typical implementation of this structure. The difference between them is the relation between the polynomials defining the transfer function. For instance, in the *ARX* model the denominators of both rational functions $G(q, \boldsymbol{\theta_G})$ and $H(q, \boldsymbol{\theta_H})$ are equal, i.e. $\psi_i = \beta_i$ in equation (8.17).

In this system identification context, our particular application would fall into the *OE (Output-Error)* models, which merely implies to assume $H(q, \boldsymbol{\theta_H}) = 1$ and therefore, that no modelling is applied to the noisy part. Since this construction does not add any dynamical information to the model we will omit it and refer the model as an *ARMA* model because indeed it has both the Autoregressive and the Moving Average part. Thus, our model becomes

$$\phi[n] = G(q, \boldsymbol{\theta}) \, T_{\text{Ti}}[n] \tag{8.18}$$

were $\boldsymbol{\theta}$ is an abbreviation for the vector of $r + s + 1$ *ARMA* parameters $\alpha_0, \dots, \alpha_r, \beta_1, \dots, \beta_s$. System identification in this approach is again based on a least squares criterion, for which a suitably defined square error needs to be defined

$$\chi^2(\boldsymbol{\theta}) = \sum_{n=1}^{N} \left\{ \phi[n] - G(q, \boldsymbol{\theta}) \, T_{\text{Ti}}[n] \right\}^2 \tag{8.19}$$

The estimates $\widehat{\boldsymbol{\theta}}$ of the parameters $\boldsymbol{\theta}$ are those which cause $\chi^2(\boldsymbol{\theta})$ to be minimum. Algorithms to find them are more robust if the additional hypothesis holds that the residuals $\{\phi[n] - G(q, \boldsymbol{\theta}) \, T_{\text{Ti}}[n]\}$, where $\phi[n]$ and $T_{\text{Ti}}[n]$ are the actually recorded data, are a white noise sequence [48]. Reassuringly, this is quite accurately true for our data. Two examples of the fit are shown in Figure 8.1, blue and red curve.

8.3 Numerical results

As stated in § 8.2, up to 25 rounds of measurements were carried through during the experiment. This is a considerable number which enables us to check the consistency of the fitting models just described. The methodology we have adopted is the following: for each run, we de-trend the data and then fit them to both the Direct Linear Regression (DLR) and the *ARMA* models. Parameter estimates are then filed for further analysis, as we now describe. An observation on the *ARMA* fit is however in order before we proceed.

Indeed, in the *ARMA* fit we also need to make a choice of *order* of the process, i.e., we need to set the number of α's and β's in equation (8.17a). Our selection criterion was based not only in the goodness of fit —the minimisation of $\chi^2(\theta)$, but also in the minimisation of the dispersion of the model parameters. If the model is able to reproduce the time evolution for different runs but it acquires different numerical values for the *ARMA* model parameters we will not be able to

---

[1] the *X* appearing in the *ARX* or *ARMAX* model comes from the *exogenous*, that is to say external, variable added in these models with respect the *AR* or *ARMA* counterparts.
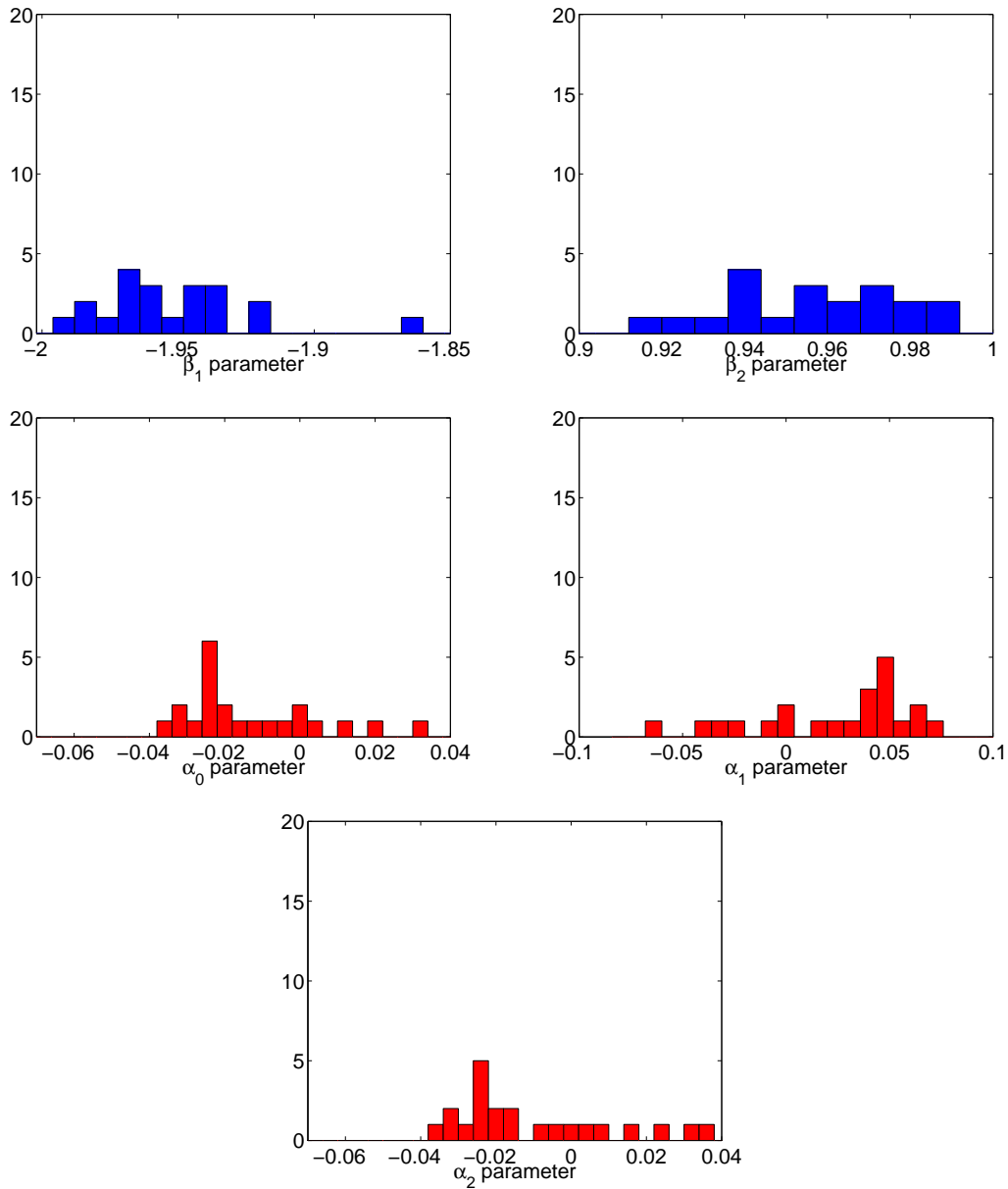
Figure 8.2: Histograms of the estimated parameters for the $ARMA(3,2)$, evaluated on the Optical Window data set.

find a physical interpretation for these values and the model will not be a reliable one. This is the case for models with increasing number of degree of freedom. For instance, in Figure 8.1, the $ARMA(3,2)^2$ is shown to be the best choice to describe the phase behaviour. However, when we

---

[2] The notation $ARMA(p,q)$ refers to the order of the numerator (p) and the denominator (q) of the $ARMA$ transfer function.
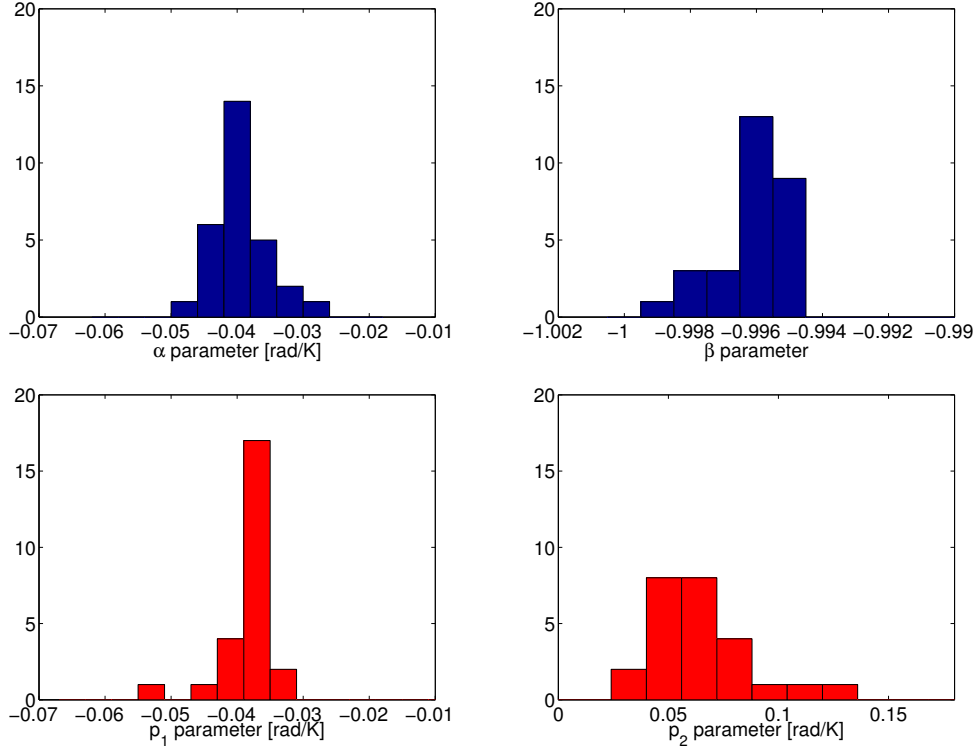
Figure 8.3: Histograms of the estimated parameters for the two fitting models described in the text. *Top:* ARMA(2,1), with $\alpha \equiv \alpha_0$ and $\beta \equiv \beta_1$. *Bottom:* DLR.

take a look at the histogram of the parameters' numerical values for this model, Figure 8.2, we find a wide range of values which implies a high uncertainty.

A reduction in the parameter space leads to the $ARMA(2,1)$ model, defined as

$$G(q, \boldsymbol{\theta}) = \frac{\alpha_0 + \alpha_1 \, q^{-1}}{1 + \beta_1 \, q^{-1}} \tag{8.20}$$

which describes the phase with discrepancies of the same order as the ones found with the DLR model but with a greater accuracy in the determination of the parameters —see Figure 8.3, top panels. When testing this model against the data set we find a systematic relation between both *MA* parameters i.e. $-\alpha_1 \simeq \alpha_0$. However, both parameters are not numerically equal and the difference between them will be of great interest since the quantity $\delta \equiv \alpha_0 + \alpha_1$ will acquire a concrete meaning when discussing the physical interpretation of the model in §8.5. Another problem to be tackled in §8.4.2 is the fact that the difference between α_0 and α_1 is much less than their variances.

A comparison between the $ARMA(2,1)$ and the DLR models brings out some relevant aspects that are worth stressing. First, a relation can be established between the *MA* coefficients and the α_0 parameter. This numerical relation, shown in Table 8.3, is given by $-\alpha_1 \simeq \alpha_0 \simeq p_1$. The latter

DLR	ARMA(2,1)
$p_1 = (-38 \pm 4) \times 10^{-3}$ rad/K	$\alpha_0 = (39.6 \pm 3) \times 10^{-3}$ rad/K
$p_2 = (65 \pm 20) \times 10^{-3}$ rad/K	$\alpha_1 = (-39.5 \pm 3) \times 10^{-3}$ rad/K
	$\beta_1 = -0.996 \pm 0.001$

Table 8.1: Mean values and *rms* variances of parameter estimates

gave us, in the DLR model, the coupling between the phase response and the titanium temperature increase. In the $ARMA(2,1)$ model, this numerical equivalence implies that the output phase data is related to the time *derivative* of the titanium temperature —we come back to this in § 8.4.1.

Another important consideration must be stressed from the statistical study performed on the data set: β_1 is strongly peaked at a nominal value, with only 0.1 % relative tolerance whereas p_2 is much more disperse, with almost 30 % variability. Regardless of the meaning of both parameters, the comparison does point out that the $ARMA(2,1)$ is a more robust model.

8.4 Developing the *ARMA* model

Once the $ARMA(2,1)$ parametrisation has proved to be useful we will now deal with some open issues we have left in the last section.

A major advantage of the $ARMA$ models is that they represent a difference equation relating its variables. We will use this property to explore the dynamics of the model but we will also take advantage of it to translate the model into a transfer function in frequency domain, which is clearly an interesting application for the particular problem of noise diagnostics in the LTP. Finally, we also need to address the problem of error estimation in the $ARMA$ parameters.

8.4.1 The *ARMA*(2,1) transfer function

We start transcribing the $ARMA$ model into frequency domain. In view of the numerical results and the relations found between parameters, it is expedient to rewrite the $ARMA(2,1)$ model in terms of the following parameters:

$$\alpha \equiv -\alpha_1 , \quad \delta \equiv \alpha_0 + \alpha_1 , \quad \beta \equiv \beta_1 \tag{8.21}$$

Hence,

$$G(z, \alpha, \beta, \delta) = \alpha \, \frac{1 - z^{-1}}{1 + \beta z^{-1}} + \frac{\delta}{1 + \beta z^{-1}} \tag{8.22}$$

is the z-transform of the process transfer function —we have replaced the shift operator q by the complex variable z [46]. It is also expedient to emphasise the structure of this formula as follows:

$$G(z, \alpha, \beta, \delta) = \alpha \, G_{\text{HP}}(z, \beta) + \delta \, G_{\text{LP}}(z, \beta) \tag{8.23}$$

with

$$G_{\mathrm{HP}}(z, \beta) \equiv \frac{1 - z^{-1}}{1 + \beta z^{-1}} \;, \quad G_{\mathrm{LP}}(z, \beta) \equiv \frac{1}{1 + \beta z^{-1}} \tag{8.24}$$

We now find *discrete Fourier transforms* (DFT) by the substitution

$$z = \exp(i\omega \Delta t) \tag{8.25}$$

where Δt is the sampling time of the time series data. The following obtains:

$$|\widetilde{G}_{\mathrm{HP}}(\omega, \beta)|^2 \;\; = \;\; \frac{4 \sin^2(\omega \Delta t / 2)}{1 + 2\beta \, \cos(\omega \Delta t) + \beta^2} \tag{8.26}$$

$$|\widetilde{G}_{\mathrm{LP}}(\omega, \beta)|^2 \;\; = \;\; \frac{1}{1 + 2\beta \, \cos(\omega \Delta t) + \beta^2} \tag{8.27}$$

$$|\widetilde{G}(\omega, \alpha, \beta, \delta)|^2 \;\; = \;\; \frac{\delta^2 + 4\,\alpha(\alpha + \delta)\,\sin^2(\omega \Delta t / 2)}{1 + 2\beta \, \cos(\omega \Delta t) + \beta^2} \tag{8.28}$$

We thus see that the transfer function G is the sum of a *high pass* term, G_{HP}, and a *low pass* term, G_{LP}. The effect of the latter is naturally dominant at low frequencies, while the high pass term dominates at high frequencies. The concepts of *low* and *high* frequencies can be made precise by means of some intermediate frequency f_{b} where the gains of G_{HP} and G_{LP} are equal. This is easily calculated:

$$f_{\mathrm{b}} \simeq \left| \frac{\delta}{\alpha} \right| \frac{1}{2\pi \Delta t} \tag{8.29}$$

and has a numerical value of $f_{\mathrm{b}} \simeq 0.2 \,\mathrm{mHz}$, which means the high pass effect dominates throughout the LTP bandwidth. We may not however neglect the relevance of the low pass at lower frequencies, as it contributes extremely valuable information for LISA.

A Bode diagram representation for the transfer functions is shown in Figure 8.4. The filter modulus is characterised by a plateau of $|\widetilde{G}| \sim 40 \times 10^{-3} \,\mathrm{rad/K}$ across the entire LTP measuring bandwidth. Temperature fluctuations at frequencies below this bandwidth are also suppressed but following a different behaviour, related to the low frequency response of the optical window. The figure also shows the phase behaviour of the filter, and indicates increasing delays for high frequency perturbations.

The DC gain of the filter is

$$|\widetilde{G}(\omega = 0, \alpha, \beta, \delta)| = \left| \frac{\delta}{1 + \beta} \right| \tag{8.30}$$

If the estimated parameters are substituted in this expression then the following is obtained:

$$|\widetilde{G}(\omega = 0, \alpha, \beta, \delta)| = (25 \pm 4) \times 10^{-3} \,\mathrm{rad/K} \tag{8.31}$$

Before analysing the physical meaning of the model, we will shortly describe how errors in the parameters are propagated to the *ARMA* model.
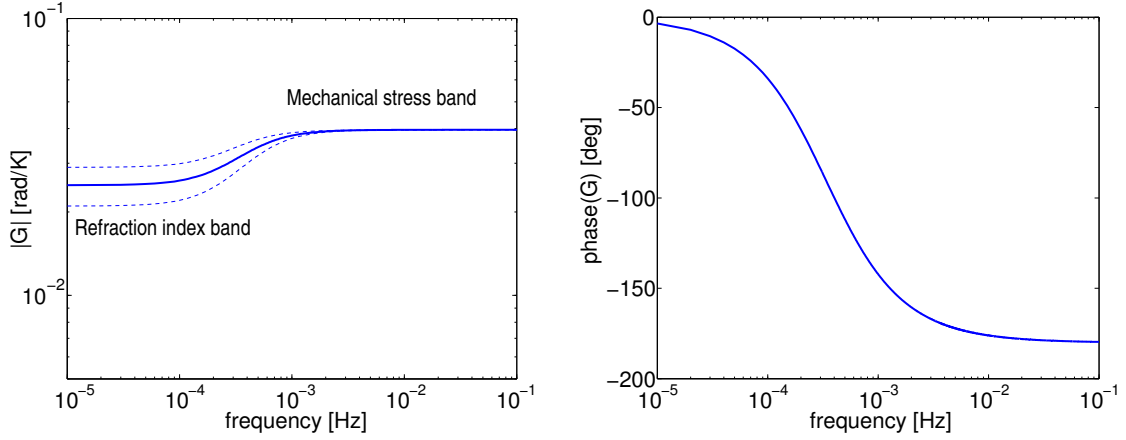
Figure 8.4: Bode diagram for the optical window $ARMA(2,1)$ transfer function estimate using the values from Table 8.3. Left panel: its modulus; dashed lines show the $1\,\sigma$ confidence region. Note that this confidence region has been extrapolated below $\sim$0.4 mHz, as actual experimental data were actually not available in that band. Right panel: phase of the transfer function.

8.4.2 Errors on the *ARMA* parameters

Since the criterion with which we have discriminated our models is a statistical study on a sample of different runs, the parameters and the errors associated with them must be derived accordingly to this approach. But even more relevant is how this uncertainties are transferred to the transfer function. In §8.3 we found that the parameter defined in (8.21) as $\delta \equiv \alpha_0 + \alpha_1$ can be poorly determined because both errors in the *MA* parameters $\Delta\alpha_0 = \Delta\alpha_1 \simeq 3 \times 10^{-3}$ are greater than the nominal value of $\delta \simeq 10^{-4}$. We found at the same time that both *MA* parameters were highly correlated through the whole data set. Our error treatment will need to include all these issues to correctly represent the uncertainty in the transfer function.

To this end, we will compute the variance of the transfer function $\widetilde{G}(\omega, \alpha, \beta, \delta)$ defined as

$$\gamma_G^2 = <G^2> - <G>^2 \tag{8.32}$$

where $< \ >$ is the expected value and we have redefined $G \equiv \widetilde{G}(\omega, \alpha, \beta, \delta)$. We can Taylor expand this function with respect the model parameters

$$G = G_0 + \partial_{\alpha_0} G_0 \, \delta_{\alpha_0} + \partial_{\alpha_1} G_0 \, \delta_{\alpha_1} + \partial_\beta G_0 \, \delta_\beta \ , \quad \left(\partial_x G_0 \equiv \frac{\partial G_0}{\partial x} \right) \tag{8.33}$$

where $G_0 \equiv \widetilde{G}(\omega, \widehat{\alpha}, \widehat{\beta}, \widehat{\delta})$. Then, substituting (8.33) in (8.32) and after some algebra we arrive to the following expression for the variance of the transfer function

$$\begin{aligned}
\gamma_G^2 &= (\partial_{\alpha_0} G_0)^2 \, \sigma_{\alpha_0 \alpha_0} + (\partial_{\alpha_1} G_0)^2 \, \sigma_{\alpha_1 \alpha_1} + (\partial_\beta G_0)^2 \, \sigma_{\beta \beta} \\
&+ \partial_{\alpha_0} G_0 \, \partial_{\alpha_1} G_0 \, \sigma_{\alpha_0 \alpha_1} + \partial_{\alpha_0} G_0 \, \partial_\beta G_0 \, \sigma_{\alpha_0 \beta} + \partial_{\alpha_1} G_0 \, \partial_\beta G_0 \, \sigma_{\alpha_1 \beta}
\end{aligned} \tag{8.34}$$

where the covariance matrix σ comes into play. The elements of this matrix are defined as

$$\sigma_{ij}^2 = < (\theta_i - \hat{\theta}_i)(\theta_j - \hat{\theta}_j) > \tag{8.35}$$

For the case of the set of runs we are working with and given the parameters $\{\alpha_0, \alpha_1, \beta\}$, the covariance matrix obtained is

$$\sigma^2 = \begin{pmatrix} 0.16 \times 10^{-4} & -0.16 \times 10^{-4} & -0.03 \times 10^{-4} \\ & 0.16 \times 10^{-4} & 0.01 \times 10^{-4} \\ & & 0.03 \times 10^{-4} \end{pmatrix} \tag{8.36}$$

The diagonal elements are the squared errors of the parameters and the non-diagonal terms contain the information about the correlation between parameters. It is thus clear from this result that α_0 and α_1 are strongly dependent on one another and also, that the much lower error in β has also a dependence on α_0. However, for our final purpose, which is the computation of the function γ_G^2, the most relevant result is the former, i.e. $\sigma_{\alpha_0 \alpha_1} = -0.16 \times 10^{-4}$. This negative value contributes to equation (8.34) reducing the variance of the transfer function $\widetilde{G}(\omega, \alpha, \beta, \delta)$ and, even if the δ value is poorly determined from the data, the correlation of both MA parameters reduces the uncertainty of the transfer function at low frequencies to the level shown in Figure 8.4, where the 1σ confidence region has been determined taking into account all the contribution in expression (8.34) and hence, this confidence region is much lower than if the non-diagonal terms of the covariance matrix had not been included in the analysis.

Pseudorandom noise input signals

Our estimation problem has as a distinctive characteristic the capability to control our input signal, i.e. we can choose the profile of the injection signal we will be using to test our system. A key point in this situation will be thus to minimise the variance of the estimated parameters.

In order to understand how this signal can be chosen to minimise the components of the covariance matrix we can consider a simplified MA model,

$$y[n] = \sum_{k=0}^{M-1} h[k] u[n-k] \qquad n = 0, 1, ..., N-1 \tag{8.37}$$

the observation matrix is therefore defined as

$$[\mathbf{H}^T \mathbf{H}]_{ij} = \sum_{n=1}^{N} u[n-i] \, u[n-j] \qquad i = 0, 1, ..., M \,; \, j = 0, 1, ..., M \tag{8.38}$$
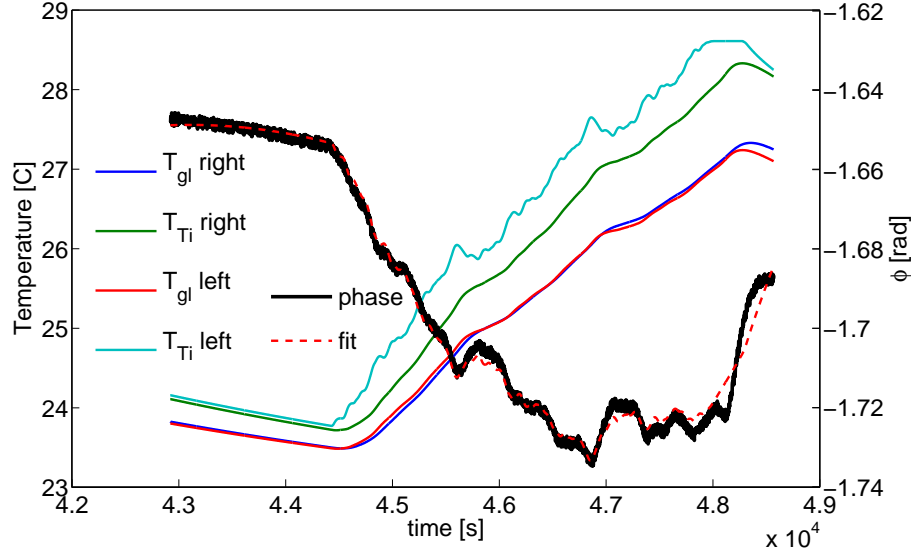
Figure 8.5: Thermal and interferometric response of the Optical Window to a BMLS signal applied to the left side heater. The signal applied were 3 sequential 6th order BMLS with 0.5 W of power applied and 20 s of minimum time step —see Appendix E for details.

which for large N becomes

$$
\begin{aligned}
[\mathbf{H}^T \mathbf{H}]_{ij} & \approx \sum_{n=1}^{N-1-|i-j|} u[n]\, u[n+k] \qquad k = 0, 1, ..., M \\
& = r_{uu}[i+j]
\end{aligned}
\tag{8.39}
$$

where r_{uu} is the autocorrelation function of $u[n]$. It can be shown that the minimum variance for the parameters estimate $\boldsymbol{\Theta}$ is only attained if $u[n]$ is chosen accordingly to make the matrix $H^T H$ diagonal [46], i.e.

$$
r_{uu} = 0 \qquad i \neq j
\tag{8.40}
$$

This property can be achieved by using the Pseudo-Random Noise (PRN) series, which are easily implemented as a Binary Maximum Length Sequence (BMLS). An overview of the generation and properties of these test signals is provided in Appendix E.

This methodology was also considered when studying the Optical Window. However, it was only applied in few data runs and therefore we can not follow the statistical approach that led us to the determination of the parameters in the $ARMA(2,1)$ case. We will only show it here for completeness but a more detailed analysis in this subject is required in order to get a well based conclusion.

Figure 8.5 shows temperature and phase evolution when applying a BMLS and the fit obtained with the $ARMA(2,1)$ model described in the previous sections. As before, only the closest sensor to the heater is being used for the $ARMA$ model and, as shown in the panel, the fit reasonably agrees with the phase curve. Another characteristic to be mentioned is that the long pulses required to cover the low frequency band with a BMLS signal imply important temperature increases, $\sim 4\,\mathrm{K}$ in Figure 8.5. Since a simple heat pulses does not reach this temperature raise, this consequence could be considered a drawback for the selection of this particular signals as a diagnostic tool.

The parameters retrieved by the fit are slightly different than the ones set by the statistical analysis in Table 8.3, though in the same order of magnitude of the ones obtained: $\alpha_0 = -\alpha_1 \simeq 22 \times 10^{-3}\,\mathrm{rad/K}$ and $\beta_1 \simeq -1$. In what respects the parameter's error, the comparison of the covariance matrix obtained with the BMLS input signal, matrix (8.41), compared with the one obtained with the data set of pulses, matrix (8.36), shows a decrease of the values of the former, i.e. a decrease on the error of the parameters of the $ARMA(2,1)$ when evaluated with a pseudorandom input.

$$\sigma^2 = \begin{pmatrix} 0.8 \times 10^{-6} & -0.8 \times 10^{-6} & 0.1 \times 10^{-8} \\ & 0.8 \times 10^{-6} & -0.1 \times 10^{-8} \\ & & 0.01 \times 10^{-8} \end{pmatrix} \qquad (8.41)$$

A worth mentioning characteristic is that the error in the β_1 parameter is two orders of magnitude lower than the errors in α_0 or α_1, contrary to what happened when applying a pulse where the error was of the same order of magnitude —see matrix (8.36). This seems to show that a BMLS input signal is indeed able to disentangle the information contained in each of $ARMA(2,1)$ parameters. Being a pseudorandom signal, its auto correlation is minimised and this translates into a minimisation of the off-diagonal elements in the covariance matrix. On the other hand, the off-diagonal element of the covariance matrix linking parameters α_0 and α_1 has the same value of the error of both parameters, implying thus that the correlation comes not from the input signal but from a physical underlying reason, as previously proposed in section §8.4.1

As stated before, a final conclusion about the possible use of BMLS signals as diagnostic tools in the LTP would require a statistical analysis, equivalent as the one performed in section §8.3.

8.4.3 The continuous time *ARMA*

On account of the empirical results reported in §8.2, and of the remarkable accuracy with which *both* DLR and *ARMA* models fit the experimental data —notwithstanding their completely different nature—, we now try to shed some light into the kind of processes which take place in the system.

For this, we attempt to picture the $ARMA(2,1)$ model relating the phase readout of the interferometer $\phi[n]$ and the temperature at the titanium flange $T_{\mathrm{Ti}}[n]$ as the digital implementation of some *analog* physical process. The starting point is of course the digital algorithm, equation (8.20),

which in this case is given by

$$G(q, \alpha, \beta, \delta) = \alpha \, \frac{1 - q^{-1}}{1 + \beta q^{-1}} + \frac{\delta}{1 + \beta q^{-1}} \tag{8.42}$$

where q is the shift operator of equation (8.16). The recursive form of the process thus defined is therefore

$$\phi[n] + \beta \phi[n - 1] = \alpha \left\{ T_{\mathrm{Ti}}[n] - T_{\mathrm{Ti}}[n - 1] \right\} + \delta \, T_{\mathrm{Ti}}[n] \tag{8.43}$$

and can be regarded as the digital implementation of a first order continuous time filter, governed by a first order differential equation:

$$\dot{\phi}(t) + \tau^{-1} \, \phi(t) = A \, \dot{T}_{\mathrm{Ti}}(t) + B \, T_{\mathrm{Ti}}(t) \, , \quad \left(\dot{\cdot} \equiv \frac{d}{dt} \right) \tag{8.44}$$

where τ is the characteristic time constant of the analog filter, and A and B are scale factors, respectively weighing the contributions of the temperature's time variation rate and the temperature itself to the phase shift effect. We have assumed the $T_{\mathrm{Ti}}(t)$ dependence in the *rhs* of (8.44) in line with the fit result expressed by the *rhs* of (8.43).

If the time constant τ is much larger than the sampling time Δt implicit in equation (8.43) then we can approximate time derivatives by

$$\dot{\phi}(t) \simeq \frac{\phi(t) - \phi(t - \Delta t)}{\Delta t} \tag{8.45}$$

and, *mutatis mutandi*, the same for $T_{\mathrm{Ti}}(t)$. Taking $t = n \Delta t$ for the timing of the n-th sample, and using the natural notation $\phi[n] \equiv \phi(n \Delta t)$, equation (8.44) is approximated by

$$
\begin{aligned}
\phi[n] - \left(1 + \frac{\Delta t}{\tau} \right)^{-1} \phi[n-1] \;=\; & A \left(1 + \frac{\Delta t}{\tau} \right)^{-1} \left\{ T_{\mathrm{Ti}}[n] - T_{\mathrm{Ti}}[n-1] \right\} \\
& + \; B \, \Delta t \left(1 + \frac{\Delta t}{\tau} \right)^{-1} T_{\mathrm{Ti}}[n]
\end{aligned}
\tag{8.46}
$$

This can be readily compared to equation (8.43) to obtain

$$\beta = - \left(1 + \frac{\Delta t}{\tau} \right)^{-1} , \quad \alpha = A \left(1 + \frac{\Delta t}{\tau} \right)^{-1} , \quad \delta = B \, \Delta t \left(1 + \frac{\Delta t}{\tau} \right)^{-1} \tag{8.47}$$

β is seen to have a value very close to -1 (Table 8.3), or $\beta = -(1 - \eta)$ with $\eta < 10^{-2}$ comfortably in all cases. Hence $\tau \simeq \Delta t / \eta$, i.e., $\tau \gg \Delta t$, which *a posteriori* justifies the approximation leading to equation (8.46).

The formal solution to equation (8.44) can be easily written down. After initial transients die out, the phase is given by

$$\phi(t) = A \, T_{\mathrm{Ti}}(t) + (B - A) \, \tau^{-1} \int_0^t e^{-(t - t')/\tau} \, T_{\mathrm{Ti}}(t') \, dt' \tag{8.48}$$

170

The meaning of this filter equation is better understood if we recast it in frequency domain:

$$\widetilde{\phi}(\omega) = \left[A \frac{i\omega\tau}{1 + i\omega\tau} + B \frac{\tau}{1 + i\omega\tau} \right] \widetilde{T}_{\text{Ti}}(\omega) \tag{8.49}$$

This equation shows again that the analog process is also the superposition of two contributions: a *high-pass* filter proportional to A, and a *low-pass* contribution proportional to B: the first arises in equation (8.43) due to the titanium temperature derivative, while the second appears related to the term proportional to the titanium absolute temperature. This split dependence of the OW response to temperature pulses points to two different physical thermal processes affecting the glass, as will be discussed in § 8.5.

We can now make use of equations (8.47) to identify the coefficients A and B in terms of the fit parameter values of Table 8.3. Taking $\Delta t/\tau \ll 1$, we find that $A \simeq \alpha$, and $B \simeq \delta/\Delta t$. In addition, we can take advantage of the relationship $\alpha \simeq p_1$ between the auto-regressive and the DLR model parameters to obtain an expression relating both models. Accordingly, equation (8.48) can be rewritten as

$$\phi(t) \simeq p_1\, T_{\text{Ti}}(t) + (\delta/\Delta t - p_1)\, \tau^{-1} \int_0^t e^{-(t-t')/\tau}\, T_{\text{Ti}}(t')\, dt' \tag{8.50}$$

If we go back to the DLR fit formula, equation (8.12), the following expression ensues:

$$T_{\text{Glass}}(t) \simeq -\frac{p_1}{p_2}\, \tau^{-1} \int_0^t e^{-(t-t')/\tau}\, T_{\text{Ti}}(t')\, dt' \tag{8.51}$$

after the term $\delta/\Delta t$ has been been safely neglected in front of p_1. We thus see that temperatures in the titanium flange and in the OW glass are related by a low-pass filter with a time constant, τ, of a few hundred seconds —note that p_1 and p_2 have different signs, Table 8.3.

It must be recalled that this relationship emerges out of the good quality of the fits by both DLR and $ARMA$(2,1) models, and is key to understanding why *only* the titanium gauge is required to make a good prediction of the OW response to temperature variations, as will be required in flight. The *physical reason* for the observed relationship between temperatures is to be sought in the properties of the interface between the titanium and the glass in the OW.

8.5   Physics of the *ARMA* process

Two different kinds of thermal effects have been identified as sources of changes in the optical path-length of a light beam traversing a plane-parallel piece of glass:

i. Temperature dependent changes of the refraction index

ii. Mechanical stress induced changes of the refraction index

We briefly describe below how these effects can be approximately evaluated.

8.5.1 Temperature dependent changes of the refraction index

The first effect, which is found under stress free conditions, is quantified by the formula [57]

$$\frac{d\phi}{dT}\bigg|_{\text{free}} = 2\pi\frac{L}{\lambda}\left[\frac{dn}{dT} + (n-1)\,\alpha_E\right] \tag{8.52}$$

where ϕ is the phase shift suffered by a beam of light traversing a glass slab of thickness L and (nominal) index of refraction n; λ is the wavelength of the used light, and α_E is the linear thermal expansion factor of the glass, $\alpha_E = L^{-1}\,dL/dT$.

The $d\phi/dT|_{\text{free}}$ effect is most prominent at very low frequencies and DC. The reason is that it happens even if the temperature of the glass is homogeneous, and without mechanical stresses. It has been measured on *naked* glass samples in the laboratory, free of any pressure or tension, with the result that it is 25 mrad/K [60], a figure very well matching the one given by equation (8.31). One however needs to consider that the latter was obtained from data of a real window, i.e., including metal flange. This consequently means that the stress contribution $d\phi/d\sigma$ must be comparatively small at very low frequencies.

The same result is endorsed by another independent evidence. If data-sheet properties of the *OHARA S-PHM52* glass used in the experiment are used to calculate the thermal related path-length variations in the optical window glass due to changes in the refractive index, the result is that $d\phi/dT|_{\text{free}}$ is $\sim$21 mrad/K, again in good agreement with equation (8.31).

8.5.2 Mechanical stress induced changes of the refraction index

This second effect is relevant to our experiment because the glass, clamped by titanium flanges to the ISH structure, is under stress due to differing thermal expansion coefficients in glass and metal. Mechanical stress also induces pathlength changes which are difficult to model. From the datasheet, the only parameter provided by the manufacturer which can be used to quantify these interactions is the *photoelastic coefficient*, β. However, it must be noticed that β does not describe the change in the refraction index due to stress, $dn/d\sigma$, but the appearance of birefringence due to stress, i.e., the change of the velocity of light along different axes of the material. Although not directly related, both parameters range in the same order of magnitude [57], and we shall thus use the photoelastic coefficient here for our order of magnitude estimate, described in the following.

Under this simplyfying assumption, the photoelastic coefficient can be related to a pathlength variation by

$$\Delta s_{\text{stress}} = \beta\,\sigma\,d \tag{8.53}$$

where $\beta = 10^{-5}\,\text{nm}\,\text{cm}^{-1}\,\text{Pa}^{-1}$, d is the glass thickness ($d = 0.6$ cm for the Optical Window), and σ is the applied stress, having dimensions of pressure.

In this case, the stress on the glass is due to *differential* thermal dilatation of the titanium flange and the OW glass itself. The situation is illustrated graphically in Figure 8.6. Because the coefficient of thermal expansion of the glass is larger than that of the titanium flange embracing it,

the latter expands less when submitted to the same temperature rise, and hence the glass is compressed radially along the rim. The opposite happens if the temperature decreases, i.e., the glass is in this case stretched outwards by the radial pull of the titanium. The contraction/expansion forces acting on glass and titanium reach an equilibrium state which determines the radii of the contracted/expanded pieces of titanium and glass. The equilibrium position thus happens when

$$[\delta\rho_T + \delta\rho_\sigma]_{\text{Ti}} = [\delta\rho_T - \delta\rho_\sigma]_{\text{Glass}} \tag{8.54}$$

where $\delta\rho_T$ and $\delta\rho_\sigma$ refers to changes in radius caused by temperature changes and by stresses, respectively. The above formula holds even if temperature changes in titanium and glass are unequal. On the other hand, we are not considering in our description possible effects coming from the *Helicoflex* ring between the titanium and the glass. As stated above, we are here trying to get an order of magnitude of the effect based on a simplified mechanical model, and interface effects are thus not included.

The contributions appearing in equation (8.54) are given by [96]

$$\delta\rho_T = \rho\,\alpha\Delta T \quad \text{and} \quad \delta\rho_\sigma = \frac{p\,\rho^2}{\ell\,E} \tag{8.55}$$

where ρ is the radius of the interface between titanium and the glass, ℓ stands for the width of the body, E is the Young modulus, α the thermal expansion coefficient and p the lateral pressure. Combining equations (8.54) and (8.55), and following the notation of Figure 8.6, we find the lateral pressure on the glass:

$$p = \frac{\alpha_{\text{Ti}}\Delta T_{\text{Ti}} - \alpha_{\text{Glass}}\Delta T_{\text{Glass}}}{(r/h)\,E_{\text{Ti}}^{-1} + E_{\text{Glass}}^{-1}} \tag{8.56}$$

The strain on the glass lateral surface is given by $\sigma_{\text{Glass}} = prd/(r\,d) = p$, where d is the thickness of the window glass —see [96]. Hence,

$$\sigma_{\text{Glass}} = \frac{\alpha_{\text{Ti}}\Delta T_{\text{Ti}} - \alpha_{\text{Glass}}\Delta T_{\text{Glass}}}{E_{\text{Ti}}^{-1} + (h/r)\,E_{\text{Glass}}^{-1}} \tag{8.57}$$

We can consider two different regimes here: the *low frequency* (LF) regime and the *high frequency* (HF) regime. The first corresponds to long duration heat pulses applied on the titanium flange, actually long enough that the temperatures of the glass and the titanium equal each other, or $\Delta T_{\text{Ti}} = \Delta T_{\text{Glass}} \equiv \Delta T$. In this case

$$\sigma_{\text{Glass}} = \frac{\alpha_{\text{Ti}} - \alpha_{\text{Glass}}}{E_{\text{Ti}}^{-1} + (h/r)\,E_{\text{Glass}}^{-1}}\,\Delta T \; , \quad \text{low frequency} \tag{8.58}$$

On the other hand, if short heat pulses are applied on the titanium then the glass does not have time to respond, and in this we can assume $\Delta T_{\text{Glass}} = 0$ and $\Delta T_{\text{Ti}} \equiv \Delta T$. Thus,

$$\sigma_{\text{Glass}} = \frac{\alpha_{\text{Ti}}}{E_{\text{Ti}}^{-1} + (h/r)\,E_{\text{Glass}}^{-1}}\,\Delta T \; , \quad \text{high frequency} \tag{8.59}$$
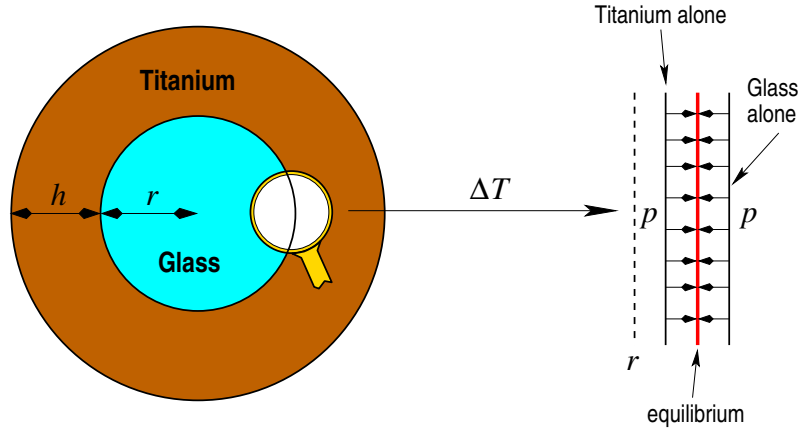
Figure 8.6: Schematics of the dilatation of the OW glass and the clamping titanium flange: the right part zooms in the profiles acquired by the interface (red) when the temperature of the block increases by ΔT. Should either the glass or the titanium be let expand freely, the boundaries would be placed as also represented. Dashed line is the interface position before heating.

We can use the above formulas in combination with (8.53) to obtain

$$\left.\frac{d\phi}{dT}\right|_{\text{Stress}} = \begin{cases} \beta\dfrac{2\pi d}{\lambda_{\text{laser}}}\dfrac{\alpha_{\text{Ti}} - \alpha_{\text{Glass}}}{E_{\text{Ti}}^{-1} + (h/r)\,E_{\text{Glass}}^{-1}} \, , & \text{low frequency} \\[4mm] \beta\dfrac{2\pi d}{\lambda_{\text{laser}}}\dfrac{\alpha_{\text{Ti}}}{E_{\text{Ti}}^{-1} + (h/r)\,E_{\text{Glass}}^{-1}} \, , & \text{high frequency} \end{cases} \tag{8.60}$$

It is recalled that $\Delta\phi = 2\pi\Delta s/\lambda_{\text{laser}}$, where λ_{laser} is the laser wavelength. We put numbers here:

$$\beta = 10^{-3} \times 10^{-9} \text{ Pa}^{-1}$$
$$d = 6 \times 10^{-3} \text{ m}$$
$$\lambda_{\text{laser}} = 1.064 \times 10^{-6} \text{ m}$$
$$\alpha_{\text{Ti}} = 8.6 \times 10^{-6} \text{ K}^{-1}$$
$$E_{\text{Ti}} = 11.6 \times 10^{10} \text{ N m}^{-2}$$
$$h = 0.02 \text{ m}$$
$$\alpha_{\text{Glass}} = 10 \times 10^{-6} \text{ K}^{-1}$$
$$E_{\text{Glass}} = 7.15 \times 10^{10} \text{ N m}^{-2}$$
$$r = 0.015 \text{ m}$$

to obtain

$$\left.\frac{d\phi}{dT}\right|_{\text{Stress}} = \begin{cases} 2.5 \times 10^{-3} \text{ rad K}^{-1} \, , & \text{low frequency} \\[2mm] 15 \times 10^{-3} \text{ rad K}^{-1} \, , & \text{high frequency} \end{cases} \tag{8.61}$$

Discussion of the results

The total thermal effect is the sum of the above two effects, i.e., optical pathlength changes induced by pure thermal expansion and by mechanical stress. The former gives a value of 21×10^{-3} rad K^{-1} throughout the frequency band, as extracted from datasheet values — see § 8.5.1 above. We can thus summarise the results as shown in Table 8.2:

	ARMA	Analytic
LF range	25 ± 4	23.5
HF range	40	36
Nude glass	—	21

Table 8.2: $d\phi/dT$, units in mrad K^{-1}.

The agreement between the results produced by our simplified model and the *ARMA* fit is quite good. Even though the model is not fully comprehensive of all the physical effects happening in the OW, it can be considered rather satisfactory from a purely empirical point of view, hence very useful for practical purposes. Work is currently in progress for a more thorough approach, and we shall report on new results in due course.

We conclude from this discussion that the low pass component of the transfer function is almost exclusively related to the $d\phi/dT|_{\mathrm{free}}$ effect, while the stress effects only show up significantly in the higher frequency band. This makes sense, as stresses applied along the glass rim quickly propagate inwards throughout the glass piece.

Although the LTP spectrum is only above $1\,\mathrm{mHz}$, an analysis at frequencies below this one, down to $10^{-4}\,\mathrm{Hz}$ and even further, must be considered of high interest, as the latter frequency band will be important for LISA. The experimental data reported in this paper can be improved to access the lower LISA band, since they typically consist in one hour long runs. This is a strong suggestion for the LTP experiment plan.

8.6 Noise projection

One of the main scientific objectives of the diagnostics system in the LTP is to measure identified environmental disturbances [100], and to provide the data and analysis tools to estimate the contribution of those disturbances to the overall mission noise budget. In practice this means the LTP Data and Diagnostics Subsystem (DDS) must be able to provide suitable *transfer functions* to convert measured disturbance noise into test mass acceleration noise. This section is devoted to describe this procedure in the case of temperature fluctuation noise in the OW, and to show how it works in an on-ground laboratory experiment —to be extrapolated to a space-borne one.

We will use the results derived in the previous analysis to obtain an estimation for the thermal contribution to the interferometer performance. We shall naturally limit ourselves to *ARMA* model, since it is the one making sense for real mission purposes, as already discussed.
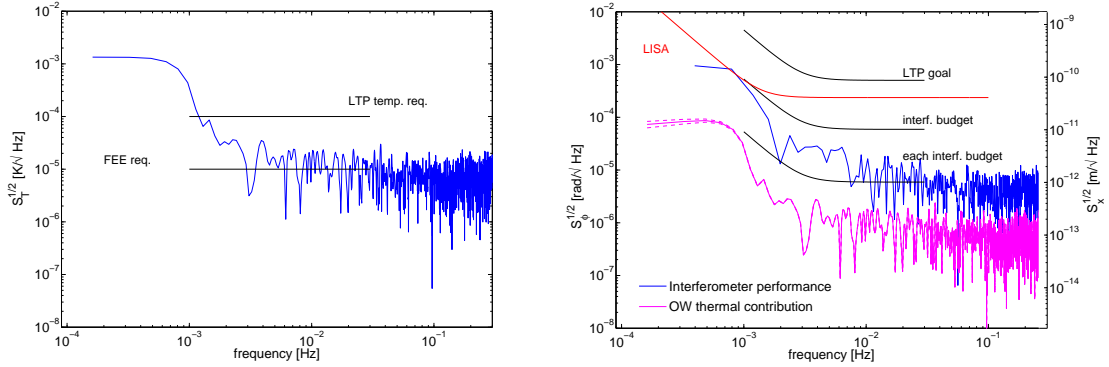
Figure 8.7: Temperature fluctuations spectrum (left) measured during the performance experiment compared to the LTP temperature requirement and the lower limit set by the front end electronics sensitivity limit. Phase fluctuations (blue curve, right panel) during the same run are compared to the optical window thermal contribution (magenta curve, right panel), as derived with the *ARMA* transfer functions given by equations (8.63) and (8.28). The 1σ confidence region is also included for the latter.

The basic idea is that the OW transfer function, as determined from high SNR system response, also applies when there is only (weaker) noise in the window [51]. For this we shall use the one in equation (8.22), i.e.,

$$G(z, \alpha, \beta, \delta) = \alpha \, \frac{1 - z^{-1}}{1 + \beta z^{-1}} + \frac{\delta}{1 + \beta z^{-1}} \tag{8.62}$$

We now show which procedures must be applied to address the problem of finding the contribution of temperature fluctuations noise in the OW to the total OW noise. To this end we consider data of temperature and phase noise generated in a different experiment, and apply to it the methodology just sketched.

The laboratory setup and the experimental details can be found in reference [59]. In this experiment, the optical window is not part of a testing Optical Bench (OB), but is glued in a lateral side of the LTP OB Engineering Model, instead. This way, a double beam pass across the window is forced: the laser light travels from the optical bench through the OW to a *dummy* mirror, faking a test mass; there, it is reflected, sent back again across the OW and out to the OB. Such setup proved to be compliant with the interferometer noise budget, showing that the inclusion of the OW does not degrade the interferometer performance. Two temperature sensors in the titanium flange and one in the glass were left in place to measure temperature values during long term runs.

No thermal disturbances were deliberately introduced, so the thermometers only read environmental temperature fluctuations. We use equation (8.28) to convert the temperature fluctuations spectral density, $S_T^{1/2}(\omega)$, into a phasemeter spectral density, $S_{\phi,T}^{1/2}(\omega)$. Thus,

$$S_{\phi,T}^{1/2}(\omega) = 2 \, |\widetilde{G}(\omega, \alpha, \beta, \delta)| \, S_T^{1/2}(\omega) \tag{8.63}$$

176

where the numerical factor 2 is required to account for the double passage of the laser beam through the window in this case. We assume both passages are completely correlated, given the extremely small time scale of their occurrence compared to thermal reaction times. Spectral densities are therefore linearly added.

Results obtained in a typical run with that setup are plotted in Figure 8.7 (noise figures obtained with the LTP Data Analysis MATLAB Package[3] can be found in [71]). The left panel shows temperature fluctuations measured in the titanium flange. As can be seen, these reach the front end electronics (FEE) floor noise in the higher frequency region of the measuring bandwidth, while keeping slightly above the LTP maximum temperature fluctuations requirements limit in the lower frequencies, around 1 mHz [55]. This is in fact a worst case condition, since the temperature power spectrum decreases as frequency increases, and thus if the LTP temperature requirement is reached at the lower frequency range then the rest of the spectrum will naturally follow a descending curve like the one shown in Figure 8.7.

The phasemeter fluctuations spectrum is however below the required noise level, as we can see in the blue curve of the right panel. The temperature fluctuations spectral data in the left panel are then submitted to the algorithm, equation (8.63), and the result is the magenta curve displayed in the right panel.

The low coupling to thermal disturbances implied by $\widetilde{G}(\omega, \alpha, \beta, \delta)$ causes the thermal contribution to only represent 5 % of the phasemeter noise at 1 mHz, and about 0.5 % of the LTP goal. We thus feel reassured that there is still considerable margin here.

---

[3]http://www.lisa.uni-hannover.de/ltpda

IV. Conclusions

" No fa falta que ataquis amb tantes respostes,
tenc preguntes per copar quatre segles d'escorça. "

Camp de Maduixes
Antònia Font

Chapter 9

Conclusions

In this study we have been dealing with some aspects around the thermal diagnostics on the LISA Technology Package (LTP) experiment on board the LISA PathFinder (LPF) mission. We conclude herein some of the main results and possible extensions of some of the problems we addressed in the previous chapters.

In order to build a stable thermal insulator at low frequencies, we have derived analytical solutions of thermal transfer functions for simple geometries. These are defined as the ratio of temperature fluctuation in a given point inside a body with respect the temperature disturbance around it. Because our final scope is the characterisation of a temperature acquisition system in the frequency band $1\,\mathrm{mHz} \leq \omega \leq 30\,\mathrm{mHz}$, we performed this analysis directly in the frequency domain which turns out to be easier than dealing with the correspondent Sturm-Liouville problem for the time domain solution. In addition we also explored the numerical evaluation of thermal transfer functions by means of thermal simulation and found a method to obtain a transfer function for a given geometry. The methodology is based on the frequency sweep procedure, usually applied to electronic systems, translated to the thermal case. The analytical expression derived, together with extensions to other geometries or the numerical methodology proposed can be applied to a wide variety of thermal problems as far as, in our case, the interesting results lies in the frequency domain behaviour of the system.

As previously stated, the transfer function formalism was developed to design a thermal test bench required to test the thermal data acquisition subsystem. The insulator finally implemented was based on a two layer scheme of a insulator material shell nesting a metallic core where the sensors were attached. Results obtained with this thermal bench showed a good agreement with the transfer function derived, both analytically and by numerical simulation, reassuring the validity of this approach. In what respects the thermal FEE performance results, although first results showed a slight noise excess in the low frequency band $\sim 1\,\mathrm{mHz}$, the noise source was detected to be mainly due to non-linearities in the A/D and solutions for this effect were faced and are currently under development. Another point which may need further development is the treatment of the

heat leaks through the wires. Our approach considered all the heat flux generated from end to end of the wire as heating up the whole metallic core, however thermal contact or self-heating effects could induce different behaviours than the first order response that we found and consequently used to size this disturbance.

The analytical expressions obtained for the design of thermal insulators, validated with the experimental results with the thermal FEE, allowed the design and construction of two more insulators, this time with an opening mechanism and therefore being a non-destructive test, which are currently being used for the evaluation of temperature sensors performance after these devices undergo a baking process.

Once the thermal FEE was characterised we addressed thermal problems related more closely with the LTP experiment. A first step was to size the heaters that will fly on board the mission. To this end the LCA thermal model developed by CGS was used to evaluate the temperature evolution of heat inputs in a extremely thermal stable environment as the LTP will be. Moreover, the thermal model can be thought not only as an evaluation tool to perform the previous studies on heaters' sizing but also a tool to obtain relevant scientific information in itself. As an example, we examined the possibility of evaluating the radiation view factor of the test mass to the electrode housing with the thermal model. This factor scales the thermal coupling of the test mass motion with thermal disturbances and is therefore of scientific interest for the mission. Our results are in the same order of magnitude as the ones obtained experimentally but are, obviously, strongly dependent on the modelling. Other relevant information can be obtained from the LCA model: we are currently working on the application of the thermal frequency sweep methodology to the thermal model in order to obtain thermal transfer functions from point to point of the LCA; also a thermal mapping tool able to predict temperature values in the LCA based on the data acquired by the sensors distributed through the experiment is also being studied, based on the information gathered in the thermal model.

Together with the results of the simulations in the thermal model, we could also perform thermal experiments in the Optical Bench Engineering Model, and with an Optical Window prototype in collaboration with the AEI-Hannover. Both simulation and experimental data were used to define a maximum power required for the heaters on board the mission. The values derived in this work were translated into a DDS requirement to be implemented by the industrial partner. Moreover, the definition of a required power has a direct impact on the technological solution to be implemented in the flight model given the very restrictive conditions on board the satellite.

The experimental campaign on the Optical Bench allowed the determination of some coupling values between the temperature increase on the Optical Bench and the flanges and the response of the interferometer. The physical mechanism behind these factors could not be clearly enough determined and thus these factors must be considered as a phenomenological approximation to the problem which requires a more thorough analysis.

In the Optical Window case, an extensive thermal test campaign yielded a good enough data set to perform a more detailed study of the data analysis techniques required to deal with the diagnostic problem. The data analysis methodology described in the previous chapters of this

thesis has allowed the description of the interferometric response of a laser beam going through the Optical Window to a heat input in terms of an *ARMA* digital filter. The dynamics described by the difference equation behind the *ARMA* has proved to be very useful to understand the physical effects contributing to the thermal noise. Moreover, the *ARMA* filter can be directly translated into a transfer function in the frequency domain which gives us the information of the noise contribution in the measuring bandwidth, which is the final scope of the diagnostics.

It is worth mentioning that the *ARMA* noise model for the Optical Window sets a parametrisation that can be useful for the LTP experiment during in-flight operations. In this sense, the current work provides a methodology to deal with the data but, at the same time, a strong recommendation to include data runs long enough to correctly evaluate the low frequency region of the *ARMA* filter which is of relevance not only for the LPF mission but also for the proposed gravitational wave detector LISA. In the same line of reasoning it is also necessary to stress the good results obtained, in terms of parameter error, with the BMLS signal. Although we do not provide conclusive results, we think that the pseudorandom signal could be considered an important data analysis tool to evaluate noise contributions in the LTP experiment.

These properties are general enough to be applied in the thermal data analysis on different locations in the LTP experiment. To confirm this approach, more data analysis on real experimental data needs to be afforded in order to test the methodology with the response of other subsystems to thermal shocks, clearly the most interesting being the GRS. On the other hand, a key point which needs improvement is the analysis of MIMO (Multiple Input-Multiple Output) data sets, which is usually the case in gravitational wave detectors. In the present work we have focused on the *ARMA* filter in a SISO (Single Input-Single Output) example which has helped us to gain physical insight, however a real implementation of this methodology will imply the description of a MIMO experiment and its associated problems.

The discussion and implementation of this technique must undergo in the framework of the current LTP Data Analysis Toolbox development, a current taskforce inside the LTP collaboration in charge of the definition and implementation of a data analysis MATLAB toolbox for the analysis of the LTP experiment data.

V Resum en català

Chapter 10

Resum

L'objectiu d'aquesta tesi és l'estudi i caracterització dels fenòmens tèrmics que actuen com a fonts de soroll en un detector d'ones gravitatòries espacial. Dintre d'aquest camp, que engloba diferents disciplines i metodologies, el present treball estudia diferents aspectes al voltant d'aquest tema: des del disseny d'un aïllant tèrmic a baixes freqüències fins a la simulació de polsos tèrmics per a diagnòstic tèrmic, així com també l'estudi d'algoritmes d'anàlisi de dades que puguin caracteritzar de forma eficient el soroll tèrmic a bord del satèl·lit.

Aquest succint capítol intenta destacar-ne els resultats més significatius, mantenint una coherència en la presentació. A continuació, i per tal de posar aquest estudi en el context adient, passem a revisar breument les principals característiques de les ones gravitatòries i la problemàtica associada a la seva detecció.

10.1 Introducció

Les ones gravitatòries van ser introduïdes per Albert Einstein en la seva Teoria de la Relativitat General com a conseqüència de la velocitat finita de propagació de la interacció gravitatòria [30]. Einstein va mostrar que les equacions regint la interacció gravitatòria acceptaven solucions radiants, tal com també succeïa amb les lleis de l'electromagnetisme de Maxwell. Tot i això, l'extrema debilitat de la interacció gravitatòria ha fet que, tot i els esforços dedicats, a dia d'avui aquesta radiació no hagi pogut ser detectada.

Malgrat això, existeixen proves experimentals de l'existència d'aquesta radiació. Així, l'any 1974 els astrònoms R.A. Hulse i J.H. Taylor van poder mesurar com el sistema binari PSR 1913+16 reduïa progressivament el seu període de rotació [43], exactament segons la predicció que feia la Relativitat General tenint en compte que el sistema estava radiant ones gravitatòries. L'any 1993 ambdós van rebre el Premi Nobel de Física per aquest descobriment.

La recerca per tal d'obtenir una mesura directa d'aquesta radiació comença amb el treball de J.Weber qui, a la dècada dels 60, va dissenyar els primers detectors. Molts grups van seguir les idees

de Weber, les quals es basaven en els coneguts com a *detectors acústics*, mentre que d'altres van desenvolupar la tecnologia que resultaria en els que avui coneixem com a *detectors interferomètrics*. Els primers basen el seu principi de detecció en la ressonància que es produeix en un cos sòlid quan aquest interacciona amb una ona gravitatòria, la qual hem d'entendre en aquest context com una pertorbació del camp gravitatori que es propaga en el temps. L'efecte doncs serà el d'una *marea gravitatòria* que establirà gradients de força entre punts separats del sòlid activant-ne els modes de ressonància. El segon mètode es basa en la detecció del desplaçament relatiu entre dues masses que actuen com a miralls en un interferòmetre Michelson. A continuació es llisten els principals experiments que han posat en pràctica aquestes tècniques:

- **Detectors acústics** que podem subdividir per la seva forma entre les barres cilíndriques ALLEGRO [62] als EUA; AURIGA [25], EXPLORER [13] i NAUTILUS [14] a Itàlia i els detectors esfèrics MINIGRAIL [29] a Holanda i MARIO SCHENBERG [7] a Brasil. A títol d'exemple el detector NAUTILUS consisteix en un cilindre de $2300\,\mathrm{kg}$ d'alumini de $3\,\mathrm{m}$ de llarg el qual es manté a una temperatura de $0.1\,\mathrm{K}$. Les seves freqüències de ressonància, on es maximitza la possibilitat de detecció, es troben a 908 i 924 Hz.

- **Detectors interferomètrics** entre els que trobem els dos detectors LIGO [5] als EUA, de 4 i 2 km de longitud de braç de l'interferòmetre; VIRGO [19] a Itàlia amb 3 km de longitud i GEO600 [105] a Alemanya i TAMA [9] a Japó amb 600 m i 300 m respectivament.

La sensibilitat d'aquests instruments es mesura en unitats de tensió ("strain") $h \equiv \Delta L/L$. En el cas, per exemple, de l'experiment LIGO s'ha assolit una sensibilitat en l'ordre de magnitud $S^{1/2} \sim 10^{-23}\,\mathrm{Hz}^{-1/2}$ expressat en termes de densitat espectral de la tensió en la banda de freqüència $\sim 100\,\mathrm{Hz}$. L'anàlisi de les dades obtingudes amb aquesta sensibilitat ha permès establir cotes màximes en la detecció d'ones gravitatòries provinents de sistemes astrofísics en els que es preveu la generació d'aquesta radiació tals com: supernoves, estrelles de neutrons, sistemes binaris d'estrelles de neutrons i sistemes binaris de forats negres. També s'han establert cotes superiors per a un possible fons d'ones gravitatòries d'origen cosmològic.

Els detectors d'ones gravitatòries veuen limitada la seva sensibilitat en la banda de freqüències inferior a $\sim 10\,\mathrm{Hz}$ degut al soroll d'origen sísmic i al degut a activitats humanes. És per aquesta raó que es va idear la missió Laser Interferometer Space Antenna (LISA) que pretén situar un observatori d'ones gravitatòries en òrbita al voltant del Sol.

10.1.1 LISA i LISA Pathfinder

LISA és una missió conjunta ESA-NASA, dissenyada com un detector d'ones gravitatòries amb sensibilitat màxima a la banda del mil·lihertz. El disseny de LISA es basa en tres naus cadascuna de les quals conté una massa (massa de test) en caiguda lliure, separades una respecte l'altre $5 \times 10^6\,\mathrm{km}$. Cada nau està connectada a les altres dues mitjançant un làser infraroig que permet observar el desplaçament relatiu entre cada parell de masses. D'aquesta manera aquestes masses actuen com a miralls de l'interferòmetre.
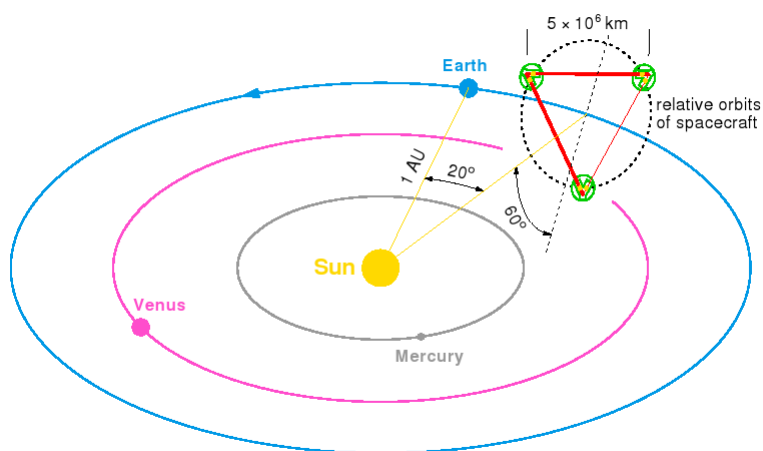
Figure 10.1: Esquema de l'òrbita de LISA

Per tal de mantenir les masses en caiguda lliure a l'interior de les naus s'utilitzen sensors capacitatius capaços de mesurar la posició de la massa test respecte de la nau fins a la resolució del nanòmetre sense necessitat d'establir contacte físic i sense pertorbar la caiguda lliure. Les mesures d'aquests sensors s'acoblen a uns propulsors que permeten corregir de forma controlada la trajectòria de la nau aplicant forces de micronewtons. El llaç de control que s'estableix entre el sensor capacitatiu i els propulsors s'anomena control *drag-free*.

Els requeriments que ha d'assolir el làser per tal de detectar ones gravitatòries en LISA són, al igual que en el cas del *drag-free*, extremadament exigents. Cal tenir en compte que la font de làser en cada nau és d'1 W de potència i que després de travessar els 5×10^6 km (que tarda en recórrer 30 s) arriba a la segona nau amb una potència d'uns 10^{-12} W i dispersada en una àrea d'uns quants quilòmetres. Aquest feix làser és el que en la segona nau es fa interferir amb un làser local per tal de determinar la posició relativa entre les dues masses de test.

La detecció d'ones gravitatòries a l'espai requereix certs desenvolupaments tecnològics sense els quals la missió LISA no és possible. Aquesta és la principal raó que conduí a la proposta d'una missió prèvia per tal de testejar aquesta tecnologia: aquesta és la missió LISA Pathfinder (LPF), en el seu inici anomenada SMART-2, que a dia d'avui té data de llançament l'any 2010. Aquesta missió consta de dos experiments que persegueixen el mateix objectiu: l'europeu LISA Technology Package (LTP) i l'americà Disturbance Reduction System (DRS).

El concepte darrera la missió LISA Pathfinder és el d'escurçar un braç de LISA dels 5×10^6 km als 30 cm. Així, la missió consta de dues masses de test situades en una mateixa nau, el sistema de control *drag-free* permet mantenir aquestes masses en caiguda lliure (no pot però seguir les dues masses de test alhora en totes les direccions) a l'interior del satèl·lit protegint-les de forces externes i de pertorbacions que afecten el seu moviment que provenen de la mateixa nau. Al mateix temps un interferòmetre s'encarrega de mesurar la distància relativa entre les dues masses fins a una
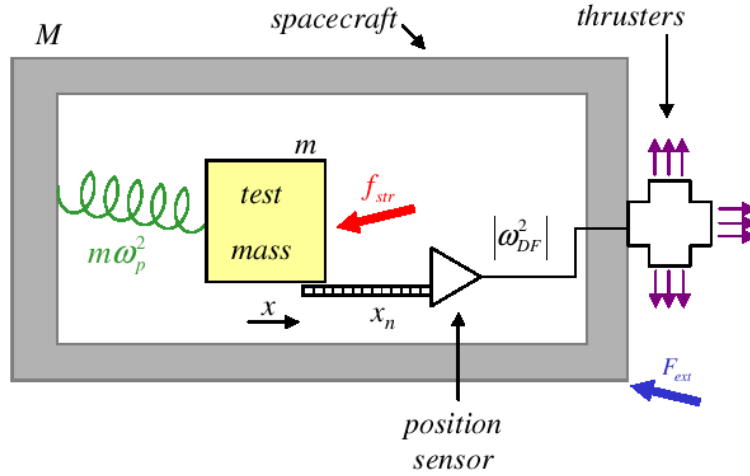
Figure 10.2: El principi de funcionament del *drag free*. La nau (M) protegeix la massa de test (m) de forces externes (F_{ext}). Per tal de mantenir-se centrada al voltant de la massa de test, la nau està equipada amb sensors de posició el senyal dels quals alimenta els propulsors en un llaç de control amb guany ω_{DF}^2. Possibles fonts de soroll són: el soroll de desplaçament del sensor x_n, forces errants f_{str} i l'acoblament de la nau a la massa de test degut a qualsevol gradient de força en DC.

resolució picomètrica.

El requeriment científic d'aquesta missió s'escriu en termes de la densitat espectral de l'acceleració relativa entre les dues masses, l'objectiu és per tant [10]

$$S_{a,\mathrm{LPF}}^{1/2}(\omega) \leq 3 \times 10^{-14} \left[1 + \left(\frac{\omega/2\pi}{3 \ \mathrm{mHz}} \right)^2 \right] \mathrm{m\,s^{-2}}/\sqrt{\mathrm{Hz}} \qquad (10.1)$$

en el rang de freqüències $1\,\mathrm{mHz} \leq \omega/2\pi \leq 30\,\mathrm{mHz}$. Es considera que l'assoliment d'aquest objectiu demostra la viabilitat de LISA, en la qual el requeriment anterior és 10 vegades més exigent tant en la magnitud de l'acceleració com en la banda de freqüències.

Si hom considera una nau de massa M protegint una massa (m) en caiguda lliure i que, mitjançant un conjunt de sensors, mesura la distància relativa entre la nau i la massa al mateix temps que utilitza aquest senyal per mantenir-se centrada al voltant de la massa, es demostra que l'acceleració sobre aquesta massa test ve donada per [42]

$$a = \frac{f_{str}}{m} + \omega_p^2 \left(x_n + \frac{F_{ext}}{M\,\omega_{DF}^2} \right) = \frac{f_{str}}{m} + \omega_p^2 \Delta x \qquad (10.2)$$

on

- F_{ext} són les forces aplicades sobre la nau.

- f_{str} és qualsevol força errant ("stray force") que s'aplica sobre la massa de test, tan provinent del satèl·lit mateix (p.ex. tèrmiques) com de l'exterior (p.ex. raigs còsmics).
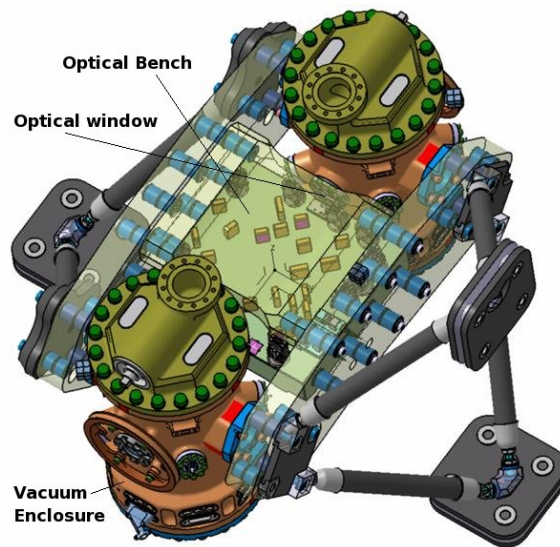
Figure 10.3: Disseny de la part central de l'experiment LTP a dia 13 d'octubre de 2006.

- x_n és el soroll del sensor de posició.

- ω_p és la rigidesa paràsita ("parasitic stiffness") per unitat de massa que acobla el moviment del satèl·lit a la massa de test.

L'exigent objectiu (10.1) estableix requeriments en cadascun dels paràmetres de l'equació anterior [100]. Aquests requeriments tenen implicacions per a tots els subsistemes del LTP que són el Sensor de Referència Gravitatòria GRS (sigles de l'acrònim anglès), el Subsistema de Metrologia Òptica OMS i el Subsistema de Diagnòstic i Dades DDS. En particular el límit que s'estableix per a f_{str} té una repercussió directa en l'estabilitat tèrmica que s'ha d'assolir en el satèl·lit. Essent l'estudi dels fenòmens tèrmics l'objectiu principal d'aquesta tesi descriurem de forma abreujada quins són els efectes tèrmics que poden ser font de soroll en la mesura en el LTP i quins són els ginys de diagnòstic tèrmic dintre el DDS encarregats de caracteritzar aquesta contribució.

10.2 Diagnòstic tèrmic

L'objectiu del sistema de diagnòstic tèrmic a bord del LTP és el de poder mesurar i caracteritzar la contribució tèrmica al soroll de la mesura de l'acceleració relativa entre les dues masses de test de l'experiment. Aquesta contribució és la conseqüència de diferents mecanismes que provoquen l'acoblament de pertorbacions tèrmiques que es puguin produir en diferents punts amb la mesura de l'acceleració, ja sigui via efectes que pertorben l'interferòmetre o efectes que pertorben la mesura del sensor capacitatiu.

10.2.1 Efectes tèrmics

A continuació es descriuen els principals efectes d'acoblament tèrmic, distingint-los segons els subsistemes que afecten.

Efectes tèrmics en el GRS

Els principals efectes que poden afectar el Sistema Inercial són aquells que impliquen un desplaçament de la massa de test deguts a pertorbacions tèrmiques. Entre ells destaquen:

- **Pressió per radiació:** diferències en la temperatura a banda i banda de la carcassa que envolta la massa de test i suporta els elèctrodes que formen el detector capacitatiu ("electrode housing") poden provocar diferències en la radiació tèrmica que el sensor pot detectar. L'acceleració que introdueix aquest fenomen es descriu com

$$\Delta a_{\text{e.m.}} = \frac{16\, A_{\text{TM}}^2 \sigma}{3\, m_{\text{TM}} c}\, \alpha_{\text{e.m.}}\, T^3 \Delta T \tag{10.3}$$

on A_{TM} i m_{TM} són l'àrea encarada als elèctrodes i la massa de la massa de test, i $\alpha_{\text{e.m.}}$ un factor de correcció geomètric.

- **Efecte radiomètric:** En ambients de baixa pressió, les diferències de temperatura en el gas es tradueixen en diferències de pressió que poden tardar a equilibrar-se degut a les condicions rarificades. Aquesta contribució es descriu segons l'expressió següent

$$\Delta a_{\text{radiometer}} = \frac{1}{2}\, \frac{p\, A_{\text{TM}}}{m_{\text{TM}}}\, \frac{\Delta T}{T} \tag{10.4}$$

- *Outgassing***:** En condicions de buit, les interaccions de les molècules amb les parets poden tenir un comportament estadístic força allunyat del de la simple interacció elàstica. El procés d'*outgassing* és el que experimenten les molècules en aquestes superfícies quan, en certes condicions, poden alliberar-se del lligam que els uneix a la superfície. L'efecte depèn tant de la pressió i la temperatura com de la geometria o els materials emprats. Aquesta contribució a l'acceleració de la massa de test pot expressar-se com:

$$\Delta a_{out} = \frac{Q(T)\, A_{\text{TM}}}{C_{eff}\, m_{\text{TM}}}\, \frac{\Theta}{T^2} \Delta T \tag{10.5}$$

on $Q(T)$ és la taxa d'outgassing, C_{eff} és la conductància efectiva i conté dependències geomètriques i Θ és una temperatura d'activació.

D'altres efectes que també es poden considerar en aquest apartat poden ser p.ex. les distorsions tèrmiques de la carcassa dels elèctrodes que podrien afectar la mesura capacitativa o la col·lisió aleatòria de molècules sobre la massa de test.

Les estimacions quantitatives d'aquest fenomen són encara objecte d'estudi experimental; dels últims resultats en podem treure que el factor d'acoblament entre pertorbacions tèrmiques a la carcassa dels elèctrodes i acceleració sobre la massa de test és $\sim 100\,\text{pN/K}$ [21].

Efectes tèrmics a l'OMS

Els efectes en el cas del Subsistema de Metrologia Òptica poden afectar la mesura en diferents posicions. En general, l'efecte que cal considerar són dilatacions tèrmiques tot i que depenent de la posició on es produeixin poden produir efectes diferents. Així, gradients tèrmics en el banc òptic es poden traduir en desplaçaments que l'interferòmetre es capaç de mesurar. El mateix succeeix en el cas de pertorbacions tèrmiques en els puntals ("struts") que subjecten l'experiment dintre l'escut tèrmic en el satèl·lit, tot i que en aquest cas també podrien produir-se tensions mecàniques degut a diferències en el coeficient d'expansió tèrmica dels diferents materials.

Un últim objecte on aquests efectes poden ser rellevants és la finestra òptica que el làser ha de travessar des del banc òptic per arribar a la massa de test dins el tanc de buit. Essent l'únic component òptic que es troba fixat en una estructura metàl·lica és susceptible d'introduir soroll en la mesura. Aquesta contribució es discutirà extensament més endavant. Podem esmentar però aquí una primera estimació d'aquest efecte basant-nos en el full d'especificacions del material utilitzat en la finestra òptica, que implicaria una contribució de l'ordre $\approx 4 \times 21 \times 10^{-3}\,\text{rad/K}$. Si es volgués assolir un soroll interferomètric de $9\,\text{pm}/\sqrt{\text{Hz}}$ ($\approx 50\,\mu\text{rad}/\sqrt{\text{Hz}}$), això requeriria en aquestes condicions una estabilitat tèrmica $S_T^{1/2} \leq 6 \times 10^{-4}\,\text{K}/\sqrt{\text{Hz}}$ en la banda de mesura.

Requeriment tèrmic a l'LTP

El requeriment per a la contribució total del soroll en l'acceleració es considera *grosso modo* que ha de representar un màxim del 10% de l'objectiu final de la missió i que per tant es pot escriure com:

$$S_{a,T}^{1/2}(\omega) \leq 3 \times 10^{-15} \left[1 + \left(\frac{\omega/2\pi}{3\,\text{mHz}} \right)^2 \right] \text{m\,s}^{-2}/\sqrt{\text{Hz}} \tag{10.6}$$

Sumant totes les contribucions breument exposades fins aquí es considera que la contribució del soroll tèrmic compleix l'especificació anterior si es manté una estabilitat tèrmica a bord del satèl·lit que compleixi

$$S_T^{1/2}(\omega) \leq 10^{-4}\,\text{K}/\sqrt{\text{Hz}} \;, \quad 1\,\text{mHz} \leq \omega/2\pi \leq 30\,\text{mHz} \tag{10.7}$$

en la banda de mesura.

10.2.2   Ginys tèrmics

Per tal de mesurar l'estabilitat tèrmica i caracteritzar els efectes que s'han descrit, l'experiment LTP comptarà amb 23 sensors de temperatura de precisió, juntament amb un conjunt de 14

escalfadors situats en punts que es consideren crítics pel que fa a la seva sensibilitat tèrmica. Amb aquest subsistema tèrmic es pretén mesurar de forma contínua l'ambient en el satèl·lit així com les pertorbacions en la banda de mesura fins a la resolució marcada pel requeriment (10.7). De la mateixa manera els escalfadors permetran realitzar experiments on la contribució tèrmica al soroll de mesura es potenciarà per tal de poder-la caracteritzar i comprendre.

10.3 Eines d'anàlisi tèrmica

Per tal d'estudiar certs aspectes del diagnòstic tèrmic ha sigut necessari desenvolupar metodologies específiques d'anàlisi tèrmica que descrivim a continuació. L'objectiu és el de fer una primera descripció concisa per tal de passar amb posterioritat a l'aplicació en casos concrets.

10.3.1 Funcions de transferència tèrmiques

Sovint en problemes d'anàlisi tèrmica és necessari poder determinar quina és la capacitat d'aïllament tèrmic que permet un cert material o també quina és la configuració més adient per a obtenir una determinada estabilitat tèrmica. Aquest serà el nostre cas d'aplicació més endavant i amb aquesta finalitat s'han desenvolupat en aquesta tesi eines per poder afrontar aquest problemes.

L'anàlisi que es duu a terme normalment en l'enginyeria és el de les resistències tèrmiques, el qual es basa en una analogia del problema tèrmic amb l'elèctric i permet una anàlisi ràpida i senzilla dels paràmetres involucrats en el problema. L'extensió evident d'aquest esquema es troba en la metodologia dels *paràmetres agrupats* ("lumped parameters") que inclou en l'anàlisi la dependència temporal fonamentada en aproximacions no sempre vàlides, com ara que els gradients tèrmics a l'interior del cos estudiat són negligibles.

La manera com s'ha abordat aquest problema en el nostre estudi és el de resoldre l'equació de calor de Fourier a l'interior del sòlid. Aquesta s'escriu com

$$\rho C \, \partial_t T(\mathbf{x}, t) = \nabla \cdot [K \, \nabla T(\mathbf{x}, t)] \tag{10.8}$$

on ρ, C, K són la densitat, la calor específica i la conductivitat tèrmica, respectivament.

Donat que els requeriments en la missió LISA Pathfinder vénen definits en una determinada banda de freqüències baixes com hem vist a (10.1), una particularitat del nostre problema és que estarem interessats en el comportament d'un aïllant tèrmic en aquesta banda. La solució desenvolupada en aquesta tesi que s'ha demostrat més pràctica a l'hora de resoldre aquest problema ha sigut la de resoldre aquestes equacions en el domini de la freqüència. D'aquesta manera es pot obtenir analíticament el que es coneix com a funció de transferència, és a dir, quina és la relació entre les fluctuacions de temperatura a l'exterior i a qualsevol punt de l'interior del sòlid que ens interessa.

En el cas concret d'una esfera homogènia sotmesa a un bany tèrmic isòtrop, es demostra que la funció de transferència en el centre es pot obtenir de forma senzilla amb aquest mètode i es pot escriure de forma concisa com
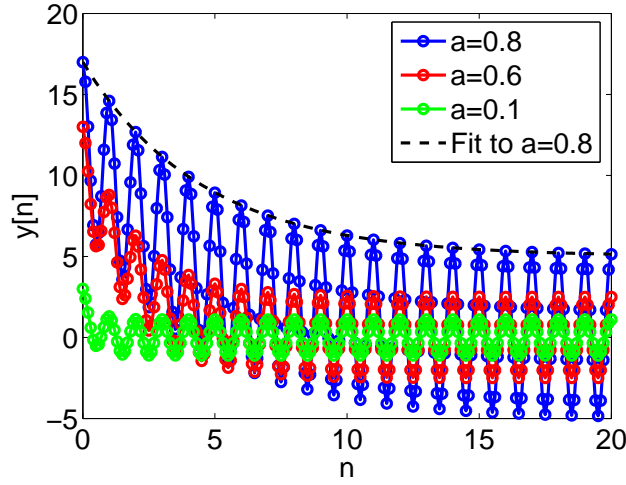
Figure 10.4: Representació gràfica de la resposta d'una equació en diferències de primer ordre a una entrada sinusoïdal considerant diferents valors per als paràmetres de l'equació en diferències. També es mostra l'ajust per obtenir l'amplitud en el cas estacionari.

$$\tilde{K}_0(0, \omega) = \frac{q\,a}{sin(q\,a)}, \qquad q^2 = -i\omega\frac{\rho C}{K} \tag{10.9}$$

que es pot expandir tenint en compte les dues components de la variables complexa q per obtenir

$$\tilde{K}(0, \omega) = \frac{(1+i)\beta}{\sinh(\beta)\cos(\beta) + i\cosh(\beta)\sin(\beta)}, \quad \beta \equiv \left|\frac{\omega\tau}{2}\right|^{1/2} \tag{10.10}$$

Aquesta metodologia s'ha estès a l'aplicació en altres geometries així com en casos de múltiples capes d'aïllament, la qual cosa serà d'especial interès més endavant.

10.3.2 Anàlisi d'escombrat tèrmic

La metodologia anterior ens dóna molta informació sobre el comportament tèrmic d'un sòlid en una certa zona de l'espai de freqüències sempre i quan puguem resoldre l'equació amb les condicions de contorn adients. Aquest últim pas no és sempre fàcil donat que la majoria de casos rellevants impliquen geometries que dificulten la solució analítica. Per aquesta raó és interessant desenvolupar una metodologia basada en un procediment numèric que ens permeti obtenir resultats mitjançant simulacions tèrmiques.

La metodologia que es descriu a continuació es basa en el que usualment es coneix com escombrat de freqüències en l'anàlisi de sistemes electrònics. En aquest mètode s'aplica una ona sinusoïdal a l'entrada del sistema i s'observa la seva resposta, repetint l'operació amb sinusoïdals a diferents freqüències es pot obtenir la funció de transferència del sistema en qüestió.

De la mateixa manera podem utilitzar en el nostre cas simulacions tèrmiques que ens permetin avaluar la resposta d'un determinat sistema a impulsos tèrmics sinusoïdals a diferents freqüències. Donat que la resposta d'un sistema la podem escriure de forma general com una resposta transitòria i una estacionària

$$
\begin{aligned}
y[n] &= y_{ss}[n] + y_{trs}[n] \\
&= H(\omega_0)\, A e^{i\,\omega_0\, n} + y_{trs}[n]
\end{aligned}
\tag{10.11}
$$

ajustant adequadament l'amplitud de la resposta a temps llargs podrem determinar la funció de transferència a la freqüència a la que estem aplicant l'ona sinusoïdal, que en l'equació (10.11) apareix indicada com $H(\omega_0)$.

La Figura 10.4 mostra un exemple d'aplicació d'aquest procediment.

10.4 Disseny del banc de proves tèrmic

Les eines prèviament descrites s'han posat a prova amb l'objectiu de dissenyar un aïllant tèrmic capaç d'atènyer el nivell d'estabilitat tèrmica necessari per demostrar que el subsistema de mesura tèrmica dissenyat per una col·laboració IEEC-UPC complia amb els requeriments necessaris.

Aquest requeriment es deriva del ja esmentat referent a l'estabilitat tèrmica en el satèl·lit, equació (10.7). Bàsicament es tracta d'assegurar que el conjunt que formen l'electrònica de mesura i els sensors de temperatura poden mesurar variacions tèrmiques fins a una estabilitat 10 vegades millor que l'estabilitat que hi haurà (nominalment) al satèl·lit. Evidentment, és necessari que la sensibilitat de l'aparell de mesures tèrmiques estigui per sota del nivell del soroll ambiental si volem estar segurs que s'ha assolit el nivell de soroll ambiental desitjat. El requeriment a complir per l'electrònica de mesures tèrmiques és

$$
S_{T,\text{FEE}}^{1/2}(\omega) \le 10^{-5}\,\text{K}\,\sqrt{\text{Hz}} \quad 1\,\text{mHz} \le \omega/2\pi \le 30\text{mHz}
\tag{10.12}
$$

Precisament seguint el mateix raonament si ara hem d'imposar quin ha de ser el nivell d'estabilitat que caldrà per demostrar el requeriment anterior és lògic aplicar la mateixa recepta i demanar una millora d'un ordre de magnitud en estabilitat tèrmica. Així tindrem que es fa necessari un ambient on sigui possible l'estabilitat donada per

$$
S_{T,\text{Bench}}^{1/2}(\omega) \le 10^{-6}\,\text{K}\,\sqrt{\text{Hz}} \quad 1\,\text{mHz} \le \omega/2\pi \le 30\text{mHz}
\tag{10.13}
$$

Donat que aquest valor es troba per sota del nivell de soroll del nostre aparell de mesura no podrem validar-lo experimentalment i caldrà basar-nos en una sòlid estudi analític del sistema analitzat com a aïllant.

El concepte de l'aïllant dissenyat es troba a la Figura 10.5 i es tracta senzillament de dues capes, una interior de metall que aporta inèrcia tèrmica i una d'exterior feta d'un mal conductor tèrmic,
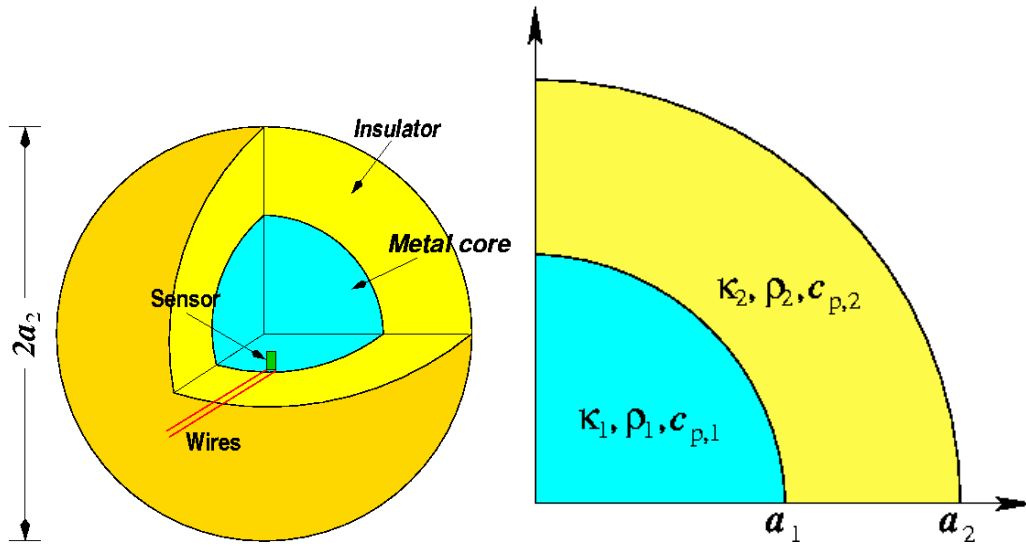
Figure 10.5: Concepte de l'aïllant tèrmic. *Esquerra:* diagrama amb la posició dels sensors a l'interior. *Dreta:* secció, amb la notació utilitzada.

que atenua les fluctuacions de l'exterior. La geometria esfèrica es considera per tal de simplificar l'anàlisi.

10.4.1 Funció de transferència de l'aïllant

De la metodologia prèviament descrita en podem obtenir una funció de transferència per a l'aïllant que ara ens ocupa. Es pot demostrar que en condicions d'un bany isòtrop, la funció de transferència ve donada per l'expressió

$$H_c(\omega) = \frac{K_2\, a_1\, a_2\, q_1\, q_2}{K_1\, \sinh(q_2\,(a_2 - a_1))\, F_1(a_1) + K_2\, \sinh(q_1\, a_1)\, F_2(a_2)} \tag{10.14a}$$

on $q^2 = -i\omega\rho\, C/K$, i $F_1(r)$ i $F_2(r)$ vénen donades per

$$F_1(r) = r\, q_1\, \cosh(q_1\, r) - \sinh(q_1\, r) \tag{10.14b}$$

$$F_2(r) = a_1\, q_2\, \cosh(q_2\,(r - a_1)) + \sinh(q_2\,(r - a_1)) \tag{10.14c}$$

A partir d'aquesta equació, i seleccionant els materials oportuns (alumini i poliuretà en el nostre cas), podem obtenir quines són les dimensions a partir de les quals es complirà el requeriment que ens hem imposat, equació (10.13), les quals vénen donades per

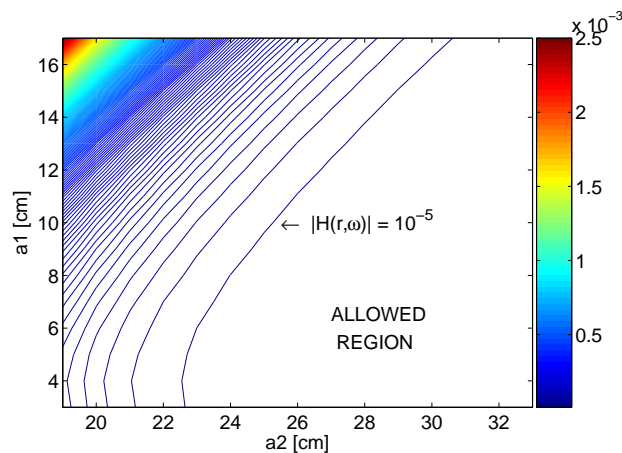$$a_1 = 15.7\,\text{cm} \quad a_2 = 57\,\text{cm} \tag{10.15}$$

Figure 10.6: Mapa de la supressió de l'amplitud de la fluctuació tèrmica a l'interior d'un aïllant format per una capa d'alumini a l'interior d'una closca de poliuretà. la supressió es mostra com a funció dels radis de les dues capes. Les línies mostren salts de 10^{-5}.

Val a dir que les prediccions del model analític s'ajusten perfectament a les que s'obtenen d'un model tèrmic on hem aplicat la metodologia de l'escombrat tèrmic. Obtenim així un acord complet entre els dos mètodes proposats en la secció anterior.

Aquestes equacions ens permeten generar un mapa com el de la Figura 10.6, on fixant els materials de l'aïllant podem veure quines són les dimensions necessàries que ha de tenir el disseny per assolir la supressió tèrmica requerida.

10.4.2 Contribució del cablejat

Un dels principals problemes que podem trobar en aquesta configuració són causats per les pertorbacions tèrmiques provinents de l'exterior entrant a l'interior de l'aïllant a través dels fils metàl·lics que connecten els sensors amb l'electrònica.

En el present treball hem establert un model senzill per a l'avaluació d'aquest efecte. Aquest es basa en la suposició que tot el flux de calor que es genera degut al gradient de punta a punta del cable es dedica completament a augmentar la temperatura del bloc intern. Les pèrdues laterals o en les interfícies entre diferents materials no es contemplen en aquesta aproximació i podrien introduir-se en una versió millorada.

Es pot demostrar que sota les aproximacions anteriors la funció de transferència que tradueix les fluctuacions de la temperatura exterior a fluctuacions en la temperatura del bloc intern pot escriure's com

$$H_w(f) = \frac{N}{2\,i\,f}\frac{r_w^2\,K_w}{L_w\left(\rho_C\,C_C\,V_C\right)} \tag{10.16}$$

on N és el nombre de cables emprats; r_w i L_w el radi i la longitud d'aquests cables; K_w la conductivitat tèrmica del material del cable, i ρ_C, C_C i V_C la densitat, la capacitat calorífica i el
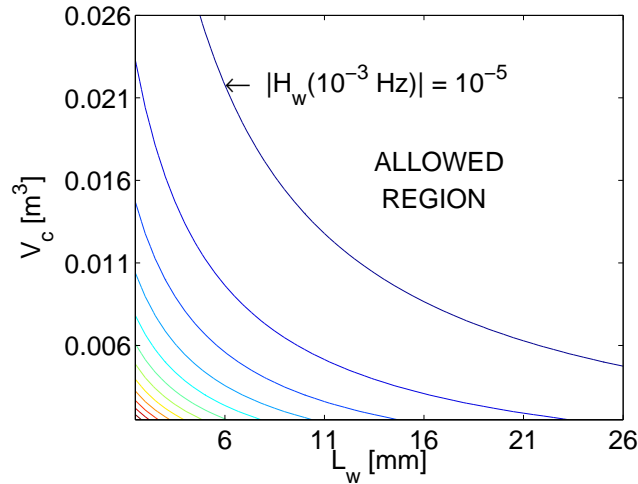
Figure 10.7: Mapa de la supressió de temperatura a l'interior d'un volum d'alumini degut a les fluctuacions tèrmiques que arriben a aquest bloc a través de 40 cables de coure. El mapa apareix com a funció de la longitud del cable i el volum d'alumini. Les línies mostren salts de 10^{-5}.

volum del material que forma el nucli interior de l'aïllant.

Anàlogament al procediment seguit amb les dimensions de l'aïllant, podem utilitzar l'equació (10.16) per generar un mapa que descrigui quin són els paràmetres òptims per al nostre disseny, tal com es descriu en la Figura 10.7.

10.4.3 Construcció de l'aïllant

L'estudi portat a terme va permetre la definició d'un aïllant capaç de complir les nostres especificacions. La construcció d'aquest disseny es va portar a terme el juliol del 2004 a NTE. El nucli intern està format per tres plaques d'alumini, cadascuna de $260\,\mathrm{mm} \times 260\,\mathrm{mm} \times 80\,\mathrm{mm}$. Un d'aquests blocs es va foradar per tal d'incloure-hi els sensors i les resistències de referència, 8 forats a banda i banda. Aquests aparells es van introduir i els orificis es van cobrir amb grassa tèrmica per tal d'assegurar un bon contacte tèrmic.

La capa de poliuretà envoltant el nucli metàl·lic es va implementar mitjançant un motlle de fusta on s'hi introduí el nucli metàl·lic per després abocar-hi el poliuretà en estat líquid. Més detalls a la Figura 10.8.

Val a dir que aquest disseny és una prova destructiva ja que els sensors no es poden recuperar una vegada introduïts. Per tal de poder mesurar l'estabilitat tèrmica utilitzant diferents remeses de sensors, en l'actualitat s'utilitzen versions millorades d'aquest disseny amb possibilitat d'obertura. Les eines utilitzades pel disseny han estat les presentades en aquesta tesi.
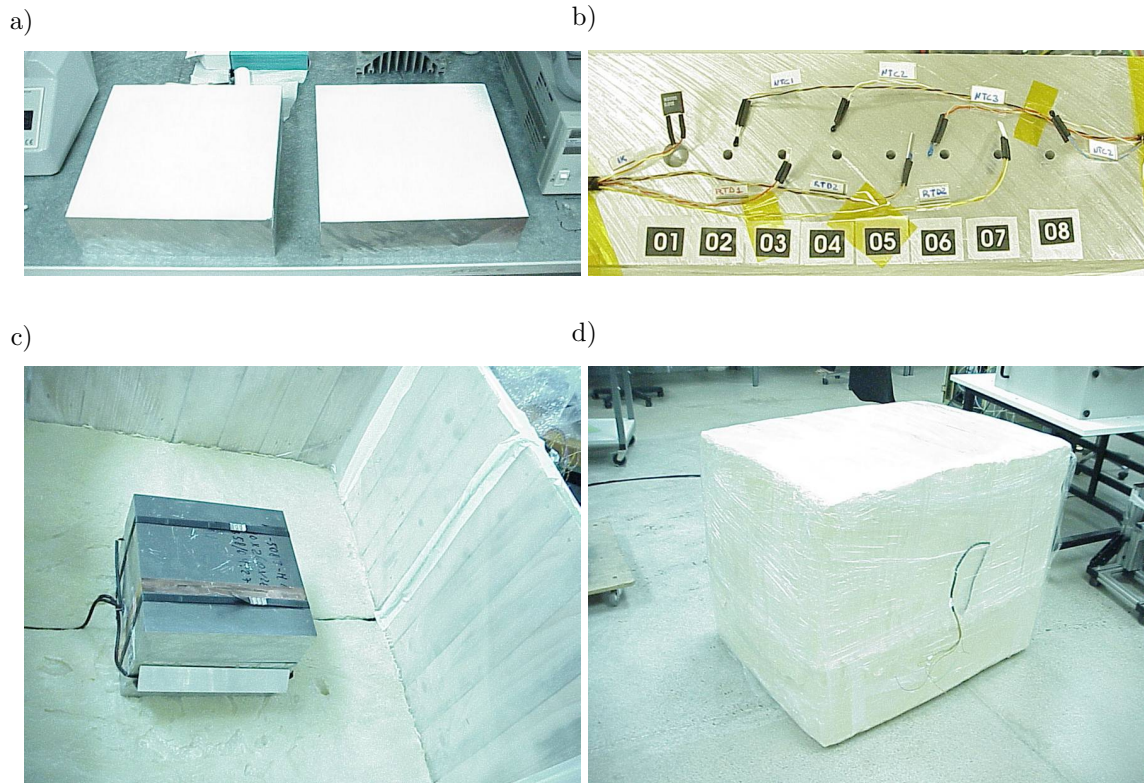
a)

b)

c)

d)

Figure 10.8: *a)* Dos dels tres blocs que composen la massa interna de l'aïllant. *b)* Distribució de sensors en el bloc. *c)* El nucli d'alumini dins el motlle. *d)* L'aïllant cobert amb plàstic.

10.5   Test experimental de qualificació

Una vegada finalitzada l'etapa de disseny és possible procedir a la validació experimental del nostre subsistema de mesures tèrmiques que, ho recordem, ha d'acomplir el nivell de sensibilitat següent

$$S_{\mathrm{T,FEE}}^{1/2}(\omega) \leq 10^{-5}\,\mathrm{K}\,\sqrt{\mathrm{Hz}} \quad 1\,\mathrm{mHz} \leq \omega/2\pi \leq 30\mathrm{mHz} \tag{10.17}$$

Per a aquesta finalitat una col·laboració IEEC-UPC va dissenyar un sistema de mesura, el prototip del qual es va testejar en el banc tèrmic prèviament descrit i que, després de superar amb èxit el test, es troba avui en dia en fase d'implementació final per tal de ser integrat en el satèl·lit LISA Pathfinder.

No entrarem en detall en la descripció d'aquest sistema de mesures, els detalls referents a aquest instrument es poden trobar a [86]. Sí val la pena però comentar que els experiments es van aprofitar per mesurar el funcionament del sistema de mesura mitjançant termistors (NTC en les sigles en anglès) i sensors de platí. Tot i ser els darrers més estables, les proves van mostrar que els primers eren més apropiats per al nostre cas donat que podien assolir valors més elevats en la sensibilitat (la resistència d'aquests sensors canvia exponencialment amb la temperatura mentre
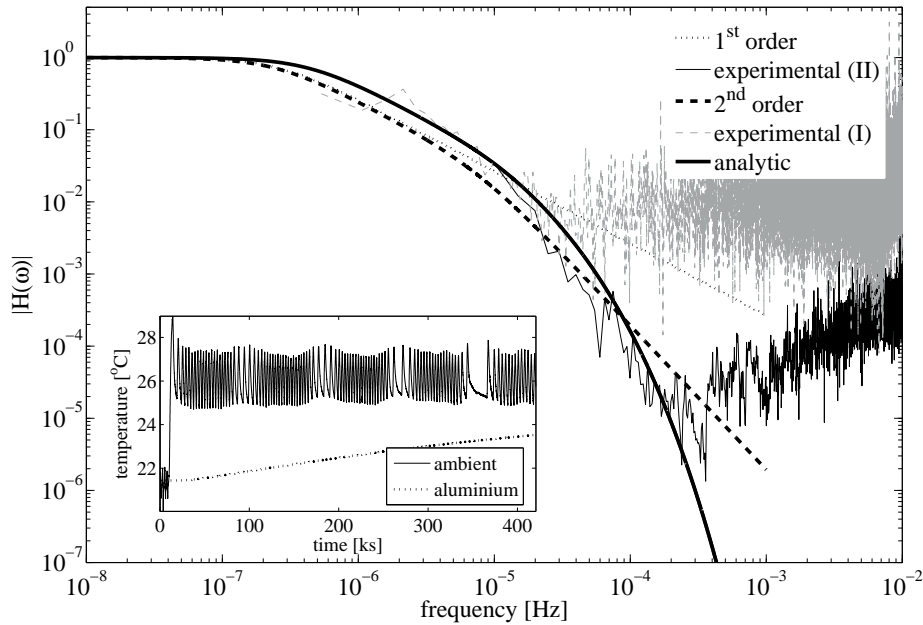
Figure 10.9: Resultats del test tèrmic. Les mesures de la funció de transferència s'ajusten a la predicció basada en un model analític.

que en els sensors de platí ho fa linealment).

L'experiment va permetre obtenir resultats en dues direccions complementàries. D'una banda, el primer que va ser necessari verificar és el correcte disseny de l'aïllant, és a dir que el seu comportament s'ajustés a aquell predit analíticament. En segon lloc, i una vegada conegut el comportament de l'aïllant, va ser possible l'anàlisi de l'estabilitat de l'electrònica de mesura.

Per al primer objectiu el sistema es va sotmetre a variacions apreciables de temperatura, les quals eren provocades pel sistema de control tèrmic de la sala climàtica de NTE. El fet que les variacions de temperatura es trobessin en el domini de freqüències del nostre interès va permetre testejar la capacitat de supressió tèrmica de l'aïllant, verificant la predicció de la nostra funció de transferència —veure Figura (10.9).

En segon lloc es va procedir a l'anàlisi de la sensibilitat tèrmica de l'instrument de mesures pròpiament. Com ja s'ha avançat, els resultats mostren que els sensors NTC permeten atènyer una millor sensibilitat tot i que mostren una major dispersió en la mesura efectuada per diferents sensors, molt probablement degut als processos d'envelliment als que es sotmeten aquests dispositius.

L'especificació requerida a (10.17) s'assoleix a tota la banda de mesura excepte en la part més baixa $\approx 1\,\mathrm{mHz}$ —Figura 10.10—on el valor mesurat excedeix lleugerament el requerit. Aquest efecte ha estat estudiat i s'ha conclòs que es degut a no-linealitats en el A/D, solucions a aquest problema es troben actualment sota estudi.
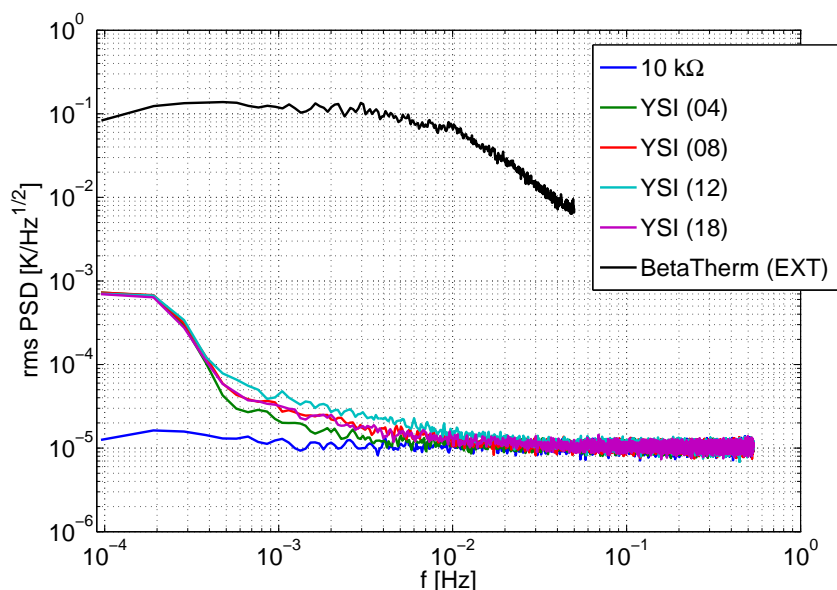
Figure 10.10: Resultats de les proves de sensibilitat de l'aparell de mesures tèrmiques amb sensors NTC.

10.6   Descripció dels experiments de diagnòstic tèrmic

Una col·laboració amb l'AEI-Hannover va permetre analitzar el comportament del model d'enginyeria del banc òptic de l'experiment LTP quan aquest és sotmès a polsos tèrmics. D'aquesta manera es van poder establir unes primeres estimacions fenomenològiques dels efectes tèrmics que podien afectar la interferometria quan el punt d'entrada de calor es trobava en el banc òptic.

Aquestes proves van encaminades a estimar l'efecte dels escalfadors que formen part del subsistema tèrmic en el satèl·lit. En el cas del banc òptic això no és cert perquè no es comptarà amb escalfadors en aquest punt.

Proves al banc òptic

Un total de 4 escalfadors i 5 sensors es varen distribuir en el banc òptic. Els polsos aplicats amb aquesta configuració mostren que la interferometria és poc sensible a aquests polsos degut a la baixa conductivitat i coeficient d'expansió tèrmica del material que forma el banc, és a dir el Zerodur. La taula 10.1 resumeix els factors d'acoblament que s'han trobat

Els resultats mostren igualment la diferència de la resposta de l'interferòmetre en funció del punt d'aplicació del calor, molt probablement degut al complex traçat de l'interferòmetre sobre el banc òptic.
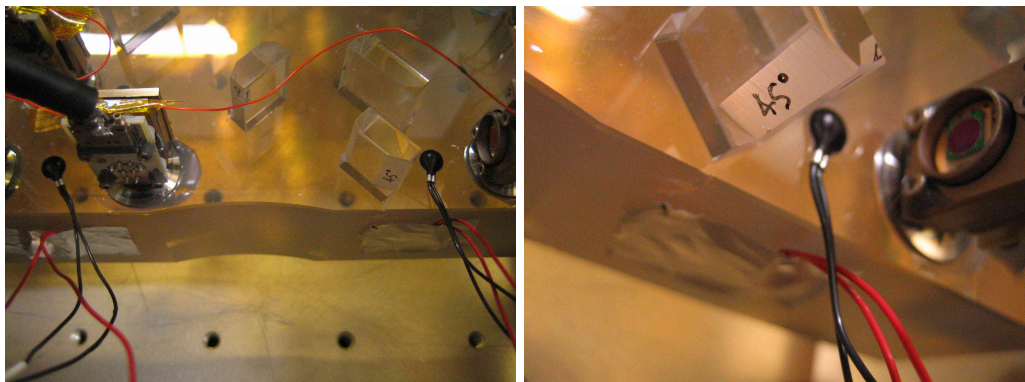
Figure 10.11: Detall del muntatge en el banc òptic. *Esquerra:* Dos escalfadors a la vora de dos elèctrodes. *Dreta:* Un sensor i un escalfador en un racó del banc òptic, el primer cobert amb paper d'alumini per disminuir la radiació tèrmica.

Heater	Coupling factor [mrad/K]	Thermal response [K/W s]
KS1	10 ± 6	1.7 ± 0.2
KS2	20 ± 7	1.6 ± 0.5
KS4	100 ± 10	1.8 ± 0.7

Table 10.1: Factors d'acoblament al banc òptic.

Proves a les pestanyes

Anomenem pestanyes ("flanges") als punts on l'experiment LTP es subjecta als puntals que el posen en contacte amb l'escut tèrmic que el protegeix de l'ambient exterior. Essent un punt on es poden establir fluxos de calor és necessari caracteritzar-lo i per aquesta raó el subsistema tèrmic comptarà amb sensors i escalfadors en aquest punt. La Taula 10.2 recull els resultats més rellevants en aquest punt.

Heater	Coupling factor [mrad/K]
KS5	-30 ± 10
KB4	110 ± 50
KB5	180 ± 60
KB3	21

Table 10.2: Paràmetre d'acoblament en el banc òptic.

Igual que en el cas anterior la dependència canvia de punt a punt. Els efectes observats mostren una dependència important de la resposta de la fase amb el gradient de temperatures que, en cas de confirmar-se, podria ser una font de soroll en el satèl·lit.
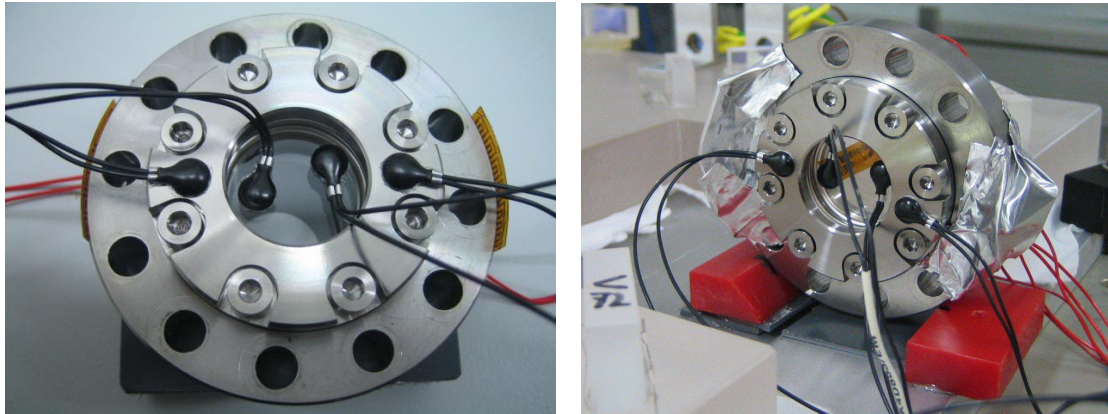
Figure 10.12: La finestra òptica (esquerra) a l'interior de l'anell de Titani. Enganxats als laterals es poden veure els escalfadors i a la superfície dos parells de sensors de temperatura. A la dreta, el muntatge experimental per mesurar l'acoblament tèrmic de la finestra.

Proves a la finestra òptica

La finestra òptica és l'únic element del subsistema òptic que no està unit a la resta d'elements mitjançant la tècnica del "silicate bonding". Aquest vidre es troba agafat dins una peça de titani que l'envolta i, per tant, les fluctuacions tèrmiques poden fàcilment propagar-se al seu interior i afectar la mesura interferomètrica. Per aquesta raó tres sensors i dos escalfadors s'encarregaran de caracteritzar aquesta contribució una vegada l'instrument estigui en vol.

La finestra òptica serà objecte d'un estudi més detallat en l'última secció d'aquest resum. De moment, però, ens limitem a resumir en una taula els mateixos valors que hem utilitzat per caracteritzar les posicions anteriors.

Heater	Coupling factor [rad/K]	Thermal response [K/W·s]
H.left	$(-32 \pm 2) \times 10^{-3}$	$(10.7 \pm 0.2) \times 10^{-3}$
H.right	$(-34 \pm 5) \times 10^{-3}$	$(10.7 \pm 0.3) \times 10^{-3}$
H.left + H.right	$(-47 \pm 16) \times 10^{-3}$	$(13 \pm 3) \times 10^{-3}$

Table 10.3: Mitjanes estadístiques de les respostes tèrmiques i òptiques.

10.7 Estudi de la potència dels escalfadors

Per tal d'aprofundir en l'estudi dels gradients que hauran de generar els 14 escalfadors que formen part dels subsistema tèrmic, l'evolució de la temperatura en el satèl·lit quan s'aplica calor en determinats punts es va estudiar mitjançant el model tèrmic de l'experiment LTP desenvolupat per Carlo Gavazzi Space (CGS). Aquesta eina, desenvolupada en el marc del programa d'anàlisi tèrmica de l'Agència Espacial Europea (ESATAN), resol les equacions tèrmiques en la regió estudiada mitjançant el mètode d'elements finits. D'aquesta manera la geometria pot ser convenientment

modelitzada i es poden incloure efectes difícils d'analitzar de qualsevol altra forma, com pot ser el cas de la radiació tèrmica.

Hem utilitzat el model tèrmic amb diferent finalitat depenent de la regió estudiada. Així, aquesta eina ha sigut d'especial utilitat en l'estudi dels escalfadors en el Sensor Inercial d'on no en teníem mesures experimentals. En el cas dels puntals i la finestra òptica, n'hem pogut comparar els resultats amb mesures prèviament obtingudes.

Paral·lelament també s'ha realitzat un treball de caracterització dels ginys que caldrà utilitzar en la missió com a escalfadors. L'estudi ha tractat d'establir una primera selecció de les coles que poden ser útils en el nostre context així com també una caracterització magnètica, mitjançant mesures de magnetometria SQUID, del material que forma aquests escalfadors.

Simulacions en el Sensor Inercial

El model tèrmic de CGS ha estat especialment útil en aquest cas. Per mitjà d'aquest programari ha sigut possible establir quin és l'efecte que l'activació alternativa dels escalfadors en la carcassa dels elèctrodes produiria en el moviment de la massa de test i, a més, definir quines són les potències necessàries per produir un senyal observable.

El procediment que hem presentat en aquest estudi per obtenir els paràmetres d'activació dels escalfadors es basa en suposar que el senyal al que és sensible el moviment de la massa de test (la diferència de temperatures a banda i banda de la carcassa d'elèctrodes) es pot modelar com un senyal triangular. Assumint el nivell de soroll fixat per les especificacions, podem obtenir una taula de valors del SNR esperat — Taula 10.4 — donada una determinada amplitud i freqüència del senyal tèrmic.

El factor que ens permet passar de variacions tèrmiques a variacions de força el prendrem de les mesures obtingudes experimentalment en la referència [21] en la qual es fixa en $\approx 100 \, \text{pN/K}$.

ΔT [mK]	$N \cdot \tau = 3000$s			$N \cdot \tau = 6000$s		
	$\tau = 100$s	$\tau = 500$s	$\tau = 1000$s	$\tau = 100$s	$\tau = 500$s	$\tau = 1000$s
1	0	7	4	0	8	6
5	1	28	26	4	39	37
10	7	56	52	9	78	74
20	13	113	104	17	156	145
40	26	223	206	37	314	291

Table 10.4: SNR per a senyals de diferent amplitud (ΔT) i període (τ), on $N \cdot \tau$ és el període d'integració.

D'aquesta taula és possible fixar quin és el gradient necessari per aconseguir un senyal que compleixi SNR > 50. Juntament amb el pas de gradient a potència aplicada que podem obtenir fàcilment de les simulacions podem definir una potència mínima requerida per als escalfadors. Aquesta està definida com a 45 mW basant-nos en el nostre estudi.

Simulacions en els puntals

El subsistema tèrmic comptarà amb escalfadors i sensors a 6 dels 8 puntals que subjecten l'experiment LTP a l'escut tèrmic dins el satèl·lit. Les simulacions tèrmiques en aquests punts poden ser difícilment comparades amb resultats experimentals ja que el model d'enginyeria no comptava amb puntals. De totes maneres, hem pogut comparar els resultats amb els valors dels gradients obtinguts experimentalment a les pestanyes i la comparació entre ambdós concorda dintre d'un factor ≈ 2 de marge. Com a valor màxim s'ha establert una potència de $2\,\mathrm{W}$ per a aquests escalfadors.

Simulacions en la finestra òptica

Els valors que defineixen els paràmetres d'activació dels escalfadors a la finestra òptica han estat definits basant-nos en les mesures experimentals, ja que en aquest cas el conjunt de dades era suficient per a aquesta finalitat. Amb aquestes dades s'ha pogut establir la Taula 10.5 de valors.

P [W]	Pulse duration [s]		
	10	50	100
2	36 ± 5	140 ± 20	260 ± 30
1	23 ± 9	66 ± 2	123 ± 7
1+1	32 ± 8	122 ± 18	262 ± 50
0.5+0.5	17 ± 2	65 ± 1	121 ± 7

Table 10.5: valors mitjans de SNR per a diferents seqüències d'activació dels escalfadors en la finestra òptica.

Aquests càlculs han permès fixar un valor de $1\,\mathrm{W}$ com a potència màxima en aquesta localització.

10.8 Modelatge de les dades de diagnòstic tèrmic

La darrera part d'aquest estudi es centra en l'ús de les dades tèrmiques per a l'anàlisi i diagnòstic a bord de la missió LISA Pathfinder. En particular hem centrat l'anàlisi en el conjunt de dades obtinguts en la finestra òptica per tal de validar la metodologia.

El muntatge experimental en aquest cas es basava en fer passar la llum del feix làser per l'interior d'un prototip de finestra òptica, el qual s'escalfava mitjançant escalfadors. Comparant un conjunt de 25 mesures on la finestra s'escalfava aplicant polsos de diferent duració hem sigut capaços de determinar un model que reprodueix la fase mesurada a partir de la temperatura mesurada també amb sensors a la finestra. El model reprodueix les característiques dinàmiques d'una equació en diferències de primer grau i es pot escriure com

$$G(q, \boldsymbol{\theta}) = \frac{\alpha_0 + \alpha_1 \, q^{-1}}{1 + \beta_1 \, q^{-1}} \tag{10.18}$$

DLR	**ARMA(2,1)**
$p_1 = (-38 \pm 4) \times 10^{-3}$ rad/K	$\alpha_0 = (39.6 \pm 3) \times 10^{-3}$ rad/K
$p_2 = (65 \pm 20) \times 10^{-3}$ rad/K	$\alpha_1 = (-39.5 \pm 3) \times 10^{-3}$ rad/K
	$\beta_1 = -0.996 \pm 0.001$

Table 10.6: Valor mig i dispersions del paràmetres per a dos models. Un ajust lineal utilitzant les temperatures del titani i el vidre i el model $ARMA(2,1)$, que només utilitza les mesures en el titani.

en el que s'anomena un procés $ARMA(2,1)$. L'estadística portada a terme sobre el conjunt de mesures ha permès determinar aquesta estructura com la més adient per descriure les nostres dades. A més, n'ha permès determinar els paràmetres tal com es mostra a la Taula 10.6.

L'estudi del model $ARMA$ ens ha permès aprofundir en els efectes físics que causen la pertorbació en la fase. En aquest sentit, el model sembla recolzar l'explicació que fonamentalment la resposta del làser que travessa la finestra ve condicionada per canvis en l'índex de refracció del vidre degut a variacions tèrmiques i forces de tensió mecàniques principalment causades per les diferències entre els coeficients d'expansió tèrmic del vidre i el titani. La interpretació dels resultats obtinguts que hem portat a terme en aquesta tesi diferencia la contribució d'aquests dos efectes en les bandes d'altes i baixes freqüències, dominant la primera l'efecte de la tensió mecànica (associat a escales de temps curtes) i la segona els canvis en el vidre deguts a pertorbacions tèrmiques.

Una de les propietats més útils per al nostre estudi del model $ARMA$ és la seva fàcil traducció en una funció de transferència en l'espai de freqüències. Donat que el nostre interès es centra precisament en la caracterització de l'instrument en la banda de mesures del LTP, aquesta descripció del model —veure la Figura 10.13— ens serà particularment útil.

Un exercici que hem pogut portar a terme és el de determinar quin és la contribució tèrmica
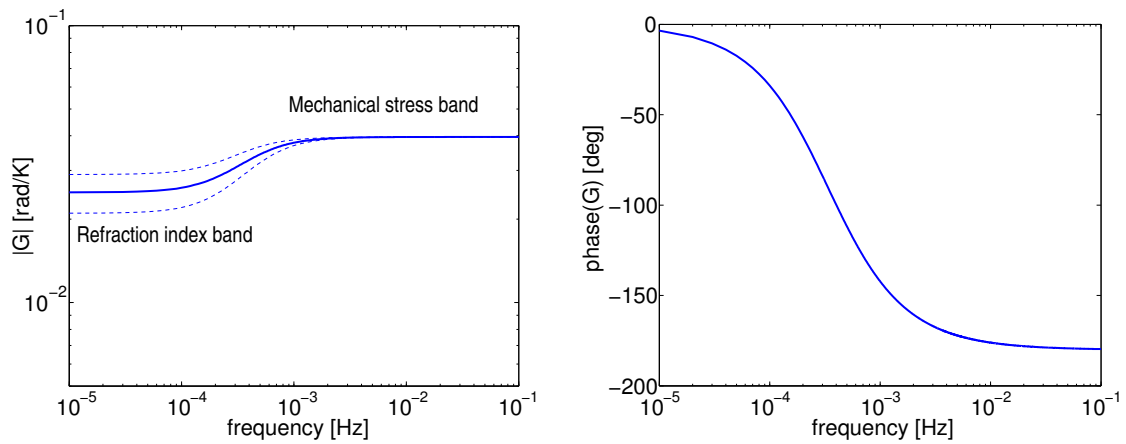

Figure 10.13: Diagrama de Bode per al model $ARMA(2,1)$ de la finestra òptica emprant els valors de la taula 10.6. En el panell esquerra, el seu mòdul; la línia discontínua marca l'interval de confiança d'$1\,\sigma$. A la dreta, la fase de la funció de transferència.
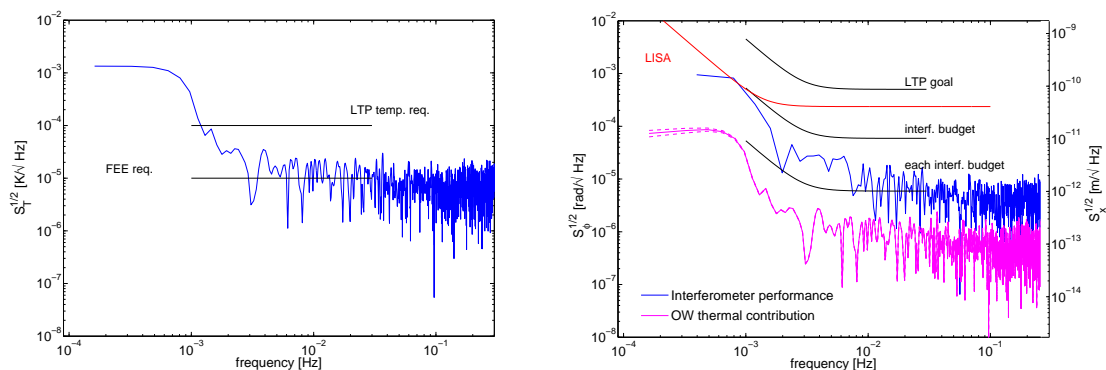
Figure 10.14: L'espectre de fluctuacions tèrmiques (esquerra) mesurat durant l'experiment comparat amb el requeriment de temperatura ambient a l'LTP i el límit inferior fixat per la sensitivitat de l'electrònica. Les fluctuacions de fase (traç blau, panell dret) es comparen amb la contribució tèrmica al soroll de la fase (traç magenta) estimada a partir del model *ARMA* de la finestra òptica amb els paràmetres de la Taula 10.6. L'interval de confiança d'1 σ s'inclou per al darrer.

al soroll de l'interferòmetre basant-nos en el modelatge que acabem de descriure. Aquesta anàlisi s'ha fet utilitzant dades d'experiments on la mesura no era pertorbada per polsos tèrmics i el làser assolia la sensibilitat requerida. En aquestes condicions i mesurant al mateix temps les fluctuacions tèrmiques hem pogut establir quina és la contribució tèrmica al soroll del làser tal i com es mostra en la Figura 10.14.

10.9 Conclusions

En aquesta tesi hem portat a terme un estudi sobre diferents fenòmens tèrmics que poden afectar la sensibilitat d'un detector d'ones gravitatòries a l'espai; en concret, la nostra feina s'ha centrat en el marc de la futura missió LISA Pathfinder (LPF). L'estudi ha recorregut diferents metodologies per tal de resoldre la varietat de problemes associats al nostre objectiu inicial.

La primera fase del treball exposat es centra en l'estudi analític de funcions de transferència tèrmiques per a volums senzills. Les solucions trobades han permès amb posterioritat dissenyar i construir un aïllant tèrmic a baixes freqüències amb el qual testejar un prototipus d'electrònica de mesures tèrmiques per al subsistema de diagnòstic tèrmic de la missió. Els test portats a terme en aquesta campanya han permès demostrar l'adequació del disseny proposat per a l'assoliment dels objectius del sistema de mesura tèrmica.

El diagnòstic tèrmic a bord de la missió LPF comptarà també amb un conjunt de 14 escalfadors els quals estaran encarregats d'introduir pertorbacions controlades que permetin caracteritzar la contribució tèrmica al soroll de l'experiment. La definició d'aquests aparells portada a terme en aquesta tesi ha requerit no solament l'ús de models tèrmics del satèl·lit on portar a terme les simulacions corresponent sinó també l'estudi experimental dels possibles efectes, el qual es va portar a terme en col·laboració amb l'AEI-Hannover. Aquest estudi ha permès definir les potències que

els escalfadors hauran de subministrar per tal d'extreure'n els paràmetres científicament rellevants, els quals han passat ha formar part del document d'especificacions industrials de la missió.

Finalment, l'extensa serie de dades obtingudes en el cas de la finestra òptica ens ha permès aprofundir en l'estudi d'aquesta, proposant una metodologia d'anàlisi de dades per tal d'assolir un diagnòstic eficient una vegada la missió es trobi en òrbita. Aquest mètode, basat en l'ús de models dinàmics *ARMA* ha permès identificar les causes físiques de la contribució tèrmica al soroll en la finestra òptica a bord del LPF i fer una projecció de la contribució de soroll en el cas on no hi ha font de calor aplicada. En aquest sentit, l'estudi realitzat estableix un primer pas per a l'estudi de les dades del sistema de diagnòstic d'aquest satèl·lit una vegada aquest es trobi operatiu al punt de Lagrange L1.

VI Appendix

*" Le petit prince ne renonçait jamais à une question,
une fois qu'il l'avait posée. "*

*Le Petit Prince
Antoine de Saint-Exupéry*
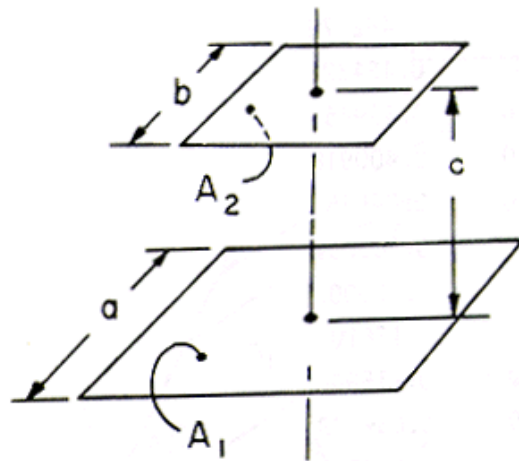
Appendix A

GRS View factor

Figure A.1: Geometry used to compute the test mass-to-electrode housing view factor.

The view factor between two differential surfaces arbitrarily oriented is defined, in general, as

$$dF_{d1-d2} = \frac{\cos\theta_1 \cos\theta_2}{\pi S^2} dA_2 \tag{A.1}$$

With the definitions

$$
\begin{aligned}
A &= \frac{a}{c} \\
B &= \frac{b}{a} \\
X &= A\,(1+B) \\
Y &= A\,(1-B)
\end{aligned}
$$

The view factor of two finite parallel rectangular surfaces is given by [41]

$$
\begin{aligned}
F &= \frac{1}{\pi A^2}\,(\ln \frac{(A^2(1+B^2)+2)^2}{(Y^2+2)(X^2+2)} \\
&+ (Y^2+4)^{1/2}\left(Y\tan^{-1}\frac{Y}{(Y^2+4)^{1/2}} - X\tan^{-1}\frac{X}{(Y^2+4)^{1/2}}\right) \\
&+ (X^2+4)^{1/2}\left(X\tan^{-1}\frac{X}{(X^2+4)^{1/2}} - Y\tan^{-1}\frac{Y}{(X^2+4)^{1/2}}\right))
\end{aligned}
\tag{A.2}
$$

If we now assume typical numerical values of the GRS

$$
\begin{aligned}
a &= 54\,\text{mm} \\
b &= 46\,\text{mm} \\
c &= 4\,\text{mm}
\end{aligned}
$$

The view factor obtained is

$$
F = 0.68
\tag{A.3}
$$

Appendix B

Wu's theory of thermal transpiration

In this Appendix we briefly describe an extension of the theory used to derive the radiometer effect which takes into account anisotropies in the flow of gas molecules.

In §2.1.1 it was described how the pressure of a rarefied gas in two different vessels at temperature T_1 and T_2 connected through a duct were related as

$$\frac{p_1}{\sqrt{T_1}} = \frac{p_2}{\sqrt{T_2}} \tag{B.1}$$

The invariant for the radiometer effect holds however based on the assumption of a Maxwellian distribution function for the gas. This assumption breaks down in situations where an anisotropy occurs, as for instance between two parallel plates at different temperatures. The solution to this problem must be found by introducing the angular dependence of the distribution function in the Boltzmann equation and work out the flux of particles coming from a given point at a point in space (θ, ϕ) which has a temperature $T_{\theta,\phi}$. In this new approach a new invariant is obtained given by [107]

$$\frac{p(\mathbf{x_1})\, I(\mathbf{x_1})}{\sqrt{T(\mathbf{x_1})}} = \frac{p(\mathbf{x_2})\, I(\mathbf{x_2})}{\sqrt{T(\mathbf{x_2})}} \tag{B.2}$$

where $I(\mathbf{x})$ is called the *isotropy function*, $0 < I(\mathbf{x}) < 1$, being the case $I = 1$ the one we have treated in §2.1.1, i.e., without angular dependence. The isotropy function is defined as [75]

$$I(\mathbf{x}) = 4\pi \frac{1}{\left[\iint d\phi\, d\theta\, T_{\theta,\phi}^{1/2}\, \sin(\phi) \times \iint d\phi\, d\theta\, T_{\theta,\phi}^{-1/2}\, \sin(\phi) \right]^{1/2}} \tag{B.3}$$

and $T(\mathbf{x})$ can be expressed as

$$T(\mathbf{x}) = \frac{\iint d\phi\, d\theta\, T_{\theta,\phi}^{1/2}\, \sin(\phi)}{\iint d\phi\, d\theta\, T_{\theta,\phi}^{-1/2}\, \sin(\phi)} \tag{B.4}$$
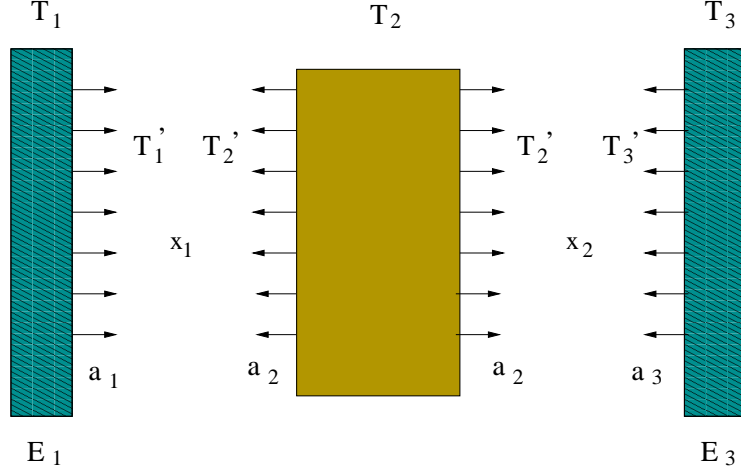
215

Figure B.1: Scheme of the geometry under study. The test mass at temperature T_2 is in the middle of two electrode housing walls at T_1 and T_3.

where $T_{\theta,\phi}$ stands for the temperature of the gas molecules coming from the (θ, ϕ) direction.

If we now are interested in a geometry such as the one in the GRS, three temperatures are to be considered: electrodes at T_1 and T_3 and the test mass at T_2. Compared to a point x_0 outside the electrode housing, a point x_1 between electrode E1 and the test mass will have a pressure given by

$$p(\mathbf{x_1}) = \frac{I(\mathbf{x_0})}{I(\mathbf{x_1})} \sqrt{\frac{T(\mathbf{x1})}{T(\mathbf{x_0})}} p(\mathbf{x_0}) \tag{B.5}$$

and consequently the pressure at point x_2 between electrode E3 and the test mass will be be given by

$$p(\mathbf{x_2}) = \frac{I(\mathbf{x_0})}{I(\mathbf{x_2})} \sqrt{\frac{T(\mathbf{x_2})}{T(\mathbf{x_0})}} p(\mathbf{x_0}) \tag{B.6}$$

In order to evaluate equations (B.5) and (B.6), we will follow the procedure also applied in [75]. To do so, we consider two noninteracting streams in the region between the surfaces to represent temperatures of the gas molecules emerging from the surfaces. These can be expressed in terms of their respective accomodation factor[1]. In the case of point $\mathbf{x_1}$ the gas streams temperatures are defined as

---

[1]The accomodation factor is a measure for the amount of energy transfer between a molecule and a surface. A molecule will reflect on a surface when the accommodation coefficient during a collision is zero.
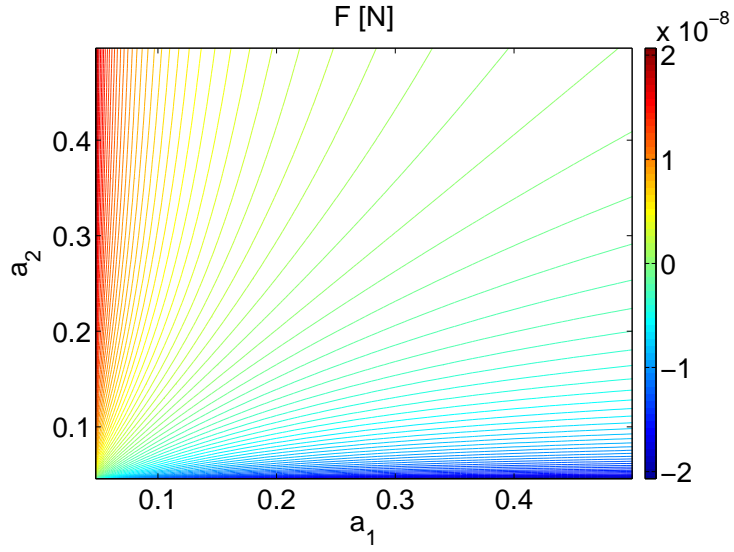
Figure B.2: Contour map of the force in the x direction being applied on the test mass at $T_2 = 293\,\text{K}$ by the flow of gas molecules coming from the electrodes' walls E1 and E3 —see Figure B— at $T_1 = 293\,\text{K}$ and $T_3 = 294\,\text{K}$ respectively. The point $(a_1 = 0.4, a_2 = 0.4)$ is at $\text{F} \simeq 30\,\text{pN}$.

$$
\begin{aligned}
T_1' &= \frac{a_1\,T_1 + a_2(1 - a_2)\,T_2}{a_1 + a_2 + a_1\,a_2} \\
T_2' &= \frac{a_2\,T_2 + a_1(1 - a_1)\,T_1}{a_1 + a_2 + a_1\,a_2}
\end{aligned}
\tag{B.7}
$$

From these, together with the corresponding equations in the point $\mathbf{x_1}$ we can now return to equations (B.3) and (B.4), which can now be rewritten as

$$
\begin{aligned}
I(\mathbf{x_1}) &= \frac{2\,(T_1'\,T_2')^{1/4}}{\sqrt{T_1'} + \sqrt{T_2'}} \\
T(\mathbf{x_1}) &= \sqrt{T_1'\,T_2'}
\end{aligned}
\tag{B.8}
$$

which can be readily translated to the point $\mathbf{x_2}$

$$
\begin{aligned}
I(\mathbf{x_2}) &= \frac{2\,(T_2'\,T_3')^{1/4}}{\sqrt{T_2'} + \sqrt{T_3'}} \\
T(\mathbf{x_2}) &= \sqrt{T_2'\,T_3'}
\end{aligned}
\tag{B.9}
$$

Expression in the point $\mathbf{x_0}$ reduces to $I(\mathbf{x_0}) = 1$ and $p(\mathbf{x_0}) = p_0$.

The force per unit surface F exerted on the test mass can be now described in terms of the previous expressions

$$
\begin{aligned}
F &= [p(\mathbf{x_1}) - p(\mathbf{x_2})] \\
&= \left[\frac{I(\mathbf{x_0})}{I(\mathbf{x_1})} \sqrt{\frac{T(\mathbf{x1})}{T(\mathbf{x_0})}} p(\mathbf{x_0}) - \frac{I(\mathbf{x_0})}{I(\mathbf{x_2})} \sqrt{\frac{T(\mathbf{x_2})}{T(\mathbf{x_0})}} p(\mathbf{x_0}) \right] \\
&= \frac{p_0}{\sqrt{T_0}} \left[\sqrt{T_1'} - \sqrt{T_3'} \right] \\
&= \frac{p_0}{\sqrt{T_0}} \left[\sqrt{\frac{a_1\, T_1 + a_2\,(1-a_1)T_2}{a_1 + a_2 - a_1 a_2}} - \sqrt{\frac{a_3\, T_3 + a_2\,(1-a_3)T_2}{a_2 + a_3 - a_2 a_3}} \right]
\end{aligned}
\tag{B.10}
$$

Equation B.10 allows to describe the problem in terms of temperatures both on both sides of the electrodes T_1 and T_3 but also in the test mass T_2. It also takes into account the accommodation factor of all the surfaces. As an example, Figure B shows a contour map of the force applied on the test mass as a function of the parameters a_1 and a_2. It is however difficult to compare these results without an estimation of the accommodation factors for our particular case, in the GRS.

Temperature distribution in a sphere subject to a fluctuating thermal bath

C.1 The general solution

The problem we aim to solve herein is to analitically describe the temperature field inside a massive body with a known temperature distribution affecting its outer layer. We will therefore need to solve the heat flow equation,

$$\rho C \, \partial_t T(\mathbf{x}, t) = \nabla \cdot [K \, \nabla T(\mathbf{x}, t)] \tag{C.1}$$

with boundary conditions

$$\begin{aligned} \text{Boundary conditions}: \quad T(\mathbf{x} = \mathbf{x_c}, t) &< \quad \infty \\ T(\mathbf{x} = \mathbf{x_b}, t) &= \quad T_0(\mathbf{x} = \mathbf{x_b}, t) \\ \text{Initial conditions}: \quad T(x, t = 0) &= \quad 0 \end{aligned} \tag{C.2}$$

For the sake of simplicity, the chosen geometry is the spherical one, with radius a, which allows to define the problem with a unique boundary condition.

In order to solve the problem it will be expedient to split up the unknown contribution as the sum of two terms

$$T(\mathbf{x}, t) = U(\mathbf{x}, t) + V(\mathbf{x}, t) \tag{C.3}$$

where $U(\mathbf{x}, t)$ will be taken such that it equals the temperature on the boundary of the sphere

$$U(\mathbf{a}, t) = T_0(\mathbf{a}, t) \tag{C.4}$$

plus an additional condition that it must be a harmonic function finite at the origin

$$\nabla^2 U(\mathbf{x}, t) = 0 \quad |U(\mathbf{0}, t)| < \infty \tag{C.5}$$

We can then solve equation (C.1) for $V(\mathbf{x}, t)$ which accordingly read

$$(\partial_t - \alpha^2 \nabla^2) V(\mathbf{x}, t) = -\partial_t U(\mathbf{x}, t), \quad \alpha^2 \equiv \frac{K}{\rho \, C}$$

$$\text{Initial conditions :} \quad V(\mathbf{x}, 0) = 0$$

$$\text{Boundary conditions :} \quad |V(\mathbf{0}, t)| < \infty, \, V(\mathbf{a}, t) = 0 \tag{C.6}$$

If we now consider the eigenvalue equation

$$\nabla^2 X(\mathbf{x}) = -k^2 X(\mathbf{x}) \tag{C.7a}$$

$$|X(0)| < \infty \quad , \quad X(\mathbf{a}) = 0 \tag{C.7b}$$

which has the solutions

$$X_{nlm}(\mathbf{x}) = N_{nlm} \, j_l(k_{nl} \, r) \, Y_{lm}(\theta, \phi), \quad j_l(k_{nl} \, a) = 0 \tag{C.8}$$

where

$$j_l(\xi) = (\xi)^l \left(-\frac{1}{\xi} \frac{d}{d\xi} \right)^l \frac{\sin(\xi)}{\xi} \tag{C.9}$$

The normalisation constants N_{nlm} will be chosen so that

$$\int_V d^3 x X^*_{n'l'm'}(\mathbf{x}) X_{nlm}(\mathbf{x}) = \frac{a^3}{2} \delta_{nn'} \delta_{ll'} \delta_{mm'} \tag{C.10}$$

This ensures that X_{nlm} are dimensionless functions, which will be convenient for clarity later on. Making use of the formula

$$2 \int_0^{\xi_{nl}} d\xi j_l(\xi) \xi^2 = \xi_{nl}^3 j_{l+1}^2(\xi_{nl}) \tag{C.11}$$

we easily determine the normalisation factor

$$X_{nlm}(\mathbf{x}) = \frac{1}{j_{l+1}(\xi_{nl})} j_l(k_{nl} \, r) Y_{lm}(\theta, \phi) \tag{C.12}$$

where ξ_{nl} is the n-th zero of $j_l(\xi)$

$$j_l(\xi_{nl}) = 0, \quad n = 1, 2, 3 \ldots \quad l = 1, 2, 3 \ldots \tag{C.13}$$

We will now take advantage of the fact that X_{nlm} is a complete set of basis functions inside the sphere to make the expansions

$$U(\mathbf{x}, t) = \sum_{n,l,m} u_{nlm}(t) X_{nlm}(\mathbf{x}) \tag{C.14}$$

$$V(\mathbf{x}, t) = \sum_{n,l,m} v_{nlm}(t) X_{nlm}(\mathbf{x}) \tag{C.15}$$

Replacing these expressions into the equation (C.6) and taking into account the completeness properties of the set $X_{nlm}(\mathbf{x})$ we readily find

$$\dot{v}_{nlm}(t) + \frac{1}{\tau_{nl}} v_{nlm}(t) = -\dot{u}_{nlm}(t) \tag{C.16}$$

where

$$\tau_{nl}^{-1} \equiv \alpha^2 k_{nl}^2 = \xi_{nl}^2 \tau^{-1}, \quad \tau \equiv \frac{a^2}{\alpha^2} \tag{C.17}$$

Because $V(\mathbf{x}, 0) = 0$, we infer $v_{nlm}(0) = 0$; hence the solution to (C.16) is

$$v_{nlm}(t) = -\int_0^t dt' e^{-(t-t')/\tau_{nl}} \dot{u}_{nlm}(t') \tag{C.18}$$

Also, because $U(\mathbf{x}, 0) = 0$, $u_{nlm}(0) = 0$; integrating by parts in C.19 we now find

$$v_{nlm}(t) = u_{nlm}(t) + \frac{1}{\tau_{nl}} \int_0^t dt' e^{-(t-t')/\tau_{nl}} u_{nlm}(t') \tag{C.19}$$

Inserting this into (C.15) and using also (C.14),

$$V(\mathbf{x}, t) = -U(\mathbf{x}, t) + \sum_{n,l,m} X_{nlm}(\mathbf{x}) \frac{1}{\tau_{nl}} \int_0^t e^{-(t-t')/\tau_{nl}} u_{nlm}(t') \tag{C.20}$$

which we can finally replace in (C.3) to recover an expression for the temperature

$$T(\mathbf{x}, t) = -U(\mathbf{x}, t) + \sum_{n,l,m} X_{nlm}(\mathbf{x}) \frac{1}{\tau_{nl}} \int_0^t dt' e^{-(t-t')/\tau_{nl}} u_{nlm}(t') \tag{C.21}$$

We must now specify $u_{nlm}(t)$ in terms of the actual boundary temperature $T_0(\mathbf{a}, t)$. To this end, we expand $T_0(\mathbf{a}, t)$ into its multipole components

$$T_0(\mathbf{a}, t) = \sum_{lm} b_{lm}(t) Y_{lm}(\theta, \phi) \tag{C.22}$$

221

Clearly, the function $U(\mathbf{x}, t)$ which verifies (C.4) and (C.5) is

$$U(\mathbf{x}, t) = \sum_{lm} b_{lm}(t) \left(\frac{r}{a}\right)^l Y_{lm}(\theta, \phi) \tag{C.23}$$

Recovering now (C.14) and the orthogonality conditions (C.10),

$$
\begin{aligned}
u_{nlm}(t) &= \frac{2}{a^3} \int_V d^3 X_{nlm}^*(\mathbf{x}) U(\mathbf{x}, t) \\
&= \frac{2}{a^3} \frac{b_{lm}(t)}{j_{l+1}(\xi_{nl})} \int_0^a dr \left(\frac{r}{a}\right)^l j_l(k_{nl\,r}) r^2 \\
&= b_{lm}(t) \frac{2}{\xi_{nl}^{l+3} j_{l+1}(\xi_{nl})} \int_0^{\xi_{nl}} d\xi \xi^{l+2} j_l(\xi)
\end{aligned} \tag{C.24}
$$

We now need the following identity

$$\xi^{l+2} j_l(\xi) = \frac{d}{d\xi}[\xi^{l+2} j_{l+1}(\xi)] \tag{C.25}$$

which imediately leads to

$$u_{nlm}(t) = \frac{2}{\xi_{nl}} b_{lm}(t) \tag{C.26}$$

The final formal solution to the proposed problem will be thus

$$T(\mathbf{x}, t) = 2 \sum_{n,l,m} \xi_{nl}^{-1} X_{nlm}(\mathbf{x}) \frac{1}{\tau_{nl}} \int_0^t dt' e^{-(t-t')/\tau_{nl}} b_{lm}(t') \tag{C.27}$$

The meaning of this expression is clearly seen in terms of its Fourier transform

$$\widetilde{T}(\mathbf{x}, \omega) = 2 \sum_{n,l,m} \xi_{nl}^{-1} X_{nlm}(\mathbf{x}) \frac{\widetilde{b}_{lm}(\omega)}{1 + i\omega \, \tau_{nl}} \tag{C.28}$$

The sphere acts as a sum of linear *low-pass* filters of progressively higher cut-off frequencies, $1/\tau_{nl} = \xi_{nl}^2/\tau$. Therefore the net effect is best characterised by the lowest of these frequencies

$$\omega_{\text{cut-off}} \leq \frac{\pi^2}{\tau} = \frac{\pi^2 K}{\rho C_p a^2} \tag{C.29}$$

where the $\leq$ sign is implied by the fact that successive filters will further damp lower frequency amplitudes; on the other hand, the π^2 comes from the fact that $\xi_{10} = \pi$ is the lowest of all zeroes ξ_{nl}.

C.2 Isotropic conditions to the spherical problem

We can now consider the solution if isotropic boundary conditions are imposed,

$$T(\mathbf{x} = \mathbf{x_b}, t) = B(t) \tag{C.30}$$

which translates into a multipole expansion with coefficients

$$b_{ml}(t) = \sqrt{4\pi} B(t)\, \delta_{n0}\delta_{m0} \tag{C.31}$$

and the temperature ditribution becomes

$$\widetilde{T}(\mathbf{x}, \omega) = 2\sum_{n=1}^{\infty}(-1)^n \frac{\sin(n\pi r/a)}{n\pi r/a}\frac{\widetilde{B}(\omega)}{1 + i\frac{\omega\tau}{n^2\pi^2}} \tag{C.32}$$

we will however be interested in a recipe to sum the series to obtain a final, more synthetic expression. In particular, the expression is simplified if one considers temperature fluctuations in the centre of the spherical body. If we recast equation (C.32) as $\widetilde{T}(\mathbf{x}, \omega) = \widetilde{K}(\mathbf{x}, \omega)\widetilde{B}(\omega)$, the equation reads

$$\widetilde{K}(0, \omega) = 2\sum_{n=1}^{\infty}\left(1 + i\frac{\omega\tau}{n^2\pi^2}\right)^{-1} \tag{C.33}$$

Although the strange expressions derived seems not to yield to what one would expect for this thermal insulator behaviour, the meaning of both equations can be grasped as limits of uniformly convergent series. To this end, let's consider the following Fourier expansion

$$f(x) \equiv e^{\mu x} = \frac{2\sinh(\pi\mu)}{\pi}\left[\frac{1}{2\mu} + \sum_{n=1}^{\infty}(-1)^n\frac{\mu\cos(n\,x) - n\sin(nx)}{\mu^2 + n^2}\right], \quad -\pi < x < \pi \tag{C.34}$$

This expression is perfectly well behaved at $x = 0$ and the rhs evaluates to $f(0) = 1$. The derivation of this expression leads to

$$f'(x) = \mu e^{\mu x} = \frac{2\sinh(\pi\mu)}{\pi}\left[\frac{1}{2\mu} + \sum_{n=1}^{\infty}(-1)^{n-1}\frac{n^2\cos(n\,x) + \mu\,n\sin(nx)}{\mu^2 + n^2}\right] \tag{C.35}$$

Setting $x = 0$ in the previous expression we obtain

$$\frac{\pi\mu}{\sinh(\pi\mu)} = 2\sum_{n=1}^{\infty}(-1)^{n-1}\left(1 + \frac{\mu^2}{n^2}\right)^{-1} \tag{C.36}$$

which can be used to recover equation (C.33) as an explicit expression,

$$\widetilde{K}(0, \omega) = \frac{(1 + i)\beta}{\sinh(\beta)\,\cos(\beta) + i\cosh(\beta)\,\sin(\beta)}, \quad \beta \equiv \left|\frac{\omega\tau}{2}\right|^{1/2} \tag{C.37}$$

Together with the sum of expression (C.33) which becomes $\widetilde{K}(0,0) = 1$. With the method above described, we are able to sum the Fourier series describing the solution and end with an

expression for temperature fluctuations at the centre of the sphere for any frequency.

Frequency domain solution of multiple layer spherical insulator

Here we present some mathematical details of the solution to the Fourier problem, equations (8.18)-(8.19). We first of all Fourier transform equations

$$\rho c_{\mathrm{p}} \, \frac{\partial}{\partial t} T(\mathbf{x}, t) = \nabla \cdot [\kappa \nabla T(\mathbf{x}, t)] \tag{D.1}$$

$$T_0(\theta, \varphi; t) = \sum_{lm} b_{lm}(t) \, Y_{lm}(\theta, \varphi) \tag{D.2}$$

to get

$$i\omega \, \rho c_{\mathrm{p}} \, \widetilde{T}(\mathbf{x}, \omega) = \nabla \cdot \left[\kappa \nabla \widetilde{T}(\mathbf{x}, \omega) \right] \tag{D.3}$$

$$\widetilde{T}_0(\theta, \varphi; \omega) = \sum_{l=0}^{\infty} \sum_{m=-l}^{l} \widetilde{b}_{lm}(\omega) \, Y_{lm}(\theta, \varphi) \tag{D.4}$$

Equation (D.3) can be recast in split form:

$$\left(\nabla^2 + \gamma_1^2 \right) \widetilde{T}(\mathbf{x}, \omega) = 0 \,, \quad 0 \leq r \leq a_1 \tag{D.5}$$

$$\left(\nabla^2 + \gamma_2^2 \right) \widetilde{T}(\mathbf{x}, \omega) = 0 \,, \quad a_1 \leq r \leq a_2 \tag{D.6}$$

where $r \equiv |\mathbf{x}|$, and

$$\gamma_1^2 \equiv -i\omega \, \frac{\rho_1 c_{\mathrm{p},1}}{\kappa_1} \,, \quad \gamma_2^2 \equiv -i\omega \, \frac{\rho_2 c_{\mathrm{p},2}}{\kappa_2} \tag{D.7}$$

To these, matching conditions at the interface[1] and boundary conditions must be added:

$$\widetilde{T}(r = a_1 - 0, \omega) = \widetilde{T}(r = a_1 + 0, \omega) \tag{D.8}$$

$$\kappa_1 \frac{\partial \widetilde{T}}{\partial r}(r = a_1 - 0, \omega) = \kappa_2 \frac{\partial \widetilde{T}}{\partial r}(r = a_1 + 0, \omega) \tag{D.9}$$

$$\widetilde{T}(r = a_2, \omega) = \widetilde{T}_0(\theta, \varphi; \omega) \tag{D.10}$$

Equations (D.5) and (D.6) are of the Helmholtz kind. Their solutions are thus respectively given by

$$\widetilde{T}(\mathbf{x}, \omega) = \begin{cases} \displaystyle\sum_{lm} A_{lm}(\omega) \, j_l(\gamma_1 r) \, Y_{lm}(\theta, \varphi) \, , & 0 \le r \le a_1 \\[2mm] \displaystyle\sum_{lm} \left[C_{lm}(\omega) \, j_l(\gamma_2 r) + D_{lm}(\omega) \, y_l(\gamma_2 r) \right] Y_{lm}(\theta, \varphi) \, , & a_1 \le r \le a_2 \end{cases} \tag{D.11}$$

$$j_l(z) = z^l \left(-\frac{1}{z} \frac{d}{dz} \right)^l \frac{\sin z}{z} \, , \quad y_l(z) = -z^l \left(-\frac{1}{z} \frac{d}{dz} \right)^l \frac{\cos z}{z} \tag{D.12}$$

and the coefficients $A_{lm}(\omega)$, $C_{lm}(\omega)$ and $D_{lm}(\omega)$ are to be determined by equations (D.8)–(D.10). These can be expanded as follows, respectively:

$$\sum_{lm} A_{lm}(\omega) \, j_l(\gamma_1 a_1) \, Y_{lm}(\theta, \varphi) =$$
$$= \sum_{lm} \left[C_{lm}(\omega) \, j_l(\gamma_2 a_1) + D_{lm}(\omega) \, y_l(\gamma_2 a_1) \right] Y_{lm}(\theta, \varphi) \tag{D.13}$$

$$\kappa_1 \gamma_1 \sum_{lm} A_{lm}(\omega) \, j_l'(\gamma_1 a_1) \, Y_{lm}(\theta, \varphi) =$$
$$= \kappa_2 \gamma_2 \sum_{lm} \left[C_{lm}(\omega) \, j_l'(\gamma_2 a_1) + D_{lm}(\omega) \, y_l'(\gamma_2 a_1) \right] Y_{lm}(\theta, \varphi) \tag{D.14}$$

$$\sum_{lm} \left[C_{lm}(\omega) \, j_l(\gamma_2 a_2) + D_{lm}(\omega) \, y_l(\gamma_2 a_2) \right] Y_{lm}(\theta, \varphi) =$$
$$= \sum_{lm} \widetilde{b}_{lm}(\omega) \, Y_{lm}(\theta, \varphi) \tag{D.15}$$

Because of the completeness property of the spherical harmonics, the above equations completely determine the coefficients $A_{lm}(\omega)$, $C_{lm}(\omega)$ and $D_{lm}(\omega)$. The result is

$$A_{lm}(\omega) = \xi_l(\omega) \, \widetilde{b}_{lm}(\omega) \, , \quad C_{lm}(\omega) = \eta_l(\omega) \, \widetilde{b}_{lm}(\omega) \, , \quad D_{lm}(\omega) = \zeta_l(\omega) \, \widetilde{b}_{lm}(\omega) \tag{D.16}$$

---

[1] The temperature and the *heat flux* are assumed continuous across the interface.

with

$$\xi_l(\omega) = \frac{1}{\Delta_l(\omega)} \left[\kappa_2\gamma_2\, j_l(\gamma_2 a_1)\, y_l'(\gamma_2 a_1) - \kappa_2\gamma_2\, j_l'(\gamma_2 a_1)\, y_l(\gamma_2 a_1)\right] \tag{D.17}$$

$$\eta_l(\omega) = \frac{1}{\Delta_l(\omega)} \left[\kappa_2\gamma_2\, j_l(\gamma_1 a_1)\, y_l'(\gamma_2 a_1) - \kappa_1\gamma_1\, j_l'(\gamma_1 a_1)\, y_l(\gamma_2 a_1)\right] \tag{D.18}$$

$$\zeta_l(\omega) = \frac{1}{\Delta_l(\omega)} \left[\kappa_1\gamma_1\, j_l(\gamma_2 a_1)\, j_l'(\gamma_1 a_1) - \kappa_2\gamma_2\, j_l'(\gamma_2 a_1)\, j_l(\gamma_1 a_1)\right] \tag{D.19}$$

and

$$\begin{aligned} \Delta_l(\omega) &= \kappa_1\gamma_1\, j_l'(\gamma_1 a_1)\, [j_l(\gamma_2 a_1)\, y_l(\gamma_2 a_2) - j_l(\gamma_2 a_2)\, y_l(\gamma_2 a_1)] \; + \\ &+ \kappa_2\gamma_2\, j_l(\gamma_1 a_1)\, [j_l(\gamma_2 a_2)\, y_l'(\gamma_2 a_1) - j_l'(\gamma_2 a_1)\, y_l(\gamma_2 a_2)] \end{aligned} \tag{D.20}$$

When the above results, equations (D.17) through (D.20), are inserted back into equation (D.11) the result stated in

$$\widetilde{T}(\mathbf{x}, \omega) = \sum_{lm} H_{lm}(\mathbf{x}, \omega)\, \widetilde{b}_{lm}(\omega) \tag{D.21}$$

where

$$H_{lm}(\mathbf{x}, \omega) = \begin{cases} \xi_l(\omega)\, j_l(\gamma_1 r)\, Y_{lm}(\theta, \varphi) \;, & 0 \le r \le a_1 \\ [\eta_l(\omega)\, j_l(\gamma_2 r) + \zeta_l(\omega)\, y_l(\gamma_2 r)]\, Y_{lm}(\theta, \varphi) \;, & a_1 \le r \le a_2 \end{cases} \tag{D.22}$$

transfer function is

$$H(r, \omega) = \begin{cases} \xi_0(\omega)\, j_0(\gamma_1 r) \;, & 0 \le r \le a_1 \\ \eta_0(\omega)\, j_0(\gamma_2 r) + \zeta_0(\omega)\, y_0(\gamma_2 r) \;, & a_1 \le r \le a_2 \end{cases} \tag{D.23}$$

Appendix E

Binary Maximum Length Sequence: Generation and properties

The input signal in a identification process is clearly an important tool to be used to extract the system description in an efficient manner. In §8.4.2 Pseudo-Random Noise (PRN) signals have proved to be an interesting choice in our case. As a disadvantage, the accuracy on the measurement can be difficult to achieve if the evaluated effect is small enough.

The main concept behind this approach is to replace an unfeasible white noise input, which would equally weight all frequencies, for a signal with the following properties:

1. The signal must be periodic with period T, taking only two possible values and changing only at discrete times $k\Delta T$.

2. The number of states on both binary positions must be approximately the same. More precisely, the difference in number should not exceed one.

3. Short runs must be more frequent that long ones. More precisely, half of the runs should be of length one, one-quarter of length two, one-eighth of length three, etc. Also for these runs it should be as many in one state than in the other.

4. The autocorrelation function should be two valued, peaking in the middle and flat towards the ends. Remarkably, this shape appears also when using a pulse signal which is one of the least random functions.

PRN sequence can be physically implemented by means of shift register generators and a modulo-two gate. The relation between the values of the sequence can be expressed as a recurrence of the r stage value to the previous stages via the modulo-two addition, written as

$$a_r = c_1 a_{r-1} \oplus c_2 a_{r-2} \oplus \ldots c_n a_{r-n} \tag{E.1}$$

where the c_i coefficients have a value corresponding to a logic 0 or a logic 1 and the '$\oplus$' sign refers to the modulo-two addition. For a given number of stages in a register there is a maximum to the number of digits which occur before the sequence repeats itself. This is then a *maximum length sequence*.

The binary maximum length sequence is therefore a sequence of binary values with complies with the maximum length requirement and has, consequently, $N = 2^{n-1}$ bits length.

Generation The generating function of the shift register is defined as

$$G(x) = \sum_{r=0}^{\infty} a_r x^r \tag{E.2}$$

It can be shown that the generating function can be expressed as [28]

$$G(x) = \frac{c_n}{1 - \sum_{i=1}^{n} c_i x^i} \tag{E.3}$$

where the denominator $F(x) = 1 - \sum_{i=1}^{n} c_i x^i$ is called the *characteristic polynomial*. This polynomial is better understood when written as

$$F(x) = x[I \oplus \sum D^j] \tag{E.4}$$

where D^i is an algebraic operator, the effect of which is to delay by i digits the variable it operates on, I is the identity operator and the sum goes through all the active shift register stages (the ones that are feeded back in the shift register implementation).

Once the mathematical framework to describe the shift register sequence has been introduced, we can proceed to recover the BMLS as a special case. We will use the following result.

Given a characteristic polynomial, F(x), the necessary and sufficient condition for F(x) to generate a BMLS is to be irreducible and primitive.

We will just need to define our application and look in the tables for the characteristic polynomial that fits in. We will need, however, to know which are the properties of the BMLS in order to be able to perform this selection.

Properties We will focus our attention to the frequency domain properties of the BMLS being these features the ones that will mainly define our input signal.

The power spectrum of a BMLS signal with period $T = N \Delta T$ can be expressed as

$$S_{BMLS}(\omega) = \frac{a^2(N+1)\Delta t}{N} \sum_{r=1}^{N} \left[\frac{\sin(r \, \pi/N)}{r \, \pi/N} \right] \qquad \text{(E.5)}$$

The power spectrum is therefore flat (since $\sin(r \, \pi/N)/(r \, \pi/N) \simeq 1$ for $r \ll N$) in an effective bandwidth arriving at the frequency where S_{BMLS} has fallen 3dB. The effective frequency band is therefore

$$f = \{ \frac{1}{N \, \Delta T}, \frac{1}{3 \, \Delta T} \} \qquad \text{(E.6)}$$

This is clearly seen in figure (E.1) where an arbitrary BMLS implementation is compared to a pulse of the same duration both in time and frequency domain. As expected, the random behavior in time domain translates into a more constant frequency spectra which can be more suitable for our purpose using the same power and time conditions than in the standard pulse application.
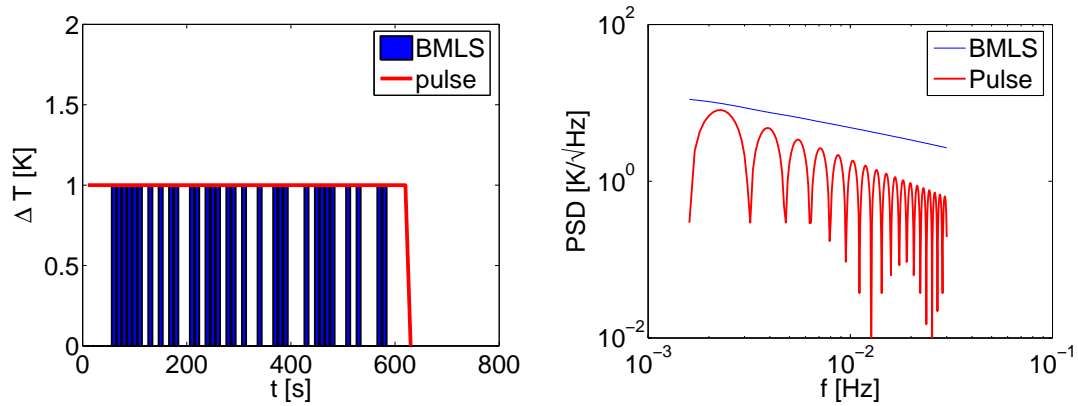

Figure E.1: BMLS versus pulse characteristics in time (left) and frequency (right) domain

LTP requirements   From the previous properties one can derive two main requirements that must to be accomplished in our application, independently of the location where these pulses may be applied in the LCA, and which can easily be traced into BMLS conditions.

In first place, the measuring bandwith is defined in the LTP as $1 \, \text{mHz} < f < 30 \, \text{mHz}$, we are therefore interested in sequences with an effective bandwith starting at $1 \, \text{mHz}$. From equation (E.6) a condition can be found for the minimum length of the sequence to fulfill this condition

$$N \, \Delta T \geq 1000 \, s \qquad \text{(E.7)}$$

We can also add a new constraint on the ΔT parameter. This will come from the DAU switching frequency which sets a limit on the minimum time step of our BMLS impulses. If we

consider that the DAU can not supply heat pulses in a timescale shorter than $1\,\mathrm{s}$ we will have

$$\Delta T \geq 1\,\mathrm{s} \tag{E.8}$$

which jointly with equation (E.7) implies $N \geq 1000$. At the same time, we know that N is related to the order of the characteristic polynomial by the relation $N = 2^n - 1$ and hence, in the case being studied it will imply a $n \geq 10$ polynomial. The only parameter to be known to generate the sequence is the amplitude which is directly related to the location considered in each case.

Bibliography

[1] B. Abbott et al. All-sky search for periodic gravitational waves in LIGO S4 data. *arXiv:0708.3818*.

[2] B. Abbott et al. First Cross-Correlation Analysis of Interferometric and Resonant-Bar Gravitational-Wave Data for Stochastic Backgrounds. *arXiv:gr-qc/0703068v1*.

[3] B. Abbott et al. Search for gravitational waves from binary inspirals in S3 and S4 LIGO data. *arXiv:0704.3368v2*.

[4] B. Abbott et al. Search for gravitational-wave bursts in LIGO data from the fourth science run. *Class. Quantum Grav.*, 24:5343–5369, 2007.

[5] A. Abramovici et al. LIGO: The Laser Interferometer Gravitational-Wave Observatory. *Science*, 256:325, 1992.

[6] M. Abramowitz and I. A. Stegun. *Handbook of mathematical functions*. Dover Publications, New York, 1972.

[7] O. Aguiar et al. The Gravitational Wave Detector "Mario Schenberg": Status of the Project. *Braz. J. Phys.*, 32, 2002.

[8] ALSTOM. ESATAN Engineering Manual (version 9.4). Technical Report EM-ESATAN-056, 2005.

[9] M. Ando et al. Stable Operation of a 300-m Laser Interferometer with Sufficient Sensitivity to Detect Gravitational-Wave Events within Our Galaxy. *Phys. Rev. Lett.*, 256:86, 2001.

[10] S. Anza et al. The LTP experiment on the LISA Pathfinder mission. *Class. Quantum Grav.*, 22:S125–S138, 2005.

[11] S. Anza, C. Navau, D. Chen, and A. Sanchez. Second proposal of Magnetic Diagnostic set up for the LTP. Technical Report S2-UAB-TN-3007, UAB, Apr. 2005.

[12] H. Araújo et al. LISA and LISA PathFinder, the endeavour to detect low frequency GWs. *J. Phys.: Conf. Ser.*, 66:012003, 2007.

[13] P. Astone et al. Long-term operation of the Rome 'Explorer' cryogenic gravitational wave detector. *Phys. Rev. D*, 47:362–375, 1993.

[14] P. Astone et al. The gravitational wave detector NAUTILUS operating at T=0.1 K. *Astroparticle Physics*, 7:231, 1997.

[15] B Lange. Experimental Gravitational Physics Using Drag-Free Satellites. http://www.dragfreesatellite.com.

[16] P. Bender et al. Laser Interferometer Space Antenna: A Cornestone Mission for the Observation of Gravitational Waves. Technical Report ESA-SCI(2000)11, ESA, 2000.

[17] P. L. Bender and D. Hils. Confusion noise level due to galactic and extragalactic binaries. *Class. Quantum Grav.*, 14:1439–1444, 1997.

[18] E. Berti, A. Buonanno, and C. M. Will. Testing general relativity and probing the merger history of massive black holes with LISA. *Class. Quantum Grav.*, 22:S943–S954, 2005.

[19] C. Bradaschia et al. The VIRGO Project: A wide band antenna for gravitational wave detection. *Nucl Instrum Methods A*, 289:518, 1990.

[20] L. Carbone. *Ground based investigation of force noise sources for LISA*. PhD thesis, 2005.

[21] L. Carbone, A. Cavalleri, , G. Ciani, R. Dolesi, M. Hueller, D. Tombolato, S. Vitale, and W. Weber. Thermal gradient-induced forces on geodetic reference masses for LISA. *submitted to Physical Review D*.

[22] L. Carbone, A. Cavalleri, R. Dolesi, C. Hoyle, M. Hueller, S. Vitale, and W. Weber. Characterization of disturbance sources for LISA: torsion pendulum results. *Class. Quantum Grav.*, 22:S509–S519, 2005.

[23] L. Carbone et al. Achieving Geodetic Motion for LISA Test Masses: Ground Testing Results. *Phys. Rev. Lett.*, 91:151101, 2003.

[24] H. S. Carslaw and J. C. Jaeger. *Conduction of Heat in Solids*. Clarendon Press, Oxford, 1959.

[25] M. Cerdonio et al. The Ultracryogenic Gravitational Wave Detector AURIGA. *Class. Quantum Grav.*, 14:1491, 1997.

[26] COMSOL. Multiphysics webpage. http://www.comsol.com.

[27] K. Danzmann. System Requirements for the LISA Technology Package on board SMART-2. Technical report, AEI, Sept. 2001.

[28] W. Davies. *System identification for self-adaptive control.* John Wiley and Sons, New York, 1970.

[29] A. de Waard and G. Frossati. MiniGRAIL, a 65 cm spherical antenna. *Proc. of the 3th Edoardo Amaldi Conference on Gravitational waves*, page 268, 1999.

[30] A. Einstein. Die Grundlage der allgemeinen Relativitätstheorie. *Annal. der Phys.*, 49, 1916.

[31] E. J. Elliffe, J. B. ad A Deshpande, J. Hough, C. Killow, S. Reid, D. Robertson, S. Rowan, H. Ward, and C. Cagnoli. Hydroxide-catalysis bonding for stable optical systems for space. *Class. Quantum Grav.*, 22:S257–S267, 2005.

[32] P. Eykhoff. *System identification.* John Wiley and Sons, New York, 1974.

[33] A. Franzoso. Assessement on the DDS power on the electrode housing. Technical Report S2-CGS-TN-3013, CGS, Feb. 2006.

[34] A. Franzoso. LISA Core Assembly Thermal Model Description. Technical Report S2-CGS-TN-3031 Issue 1.0, CGS, Feb. 2007.

[35] J. R. Gair et al. Event rate estimates for LISA extreme mass ratio capture sources. *Class. Quantum Grav.*, 21:S1595–S1606, 2004.

[36] P. Gibbs. How does a light mill work ?
http://www.math.ucr.edu/home/baez/physics/General/LightMill/light-mill.html.

[37] G. Heinzel et al. Interferometry for the LISA technology package (LTP) aboard SMART-2. *Class. Quantum Grav.*, 22:S153–S161, 2003.

[38] G. Heinzel et al. The LTP interferometer and phasemeter. *Class. Quantum Grav.*, 21:S581–S588, 2004.

[39] G. Heinzel et al. Successful testing of the LISA Technology Package (LTP) interferometer engineering model. *Class. Quantum Grav.*, 22:S149–S154, 2005.

[40] J. P. Holman. *Heat Transfer.* Mc Graw-Hill, New York, 1976.

[41] J. R. Howell. A catalog of radiation heat transfer configuration factors.
http://www.me.utexas.edu/~howell/.

[42] M. Hueller. *Geodesic motion of LISA test masses: development and testing of drag-free position sensors.* PhD thesis, 2003.

[43] R. A. Hulse and J. H. Taylor. Discovery of a pulsar in a binary system. *Astrop. Jour.*, 195:L51, 1975.

[44] F. P. Incropera, D. P. DeWitt, T. L. Bergman, and A. S. Lavine. *Fundamentals of Heat and Mass Transfer.* John Wiley and Sons, New York, 1996.

[45] G. Kahl. DDS Subsystem Specification. Technical Report S2-ASD-RS-3004 Issue 4.2, EADS Astrium (Germany), May 2006.

[46] S. M. Kay. *Modern spectral estimation : theory and application.* Prentice Hall, Englewood Cliffs, NJ, 1988.

[47] C. Kittel and H. Kroemer. *Thermal Physics.* W. H. Freeman and Co., San Francisco, 1980.

[48] L. Ljung. *System Identification: Theory for the user.* Prentice Hall, Englewood Cliffs, NJ, 1999.

[49] A. Lobo. Effect of a weak plane GW on a light beam. *Class. Quantum Grav.*, 9:21385–1394, 1992.

[50] A. Lobo. The detection of gravitational waves. *Lect.Notes Phys.*, 617:210–241, 2003.

[51] A. Lobo. DDS Science Requirements Document. Technical Report S2-IEEC-RS-3002, IEEC, Feb. 2005.

[52] A. Lobo et al. In-flight diagnostics for LISA Pathfinder. *AIP Conf. Proc.*, 873:S171–S176, 2005.

[53] A. Lobo and M. Nofrarias. Thermal Insulator Design for Temperature Sensors. Technical Report S2-IEEC-TN-3002, IEEC, Nov. 2004.

[54] A. Lobo, M. Nofrarias, J. Ramos, P. Riu, and J. Sanjuan. Temperature Sensors and FEE Prototype Test Plan and Procedure. Technical Report S2-IEEC-TP-3001, IEEC, Nov. 2004.

[55] A. Lobo, M. Nofrarias, J. Ramos, and J. Sanjuan. On-ground tests of LISA PathFinder thermal diagnostics system. *Class. Quantum Grav.*, 23:5177–5193, 2006.

[56] A. Lobo, M. Nofrarias, and J. Sanjuan. LTP thermal diagnostics. *Class. Quantum Grav.*, 22:S171–S176, 2005.

[57] A. F. G. Marín. *Minimisation of optical pathlength noise for the detection of gravitational waves with the spaceborne laser interferometer LISA and LISA Pathfinder.* PhD thesis, 2007.

[58] A. F. G. Marín et al. Phase locking to a LISA arm: first results on a hardware model. *Class. Quantum Grav.*, 22:S235–S242, 2005.

[59] A. F. G. Marín et al. Interferometric characterization of the Optical Window for LISA and LISA Pathfinder. *AIP Conf. Proc.*, 873:344–348, 2006.

[60] A. F. G. Marín et al. On-orbit alignment and diagnostics for the LISA Technology Package. *Class. Quantum Grav.*, 23:S133–S140, 2006.

[61] L. M. Martínez and S. Garcia. LISA Pathfinder Test Masses Magnetic Field and Magnetic Field Gradient Monitoring. Technical Report S2-IEC-TN-3024, IEEC, May 2006.

[62] E. Mauceli et al. The Allegro gravitational wave detector: Data acquisition and analysis. *Phys. Rev. D*, 54:1264 – 1275, 21996.

[63] C. W. Misner, K. S. Thorne, and J. A. Wheeler. *Gravitation*. W. H. Freeman and Company, New York, 1973.

[64] NASA. Outgassing Data for Selecting Spacecraft Materials Online.
http://outgassing.nasa.gov/.

[65] A. M. Nobili. Radiometer effect in space missions to test the equivalence principle open discussion.
http://eotvos.dm.unipi.it/opendiscussion/.

[66] A. M. Nobili, D. Bramanti, G. Comandi, R. Toncelli, E. Polaco, and G. Catastini. Radiometer effect in space missions to test equivalence principle. *Phys. Rev. D*, 63:101101, 2001.

[67] M. Nofrarias. Heaters signal on the inertial sensor. Technical Report S2-IEC-TN-3013, IEEC, July 2005.

[68] M. Nofrarias. DDS heaters characterisation. Technical Report S2-IEC-TN-3025, IEEC, June 2006.

[69] M. Nofrarias. Thermal simulations for the thermal sensors insulator test design . Technical Report S2-IEC-TN-3005, IEEC, Feb. 2006.

[70] M. Nofrarias, A. G. Marín, G. Heinzel, A. Lobo, J. Ramos-Castro, J. Sanjuan, and K. Danzmann. Thermal diagnostic test in the LTP experiment. *AIP Conf. Proc.*, 873:199–203, 2006.

[71] M. Nofrarias, A. G. Marín, A. Lobo, G. Heinzel, J. Ramos-Castro, J. Sanjuan, and K. Danzmann. Thermal diagnostic of the Optical Window on board LISA Pathfinder. *Class. Quantum Grav.*, 24:5103–5121, 2007.

[72] M. Nofrarias and J. Sanjuan. Thermal noise due to wiring in the thermal test. Technical Report S2-IEEC-TN-3003, IEEC, Oct. 2004.

[73] J. A. Ortega-Ruiz, A. Conchillo, X. Xirgu, and C. Boatella. Mission Critical Software in LISA Pathfinder. *AIP Conf. Proc.*, 873:697–701, 2006.

[74] R. Pallás Areny. *Sensores y acondicionadores de señal*. Marcombo, Barcelona, 2003.

[75] A. Passian, A. Wig, F. Meriaudeau, T. L. Ferrell, and T. Thundat. Knudsen forces in microcantilevers. *Journal Applied Physics*, 92:6326–6333, 2002.

[76] H. Peabody and S. Merkowitz. LISA thermal design. *Class. Quantum Grav.*, 22:S403–S411, 2005.

[77] S. Pollack, S. Schlamminger, and J. H. Gundlach. Outgassing, Tmeperature Gradients and the Radiometer Effect in LISA: A Torsion Pendulum Investigation. *AIP Conf. Proc.*, 873:158–164, 2007.

[78] J. G. Proakis and D. G. Manolakis. *Digital Signal Processing*. Prentice Hall, Englewood Cliffs, NJ, 1996.

[79] J. Ramos and J. Sanjuan. DDS Thermal Diagnostic Prototype Design. Technical Report S2-UPC-DDD-3001, UPC, Apr. 2005.

[80] A. Roth. *Vacuum Technology*. Elsevier Science Publishers, New York, 1982.

[81] A. Rüdiger. Residual gas effects in space-borne position sensors. *unpublished*, 2002.

[82] J. Sanjuan. Temperature sensors market survey and trade-off. Technical Report S2-IEEC-TN-3001, IEEC, Oct. 2004.

[83] J. Sanjuan. Diagnostic elements DAUs interface configuration. Technical Report S2-IEEC-TN-3023, IEEC, May 2006.

[84] J. Sanjuan. Feasibility analysis of using a NTC thermistor as a heater on the Inertial Sensor and Optical Window. Technical Report S2-IEEC-TN-3022, IEEC, Feb. 2006.

[85] J. Sanjuan. New Thermal Insulator Design. Technical Report S2-IEC-TN-3026, IEEC, Sept. 2006.

[86] J. Sanjuan, A. Lobo, M. Nofrarias, J. Ramos-Castro, and P. Riu. Thermal diagnostics Front-End Electronics for LISA Pathfinder. *Rev. Sci. Instr.*, 78:104904, 2007.

[87] J. Sanjuan and J. Ramos. Temperature sensors and FEE Test Report. Technical Report S2-IEEC-TR-3001, IEEC, Apr. 2005.

[88] P. Sarra. Inertial Sensor Head Vacuum control Document. Technical Report S2-CGS-TN-3003, CGS, Oct. 2005.

[89] B. Schumaker. Disturbance reduction requirements for LISA. *Class. Quantum Grav.*, 20:S239–253, 2003.

[90] B. Schutz. *A First Course in General Relativity*. Cambridge University Press, 1985.

[91] B. S. Sheard. Laser frequency stabilization by locking to a LISA arm. *Phys. Lett. A*, 320:9, 2003.

[92] SRL. Sensitivity Curve for Spaceborne Gravitational Wave Observatories. http://www.srl.caltech.edu/~shane/sensitivity/index.html.

[93] Stanford University. Gravity Probe B Experiment Web page. http://einstein.stanford.edu/.

[94] R. T. Stebbins, P. L. Bender, J. Hanson, C. D. Hoyle, B. L. Schumaker, and S. Vitale. Current error estimates for LISA spurious accelerations. *Class. Quantum Grav.*, 21:S653–S660, 2004.

[95] A. Stroeer and A. Vecchio. The LISA verification binaries. *Class. Quantum Grav.*, 23:S809–S818, 2006.

[96] S. Timoshenko. *Strength of Materials*. Van Nostrand, New York, 1956.

[97] M. Tinto and S. V. Dhurandhar. Time-Delay Interferometry. *Living Rev. Relativity*, 8, 2005.

[98] P. Touboul and M. Rodrigues. The MICROSCOPE space mission. *Class. Quantum Grav.*, 18:2487–2498, 2001.

[99] S. Vitale. The LISA Technology Package on board SMART-2. Technical Report Unitn-Int 10-2002, University of Trento, 2002.

[100] S. Vitale. Science Requirements and Top-level Architecture Definition for the LISA Technology PAckage (LTP) on Board LISA Pathfinder (SMART-2). Technical Report LTPA-UTN-ScRD-Iss003-Rev1, University of Trento, 2005.

[101] V. Wand, F. Guzmán, G. Heinzel, and K. Danzmann. LISA Phasemeter development. *AIP Conf. Proc.*, 873:689–696, 2006.

[102] D. Wealthy. LTP Mission Performance Budgets. Technical Report S2-ASU-RP-2007, EADS Astrium (UK), 2004.

[103] J. Weber. Evidence for Discovery of Gravitational Radiation. *Phys. Rev. Lett.*, 22:1320 – 1324, 1969.

[104] S. Weinberg. *Gravitation and Cosmology*. John Wiley and Sons, New York, 1972.

[105] B. Willke et al. The GEO 600 gravitational wave detector. *Class. Quantum Grav.*, 19:1377 – 1387, 2002.

[106] P. Worden, J. Mester, and R. Torii. STEP error model developement. *Class. Quantum Grav.*, 18:2543–2550, 2001.

[107] Y. Wu. Theory of Thermal Transpiration in a Knudsen gas. *Journal of Chemical Physics*, 48:889–894, 1968.